JOHANNES GUTENBERG UNIVERSITÄT MAINZ

Organofunctionalized Polyoxometalates as Functional Components in (Photo-)Catalysis

Dissertation zur Erlangung des Grades “Doktor der Naturwissenschaften” im Promotionsfach Chemie am Fachbereich Chemie, Pharmazie, Geographie und Geowissenschaften der Johannes Gutenberg-Universität Mainz

Garima Sachdeva

Born in Rewari, India

Mainz, 2026

Betreuer: [redacted]

Zweitgutachterin: [redacted]

Tag der mündlichen Prüfung:

“Everything comes to us that belongs to us if we create the capacity to receive it”

-Rabindranath Tagore

Dedicated to my parents

Abstract

Molecular metal oxides, or polyoxometalates (POMs), are a unique class of compounds due to their tunable structures and rich redox chemistry. The possibility of covalent functionalization of POMs with organic ligands enables the formation of inorganic-organic POM hybrids, thereby expanding their physicochemical properties. In particular, Anderson-type POMs provide a modular platform for covalent functionalization with organic groups and metal complexes to design multifunctional hybrids. Such hybrids have been explored in the areas of catalysis, energy conversion and storage, supramolecular chemistry, molecular devices, and biomedicine. Despite substantial efforts to covalently attach metal complexes onto POMs, the formation of such architectures is still challenging. Furthermore, most studies on Anderson POMs focus on symmetric functionalization, where similar moieties are attached on both sides of the cluster. There is therefore a need to design POM hybrids with asymmetric modifications, as this allows the incorporation of multiple functions within a single molecular framework. Organofunctionalized Anderson POMs can also assemble to form 3D supramolecular architectures through metal coordination, thus broadening the application scope. This work focuses mainly on the development of asymmetric Anderson POM hybrids, which were tested for the light-driven hydrogen evolution reaction. Additionally, the formation of supramolecular POM-based aerogel was studied.

In the first project, a stoichiometrically controlled complexation strategy was employed to design two rigid POM-based hybrids consisting of mono- and di-functionalized Pt HER catalysts covalently attached to Anderson POM anions. The electrostatic coupling of the synthesized dyads with a ruthenium photosensitizer enabled visible-light-driven HER in a homogeneous system. The photocatalytic studies revealed a direct correlation between the number of Pt-based HER catalytic sites and the hydrogen evolution activity.

In the second project, stepwise coordination of a Pt HER catalyst and an iridium photosensitizer onto a bpy-functionalized polyoxomolybdate resulted in the formation of a POM-based photoactive triad. The triad was fully characterized using FT-IR, 1D and 2D NMR, UV-Vis spectroscopy, XPS, and MALDI-TOF. Initial photocatalytic results

demonstrated the principal reactivity of the molecular species. Furthermore, mechanistic photophysical and computational studies provided insights into the electronic structure as well as charge-separation and charge-transfer properties.

For the third project, a facile approach to convert a POM-based organogel into an aerogel using a scalable freeze-drying procedure was developed. The organogel was achieved by the reaction of $ZnCl_2$ with $\{MnMo_6\}$ in acetonitrile solution. Insights into the factors influencing gelation were obtained by varying parameters such as POM type, metal salt, and solvent. Various experimental techniques were used to characterize the organogel and aerogel. The aerogel was tested as a heterogeneous catalyst for the selective oxidation of primary alcohols. Additionally, initial recyclability and stability studies were performed to evaluate the catalytic performance of the aerogel.

Zusammenfassung

Molekulare Metalloxide, so genannte Polyoxometalate (POMs) stellen aufgrund ihrer modifizierbaren Strukturen und ihrer vielfältigen Redoxchemie eine einzigartige Klasse molekularer Verbindungen dar. Die Möglichkeit der kovalenten Funktionalisierung von POMs mit organischen Liganden ermöglicht die Bildung von anorganisch-organischen POM-Hybriden, wodurch sich deren physikalisch-chemische Eigenschaften erweitern. Insbesondere POMs vom Anderson-Typ bieten eine modulare Plattform für die kovalente Funktionalisierung mit organischen Gruppen und Metallkomplexen, um multifunktionale Hybride zu entwickeln. Solche Hybride wurden in den Bereichen Katalyse, Energieumwandlung und -speicherung, supramolekulare Chemie, molekulare Bauelemente und Biomedizin untersucht. Trotz erheblicher Anstrengungen, Metallkomplexe kovalent an das POM zu binden, stellt die Synthese solcher Architekturen nach wie vor eine Herausforderung dar. Darüber hinaus konzentrieren sich die meisten Studien zu Anderson POMs auf die symmetrische Funktionalisierung, bei der identische Molekülgruppen an beiden Seiten des Clusters angebracht werden. Es besteht daher ein Bedarf an der Entwicklung von POM-Hybriden mit asymmetrischen Modifikationen, da dies die Einbindung mehrerer Funktionen in ein einziges molekulares Gerüst ermöglicht. Organofunktionalisierte Anderson POMs können sich durch Metallkoordination auch zu dreidimensionalen supramolekularen Strukturen zusammenlagern, wodurch sich ihr Anwendungsspektrum erweitert. Diese Arbeit konzentriert sich zum einen auf die Entwicklung asymmetrischer Anderson POM-Hybride, die im Hinblick auf die lichtgetriebene Wasserstoffentwicklungsreaktion getestet wurden. Darüber hinaus wurde die Bildung supramolekularer, katalytisch aktiver Aerogele auf POM-Basis untersucht.

Im ersten Projekt wurde eine stöchiometrisch kontrollierte Strategie zur Komplexierung angewandt, um zwei starre POM-basierte Hybride zu entwickeln, die aus mono- und di-funktionalisierten Pt HER-Katalysatoren bestehen, die kovalent an Anderson POM Anionen gebunden sind. Die elektrostatische Kopplung der synthetisierten Dyaden mit einem Ruthenium-Photosensibilisator ermöglichte die durch sichtbares Licht getriebene HER in einem homogenen System. Photokatalytische Studien zeigten einen direkten Zusammenhang zwischen der

Anzahl der Pt-basierten HER-aktiven Zentren und der Wasserstoffentwicklungsaktivität.

Im zweiten Projekt führte die schrittweise Koordination eines Pt HER-Katalysators und eines Iridium-Photosensibilisators auf ein mit bpy funktionalisiertes Polyoxomolybdat zur Bildung einer POM-basierten photoaktiven Triade. Die Triade wurde mittels FT-IR, 1D- und 2D-NMR, UV-Vis-Spektroskopie, XPS und MALDI-TOF vollständig charakterisiert. Erste photokatalytische Ergebnisse belegten die grundsätzliche Reaktivität der Molekülspezies. Darüber hinaus lieferten mechanistische, photophysikalische und theoretische Untersuchungen Einblicke in die elektronische Struktur sowie in die Ladungstrennungs und den Ladungstransfer.

Im Rahmen des dritten Projekts wurde ein einfaches Verfahren entwickelt, um ein POM-basiertes Organogel mittels eines skalierbaren Gefriertrocknungsverfahrens in ein Aerogel umzuwandeln. Das Organogel wurde durch die Reaktion von $ZnCl_2$ mit $\{MnMo_6\}$ in einer Acetonitril-Lösung hergestellt. Durch Variation von Parametern wie POM-Typ, Metallsalz und Lösungsmittel wurden Erkenntnisse über die Faktoren gewonnen, die die Gelierung beeinflussen. Zur Charakterisierung des Organogels und des Aerogels wurden verschiedene experimentelle Techniken eingesetzt. Das Aerogel wurde als heterogener Katalysator für die selektive Oxidation von primären Alkoholen getestet. Darüber hinaus wurden erste Untersuchungen zur Wiederverwendbarkeit und Stabilität durchgeführt, um die katalytische Leistung des Aerogels zu bewerten.

Table of Contents

List of Abbreviations

The following abbreviations were used in this thesis:

POM	Polyoxometalate
M	Metal
X	Heteroatom
e.g.	Exempli Gratia (for example)
i.e.	Id Est (that is)
ca.	Circa (approximately)
FT-IR	Fourier Transform Infrared Spectroscopy
NMR	Nuclear Magnetic Resonance
DOSY	Diffusion-Ordered Spectroscopy
UV-Vis	Ultraviolet-Visible Spectroscopy
MALDI-TOF	Matrix-assisted Laser Desorption/Ionization Time-of-Flight
XRD	X-ray Diffraction
pXRD	powder X-ray Diffraction
XPS	X-ray Photoelectron Spectroscopy
SEM	Scanning Electron Microscopy
CV	Cyclic Voltammetry
SWV	Square-Wave Voltammetry
μXRF	Micro X-ray Fluorescence Spectroscopy
TGA	Thermogravimetric Analysis
BET	Brunauer-Emmett-Teller
BJH	Barrett-Joyner-Halenda
TEM	Transmission Electron Microscopy
HAADF	High-angle Annular Dark Field
STEM	Scanning Transmission Electron Microscopy
HRTEM	High-Resolution Transmission Electron Microscopy
SAED	Selected Area Electron Diffraction
EDX	Energy Dispersive X-ray
fs-TA	Femtosecond Transient Absorption Spectroscopy
RP-HPLC	Reverse Phase-High Performance Liquid Chromatography
D	Diffusion Coefficients

DMF	N,N-dimethylformamide
MeCN	Acetonitrile
DMA	Dimethylammonium
DMSO	Dimethyl sulfoxide
*t*BuOOH	*Tert*-butyl hydroperoxide
OAc	Acetate Ion
DFT	Density Functional Theory
TD-DFT	Time-Dependent Density Functional Theory
HER	Hydrogen Evolution Reaction
OER	Oxygen Evolution Reaction
OEC	Oxygen Evolving Complex
$NADP^+$	Nicotinamide Adenine Dinucleotide Phosphate
SED	Sacrificial Electron Donor
SEA	Sacrificial Electron Acceptor
PS	Photosensitizer
Cat	Catalyst
TEOA	Triethanolamine
TEA	Triethylamine
LED	Light Emitting Diode
MLCT	Metal-to-Ligand Charge Transfer
LMCT	Ligand-to-Metal Charge Transfer
CT	Charge Transfer
LC	Ligand-Centered
ESA	Excited-State Absorption
DAS	Decay Associated Spectra
ISC	Intersystem Crossing
TONs	Turnover Numbers
TOF	Turnover Frequency
ps	Picosecond
ns	Nanosecond
π	Pi
tris	Tris(hydroxymethyl)aminomethane
$n\text{Bu}_4\text{N}$	Tetrabutylammonium

TMA	Tetramethylammonium
1D	One-dimensional
2D	Two-dimensional
3D	Three-dimensional
bpy	2,2′-Bipyridine
ppy	Phenyl pyridine
dtbbpy	4,4′-Di-tert-butyl-2,2′-dipyridyl
HOMO	Highest Occupied Molecular Orbital
LUMO	Lowest Unoccupied Molecular Orbital
PHEMDs	Photo-Hydrogen-Evolving Molecular Devices
N^N	Diimine Ligand
E_I	Ionization Energy
E_{ea}	Electron Affinity
LMWGs	Low Molecular Weight Gelators
DCTB	Trans-2-[3-(4-tert-butylphenyl)-2-methyl-2-propenyliden]malononitrile

Notation

Polyhedral building blocks are presented using a square bracket notation, [MO_x] (M = addenda atom, and x = 4–7) without the charge to provide structural information only. For example, an octahedral building block where six oxygen ligands (O) coordinate to the transition metal (M) will be indicated as [MO_6]. Metal-oxygen bonds are denoted as M–O for single bonds, and M=O for double bonds.

In addition to the standard square bracket notation, an abbreviated notation will be used for clarity, in which the number and type of the addenda atoms will be enclosed in curly brackets. For example, (nBu$_4$N)$_3$[MnMo$_6$O$_{18}${(OCH$_2$)$_3$CNH$_2$}$_2$] will be abbreviated as {MnMo$_6$}.

Table of Compounds

The following abbreviations were used for the compounds:

Formula	Abbreviation
$(n\mathrm{Bu_4N})_3[\mathrm{MnMo_6O_{18}\{(OCH_2)_3CNH_2\}_2}]$	$\{\mathrm{MnMo_6}\}$
$(n\mathrm{Bu_4N})_3[\mathrm{MnCo_6O_{18}\{(OCH_2)_3CNH_2\}_2}]$	$\{\mathrm{CoMo_6}\}$
$(n\mathrm{Bu_4N})_3[\mathrm{MnFe_6O_{18}\{(OCH_2)_3CNH_2\}_2}]$	$\{\mathrm{FeMo_6}\}$
$[\mathrm{Mo_{154}(NO)_{14}O_{448}H_{14}(H_2O)_{70}}]^{28-}$	$\{\mathrm{Mo_{154}}\}$
$[\mathrm{Mo^{VI}_{72}Mo^{V}_{60}O_{372}(OAc)_{30}(H_2O)_{72}}]^{42-}$	$\{\mathrm{Mo_{132}}\}$

1 Introduction

1.1 Hydrogen as a Sustainable Energy Carrier

The steady rise in global population and industrialization has led to a continuous increase in energy demand. To meet this growing demand, the consumption of fossil fuels has increased over the years. However, the major challenges associated with fossil fuels are their limited availability, complex extraction processes, and the release of greenhouse gases during their combustion.[1] The extensive use of fossil fuels thus leads to both resource depletion and significant climatic changes.[2,3] Currently, fossil fuels contribute *ca.* 75% of global greenhouse gas emissions and about 90% of all carbon dioxide emissions.[4] To address this critical environmental concern and reduce dependency on fossil fuels, a shift towards clean, renewable, and CO_2-emission-free energy resources is required.[5,6] One of the promising energy alternatives is the generation of hydrogen. The oxidation of hydrogen, either *via* a fuel cell or combustion generates only water as a by-product, thereby making it an environmentally benign energy carrier.[7] Furthermore, it has a higher gravimetric energy density compared to other carbon-based fuels.[8] At present, the production of hydrogen mainly relies on the conversion of natural gas, oil, and coal, which release CO_2. In contrast, around 4% of hydrogen is produced from renewable sources such as water, as shown in Figure 1.[9,10] Therefore, there is a need to use more renewable sources to reduce the emission of CO_2 into the atmosphere. A promising alternative is the use of solar energy, which is the most abundant energy resource on our planet.[11] Therefore, solar energy conversion and storage are an effective strategy to generate hydrogen, namely “solar hydrogen”. This concept will be discussed in detail in the following section.

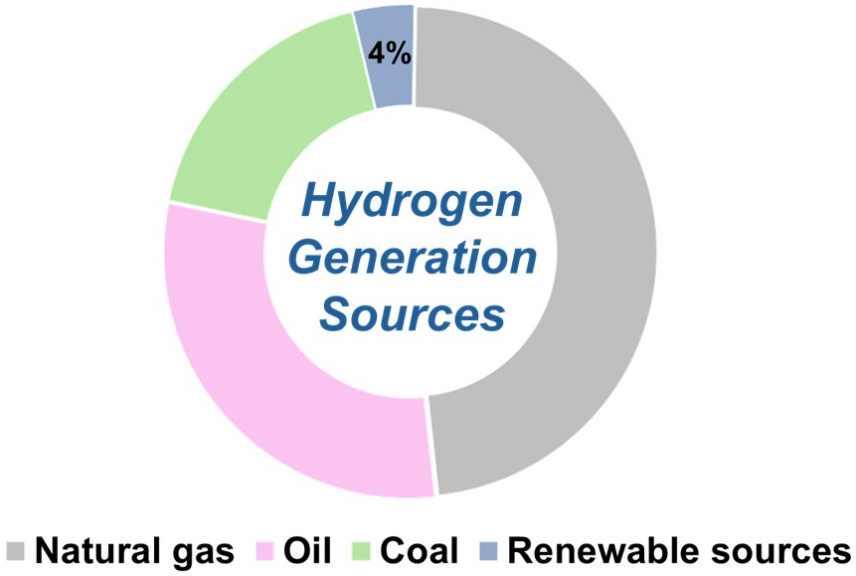

Figure 1: Illustration of global hydrogen production from various sources, according to reference. [9,10]

1.1.1 Artificial Photosynthesis: Mimicking Natural Photosynthesis

In order to generate solar hydrogen, solar energy should first be captured and converted into chemical bonds, as occurs in natural photosynthesis. In natural photosynthesis, sunlight is absorbed and transformed into higher energy components such as carbohydrates.[12] In this process, the initial step is the absorption of sunlight by photosystem II located in chloroplasts. This results in charge separation (or electron-hole pair generation) and further provides energy to carry out required redox events. The activation of the oxygen-evolving complex (OEC) occurs *via* oxidative holes to oxidise water to molecular oxygen. The excited electrons are transferred to photosystem I through an electron transfer chain. Upon a second light-induced excitation, electrons are transferred to the enzyme $NADP^+$ (Nicotinamide Adenine Dinucleotide Phosphate) reductase to produce the bio-reducing agent NADPH (reduced form of $NADP^+$).[13,14] The formed NADPH is further used in the Calvin cycle to reduce atmospheric CO_2 into carbohydrates.[15] This mechanism is called the Z-scheme of natural photosynthesis, see Figure 2.

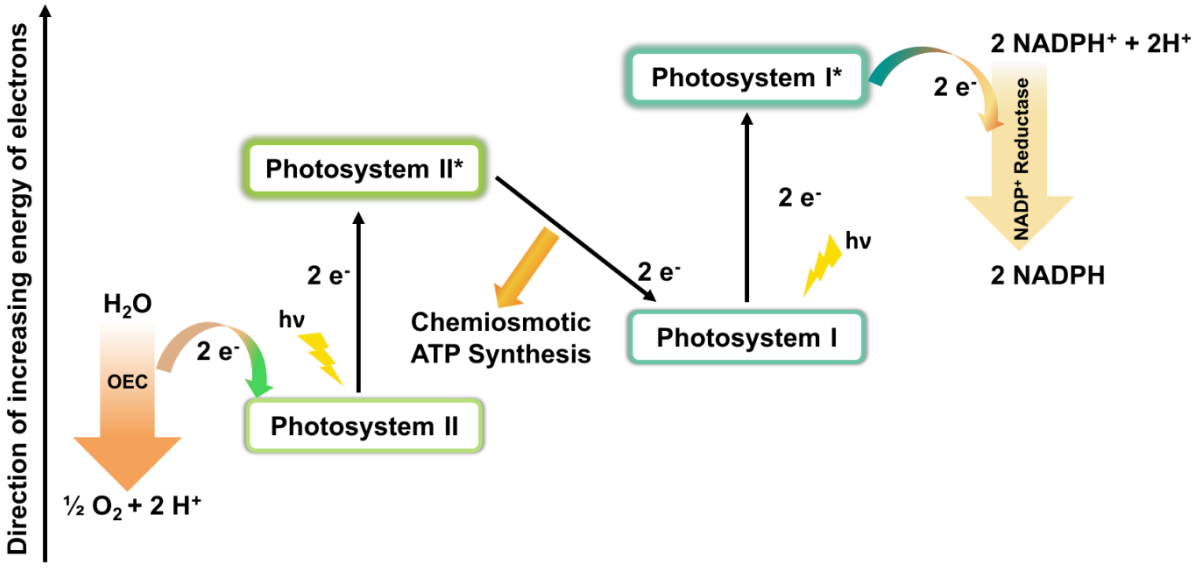

Figure 2: Simplified Z-scheme representation of the light-driven reactions in natural photosynthesis, where OEC: oxygen-evolving complex. The scheme is adapted from reference.[14]

Inspired by nature, artificial photosynthetic systems can be designed. In these systems, electrons from water oxidation can be used to reduce CO_2 to carbon-based fuels or to reduce protons to form molecular hydrogen.[13]

The key step in natural photosynthesis is the formation of light-induced charge-separated states that allow the conversion of light energy into chemical energy. Therefore, to perform artificial photosynthesis, light absorption through chromophores should result in charge separation, followed by charge transfer to obtain reducing and oxidising equivalents at the catalytic site, where hydrogen or oxygen evolution occur separately.[16] Due to the complexity of the entire reaction, it is better to split the overall process into two half-reactions i.e., the hydrogen evolution reaction (HER) and the oxygen evolution reaction (OER). In this way, both systems can be studied and optimized separately to obtain higher activity for HER and OER. For both half-reactions, a sacrificial electron donor (SED) or sacrificial electron acceptor (SEA) is needed for reductive or oxidative equivalents, respectively. Based on these requirements, hybrid materials represent a suitable class for designing artificial photosynthetic systems.

1.2 Hybrid Materials

In recent decades, the demand for improved performance and novel functions has driven the rapid development of hybrid materials. According to the International Union of Pure and Applied Chemistry (IUPAC), a hybrid material is described as a mixture of organic and inorganic components.[17] Such a combination allows the hybrid material to integrate the features of both components, resulting in unique properties.[18] Nowadays, hybrid materials are utilized in areas ranging from catalysis and energy conversion and storage to biomedical engineering and drug delivery.[19] The concept of hybrid materials dates back to ancient cave paintings, where nanocomposite paints were created by mixing aluminosilicate clays with mineral pigments and organic binders.[20] The field has expanded over the years, and a dramatic shift is seen in the 21st century due to advances in synthesis and characterization techniques that have broadened both fundamental understanding and application scope, see Figure 3.

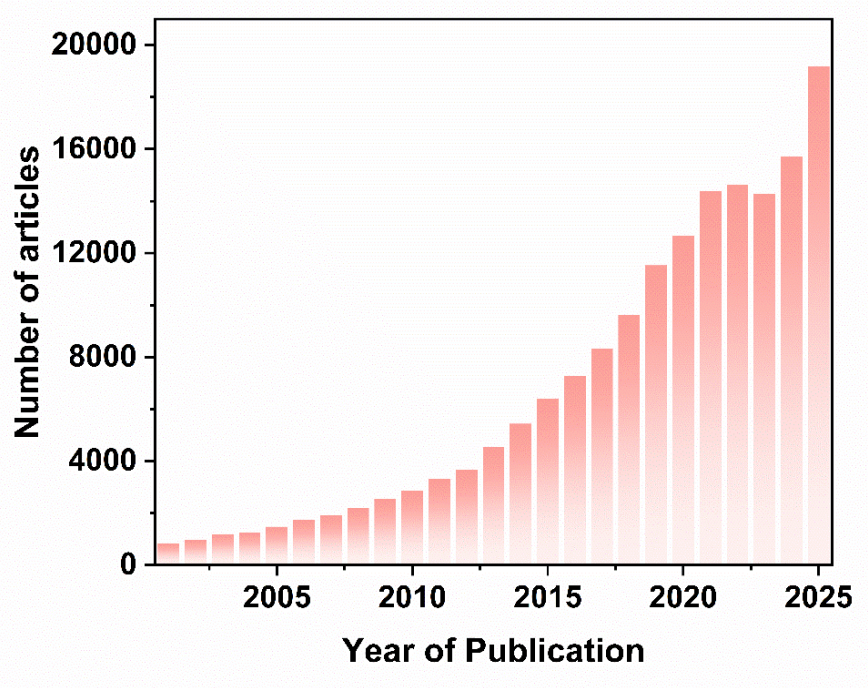

Figure 3: Illustration of publication trends for the keyword “hybrid material” from 2001 to 2025, highlighting the growing research interest in the field of hybrid materials. Data taken from Web of Science database.

The properties of hybrid materials are governed not only by the sum of the individual components, but also by the synergistic effects at their interface. One key advantage of inorganic-organic hybrid materials is the design of complex multifunctional systems from relatively simple building blocks.[21] Based on the nature of interactions between the components, hybrid materials are commonly classified into two categories. ***Class I*** hybrid materials are characterized by weak interactions such as van der Waals forces or hydrogen bonding. In contrast, ***Class II*** hybrid materials exhibit strong chemical interactions, including covalent bonds.[22] This classification illustrates how different interactions between organic and inorganic components in hybrid materials help to achieve tailored structural and functional characteristics. While both components influence the structure and properties of a hybrid material, the inorganic component governs properties such as structural integrity, electronic behaviour, and redox activity.[23] Among the wide range of inorganic building blocks, polynuclear metal oxide clusters, “polyoxometalates”, have emerged as versatile candidates. Their remarkable properties, such as rich redox chemistry and structural tunability make them suitable for designing hybrid materials. Their formation, characteristics, and functionalization will be discussed in detail in the subsequent chapters.

1.3 Polyoxometalates

1.3.1 History, Classification and General Structural Principles

The story of polyoxometalates began in 1826, when J.J. Berzelius reported the formation of a light-yellow crystalline solid after the addition of phosphoric acid to a molybdate solution.[24] Subsequent studies on molybdates and related tungsten-based compounds were carried out to understand their structure and composition. Around 100 years later, J.F. Keggin reported the structure of 12-phosphotungstic acid ($[PW_{12}O_{40}]^{3-}$) using powder X-ray diffraction images. Since then, this compound type has been referred to as the “Keggin” structure.[25,26]

Polyoxometalates (POMs) are discrete polyoxoanions composed of early transition metals as addenda atoms (M) (M = V, Mo, Nb, W, and Ta) in their higher oxidation states, typically in d^0 or d^1 electronic configurations. Their formation involves the self-assembly of $[MO_x]$ polyhedral units (x = 4–7), which are bridged through one oxo group (corner-sharing), two oxo groups (edge-sharing) or more rarely, three oxo groups (face-sharing), as illustrated in Figure 4.[27–29] The oxo-ligands may either bridge

neighbouring metal centers (M–O–M), connecting the polyhedra, or remain as terminal groups (M=O, M–O(H)) that define the cluster surface.

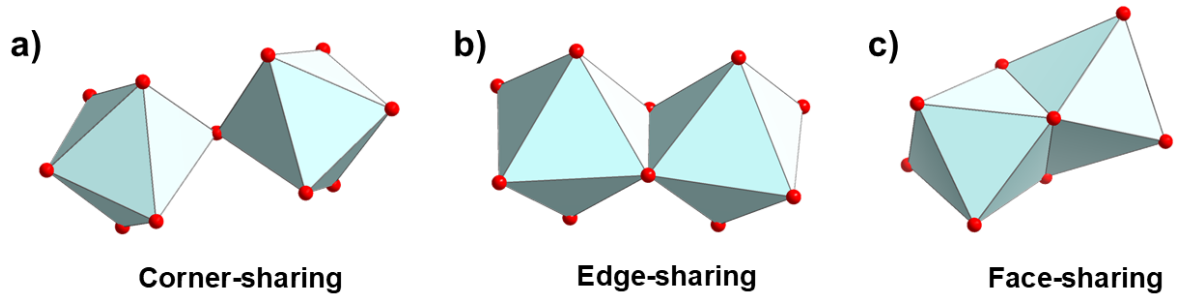

Figure 4: Representation of the three linking modes of two octahedral [MO_6] units: a) corner-sharing, b) edge-sharing, and face-sharing mode.[28] Colour scheme: O = red, and [MO_6] polyhedra = turquoise.

As mentioned earlier, the addenda metals in POMs are typically found in their higher oxidation states. This, in turn, allows for significant pπ-dπ overlap between the oxygen ligand and the addenda metal because of the availability of vacant metal d-orbitals. This reduces the nucleophilicity and basicity of terminal (M=O) bonds, thereby slowing down the growth of metal oxide structures. As a result, the formation of discrete molecular metal oxide clusters is favoured over infinite solid structures.[28,30] Notably, the polarization of the terminal oxygen atoms by the metal centers leads to weak proton binding and accounts for the high acidity of polyoxometalates.[31] Moreover, the ability of Mo- and W-based POMs to bind different numbers of oxygen atoms arises due to their favourable charge-to-ionic radius ratio, which enables the generation of coordination polyhedra ranging from [MO_4] to [MO_7] building blocks.

The wide variety of POM structures can be broadly classified into three categories: isopolyoxoanions, heteropolyoxoanions, and Mo-blues and Mo-browns.[32,33]

Isopolyoxoanions are the simplest POMs, consisting only of addenda and oxygen atoms without any heteroatoms, with the general formula $[M_xO_y]^{n-}$, except for protonated isopolyoxoanions, which contain protons. They are less stable than heteropolyoxoanions. Nevertheless, isopolyoxoanions possess some striking features such as strongly basic oxygen surfaces and high charges, which make them ideal building blocks for the synthesis of larger clusters.[34] One of the most common examples of this class is the Lindqvist hexametalate $[M_6O_{19}]^{n-}$, which consists of six edge-sharing octahedral [MO_6] units forming a large octahedron. An example of a hexaniobate Lindqvist structure is shown in Figure 5a.

Heteropolyoxoanions are the most widely studied class of POMs. They are represented by the general formula $[X_aM_xO_y]^{n-}$, where X is a heteroatom with x ≥ a. A wide range of heteroatoms (X) (e.g., Mn, Fe, Si, Ge, P, Cr, Zn) can be introduced into the metal-oxide framework, which can serve either as templating ions (e.g., PO_4^{3-} in the well-established Keggin structure $[PMo_{12}O_{40}]^{3-}$) or as linkers between several POM units to build supramolecular architectures.[35] Insertion of heterometals in the polyanions provides huge structural diversity and enables fine-tuning of catalytic, redox, and structural properties.[36,37] Some extensively studied heteropolyoxoanions structures are the Keggin $[XM_{12}O_{40}]^{n-}$, Anderson-Evans $[XM_6O_{24}]^{n-}$, and Wells-Dawson $[X_2M_{18}O_{62}]^{n-}$ structures, where M = Mo, W, and X = heteroatom. Examples of these structures are shown in Figure 5b, c, and d. The Anderson-Evans type POM is the focus of the present work and will be discussed in detail later.

Mo-blues and Mo-browns are reduced Mo-based POMs. They were first reported by C.W. Scheele in 1783, when a deep-blue solution was observed upon heating MoO_3 in concentrated nitric acid. However, in 1995, A. Müller reported the synthesis and structural characterization of a giant cluster $[Mo_{154}(NO)_{14}O_{448}H_{14}(H_2O)_{70}]^{28-}$ (= $\{Mo_{154}\}$), possessing a wheel-like topology (Figure 5e).[38] Another prominent example of a self-assembled Mo-blue species is $[Mo^{VI}_{72}Mo^{V}_{60}O_{372}(OAc)_{30}(H_2O)_{72}]^{42-}$ (= $\{Mo_{132}\}$), resembling a fullerene structure with integrated icosahedral symmetry.[39] The cluster is composed of 12 pentagonal $\{(Mo)Mo_5\}$ units linked by 30 $\{Mo_2\}$ groups *via* corner-sharing oxygen bridges.

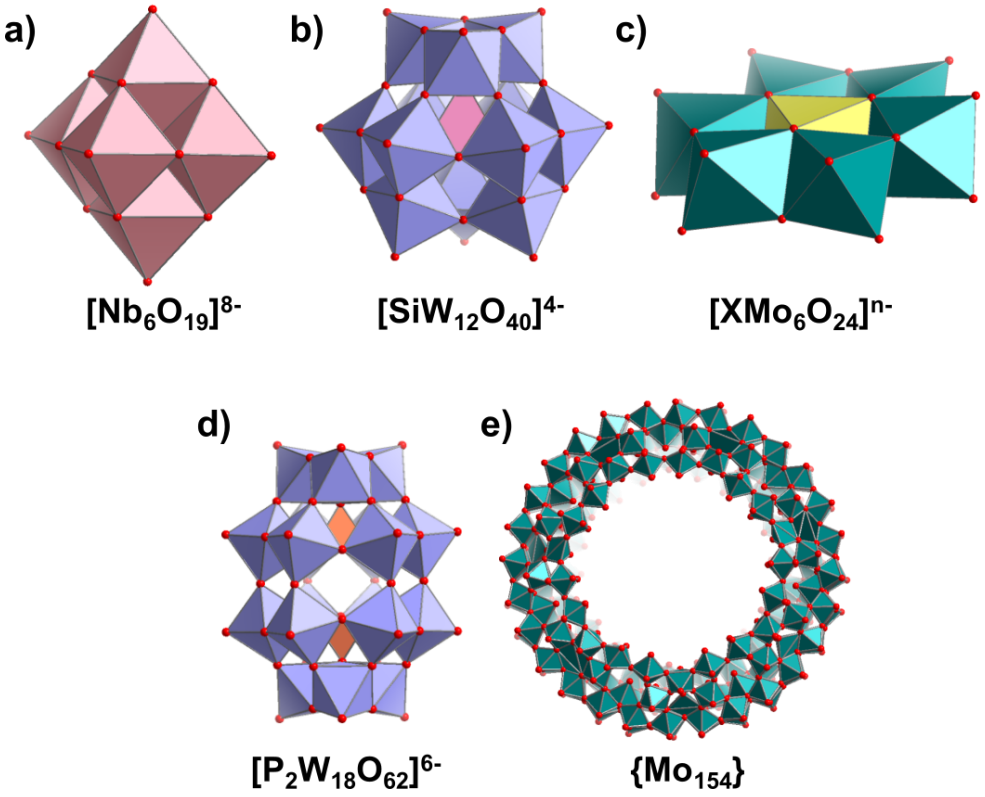

Figure 5: Polyhedral depictions of some polyoxometalates archetypes illustrating their structural diversity. a) hexaniobate Lindqvist structure, b) Keggin tungstate, c) Anderson-Evans molybdate, d) Wells-Dawson tungstate, and e) supramolecular {Mo_{154}} cluster. Colour scheme: O = red, addenda atoms: Nb = pink, W = purple, Mo = teal, heteroatom: Si = light pink, P = orange, X = yellow.

The remarkable structural versatility of POMs allows them to organise into structures that range from the nanoscale to the micrometre scale.[40] Due to their unique physical, chemical, and electronic properties, POMs have been explored in the fields of photo- and electrocatalysis, molecular magnetism, energy conversion and storage, water purification and medicine.[41–46] This diversity is related to their self-assembly process in solution, which defines their structural and electronic properties.

1.3.2 Polyoxometalate Formation: Self-Assembly Process

The synthetic strategies for POMs have advanced from aqueous media to organic and mixed-solvent systems to access structures with specific functions. Several synthetic approaches can be employed, ranging from conventional one-pot and hydrothermal synthesis to modern microwave-assisted and continuous-flow methods.[32,47,48] In addition, photo-assisted synthesis of POMs has been reported; however, this approach is less established.[49]

Typically, high-nuclearity POM clusters are obtained in aqueous acidic solution *via* a self-assembly process, in which small building blocks undergo polycondensation to form larger clusters. As a result, the assembled clusters show a higher degree of order and display properties that differ from those of the initial fragments.

Upon acidification of the metal oxide, the coordination sphere expands from tetrahedral [MO_4] to octahedral [MO_6] geometry. This makes the terminal M=O bonds more polarized and results in elongation of the M–O distances, which facilitates nucleophilic attack by an oxo ligand from another monomeric unit. Moreover, protonated oxo ligands (i.e., hydroxo or aquo) act as leaving groups and can easily be replaced in condensation reactions to form multinuclear units, as shown in Figure 6.[27] The cluster formation is significantly influenced by the strong π-bonding of the terminal oxygen ligand to the vacant d-orbitals of the metal. Therefore, the basicity and nucleophilicity of the terminal oxo ligand are reduced, enabling the formation of discrete molecular clusters.

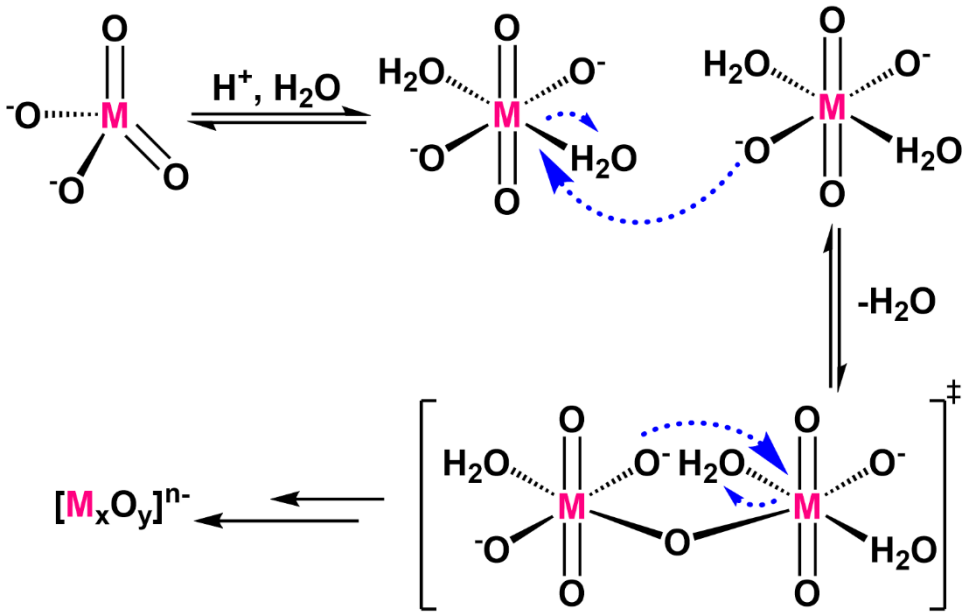

Figure 6: Schematic illustration of the self-assembly process. The coordination environment at the metal center expands from tetrahedral to octahedral geometry upon acidification. Condensation reaction between two octahedral reactive intermediates give rise to a dinuclear complex, which can further undergo condensation reaction to form a discrete polynuclear cluster $[M_xO_y]^{n-}$ (M = Mo, V, W).[27]

Although numerous analytical techniques, including ^{1}H-, ^{31}P-, ^{17}O-, ^{183}W-NMR, ESI-MS, and UV-Vis spectroscopy, have been extensively utilized to understand the self-assembly process, the exact reaction mechanism is not clearly understood.[50–53] While pH is the main parameter governing the self-assembly process, several other factors such as metal oxide concentration, solvent, temperature, reaction time, and counter-ions also impact cluster formation and are discussed in the subsequent chapter.

1.3.3 Influence of Other Parameters on Polyoxometalate Structures

Initially, the formation of POMs from the self-assembly mechanism might appear straightforward. However, the resulting clusters are strongly influenced by a range of synthetic parameters. Among these parameters, the ***choice of solvent*** plays a critical role. Aqueous media, being strongly ***pH***-dependent, allow access to only a limited number of well-defined POM species. In contrast, the use of organic solvents or mixed-solvent systems can separate the reactive fragments and isolate new assemblies.[54] Furthermore, the use of an appropriate solvent depends on the nature of the precursor. The ***type and concentration of the metal oxide*** precursor, together with the ***concentration of the heteroatom***, often added in excess, play a crucial role in stabilizing and accessing new polyoxoanions.[33] Tuning the reaction ***temperature and pressure*** can stabilize metastable intermediates, enabling subsequent aggregation. ***Counter cation*** choice is another essential factor, as it can adjust solubility, lead to precipitation of the compound, and act as a templating ion during cluster formation.[29] Alkali metals, quaternary alkylphosphonium, and alkylammonium salts are commonly used as counter cations, with quaternary alkylammonium species (e.g., *n*Bu_4N, TMA) being effective for precipitating POMs in non-aqueous solvents.[55] Furthermore, the presence of an ***additional ligand*** in the reaction mixture helps in obtaining supramolecular 3D architectures.[56] Since these parameters govern the assembly process, which yield structures ranging from discrete clusters to supramolecular assemblies. Thus, they should be carefully considered and optimized during synthesis to enable the formation of well-defined POMs.

1.4 Functionalization of Polyoxometalates

One key aspect behind the rapid growth of the POM field is its broad structural and compositional diversity. This arises from the ability to functionalize POM clusters either through purely inorganic routes or by hybridizing them with organic or organometallic moieties, thereby forming inorganic-organic hybrid POMs. Three principal routes are commonly used for POM functionalization:

1. Substitution of addenda atoms with transition metals or main-group elements.
2. Exchange of counter cations (e.g., protons or alkali metal cations) with organocations (e.g., nBu$_4$N).
3. Functionalization of lacunary species (defect sites generated by the removal of one or more MO units under controlled partial hydrolysis) or terminal sites with organic groups.

These approaches are widely employed to access new POM structures or to enhance specific physicochemical properties within the cluster.[57]

1.4.1 Metal Functionalization

The formation of purely inorganic POM clusters is generally achieved through metal functionalization. This involves either one-pot synthesis in the presence of main-group elements or transition metals,[58] or controlled addition of metal cations to one or more lacunary sites on the POM.[59] Transition metal substituted POMs have been extensively investigated because they can stabilize high valent metal ions and remain robust under harsh conditions that typically decompose organic ligands.[57] Various properties, including redox, magnetic, and catalytic behaviour, are strongly influenced by the type of transition metal incorporated. For instance, the introduction of Ce^{3+} into the silicotungstate framework has been shown to activate the system toward visible-light-induced photoredox catalysis.[60]

1.4.2 Organic Functionalization

In addition to metal functionalization, organic modification provides a versatile route to extend the diversity of POM-based materials.[61] Grafting organic ligands onto POMs enables the formation of inorganic-organic POM-based hybrids, thereby offering an effective approach to tailor their structural and functional characteristics.

POM-based hybrids also follow the interaction-based classification as described in Chapter 1.2, and their formation involves both non-covalent and covalent strategies. A prime example of a non-covalent approach is the exchange of inorganic cations (e.g., K^+, Na^+) with bulky organocations (e.g., nBu$_4$N) to enhance solubility in organic solvents.[57] In contrast, covalent routes involve either the reaction of organic groups with terminal oxygen atoms or the addition of organic species to the vacant sites of lacunary POMs. Since lacunary species are obtained by the loss of one or more MO units, they possess highly nucleophilic terminal oxo sites. These sites can bind to p-block organo-bridges, such as organosilyl, organophosphonyl, and organostannyl derivatives. The lacunary species are commonly found in polyoxotungstates (such as Keggin and Wells-Dawson POMs) and are rare in polyoxomolybdates and polyoxovanadates due to uncontrolled solution equilibria, and the tendency to undergo structural transformation.[57,62,63] Stabilization can be achieved by a ligand-directed approach, as demonstrated by Suzuki et al. for generating lacunary polyoxomolybdates in organic media. The authors used a pyridyl ligand to stabilize the highly reactive metastable species and to suppress undesired isomerization and dimerization.[64,65] Furthermore, substitution of oxo-ligands with tris-alkoxide ligands ($(OCH_2)_3CR$, where R = NH_2, OH, CH_3) is possible in Anderson-Evans polyoxomolybdates and vanadium Lindqvist POMs, commonly referred to as organoalkoxylation.[66,67] Additional diversification in Lindqvist POMs is possible through formal substitution of terminal oxo-ligands with nitrogen-based groups (organoimidation). Among these organo-functionalized strategies (Figure 7), organoalkoxylation is the most promising approach, which is commonly employed on Anderson-Evans POMs. This approach benefits from the strong metal-oxygen-carbon linkage, yielding highly stable hybrids with a broad range of applications.

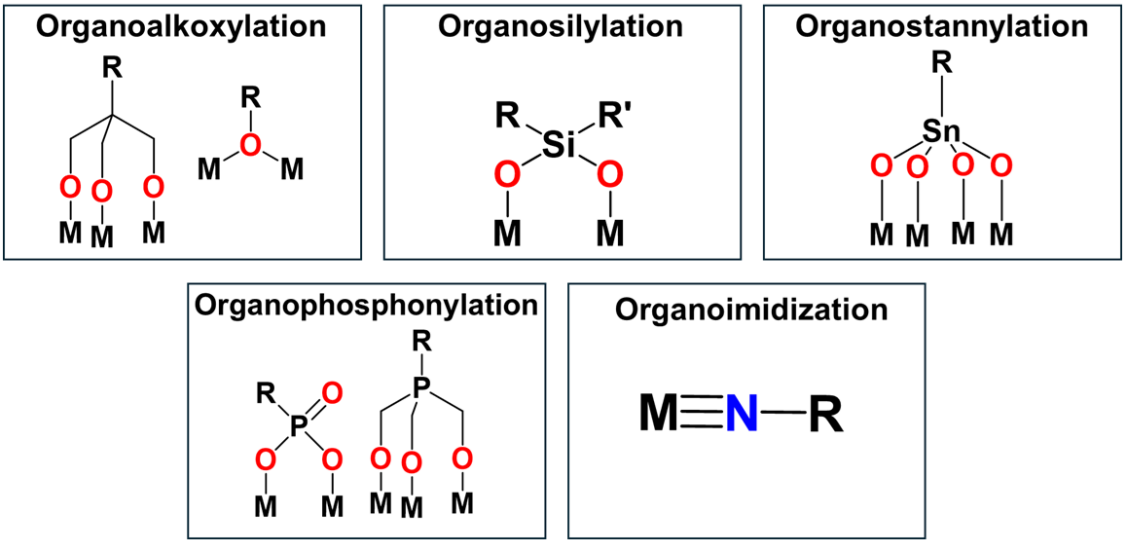

Figure 7: Illustration of widely used synthetic routes for the covalent attachment of organic moieties to POM clusters, where R or R' = CH_3, OH, and NH_2.[68]

Hybrid POMs bearing reactive functional groups (e.g., -OH, -NH_2) act as anchoring sites for further linkage with metal complexes or organic molecules to generate complex structures. For instance, Parac-Vogt and colleagues designed a hybrid Lindqvist hexavanadate with a tris-linker in good yield, which is usually difficult to access due to the reduction of vanadium(V) centers. The developed hybrid hexavanadate was used for nucleophilic substitution with different carboxylic acids, namely valeric acid, phenylacetic acid, adamantanecarboxylic acid, and biotin. Interestingly, the single crystals of the valeric acid functionalized vanadate were isolated (Figure 8).[69]

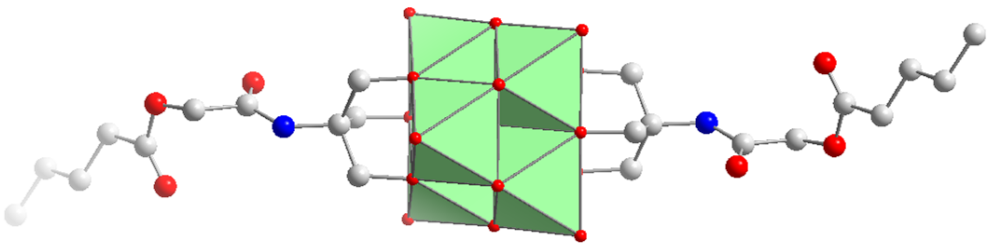

Figure 8: Representation of the vanadium Lindqvist hybrid functionalized with valeric acid. Colour scheme: V = green, O = red, N = blue, and C = grey.

To show another interesting example, Izzet and co-workers used pyridyl-functionalized Dawson POM hybrid as a platform for the attachment of Pd(II) complex to obtain supramolecular trimer species, as shown in Figure 9.[70]

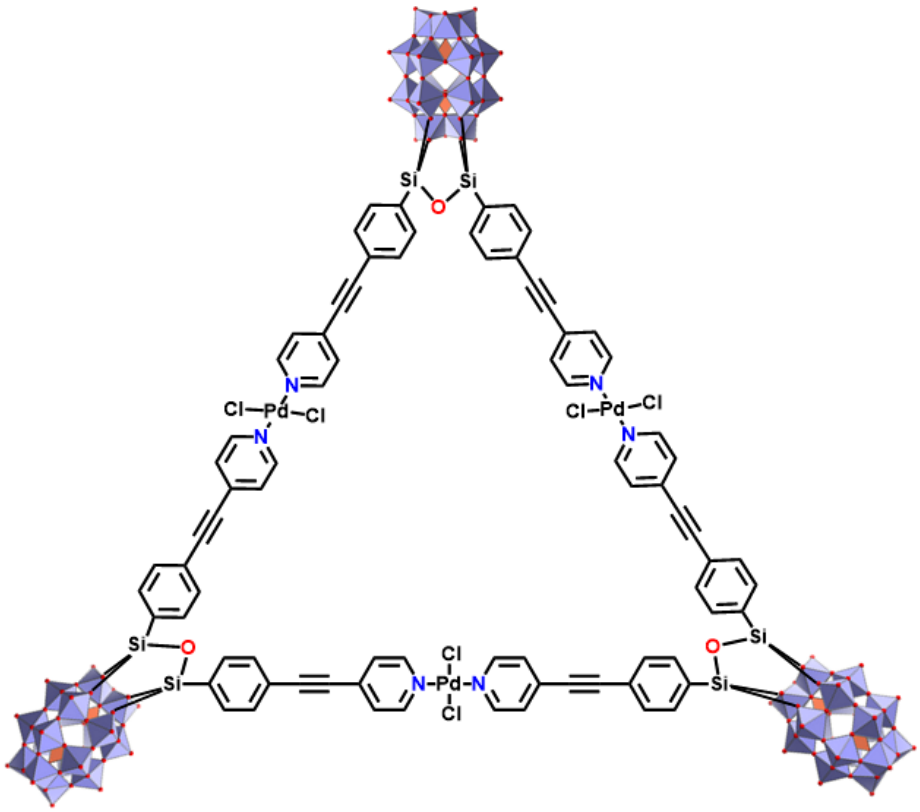

Figure 9: Illustration of the molecular triangular species formed from the hybrid Dawson POM. Colour scheme: W = purple, P = orange, and O = red.

In addition, hybrid POM scaffolds serve as building blocks for designing oligomers or 3D network materials (see Chapter 1.8).

1.5 Anderson-Evans Polyoxometalates

1.5.1 Structural Features and Diversity

Among the various heteropolyoxoanions, the Anderson-Evans structure provides a versatile platform for structural and functional modification. The Anderson-Evans structure was proposed by J.S. Anderson in 1937[71] and was confirmed a decade later by H.T. Evans through X-ray diffraction analysis of $[TeMo_6O_{24}]^{6-}$.[72] Since then, this family of clusters has been known as Anderson-Evans or Anderson POMs. The general formula of Anderson POMs is represented as $[H_y(XO_6)M_6O_{18}]^{n-}$, where y = 0–6, n = 2–8, X = central heteroatom (Mn, Fe, Co), and M = addenda atom (Mo, W).[73]

The topological structure consists of a central XO_6 octahedral unit surrounded by six edge-sharing MO_6 octahedral units, resulting in a planar arrangement. Three types of coordination modes of oxygen atoms are observed: six (μ_3-O) atoms bridging two addenda atoms and the central heteroatom, six (μ_2-O) atoms linking two addenda atoms, and two terminal oxygen atoms (O_t) on each addenda atom (Figure 11a). Further structural diversity arises due to the existence of α- and β-isomers. The α-isomer possesses a planar topological structure as described above, whereas the β-isomer displays a non-planar structure with a different oxygen-coordination environment. In the β-isomer, two μ_4-O atoms connect three addenda atoms and the central heteroatom, two μ_3-O atoms link two addenda atoms and the central heteroatom, and two types of μ_2-O atoms are present: two μ_2-O atoms connect one addenda atom and the central heteroatom, while six μ_2-O atoms link two addenda atoms, and each addenda atom has two terminal oxygen atoms (O_t).[73] The α-isomer is further subdivided into A- and B-type structures based on the protonation of μ_3-O atoms. For the ***A-type structure***, the six μ_3-O atoms are unprotonated with the central heteroatom usually in a high oxidation state. The general formula of the A-type is $[X^{n+}M_6O_{24}]^{(12-n)-}$, where X = Te(VI), I(VII). On the other hand, in the ***B-type structure***, μ_3-O atoms are protonated, and the central heteroatom is in a low oxidation state. Their general formula is $[X^{n+}(OH)_6M_6O_{18}]^{(6-n)-}$, where X = Fe(III), Cr(III).[74]

Furthermore, the possibility of incorporating a wide range of heteroatoms, ranging from oxidation states II to VII, significantly broadens the versatility of $[XMo_6]$-type clusters. Nearly all first-row transition metals (except Sc and Ti) have been introduced as heteroatoms in $[XMo_6]$ structures. Only a limited number of heteroatoms have been incorporated into the $[XW_6]$ structures compared with $[XMo_6]$ systems. In addition, a broad range of alkali metals, alkaline-earth metals, as well as the entire lanthanide series, has been explored as counter cations, see Figure 10.[74] Thus, the vast versatility and excellent physicochemical properties of Anderson POMs depend on the heteroatom, the counter cation, and their ability to undergo organic functionalization. The routes to organic functionalization are discussed in the following chapter.

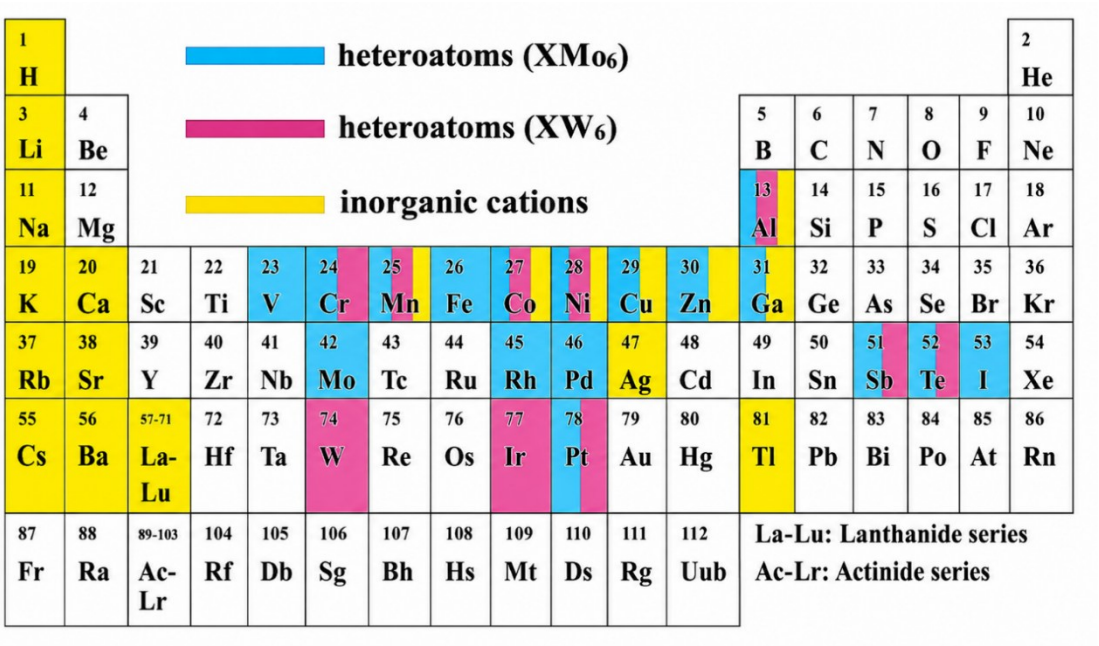

Figure 10: Illustration of the periodic table highlighting the incorporation of heteroatoms in [XMo_6] and [XW_6] structures, along with the various cations successfully employed so far. Reproduced with permission from *Nanoscale*, **2021**,*13*, 7119-7133. Copyright © 2021, Royal Society of Chemistry.[73]

1.5.2 Organic Functionalization of Anderson POMs

Beyond their structural diversity, Anderson POMs undergo organic functionalization through formal substitution of oxo-ligands on the [MO_6] units with various tris-alkoxide ligands ($(OCH_2)_3CR$, where R = NH_2, OH, bpy). This functionalization is mainly observed in the polyoxomolybdates than in polyoxotungstates species due to the labile nature of Mo–O bonds.[63] Tris-functionalized Anderson POMs have two isomers: the ***δ-isomer***, which is the most common form, where all the μ_3-O atoms are substituted by tris-alkoxide groups (Figure 11b,c), and the ***χ-isomer***, in which tris-ligands are bonded to two μ_3-O atoms and a μ_2-O atom.[73] The highly symmetric nature of the Anderson POM naturally favours the formation of double-sided products. However, some examples of single-sided tris-functionalized Anderson POMs are also reported.[75,76]

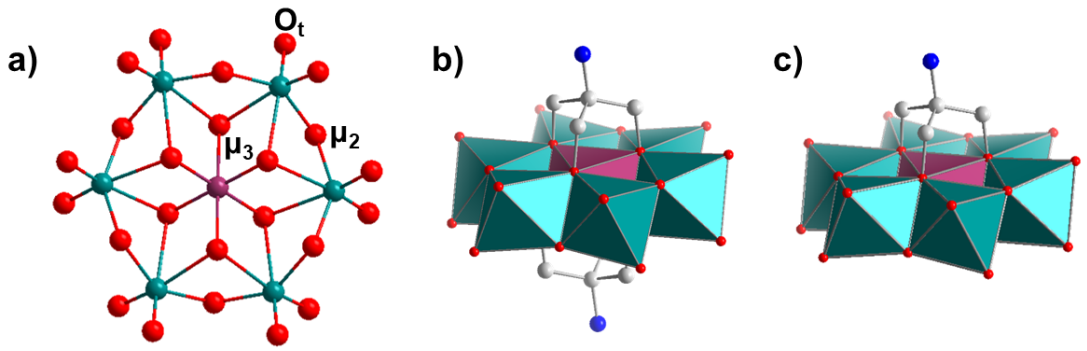

Figure 11: a) Ball and stick representation of α-isomer, b) and c) polyhedral representation of double-sided and mono-sided δ-isomer. Colour scheme: O = red, C = grey, N = blue, addenda atom = teal, and heteroatom = plum.

Synthesis of asymmetric hybrids is challenging, as it often yields mixtures of both symmetric and asymmetric products that are difficult to separate and purify.[63,77] One strategy to obtain asymmetric products is by controlling the degree of protonation during the reaction.[78] This allows the addition of two different moieties on both sides of the POM to tailor the functions and physicochemical properties for advanced applications. Cronin et al. reported a "universal" asymmetric Mn-Anderson hybrid with a protecting group, which could potentially serve as a precursor to synthesize other Mn-Anderson hybrids (Figure 12). The asymmetric hybrid was isolated from the undesired symmetric by-products based on the difference in the affinities of organic ligands for the stationary phase *via* C_{18} RP-HPLC (reverse phase-high performance liquid chromatography) method.[79]

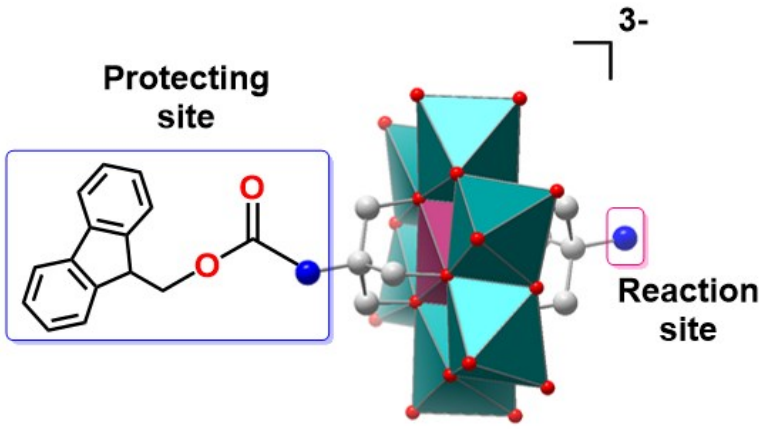

Figure 12: Structure of the "universal" asymmetric Mn-Anderson POM hybrid containing the 9-fluorenylmethyloxycarbonyl as the protecting group. Colour scheme: Mn = plum, Mo = teal, O = red, C = grey, and N = blue.

Further, the R-groups from the tris-ligands can attach to the organic or metal complexes, leading to the formation of extended hybrid structures. This can be performed *via* two approaches: pre-functionalization and post-functionalization. In pre-functionalization, the tris-ligand is modified first with other organic groups, often involving multi-step synthesis to generate the desired tris-functionalized ligand, and is then grafted onto the POM unit.[80] However, in post-functionalization, the tris-ligand is first attached to the POM, followed by reaction with organic groups. Post-functionalization is often preferred because it maintains the cluster core and minimizes the formation of side products.[73] To illustrate one example, Anjass et al. reported two pyrene-functionalized Anderson-type POM hybrids, obtained by covalent attachment of 4-(pyrene-1-yl) phenol and 3,5-di(pyrene-1-yl) phenol to a chloride functionalized POM in a one-pot synthesis, see Figure 13.[81]

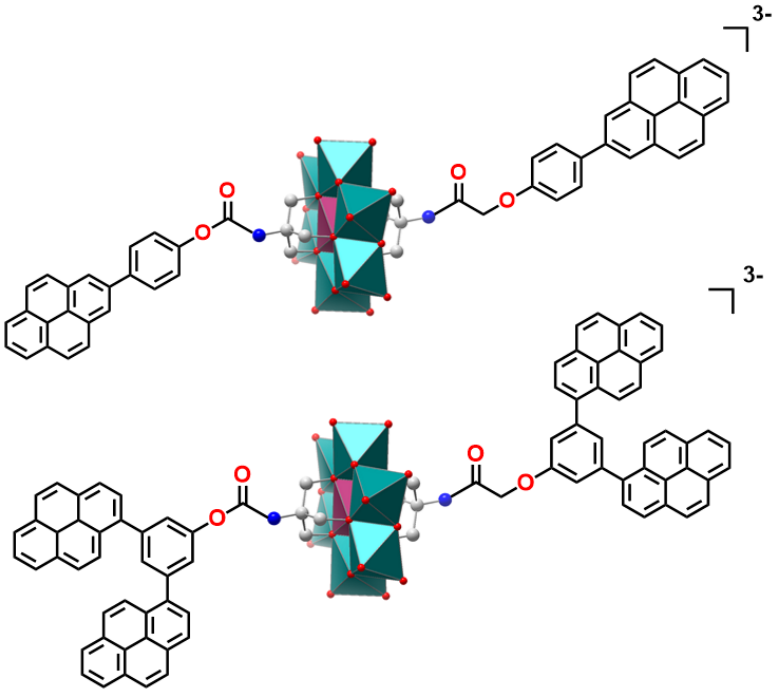

Figure 13: Illustration of the pyrene-functionalized Anderson POMs, where the pyrene moieties are introduced *via* post-functionalization route through a tris-linker. Top: functionalization with 4-(pyrene-1-yl)phenol; bottom: 3,5-di(pyrene-1-yl)phenol. Colour scheme: Mn = plum, Mo = teal, O = red, C = grey, and N = blue.

Post-functionalization strategy is also adopted in the present work. The synthesis of organofunctionalized Anderson POMs (δ-isomer) in the projects is carried out through the rearrangement of the α-octamolybdate precursor. Firstly, α-octamolybdate synthesis is done in the presence of aqueous acidic media, followed by the reaction of the Mn(III) template with a suitable tris-ligand in MeCN or DMA. Further functionalization is performed by tethering tris-ligand onto the POM with reactive groups.

In general, a variety of functional materials have been synthesized from Anderson POMs due to the wide range of possible functionalization. These functional materials have been used for various applications, ranging from biochemistry to catalysis, particularly in photocatalysis.[82,83]

1.6 Photocatalytic Principles and Electron Transfer Pathways

To design artificial photosynthetic systems for solar energy conversion, an ideal approach is to imitate the molecular and supramolecular alignment of natural photosynthesis. As discussed previously, for artificial photosystems, it is better to study HER and OER pathways individually to improve their mechanistic understanding and catalytic performance. Since this work is mainly focused on the reduction half-reaction, a molecular system typically consists of a chromophore or photosensitizer (PS) to absorb light, a catalyst to reduce protons from a proton source, and a sacrificial electron donor to supply electrons for H_2 formation and regenerate the excited PS.[84] Regeneration of the excited PS can take place either *via* oxidative or reductive quenching pathways, as illustrated in Figure 14. In the ***oxidative quenching***, the excited PS (PS*) is oxidatively quenched by the catalyst, leading to the formation of PS^+. This oxidized PS is then reduced by the SED to its ground state (PS), leading to the cycle closure. However, the ***reductive quenching*** pathway involves the reductive quenching of the excited PS by the SED to form PS^-. The reduced PS then transfers electrons to the catalyst and is regenerated.[85,86]

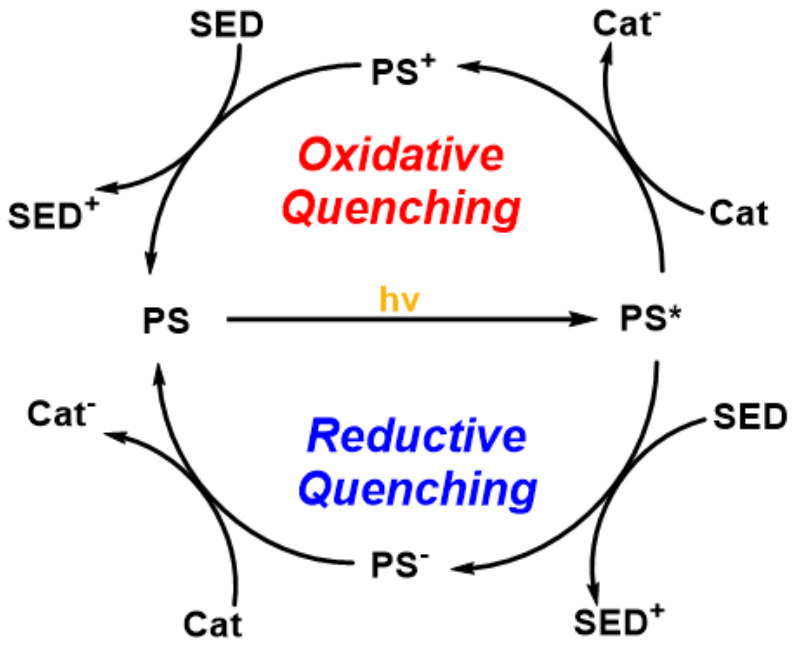

Figure 14: Schematic representation of the oxidative and reductive quenching mechanisms, containing a photosensitizer (PS), SED (sacrificial electron donor), and Cat (Catalyst), modified according to reference.[87]

For artificial photosynthetic systems to perform the key steps ranging from photophysical and redox processes to catalytic conversion, effective coupling among the components is required.[88] Photo-induced electron transfer between the photosensitizer and catalyst is one of the crucial steps enabling catalysis.[89] For effective multi-electron transfer between the photosensitizer and the catalyst, two approaches are commonly used: inter- and intramolecular electron transfer. In an intermolecular or multi-component system, the linkage between PS and catalyst is governed by non-covalent interactions such as electrostatic interactions, hydrogen bonding (Figure 15b). The electron transfer process relies on diffusion-controlled collisions and is hard to control. Whereas in an intramolecular or single-component system, the PS and the catalyst are connected through a bridging unit *via* covalent or coordinate interactions (Figure 15a). Since the arrangement of the PS and the catalyst is fixed, more efficient electron transfer can be expected. Although the synthesis of these systems is challenging, it offers advantages of tuning the photophysical and photochemical properties through structural design, e.g., by modifying ligands with different substituents. Moreover, a slight modification might lead to significant changes in the reactivity.[90]

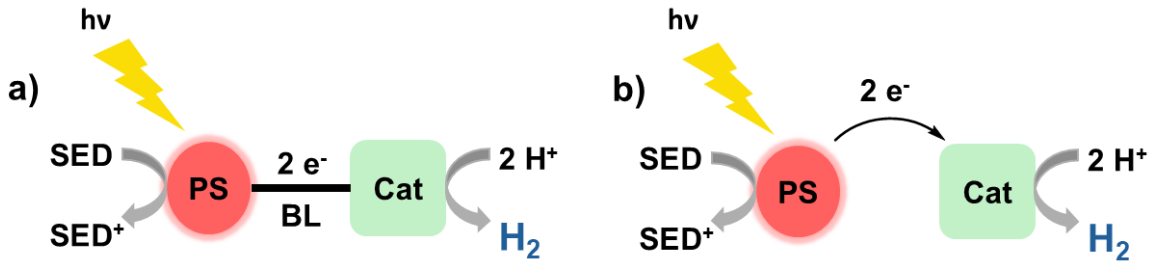

Figure 15: Illustration of a) intramolecular and b) intermolecular electron transfer in photoexcited hybrid materials for hydrogen production, where PS: photosensitizer, Cat: catalyst, and BL: bridging ligand. Adapted from reference.[91]

1.7 Photosensitizer-Catalyst Systems for HER

1.7.1 Photosensitizer-The Light-Harvesting Component

A photosensitizer plays a key role in photocatalytic systems because it absorbs light and transfers an electron from its excited state to the acceptor or catalytic unit.[92] There are three crucial parameters that govern photosensitizer performance in a photoredox reaction: light absorption, excited-state lifetime, and excited-state redox potentials.

Light absorption of the photosensitizer is assessed by UV-Vis spectroscopy, which provides absorption maxima and absorbance values. The molar absorption coefficient (ε) at a given wavelength is then determined using the Beer-Lambert law. It is crucial that the PS absorption lies in a different region from that of the other components (e.g., catalyst, donor) in the reaction vessel to ensure maximum photon absorption by the PS and to prevent side reactions. Moreover, methods such as ligand modification and tuning HOMO-LUMO gaps are used to excite the PS in the visible or near-infrared region, i.e., to longer wavelengths, to maximize the utilization of the sunlight in artificial photosynthesis.[93,94]

Excited-state lifetime (τ) of the photosensitizer is one of the essential parameters for solar-fuel applications. For bimolecular charge-transfer reactions, the lifetime of the excited-state should be long enough to enable diffusion-controlled processes and electron transfer steps to overcome the radiative and non-radiative processes (the processes are shown in Figure 17a). Triplet excited states typically have a longer lifetime than the singlet states due to the spin-forbidden T_1 to S_0 transition, which is advantageous for applications like photocatalytic HER. ^{3}MLCT states generally decay

with first-order rate constants in the range of 10^5–10^7 s, and bimolecular electron transfer rate constants often reach the diffusion limit (~10^9 $M^{-1}s^{-1}$), even at low driving forces. Thus, even at low quencher concentration (millimolar range), electron transfer processes can effectively compete with the excited-state deactivation pathways, enabling efficient electron transfer.[94,95]

The ***excited-state redox potentials*** of PS are also an important criterion for photocatalytic applications, as they govern whether the photo-induced electron transfer is thermodynamically feasible. In the excited-state, PS either works as a photoreductant by transferring an electron or as a photooxidant by accepting an electron. A strong photoreductant features more negative oxidation potentials, whereas a strong photooxidant is characterized by a more positive reduction potential. Photosensitizers can be quenched by the SED when the driving force is not sufficient to act on the catalyst. This results in a net redox shift of the catalytic cycle and formation of by-products. Therefore, developing photosensitizers with strong reducing and oxidising power is beneficial for effective electron transfer and improving catalytic activity.[93,95]

In addition, other factors such as photo- and chemical stability of the PS should be considered for the long-term performance of the PS, even at low catalyst concentrations.

Over the last decades, a variety of photosensitizers have been explored, ranging from organic dyes to metal complexes for photocatalytic applications. [96] Despite significant efforts, many chromophores still display a short lifetime of the excited-state, and moderate long-term photostability.[88] Notably, cyclometalated ruthenium and iridium complexes are considered as effective photosensitizers because of their absorption in the visible region, long excited-state lifetime, and photoredox properties.[85,97,98] These complexes are typically coordinated with organic ligands (such as bpy, ppy) that feature low-lying unoccupied π* orbitals. The electronic structure of these complexes comprises a set of filled π orbitals from the ligands and three closely spaced dπ orbitals on the metal. One of these dπ orbitals forms the HOMO, while LUMO contains π* orbitals on one or more of the ligands, see Figure 16. Each of these orbitals can be involved in the excited state processes that are crucial for the activity of the photosensitizer for diverse applications.[94]

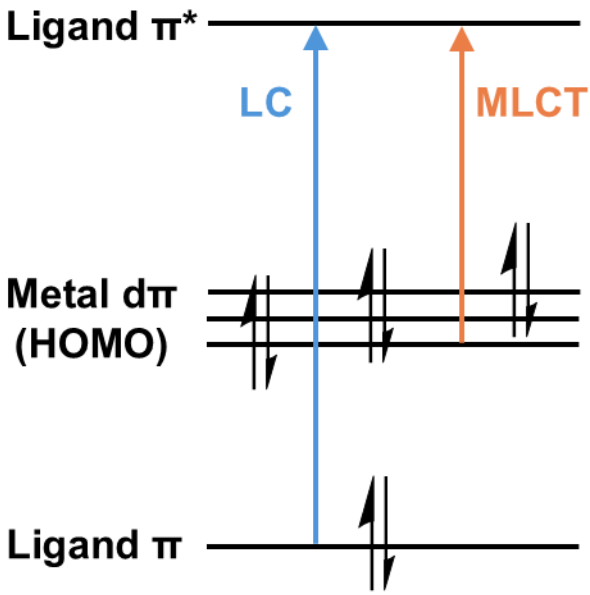

Figure 16: Illustration of the simplified frontier orbital diagram for metal-based photosensitizers, according to reference.[94] For simplicity, only one ligand π and π* orbitals is shown, although depending on the nature of the ligand and coordination geometry, multiple orbitals can be involved.

Two types of electronic transitions are observed upon visible-light irradiation: ligand-centered transitions (LC) between π and π* orbitals of the ligand, and metal-to-ligand charge transfer (MLCT) transitions due to electron transfer from the metal-centered dπ orbitals to the ligand π* orbital. The photophysics of these complexes can be explained with the Jablonski diagram (Figure 17b). Promotion of an electron from the ground state (S_0) generates the corresponding singlet excited state (S_1), typically ^{1}LC, and ^{1}MLCT. However, MLCT electronic transitions are more advantageous than LC transitions due to the small gap between singlet and triplet states, as compared to LC transitions which exhibit a large stokes shift. During intersystem crossing (ISC), some amount of excitation energy is dissipated as heat. In the MLCT state, this energy loss is small because the triplet state is accessed. In principle, the formed S_1 state could return to S_0 either by fluorescence, with rate constant K_r, or through non-radiative decay, with rate constant K_{nr}. Nevertheless, for Ru(II) and Ir(III), rapid intersystem crossing (ISC) to the triplet state (T_1) takes place. The ISC rate constant K_{ISC} is larger than K_r and K_{nr}, resulting in efficient transfer of population to the T_1 state. These triplet states are generally long-lived because phosphorescence to S_0 is spin-forbidden and slow. As a result, electron transfer to the catalyst is possible leading to the generation of the desired product. Furthermore, because of the large spin-orbit coupling constant for ruthenium and iridium, phosphorescence is possible.[94,98–100]

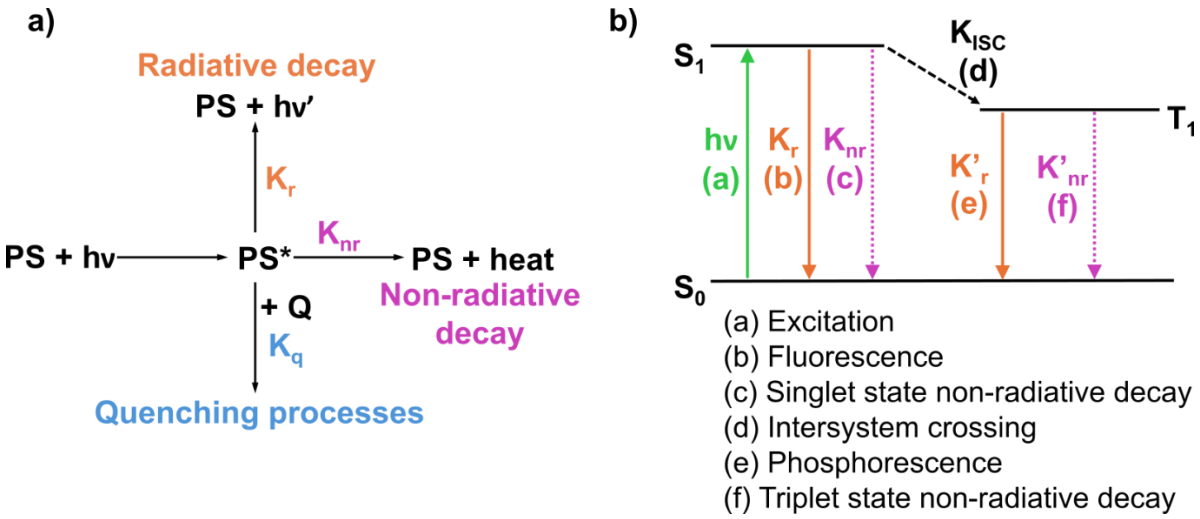

Figure 17: Illustration of a) excited-state decay pathways and b) Jablonski diagram showing different electronic processes for metal-based photosensitizers, where K_r and K'_r: rate constants for radiative processes, K_{nr} and K'_{nr}: rate constants for non-radiative processes, K_q: rate constant for quenching processes.[93,94,99]

1.7.2 Catalyst-The Hydrogen-Evolution Component

Solar hydrogen production is a two-electron process. Thus, an ideal molecular model should consist of a catalyst ("charge-pool") capable of accepting electrons at a constant potential from a one-electron reducing species and transferring them to a substrate in a concerted way, thereby preventing the generation of high-energy intermediates.[16]

Over the past decades, numerous catalysts have been investigated for photocatalytic HER, ranging from Fe-hydrogenases (nature's proton reduction enzymes) to transition metal systems such as Co, Ni complexes, and polyoxometalates.[101–103] These catalysts have been employed in both inter- and intramolecular systems (Figure 18 and 19). Among these systems, Pt-based complexes are the most widely studied as HER catalysts or co-catalysts, and they remain as the benchmark. The Pt-based complexes will be discussed in detail in the following section.

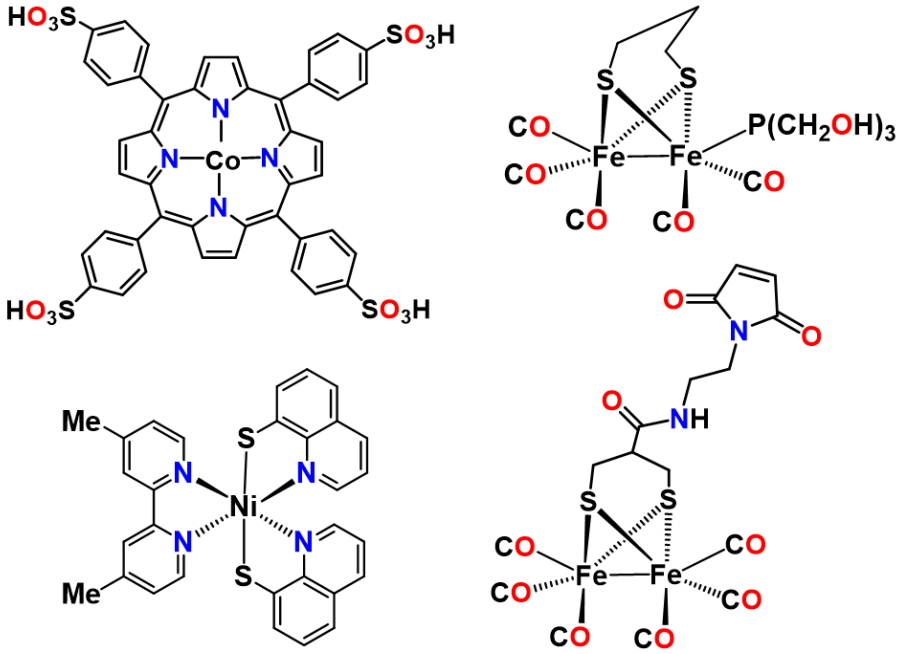

Figure 18: Some examples of catalysts employed in homogeneous HER catalysis.

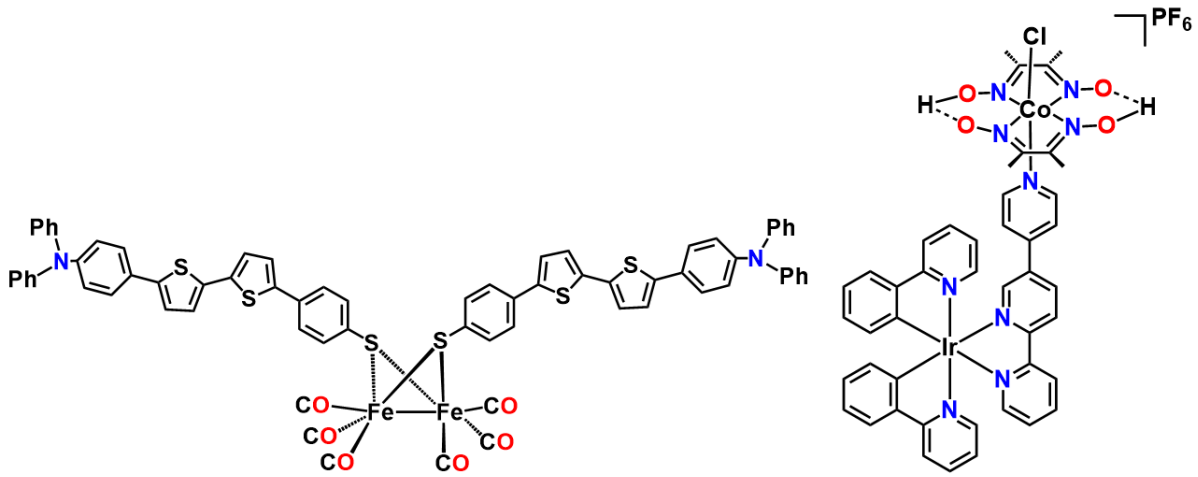

Figure 19: Representative examples of covalently linked photosensitizer-catalyst systems investigated for photocatalytic HER.[104,105]

1.7.2.1 Platinum as Catalyst for HER

Platinum complexes have been investigated under different HER conditions in both homogeneous and heterogeneous reactions. Despite the high efficiency of Pt colloids towards HER, it is crucial to understand the molecular systems that govern the proton reduction cycle. Therefore, using Pt(II)-based molecular systems for photocatalytic HER has several benefits: (a) all metal atoms in a molecular catalyst may participate in the catalytic reaction, while only surface metal atoms of colloidal particles contribute

to catalysis, (b) the molecular structure can be modified to tune the catalytic activity and selectivity, (c) reaction mechanisms could be understood at the atomic level.[106]

In view of this, Sakai et al. and Rau et al. have examined several Pt-based molecular systems (mononuclear and dinuclear) in multi-component and single-component systems, see Figure 20 and 21.[106–108] In a multi-component system, electron transfer among the photosensitizer, sacrificial electron donor, electron relay and catalytic center takes place *via* intermolecular interactions such as van der Walls forces or hydrogen bonding. Since multi-component systems are diffusion-controlled processes, the components should be close enough for effective electron transfer to produce hydrogen.

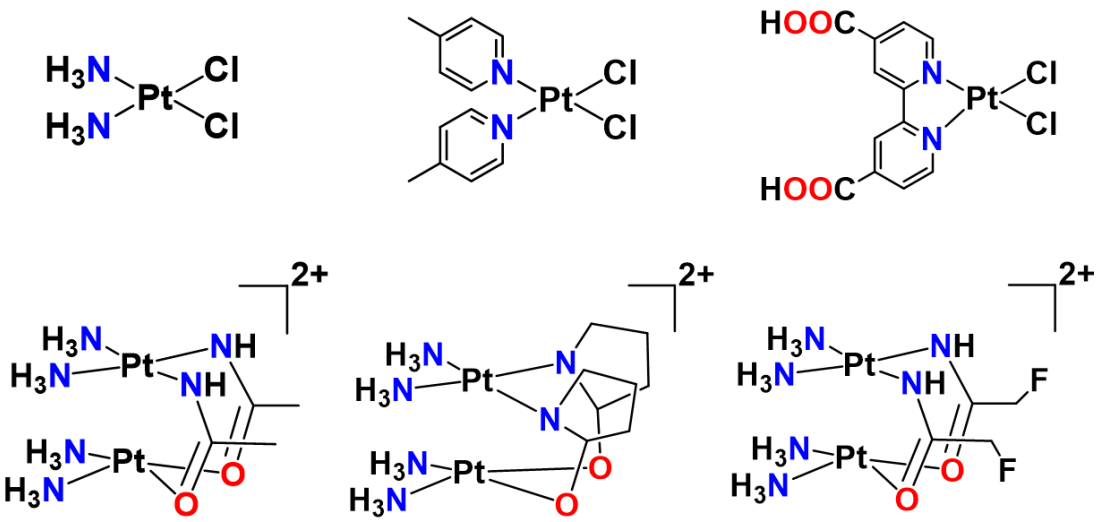

Figure 20: Few examples of mononuclear and dinuclear Pt(II)-based catalysts for proton reduction.[106]

On the other hand, in a single-component system, the PS and the catalyst are linked *via* a bridging ligand by covalent bonds to form photo-hydrogen-evolving molecular devices (PHEMDs). Several modifications in this type of system, such as variations in peripheral or bridging ligands, tuning the catalytic center can alter the catalytic activity, and photophysical and photochemical properties.[108]

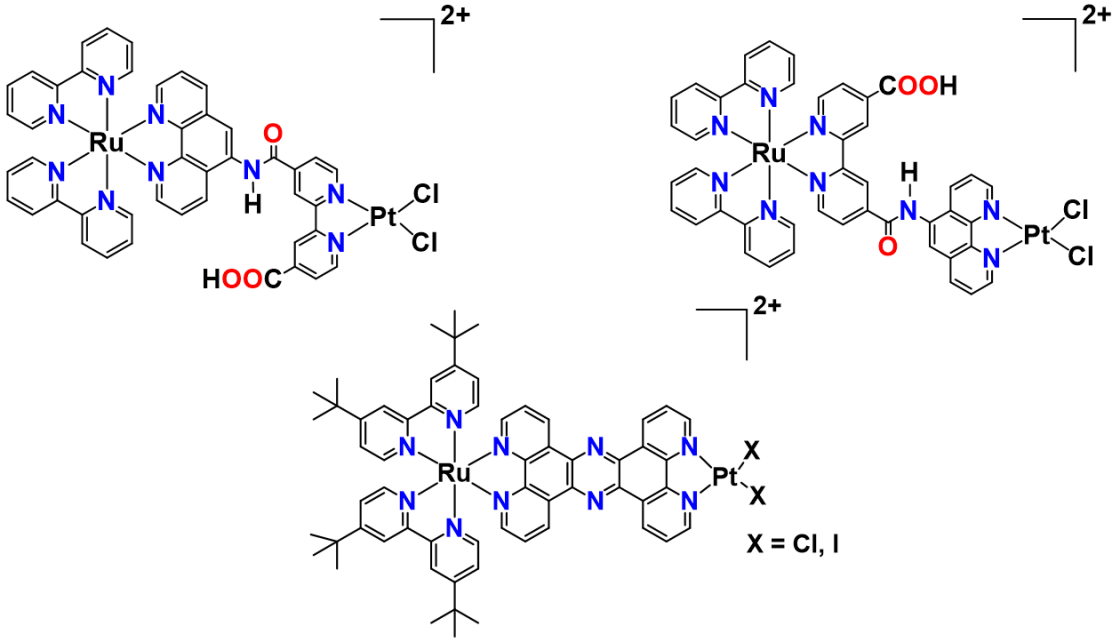

Figure 21: Structures of covalently linked Ru-Pt dyads for photocatalytic hydrogen evolution reported by Sakai et al. (top left and right) and Rau et al. (middle).[108–110]

Furthermore, to enhance the photocatalytic efficiency and stability of Pt(II) proton reduction catalysts, the concept of an electron-reservoir was employed to design Pt-based complexes. A molecular electron reservoir stores and transfers multiple electrons without decomposition. In this context, Sakai and co-workers designed several Pt(II) catalysts linked to multiple viologen units, which act as an electron-reservoir. It was observed that the catalytic activity was enhanced significantly as compared to other Pt(II)-based catalysts by the insertion of temporary electron-reservoir sites (Figure 22).[111,112] Following this approach, Park et al. reported the introduction of tetraphenyl silyl units to the N^N ligand of a Pt(II) catalyst, creating electron-reservoir features that enhance photocatalytic hydrogen production activity.[113] Inspired by these studies, a similar strategy was used in the present work, where POMs have been used as electron-reservoirs and catalysts for photocatalytic HER. The role of POMs as a catalyst and an electron-reservoir will be discussed in the next sections.

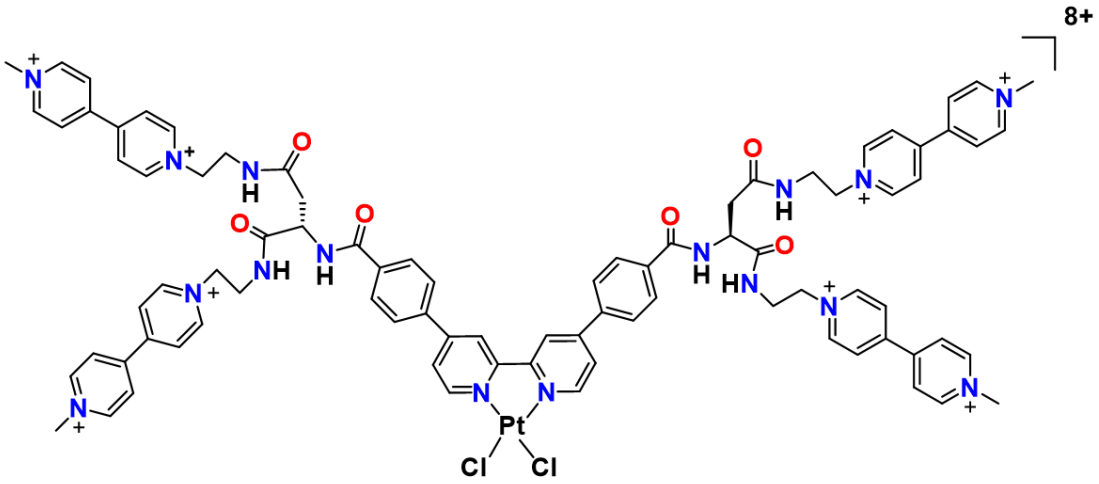

Figure 22: Structure of covalently linked pigment-acceptor-catalyst triads for photocatalytic hydrogen evolution.[111]

1.7.2.2 Polyoxometalates as Photocatalysts and their Photochemistry

Over the last decades, POMs have gained attention in the photocatalysis field due to their rich redox chemistry, versatility, and tunability in electronic structures. Since molybdate and tungsten-based clusters usually have a d^0 electronic configuration, light absorption is governed by O ⟶ M, ligand-to-metal charge transfer bands (LMCT) in the UV region. This leads to the promotion of an electron from HOMO to LUMO that results in the formation of an oxo-centered radical. Therefore, the photoexcited cluster is highly reactive and acts as both a better oxidant (higher electron affinity, E_{ea}) and a better reductant (lower ionization energy, E_I) than the ground-state species (Figure 23).[114] In addition to their photoredox activity, POMs are used as photocatalysts for various homogeneous and heterogeneous reactions because of their ability to undergo multi-electron redox processes, and maintain structural integrity during photoredox processes.[114–116]

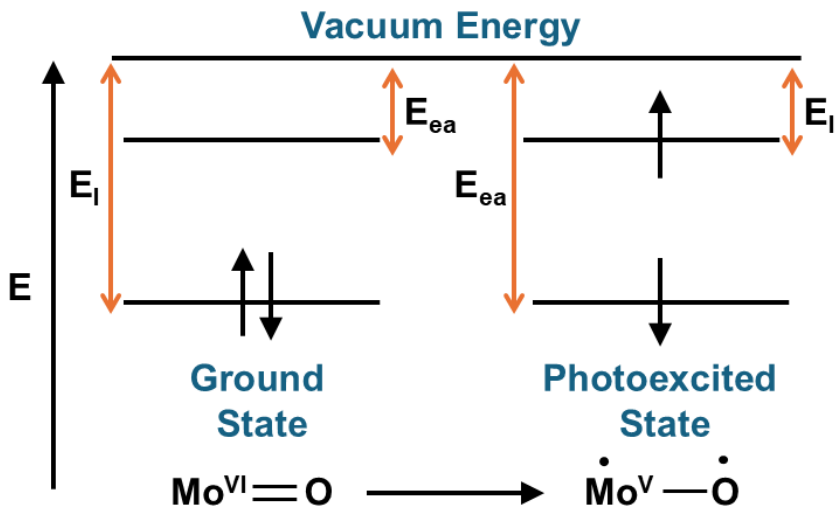

Figure 23: Simplified orbital diagram of a photoexcited POM. Photoexcitation promotes an electron from a bonding to an anti-bonding orbital, generating an excited-state species with lower ionization energy (E_I) and higher electron affinity (E_{ea}) than the ground-state.[114]

In spite of significant advances, POM photochemistry is restricted by the energy required to allow LMCT (usually UV irradiation). To further explore photochemical applications with POMs (e.g., solar-fuel applications) two strategies can be used: direct manipulation of the LMCT bands of the cluster or incorporation of the secondary chromophores or photosensitizers to form so-called “hybrid POMs”.[57] In particular, hybrid POMs have played a crucial role in the development of this field.

A wide variety of metal complexes or organic dyes have been investigated as photosensitizers with POMs to form photoactive dyads.[117–120] In these dyads, either inter- or intramolecular charge transfer can occur between the light-harvesting unit and the POM cluster.

Briefly, upon photoexcitation, the high energy excited-state of the PS transfers an electron to the POM, which results in the generation of a short-lived charge-separated state and a reduced POM core. Effective quenching (oxidative or reductive) by a suitable SED provides electrons required for the catalytic cycle, thereby preventing charge recombination, see Figure 24.[57]

Figure 24: Illustration of the photo-induced charge separation between an oxidized PS and a reduced POM. The photoexcitation of the PS leads to an inter- or intramolecular charge transfer to the POM, followed by the quenching with the SED to prevent charge recombination, where PS: photosensitizer, CT: charge transfer, SED: sacrificial electron donor.

1.7.3 Photosensitizer-Polyoxometalate Dyads for Light-Driven Catalysis

Hybrid assemblies consisting of a photosensitizer and a POM cluster have been explored for photocatalytic applications by several groups, involving both covalent and non-covalent interactions. Harriman, Odobel, and colleagues designed dyads based on mono-lacunary Dawson POMs functionalized with perylene-monoimide through organosilane and organophosphonate linkages. Intramolecular charge transfer was observed in these dyads, leading to the formation of a one-electron reduced POM under the irradiation of λ = 400 nm. In spite of the favourable driving force, the formation of two-electron reduced POM species was not possible because of the rapid charge-shift reaction between the mono-reduced POM and the perylene moiety.[121] Since the production of solar fuels requires multi-electronic processes, the group took inspiration from nature and reported multi-porphyrin assemblies covalently linked to the Dawson POM cluster. These multi-porphyrin assemblies consisted of three Zinc(II) porphyrins (ZnP) donors covalently linked to a free-base porphyrin to enhance charge transfer and prevent rapid charge recombination between the ZnP and the POM cluster. It was observed that in the presence of the sacrificial electron donor (TEOA, triethanolamine), the oxidized π-radical cations of both free-base porphyrin and ZnP were effectively quenched before charge recombination. Moreover, a slow two-electron reduction on the POM was found in the absence of oxygen.[122]

Further progress in the field of covalently linked PS-POM dyads was made by Proust, Izzet, and co-workers, where organosilyl and organotin functionalized Keggin and Dawson-type POMs were attached to a heteroleptic Ir(III) complex *via* a Sonogashira cross-coupling reaction. Electrochemical measurements revealed that the redox properties of the dyads differ based on the structural class and chemical functionalization. Spectroelectrochemical measurements together with transient absorption spectroscopy showed photo-induced electron transfer from the Ir-complex

to the POM and the existence of a long-lived charge-separated state (in the range of ns to hundreds of ns). Furthermore, computational studies indicated the influence of the picolinate ligand for the directional electron transfer and delayed charge recombination.[123,124] Due to the effective charge separation and lifetime of the charge-separated state for further redox processes with external substrates, the siloxane functionalized Dawson-Ir dyad was chosen for charge photo-accumulation and visible-light-driven HER. Steady-state irradiation (λ > 400 nm) of the dyad in DMF in the presence of triethylamine (TEA) as a reductant led to the rapid formation of one-electron reduced POM ($\tau_{1/2}$ = 43 s), followed by slower reduction to two-electron reduced POM species ($\tau_{1/2}$ = 270 s), see Figure 25. Moreover, the photoreduction of POM in the presence of acetic acid significantly increased the rate of the second reduction ($\tau_{1/2}$ = 60 s). Based on this, authors tested the dyad for visible-light-driven hydrogen evolution in the presence of TEA as a SED and acetic acid as a proton source. Photocatalytic hydrogen production was observed over a week with turnover numbers (TONs) of *ca.* 41, without photodegradation.[125]

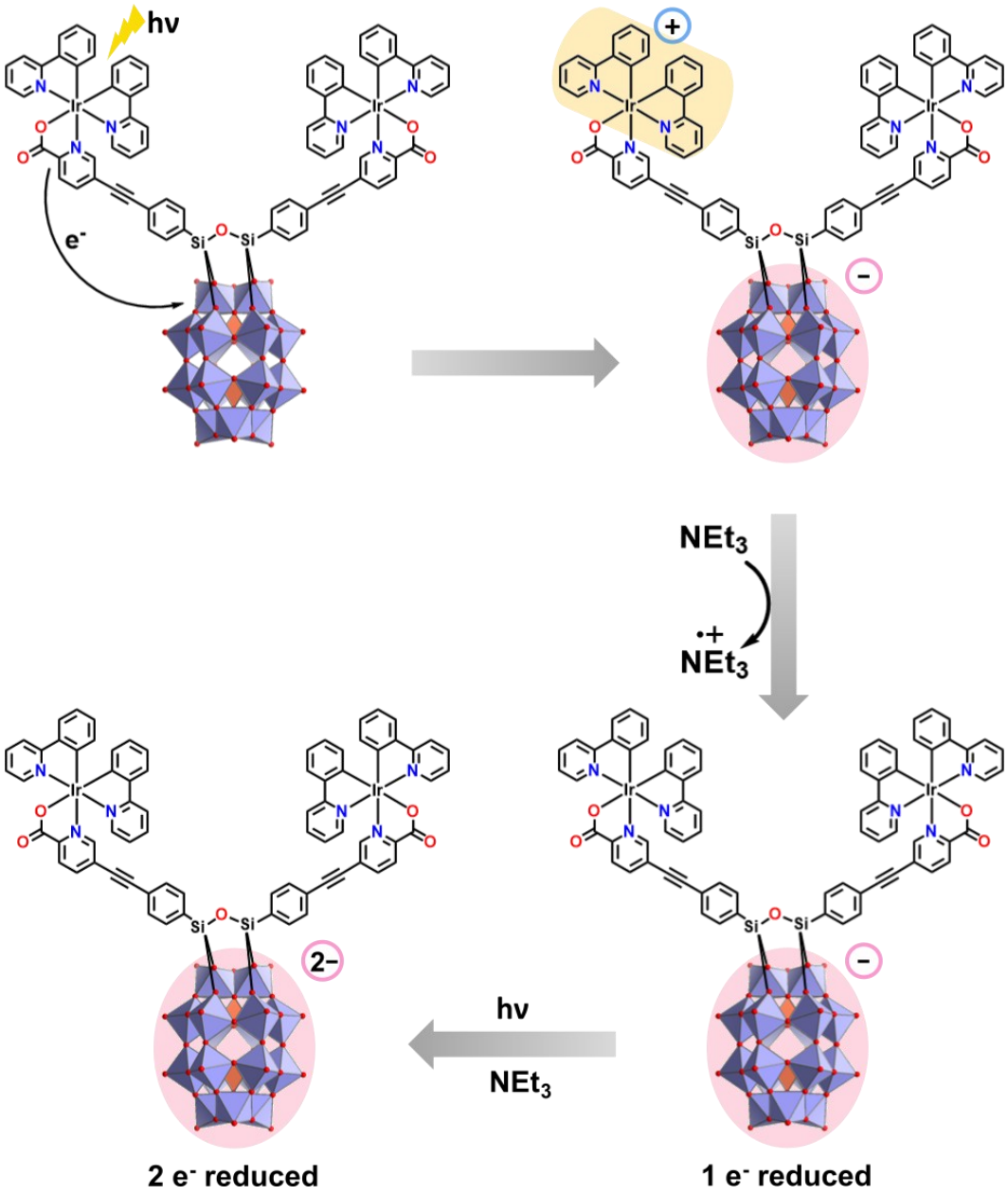

Figure 25: Schematic illustration for the stepwise formation of two-electron reduced POM species in a Dawson POM-Ir dyad.[125] Upon visible-light absorption and in the presence of an electron donor POM is capable of photo-accumulating two electrons. Colour scheme: W = purple, P = orange, and O = red.

Our team employed a similar strategy in which bpy-functionalized Anderson POM hybrids were covalently attached to a heteroleptic Ir-complex to form (*nBu*$_4$*N*)[MnMo$_6$O$_{18}${(OCH$_2$)$_3$CNCH(IrC$_{33}$H$_{26}$N$_4$)}$_2$] (= Ir-POM$_M$, M= Mn, Fe, and Co) dyads, see Figure 26. By varying the heteroatoms, the reactivity of the dyads was tuned, and the resulting dyads were investigated for the homogeneous visible-light-driven HER. All the dyads showed hydrogen evolution over a period of 7 days in the presence of TEA as an electron donor and acetic acid as a proton source when

irradiated with a monochromatic LED of λ = 470 nm. Significant differences in their catalytic activity after 7 days were noted based on the obtained TONs: Ir-POM$_{Mn}$ displayed the highest catalytic activity with TONs of 80, followed by Ir-POM$_{Co}$ (TONs = 34) and Ir-POM$_{Fe}$ (TONs = 20). Moreover, HER results aligned well with the results of emission quenching of the dyads and electronic structures of the cluster anions. Notably, higher quenching efficiency was observed for Ir-POM$_{Mn}$ (80 %) as compared to Ir-POM$_{Co}$ (32 %) and Ir-POM$_{Fe}$ (21 %). Theoretical studies revealed the highest electron affinity of {MnMo$_6$} compared to {CoMo$_6$} and {FeMo$_6$}, indicating {MnMo$_6$} species is the easiest to reduce. Thus, combined experimental and theoretical studies supported the higher HER activity of Ir-POM$_{Mn}$. Additionally, the non-covalent reference system showed significantly lower TONs, suggesting the advantage of the covalent attachment under the given conditions.[126,127]

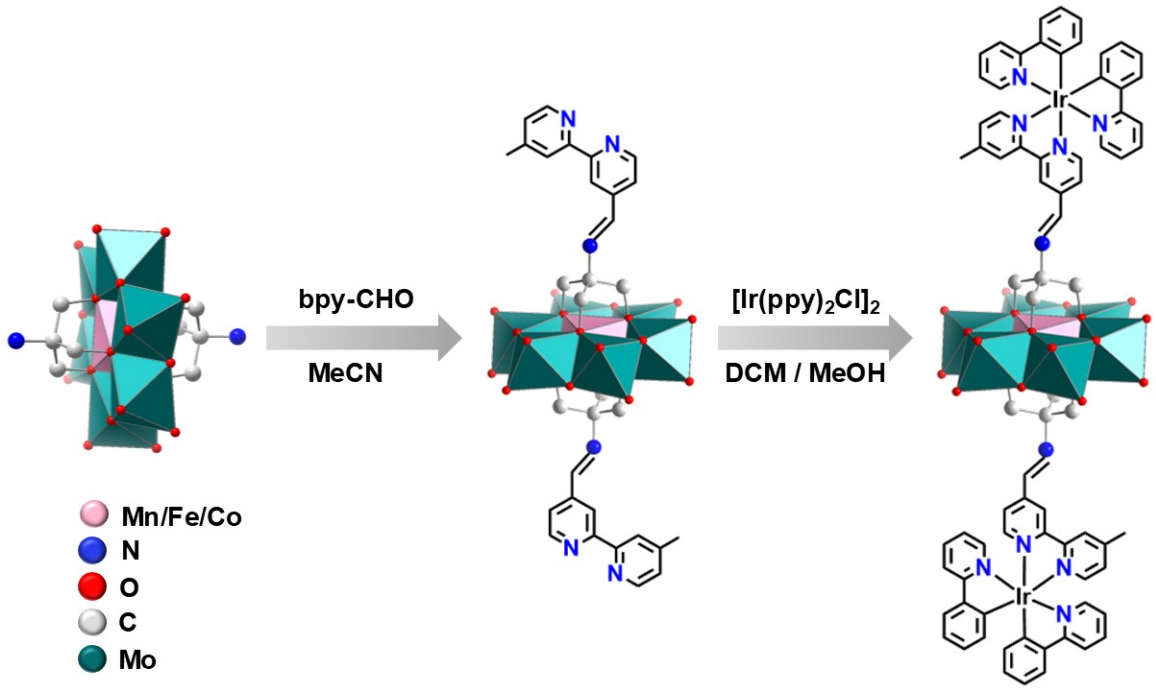

Figure 26: Schematic representation of the formation of covalently linked Anderson POM-Ir dyads (Ir-POM$_M$) starting from the tris-functionalized Anderson POM {MMo$_6$}, M = Mn, Fe, and Co. In step 1, two bpy units are attached onto the POM *via* Schiff base formation, followed by the coordination of Ir photosensitizer to the coordinating sites of bpy.[126]

In addition to the covalent photosensitizer-POM dyads, considerable efforts have been made toward non-covalently linked PS-POM systems because they can be assembled using a relatively simple strategy. In these systems, the POM cluster is closely associated with organic or metal complexes *via* electrostatic interactions, and these assemblies have been employed for different photocatalytic applications.[128–130]

A study by Keyes and colleagues demonstrated the formation of photostable ion-cluster between $[Ru(bpy)_3]^{2+}$ and $[S_2Mo_{18}O_{62}]^{4-}$ in solution *via* electrostatic interactions. Photophysical and spectroscopic studies suggested the quenching of $[Ru(bpy)_3]^{2+}$ by $[S_2Mo_{18}O_{62}]^{4-}$ follows a static mechanism. Effective electronic communication was observed between the ions, and the existence of luminescent inter-ion charge transition was assigned to charge transfer from $[Ru(bpy)_3]^{2+}$ to $[S_2Mo_{18}O_{62}]^{4-}$ by Resonance Raman spectroscopy.[131] The authors also reported ion cluster formation between $[Ru(bpy)_3]^{2+}$ and the tungstate analogue $[S_2W_{18}O_{62}]^{4-}$. While significant electronic communication was observed, this system differs from the polymolybdate species due to the presence of a comparatively long-lived charge transfer component.[132] Building on these findings, Hill and co-workers used a three-component system for the photocatalytic reduction of water, comprising of a tetra-manganese-containing V-centered polyoxotungstate, $Na_{10}[Mn_4(H_2O)_2(VW_9O_{34})_2]$ as a catalyst, $[Ru(bpy)_3]^{2+}$ as a photosensitizer, TEOA as a sacrificial electron donor, and water as a proton source. Steady-state and time-resolved fluorescence spectroscopy revealed that the system follows an oxidative quenching mechanism for hydrogen production. Also, the amount of hydrogen production increased with higher concentration of $[Ru(bpy)_3]^{2+}$ and higher pH.[133] Moreover, the authors designed a tetra-nickel-substituted polyoxotungstate as an efficient and robust photocatalyst for hydrogen evolution. The catalytic activity of the synthesised polyoxotungstate was examined using $[Ir(ppy)_2(dtbbpy)]^{+}$ as a photosensitizer, TEOA as a sacrificial electron donor using a blue LED (λ = 455 nm). The photocatalytic hydrogen evolution was detected over a week with TONs of *ca.* 6500 without a significant loss in its activity. Photophysical studies elucidated that the catalytic system follows both oxidative and reductive quenching mechanisms.[134]

The use of POMs as multifunctional platforms for light-driven HER has been reported by Streb and colleagues, where the HER-active Pt catalysts (with chloride or iodide ions on the Pt center) were covalently linked to the bpy-functionalized Anderson POM to form POM-PtX hybrids ($(n\text{Bu}_4\text{N})_3[\text{MnMo}_6\text{O}_{18}\{(\text{OCH}_2)_3\text{CNCH}(\text{C}_{11}\text{H}_9\text{N}_2)\ \text{PtX}_2\}_2]$, X = Cl, I) dyads, as shown in Figure 27.[135]

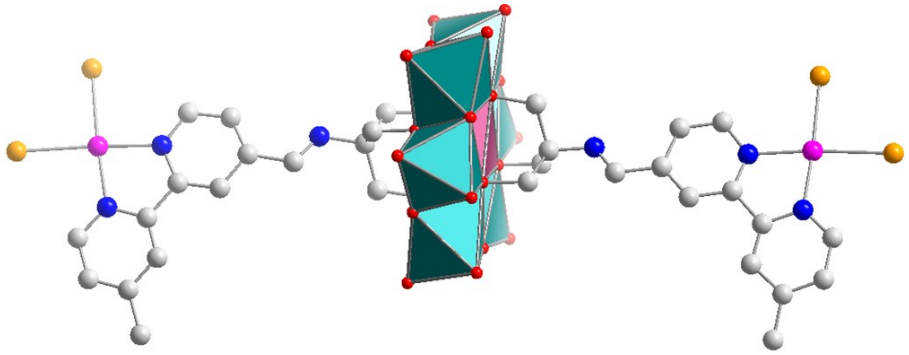

Figure 27: Representation of the molecular structure of POM-PtX dyad, where Pt-X units are covalently attached to the N-coordinating sites of the bpy-functionalized Anderson POM. Colour scheme: Mn = teal, Mo = plum, Pt = purple, N = blue, C = grey, and X (Cl or I) = orange.[135]

Supramolecular electrostatic coupling of the POM-PtX systems to an iridium photosensitizer in the presence of TEA as an electron donor and acetic acid as a proton source enabled hydrogen production. It was shown that substantially higher TONs were observed with the POM-PtI system compared to the POM-PtCl after 10 h of irradiation, highlighting the role of tuning the ligands to enhance the HER reactivity. Mechanistic photophysical and theoretical studies were conducted to understand the role of individual components, which also supported the catalytic results.

1.8 Organofunctionalized Polyoxometalates in the Formation of Supramolecular Assemblies

Beyond molecular photocatalytic systems, organofunctionalized POMs can be assembled to build extended supramolecular architectures.[136–138] As these POMs typically contain oxygen or nitrogen donor groups from their organic ligands, they can coordinate with various transition metals (e.g., Co, Pd, Zn) to form POM-based metal-organic complexes. In these complexes, the transition metal can bind to a single POM cluster or act as a bridging unit to connect multiple POMs to form a 3D supramolecular network. The resulting 3D network can either form a solid crystal or a supramolecular

gel depending on factors such as inter- or intramolecular interactions, concentration, and solvent effects.[139–141]

Supramolecular gels are soft materials formed through self-assembly of low molecular weight gelators (LMWGs) *via* non-covalent interactions such as hydrogen bonding, metal coordination, and electrostatic interactions.[142–145] This results in the formation of 3D entwined fibrillar networks in which solvent molecules are immobilized by capillary action, and surface tension,[146,147] see Figure 28. Various compounds have been employed as LMWGs such as peptides, bis(urea) derivatives, and amino acid derivatives in the formation of supramolecular gels.[148,149] The weak interactions in supramolecular gels make them responsive to external stimuli such as temperature, pH, light, or mechanical force, resulting in sol-gel transformation.[150–152] This dynamic and reversible nature enables tuning of the gel properties through the incorporation of specific functional units, thereby broadening their application range.[153] Metallogels are an attractive sub-class of supramolecular gels, in which gel formation is governed by the coordination chemistry between the metal cations and the organic ligands. The incorporation of different metal ions or metal-organic components can be used to alter properties such as magnetic, luminescent, catalytic, and redox activity in these gels.[154]

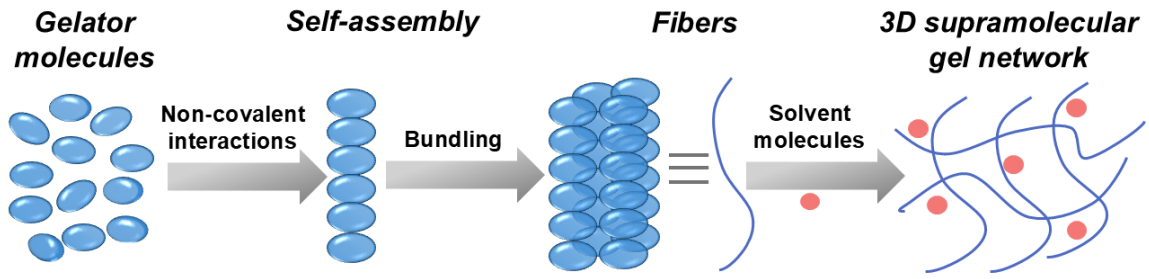

Figure 28: Illustration of the general mechanism of supramolecular gel formation. Self-assembly of low molecular weight gelator molecules through non-covalent interactions forms fibers which intertwine to form a 3D network. The solvent is immobilized inside the 3D network.[155,156]

Recently, POMs have emerged as promising building blocks in the formation of metallogels due to their versatile redox properties and structural tunability. As described earlier, the covalent attachment of organic ligands to POMs provides anchoring sites through which metals can coordinate, leading to the formation of POM-based metallogels. A seminal work by Hasenknopf and co-workers showed that coordination of Pd(II) to pyridyl-functionalized Anderson POMs leads to the formation

of an anisotropic metallogel. The formed gel showed good thermal stability and birefringence.[139] In another example, Izzet et al. designed dumbbell-shaped dimers by linking terpyridine-functionalized Keggin and Dawson POMs with Co(II) or Co(III). Washing the formed precipitates of these dimers with ethanol led to the formation of a metallogel. Furthermore, the obtained metallogel exhibited interesting solvent exchange behaviour, leading to hydrogel formation. The authors confirmed hydrogel formation by TGA analysis, which showed that the hydrogel contained *ca.* 95% water, similar to the ethanol content in the metallogel.[157]

Furthermore, metallogels can be converted into aerogels by using a freeze-drying approach to impart additional properties.[158] This method removes the solvent from the gel, while preserving the 3D architecture.[159] Aerogels are defined as solid materials where the solvent is replaced with air. They feature hierarchical pore structure, high specific surface area, and low density.[160,161] The possibility to use various materials such as polymers, carbon-based materials, metals, and metal oxides in the preparation of aerogels has increased their application area.[162] Among these, metal-based aerogels have gained significant interest due to their synergistic properties such as catalytic activity, redox properties, and porosity. Owing to their unique properties, metal-based aerogels have been widely investigated in catalysis, biosensing, and wastewater treatment.[163–165]

Recently, there has been significant interest in POM-containing aerogels because of their tunable redox behaviour, structure, and versatility. The incorporation or immobilization of POMs into aerogels enables their transition from homogeneous to heterogeneous catalysis.[166,167] The POM-based aerogels thus have been explored as heterogeneous catalysts for various applications, including electrocatalysis, oxidation catalysis, and pollutant removal.[167–169] These developments highlight the versatility of polyoxometalates as ideal candidates in the synthesis of supramolecular and porous materials.

2 Objective

Organic functionalization of polyoxometalates is attracting much attention as it enables the formation of inorganic-organic POM hybrids and supramolecular architectures. POM-based hybrids have been explored for various applications such as oxidation catalysis, photocatalysis, and energy conversion and storage, owing to their structural tunability and redox properties. Despite significant efforts, the synthesis of covalent POM-based hybrids remains challenging. However, such systems offer advantages, including increased electronic interactions between the components, robustness, higher stability, and fewer chances of formation of ion-paired products or precipitation, as observed for non-covalent systems. In contrast, multi-component supramolecular systems are relatively simple to build as they are often assembled by mixing the components. Therefore, both covalent and multi-component POM-based systems have their respective benefits in the context of solar energy conversion. Since the design of covalent systems is synthetically challenging, the main goal of this work is to develop Anderson POM-based hybrids for photocatalytic hydrogen evolution. In addition, the formation of supramolecular POM-based aerogels was investigated in the context of oxidation catalysis.

Three projects were addressed within this work:

1. **A new strategy for the design of symmetric and asymmetric Anderson POM hybrids for photocatalytic HER**

Functionalization of Anderson polyoxometalates with tris-ligands and their derivatives is one of the most widely used strategies for constructing Anderson POM hybrids. Streb et al. reported the covalent attachment of two Pt(II) HER catalysts onto a bpy-functionalized Anderson polyoxomolybdate, where bpy ligands were attached to the POM through labile imine bonds. It was shown that the electrostatic coupling between an iridium photosensitizer and the di-functionalized Anderson anions enabled light-driven hydrogen evolution under water-free conditions.[135] In this work, the aim was to develop rigid and robust Anderson POM hybrids capable of visible-light-driven hydrogen evolution in the presence of water as a proton source. Two supramolecular polyoxometalate-based dyads with mono- and di-functionalized Pt(II) complex were developed *via* a stoichiometrically controlled complexation approach. The structural identity of the dyads was confirmed by analytical techniques such as NMR

spectroscopy, XPS, and MALDI-TOF. Light-driven HER was investigated using symmetric and asymmetric Anderson dyads electrostatically attached to a ruthenium photosensitizer in homogeneous solution. The HER activity of the dyads can be controlled by varying the number of Pt-catalytic sites. This approach provides a foundation for designing molecular complexes with two different functionalities onto a POM platform.

2. **Photosensitizer-polyoxometalate-catalyst triad for light-driven hydrogen evolution**

Asymmetrically functionalized polyoxometalates offer the advantage of developing multifunctional hybrid materials with enhanced structural diversity and complexity for specific applications. However, due to the synthetic and purification challenges associated with asymmetric POM hybrids, only a limited number of reports are available. Based on the stepwise metal complexation strategy, we designed the first example of an Anderson POM-based triad for visible-light-driven HER. The triad was obtained by grafting a Pt(II) HER catalyst unit onto one side of a bpy-functionalized Anderson POM, followed by the addition of an iridium photosensitizer on the other side of the POM to yield the Ir-POM-Pt triad. Insights into the electronic structure and charge-transfer mechanism within the triad were gained by theoretical and mechanistic photophysical studies. In addition, spectroscopic analysis provided information about the stability of the molecular triad under photocatalytic conditions.

3. **Organofunctionalized Anderson POMs as building block for aerogel formation**

The use of organofunctionalized POMs is a promising approach to access 3D supramolecular architectures that enables their use in heterogeneous catalysis. The aim of this study was to develop a catalytically active Anderson POM-based aerogel. The addition of $ZnCl_2$ solution to $\{MnMo_6\}$ led to instantaneous organogel formation (gelation time *ca.* 10 s), which was further freeze-dried to obtain an aerogel. To gain insights into the gelation, the role of individual components was investigated. Furthermore, to follow the conversion of $\{MnMo_6\}$ into organogel and aerogel, various experimental techniques were employed. The catalytic activity of the aerogel was tested for the selective heterogeneous oxidation of primary alcohols to provide a basis for the application.

3 Results and Discussion

3.1 A new strategy for the design of symmetric and asymmetric Anderson POM hybrids for Photocatalytic HER

Note: This chapter is based on the published journal article: P. Endres, G. Sachdeva, A. Winter, D. Díaz, H. Görls, N. Fritz, C. Neumann, A. Turchanin, C. Streb, and U.S. Schubert*. Stepwise synthesis of symmetric and asymmetric Anderson-polyoxometalates for light-driven hydrogen evolution. ***Inorg. Chem. Front.***, 2026, **13**, 1442-1448. These authors contributed equally: Patrick Endres, Garima Sachdeva. The corresponding author(s) are indicated with an asterisk "*".

3.1.1 Introduction

Functionalized polyoxometalates (POMs), in which organic moieties are grafted to metal–oxide clusters, have attracted widespread interest due to the ability to combine various functions (e.g., light absorption, redox activity, etc.) into one molecular array.[63,78,170] Covalently organo-functionalized POMs have been used in various fields of research, including the light-driven HER, photo-electrochemistry, biomedicine, redox-active nanomaterials, (electro)catalysis, and energy storage.[43,171,172] Regarding the use in the context of the photochemical HER, various strategies have already been successfully demonstrated. In an intermolecular scenario, i.e., the photosensitizer (PS), typically a light-absorbing transition-metal complex or an organic dye is combined with a redox-active POM. Due to strong non-covalent (e.g., electrostatic) interactions between the two components, electron transfer and H_2 evolution are facilitated.[173] However, often, this approach is complex, as interactions between PS and POM can lead to undesired side reactions including ion pairing and precipitation. The alternative, i.e., an intramolecular scenario, can be achieved by covalently linking metal complexes[125,174,175] or organic dyes[121,176–178] as PS to suitable organo-functionalized POMs. This has been explored using either post-synthetic modification of pre-synthesized organo-POMs[125,127,179,180] or by direct functionalization of an appropriate POM precursor with a suitable PS.[175] The resulting

covalently linked PS-POM dyads feature H_2 evolution and have even been employed for solar-energy storage and on-demand hydrogen release.[175]

In order to increase the structural complexity of organofunctionalized POMs, the toolbox of available post-functionalization methods has been significantly extended in recent years.[63] However, the asymmetric functionalization, in particular of POMs from the Anderson-Evans family, remains challenging, but offers unique abilities to introduce two different functionalities (e.g., photosensitizer and catalyst) on one POM platform.[73,79,181–183] The one-pot synthesis of asymmetric POMs using two different organic ligands is intricate due to the tedious removal of the simultaneously formed symmetric POMs.[79] Whereas, the stoichiometry-controlled one-sided modification of H_2N-[$MnMo_6$]-NH_2, which is recognized as the “universal” precursor in this field, is often less demanding. In order to establish a new route towards asymmetrically functionalized POMs, we relied on the bpy-[$MnMo_6O_{24}$]-bpy POM (**1**), which was previously used to assemble the symmetric bis-complexes **2** by coordinating $[Ir(ppy)_2]^+$ or $[Rh(ppy)_2]^+$ fragments to both of the POM’s binding sites (bpy: 2,2′-bipyridine; ppy: 2-phenyl-pyridinato; Figure 29).[179] The Ir(III)-containing derivative (**2a**) was further used as a photosensitizer-catalyst (PS-Cat) dyad for the light-driven HER.[180,184]

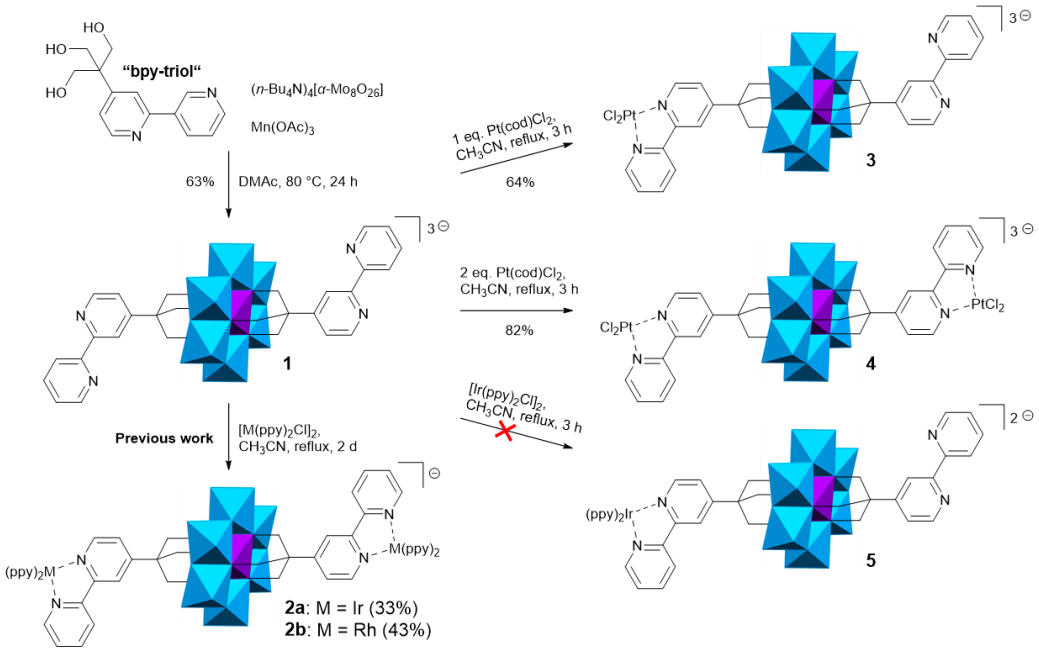

Figure 29: Schematic representation of the synthesis of the symmetric and asymmetric complexes of bpy-[$MnMo_6O_{24}$]-bpy (**1**) with $PtCl_2$ fragments. The respective *tetra*-n-butyl ammonium (TBA) counterions are omitted for clarity. Colour scheme for the POM moiety: Mo: blue, Mn: purple.

3.1.2 Results and Discussion

Here, we expand this approach to establish a more generalized access route to symmetric and asymmetric Anderson anions, functionalized with photoactive or catalytically active metal complex fragments. The $[Pt(cod)Cl_2]$ precursor was used to prepare the mono- and bis-complexes of **1** by a straightforward stoichiometry-controlled complexation strategy (cod: cycloocta-1,5-diene; Figure 29). The products **3** and **4** were obtained in 82% and 64% yield, respectively, after precipitation or crystallization from the reaction mixture. The product formation was facilitated by the ease of complexation under mild conditions, that were not given when dealing with the $[Ir(ppy)_2Cl]_2$ precursor. The targeted synthesis of **5** remained unsuccessful and provided mixtures of products which could not be separated. Research to overcome this shortcoming is still ongoing. Compounds **3** and **4** were thoroughly characterized by NMR spectroscopy (^{1}H-, ^{195}Pt-, ^{1}H-diffusion-ordered spectroscopy (^{1}H-DOSY)), matrix assisted laser desorption/ionization time-of flight (MALDI-TOF) mass spectrometry as well as high-resolution X-ray photoelectron spectroscopy (XPS). The ^{1}H NMR spectra featured the signal of the OCH_2 moieties at *ca.* 64 ppm (see SI). The remarkable downfield shift of the signal of the alkoxy linkage is due to its proximity to the paramagnetic Mn(III) centre, which is in a triplet high-spin state.[185]

Moreover, the signals of the bpy ligand of the [Pt(bpy)Cl_2] moiety were unambiguously identified (see Figure 30).[186,187] However, considerable signal broadening prevented the precise assignment and accurate integration. Nonetheless, due to the symmetric nature of **4**, the aromatic region revealed less signals as in the case of asymmetric **3** (this behaviour resembles that of **2a/b**, which were reported beforehand).[179] The ^{1}H NMR spectrum of **3** showed signals of the coordinated and non-coordinated bpy ligands, indicative of the selective single-site complexation of **1**. Whereas, compounds **3** and **4** could not be distinguished by ^{195}Pt NMR spectroscopy: In either case, a signal at *ca.* −2325 ppm was observed, which is in the typical range for a [Pt(bpy)Cl_2] complex.[188]

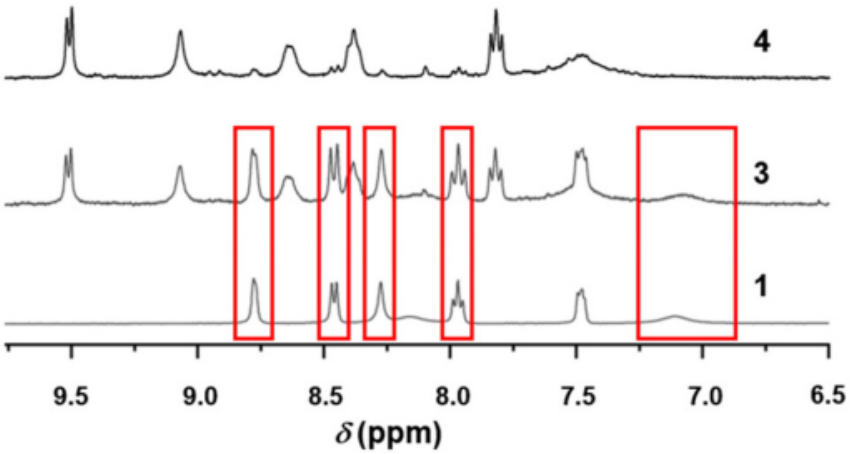

Figure 30: ^{1}H NMR spectra of **1**, **3** and **4** (300 MHz, d_6-DMSO, 298 K). For clarity, only the aromatic region is shown here.

^{1}H-DOSY measurements were also carried out to confirm the structure and homogeneity of compounds **1**, as well as **3** and **4**. In all cases, the diffusion of the respective polyoxoanion independent from the TBA (nBu$_4$N$^+$) cations was observed (an overlay of the DOSY spectra is shown Figure 31, the full spectra are displayed in the SI). The SEGWE model was applied to correlate the measured diffusion coefficients (D) to the calculated ones.[189,190] Albeit not developed for the analysis of complex, metal-containing molecules, such as the rigid hybrid POMs, a remarkably good agreement of the experimental and theoretical D values was obtained for **1**, **3** and **4** (i.e., deviation of ≤4%, Table 1). Thus, ^{1}H-DOSY represents a powerful, yet rarely used method to analyse (hybrid) POMs in solution.

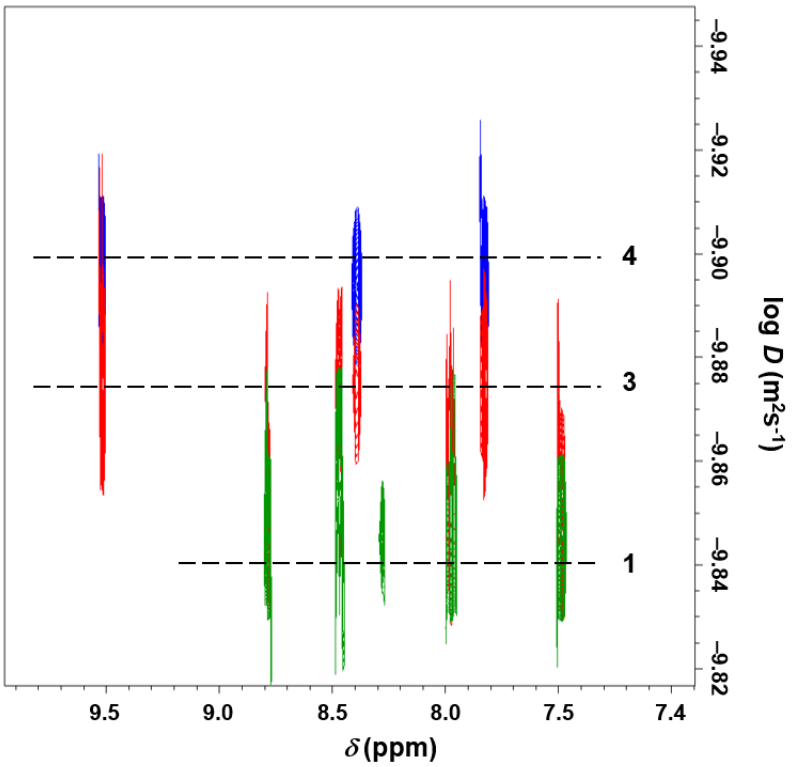

Figure 31: Overlay of the ^{1}H-DOSY spectra of **1** (green), **3** (red) and **4** (blue) showing the diffusion behaviour of the respective polyoxoanions (500 MHz, d_6-DMSO, 298 K). For clarity, only the aromatic region is shown here, full spectra are included in the SI.

MALDI-TOF MS was applied to confirm the identity of **3** and **4**. However, careful optimization of the measurement conditions was required. In the case of compound **3**, the spectra were recorded in the positive reflector mode using KCl as the additive. Whereas the most meaningful spectra of **4** were obtained in the negative mode. The MALDI-TOF mass spectra of **3** and **4**, which were measured with trans-2-[3-(4-tert-butylphenyl)-2-methyl-2-propenyliden]malononitrile (DCTB), as the matrix, are displayed in the SI. In both cases, the intact polyoxoanions with accompanying TBA cations were observed. In contrast to **3**, hybrid POM **4** featured a more complex fragmentation pattern.

Furthermore, the elemental composition of compounds **3** and **4** was determined by high-resolution XPS measurements. The overview spectra, as shown in the SI, revealed the expected elements of the hybrid POMs. The relevant elemental ratios, which were derived from these spectra, were in very good agreement with the calculated ones, thus confirming the compound purity. For example, the observed Pt-to-Mn atomic ratios were 1 : 0.9 (±0.1) (for **3**) and 1 : 2.1 (±0.2) (for **4**). These ratios corroborate the success of the single-side and two-fold complexation, respectively.

Table 1: Results of the 1 H-DOSY measurements[a]

		D (10^{-10} m^2s^{-1})	
	Mw[b] (g mol−1)	Measured	Calculated[c]
1	1433.150	1.33	1.31
3	1699.142	1.27	1.25
4	1965.126	1.22	1.18

[a] Further details on the DOSY results can be found in the SI. [b] Molar mass of the polyoxoanion excluding the three TBA cations. [c] The D values were estimated using Morris' SEGWE D/MW calculator.[191]

In the case of compound **4**, single-crystals suitable for single-crystal X-ray diffraction (XRD) analysis were obtained by the slow diffusion of diethyl ether into a concentrated solution of **4** in CH_3CN. The XRD data revealed a strictly linear arrangement of the molecule, in which the two [Pt(bpy)Cl_2] arms were perfectly coplanar (∠Pt–Mn–Pt = 180°; Figure 32). The intramolecular centre-to-centre distance of two Pt(II) complexes, which were oriented in a transoid fashion, was 18.62 Å. The bond lengths and angles of the [$MnMo_6O_{24}$] cluster were in very good agreement with the values reported elsewhere for related hybrid POMs.[66,179,185,192] Thus, the typical quintet high spin state (S = 2) of the central Mn(II) ion is expected.[185] In particular, very little deviation from the parent structure **1** was observed in terms of bond lengths and angles.[179] The [Pt(bpy)Cl_2] fragments were slightly asymmetric; The Pt–N bonds towards the POM were elongated by a factor of *ca.* 1.1 when compared to those to the more remote N-atoms (i.e., 2.0268 Å vs. 2.0014 Å). This suggests that the coordination *via* the pyridine rings in proximity to the cluster is slightly weaker, due to the electron-withdrawing nature of the polyoxoanion.

The crystal lattice of **4** was comprised of 1D chains, in which the individual Pt-[$MnMo_6O_{24}$]-Pt polyanions interacted *via* metallophilic interactions of their [Pt(bpy)Cl_2] complexes; thereby the adjacent Pt(II) centres were in proximity of 3.60 Å. These chains formed 2D layers, in which the chains were separated by 17.77 Å (resembling the closest distance between two Mn(III) centres of different chains). The 3D lattice represented a highly regular AB-type layered structure, in which the chains within the B layers[185] were rotated by *ca.* 90° with respect to those of the A layer. This 3D

arrangement gave rise to a highly porous structure whose channels and voids contributed *ca.* 40% to the overall volume of the unit cell.

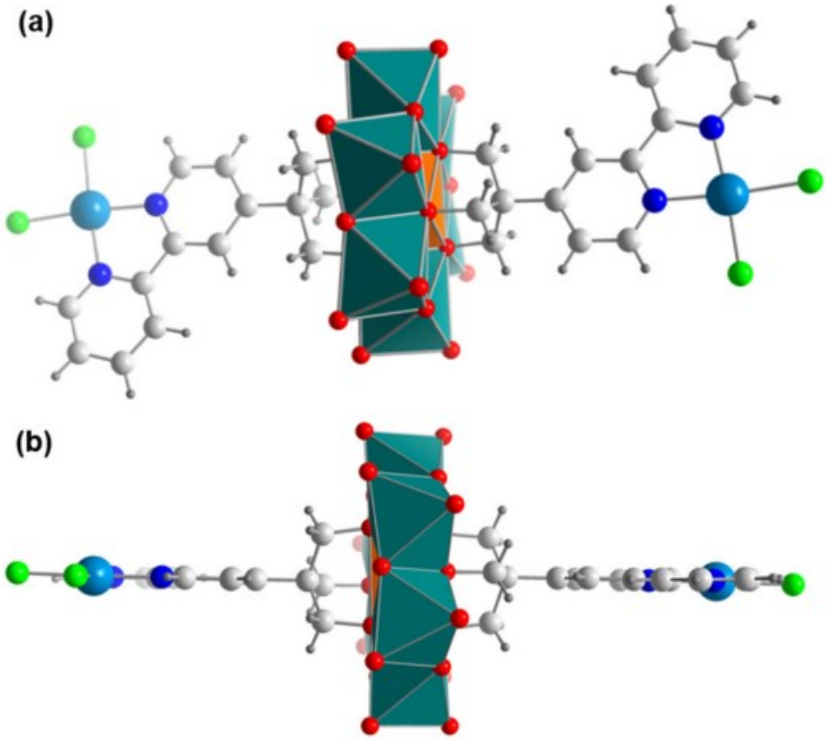

Figure 32: (a and b) Two different views of the solid-state structure of **4** (TBA cations and solvent molecules are omitted for clarity). Colour scheme: Mo: teal, Mn: orange, Pt: light blue, Cl: green, N: dark blue, C: light grey, H: dark grey.

The visible-light-driven HER activity of **3** and **4** was studied using $[Ru(bpy)_3(PF_6)_2]$ as a photosensitizer (PS), because of its well-known ability to transfer electrons to POMs.[133,175,193] In brief, the standard catalytic studies involved water-free, deaerated DMF solutions containing the corresponding catalyst (12.5 µM), PS (125 µM), triethylamine (0.9 M) as a sacrificial electron donor (SED), and water (0.7 M) as a proton source in a microwave vial. Note that DMF was chosen as a solvent due to the chemical compatibility and solubility of all relevant components. The experimental conditions were adapted from previous work.[135] The reaction solution was irradiated with a monochromatic LED source (λ_{max} = 465 nm, P ~13 mW) at ambient temperature conditions, and hydrogen evolution was measured by head-space gas chromatography. The experiments were performed in duplicate and averaged turnover numbers (TONs) are reported. Two in-house synthesized POM based catalysts, $(TBA)_3[MnMo_6O_{18}\{(OCH_2)_3C(C_6H_5)\}_2]$ (**6**)[179] and $(TBA)_3[MnMo_6O_{18}\{(OCH_2)_3CH\}_2]$ (**7**)[185] were used as references under otherwise identical conditions.

As shown in Figure 33, significant differences in the reactivity were noticed after 7 h. Catalyst **4** exhibited turnover numbers (TONs) of *ca.* 451 (TOF *ca.* 1.1 min^{-1}), whereas **3** revealed TONs of *ca.* 345 (TOF *ca.* 0.8 min^{-1}), after seven hours of continuous irradiation. This initial data shows that the HER activity of Anderson HER-catalysts can be controlled by variation of the number of Pt-HER sites present in the catalyst. However, the data also shows that the underlying mechanism requires further analyses, as HER evolution only increases by 30%, not by 100%, as could be theoretically expected. This modest increase in TON is currently under study by time-resolved photophysical methods and computational analysis; however, one plausible explanation is the formation of supramolecular photosensitizer-catalyst aggregates which could lead to different rates of intermolecular electron transfer.

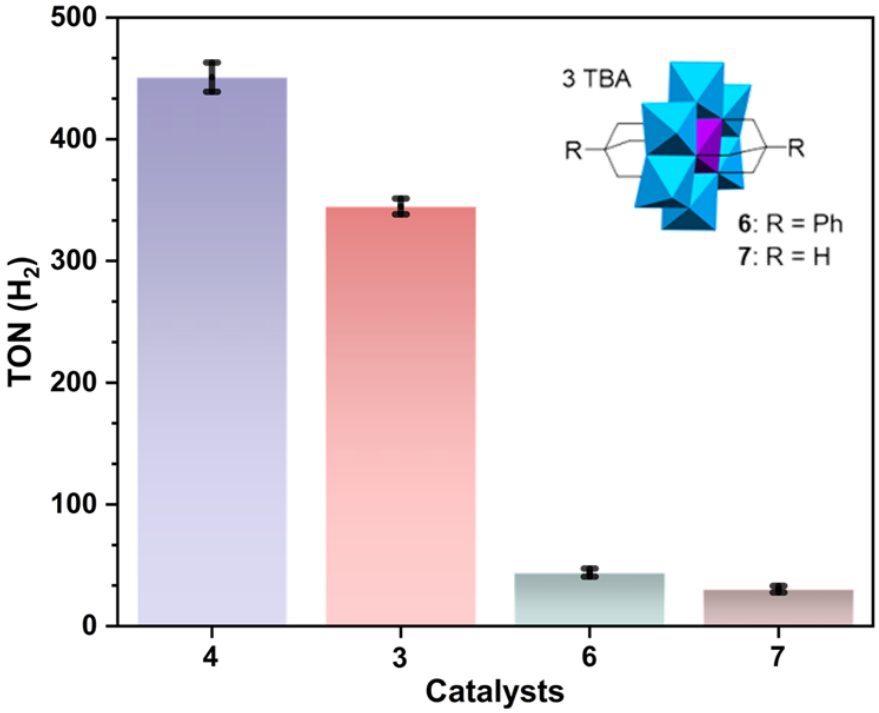

Figure 33: Comparison of the active compounds **3** and **4**, as well as reference compounds **6** and **7** for light driven HER catalysis. Conditions: Catalyst (12.5 µM), PS (125 µM), TEA (0.9 M), H_2O (0.7 M), in water-free, de-oxygenated DMF, λ_{max} = 465 nm, $t_{irrad.}$ = 7 h.

In contrast, when the noble metal-free POM-based reference catalysts **6** and **7** were investigated under identical experimental conditions, only very low TONs were observed (**6**: TON = 44; **7**: TON = 30). This is in line with previous observations which suggest that the Pt-centres represent the actual HER active sites, while the pure POM exhibits only limited HER activity.[126,135,184,194] The observed TONs for **4** are comparable with a previous study on a di-Pt-functionalized Anderson anion, where a

labile imine bond was used to link Anderson POM to the bpy ligands.[135] For this system, TONs of *ca.* 460 were observed after 7 h irradiation when using $[Ir(ppy)_3]^+$ as a photosensitizer. Note that this system could only be operated in water-free conditions due to the hydrolytic lability of the imine bond. In contrast, the present system reaches nearly identical TONs when operated in the presence of water, demonstrating the superior stability of the purely C–C linked organo-functionalization. Detailed mechanistic and photophysical studies are planned to assess solution interactions between PS and POM, and to assess charge-transfer dynamics, supramolecular interactions, and possible back-electron transfer during catalysis.

3.1.3 Conclusion

In sum, this study reports the symmetric and asymmetric functionalization of an Anderson polyoxomolybdate with one or two Pt(I)-complex reaction sites, enabling the light-driven hydrogen evolution reaction when combined with a Ru(II)-based metal-complex photosensitizer. The study demonstrates that the number of Pt sites controls HER activity and paves the way for the design of molecular dyads where in principle, a metal complex PS and a metal complex catalyst could be combined in one molecule. Also, replacement of the noble metal complexes with noble metal-free analogues can be envisaged for enhanced technological relevance.

3.2 Supplementary Information

3.2.1 Materials and Instrumentation

All solvents (HPLC grade) and reagents were purchased from commercial suppliers and used as received. The starting materials (n-$Bu_4N)_4[\alpha$-$Mo_8O_{26}]$,[195] 2-(2,2'-bipyridin-4-yl)-2-(hydroxymethyl)propane-1,3-diol,[179] compound **1**[179] and $[Ir(ppy)_2Cl]_2$[196] were synthesized as described elsewhere.

1D ^{1}H- and ^{195}Pt- NMR spectra were recorded at 298 K on a Bruker Avance III 400 MHz spectrometer equipped with a BBF broadband probe head. The spectra were acquired in d_6-DMSO, which was purchased from Euristop. The ^{1}H-NMR resonances were referenced to the residual solvent signal at 2.50 ppm. Whereas the ^{195}Pt resonances were referenced to the unified Ξ scale[197] using K_2PtCl_4, as the external reference. For these measurements, a spectral width of 200 ppm was used, the data size was 16 k and the number of scans were 200,000. The NMR spectra were processed and analysed with the Topspin software (ver. 4.4) from Bruker.

2D 1H-DOSY spectra were recorded on a Bruker Avance NEO spectrometer (500 MHz) equipped with a Prodigy broadband probe head. For these experiments, the double-stimulated echo (DSTE) sequence with bipolar gradient pulses and three spoil gradients with convection compensation was used (i.e., Bruker's pulse program dstebpgp3s). The diffusion time and the duration of the magnetic field pulse gradients were 50 ms and 2 ms, respectively. The delay for gradient recovery and the eddy current delay were 0.2 ms and 5 ms, respectively. For each experiment, a series of 32 spectra on 32 k data points were collected. After Fourier transformation and baseline correction, the diffusion dimension was processed with the Topspin software (ver. 4.4) from Bruker, and the diffusion coefficients were calculated by Gaussian fits with the relaxation T1/T2 tool implemented in Topspin. The theoretical diffusion coefficients were calculated from the compounds molar masses using the Stokes-Einstein (SE) and the modified Stokes-Einstein Gierer-Wirtz Estimation (SEGWE) model; likewise, the apparent molar masses were calculated from the experimental diffusion coefficients. The calculations were performed using the SEGWE D/W calculator, which is available online free-of-charge.[189–191]

Matrix-assisted laser desorption/ionization time-of-flight (MALDI-TOF) mass spectra were acquired with a rapifleX™ MALDI TOF/TOF from Bruker Daltonics. The instrument was equipped with a smartbeam™ 3D laser (355 nm wavelength). All spectra were measured in the positive and negative reflector mode. The instrument was calibrated with fleXstandard Polymers from Bruker Daltonics in the positive ionization mode; whereas, Merck's CsI3 was used as the standard for the negative ionization mode. Samples were spotted using the dried droplet technique applying DCTB (trans-2-[3-(4-tert-butylphenyl)-2-methyl-2-propenyliden]- malononitrile) as the matrix. In the positive ionization mode, KCl was used to support the ionization. For data processing Bruker's flex Analysis software (ver. 4.0) was used.

X-ray photoelectron spectroscopy (XPS) was performed in a UHV Multiprobe system equipped with a monochromatic X-ray source (Al-Kα) and an electron analyser (Argus CU) with an energy resolution of 0.6 eV (Scienta Omicron). The samples were prepared by drop casting a CH_3CN solution of the material (2 µL) onto Au substrates, which were pre-cleaned by O_2-plasma treatment. Subsequently, the samples were dried under ambient conditions and introduced into the UHV system for measurements. For quantitative analysis, the secondary electron background was subtracted from the high-resolution spectra, and the peaks were fitted using Voigt functions.

Cyclic voltammetry (CV) measurements were carried out using an Autolab PGSTAT30 potentiostat (Metrohm), which was equipped with a standard three-electrode configuration i.e., a glassy-carbon working electrode, a platinum-rod auxiliary electrode and an AgCl/Ag reference electrode. The experiments were carried out at room temperature in degassed DMF (HPLC grade) containing 0.1 M $TBAPF_6$, as a supporting electrolyte. At the end of each measurement, ferrocene (Fc) was added as an internal standard [Fc^+/Fc redox couple at 0.45 V *vs.* the saturated calomel electrode (SCE)]. Basically, the same experimental setup was also used for the square-wave voltammetry (SWV) measurements. These measurements were executed with ferrocene, as an internal standard, using the following parameters: pulse height of 5, pulse width of 150 and step height of −10.

Hydrogen evolution was measured by headspace gas chromatography (GC) on a Shimadzu GC-2030 equipped with a barrier ionization discharge (BID) detector. Helium gas with a purity of 99.9999% was used as carrier gas.

3.2.2 Synthesis

$TBA_3[C_{28}H_{26}Cl_2MnMo_6N_4O_{26}Pt]$ (**3**)

A microwave vial (20 mL) was equipped with **1** (250 mg, 115 µmol), $Pt(DMSO)_2Cl_2$ (48.85 mg, 115.7 µmol) and acetonitrile (11.5 mL). After purging the suspension for 5 min with N_2, the vial was capped. The reaction mixture was stirred for 3 h at 80 °C. A fine precipitate was removed by filtration. The product was isolated by dropping the reaction mixture into diethyl ether (30 mL). **3** was obtained as an orange-yellow powder (229 mg, 82% yield). ^{1}H NMR (400 MHz, d_6-DMSO, 298 K): δ = 9.49 (d, ^3J = 5.4 Hz, 1H), 9.06 (brs, 1H), 8.76 (m, 2H), 8.64 (brs, 1H), 8.44 (d, ^3J = 7.82 Hz, 2H), 8.35 (brs, 1H), 8.26 (brs, 1H), 8.13 (brs, 1H), 7.95 (m, 1H), 7.81 (m, 1H), 7,47 (m, 1H), 7.10 (brs, 1H), 3.16 (brs, 24H), 1.56 (brs, 24H), 1.30 (m, 24H), 0.93 (t, ^3J = 7.1 Hz, 36H) ppm.

^{195}Pt-NMR (400 MHz, d_6-DMSO, 298 K): δ = –2325.63 ppm.

MALDI-TOF MS (DCTB + KCl, positive mode): m/z calcd. for [**3** + TBA]$^+$ corresponding to $[C_{92}H_{170}Cl_2MnMo_6N_8O_{24}Pt]^+$ 2678.505; found 2678.545.

$TBA_3[C_{28}H_{26}Cl_4MnMo_6N_4O_{26}Pt_2]$ (**4**)

The synthesis of **4** was performed similar to that of **3**, but 2 eq. of Pt(DMSO)2Cl2 were used. Specifically, **1** (160.49 mg, 24.28 µmol) and $Pt(DMSO)_2Cl_2$ (62.73 mg, 148.56 µg) were reacted in acetonitrile (20 mL). Single crystals suited for XRD analysis were obtained by the diffusion of diethyl ether into a concentrated solution of the crude product in acetonitrile. 4 was obtained as orange-yellow crystals (133 mg, 56% yield). ^{1}H NMR (400 MHz, d_6-DMSO, 298 K): δ = 9.51 (d, ^3J = 5.8 Hz, 2H), 9.07 (brs, 2H), 8.64 (brs, 2H), 8.39 (brs, 2H), 7.82 (m, 2H), 7.63–7.33 (brs, 4H), 3.16 (brs, 24H), 1.57 (brs, 24H), 1.31 (m, 24H), 0.93 (t, ^3J = 7.2 Hz, 36H) ppm.

^{195}Pt-NMR (400 MHz, d_6-DMSO, 298 K): δ = –2329.14 ppm.

MALDI-TOF MS (DCTB, negative mode): m/z calcd. for [**4** – TBA]$^-$ corresponding to $[C_{60}H_{98}Cl_4MnMo_6N_6O_{24}Pt_2]$ – 2458.839; found 2458.727.

3.2.3 Characterization

1 ^{1}H-NMR spectra

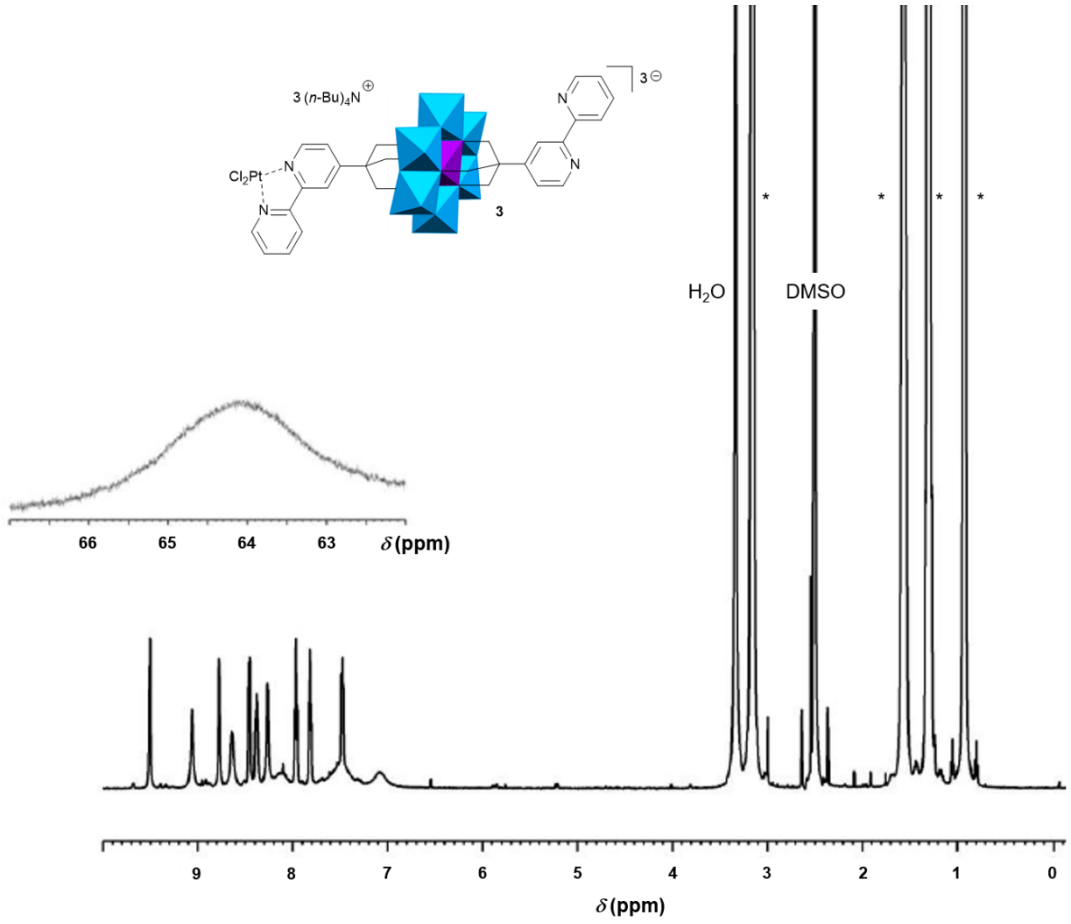

Figure 34: ^{1}H-NMR spectrum of **3** (400 MHz, d_6-DMSO, 298 K). The intense signals of the TBA cations are marked with an asterisk.

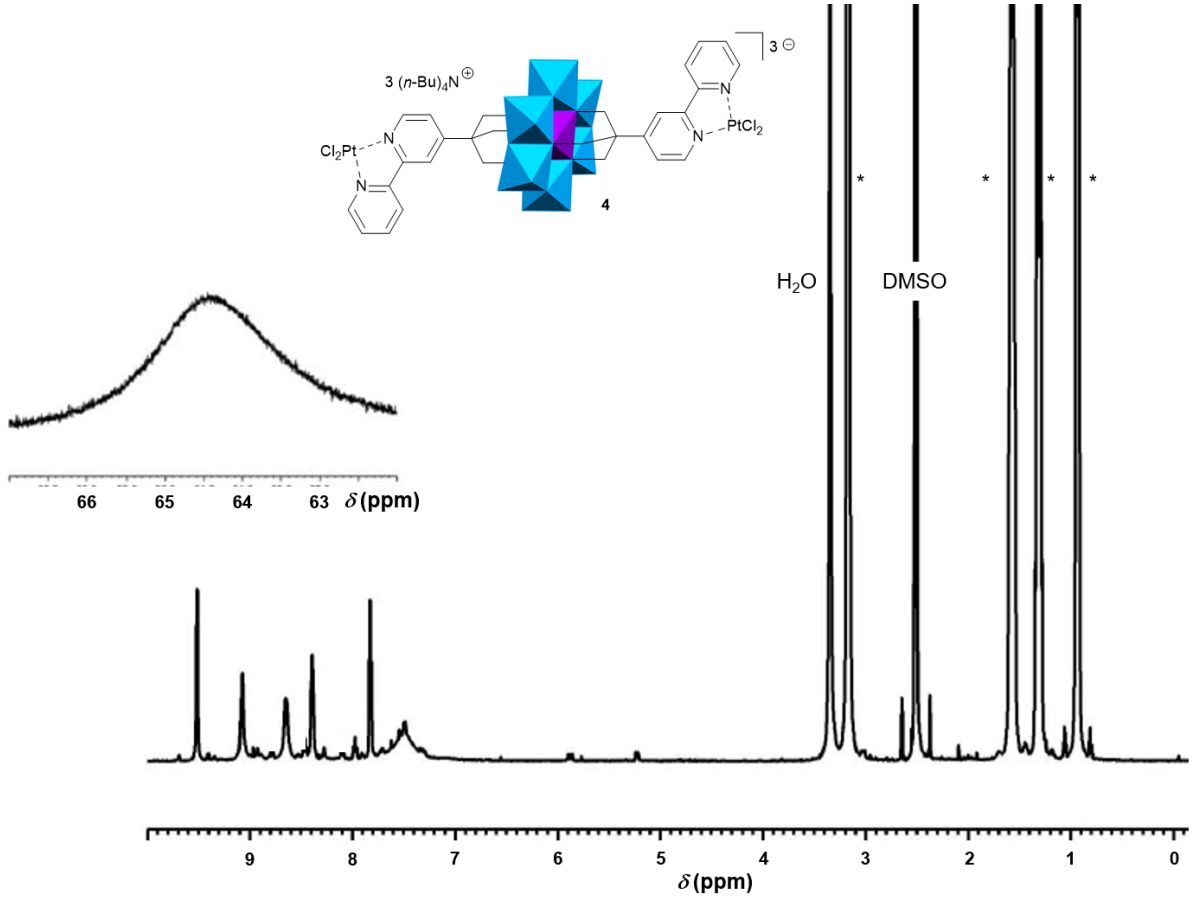

Figure 35: ^{1}H-NMR spectrum of **4** (400 MHz, d_6-DMSO, 298 K). The intense signals of the TBA cations are marked with an asterisk.

2 ^{195}Pt-NMR spectra

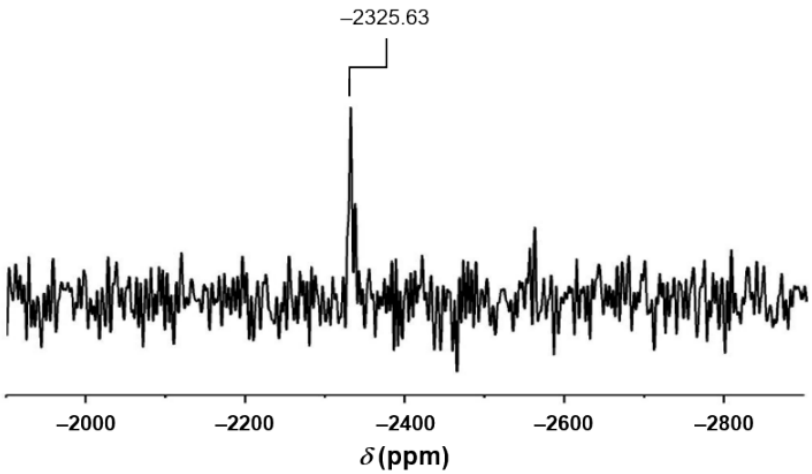

Figure 36: ^{195}Pt-NMR spectrum of **3** (400 MHz, d_6-DMSO, 298 K).

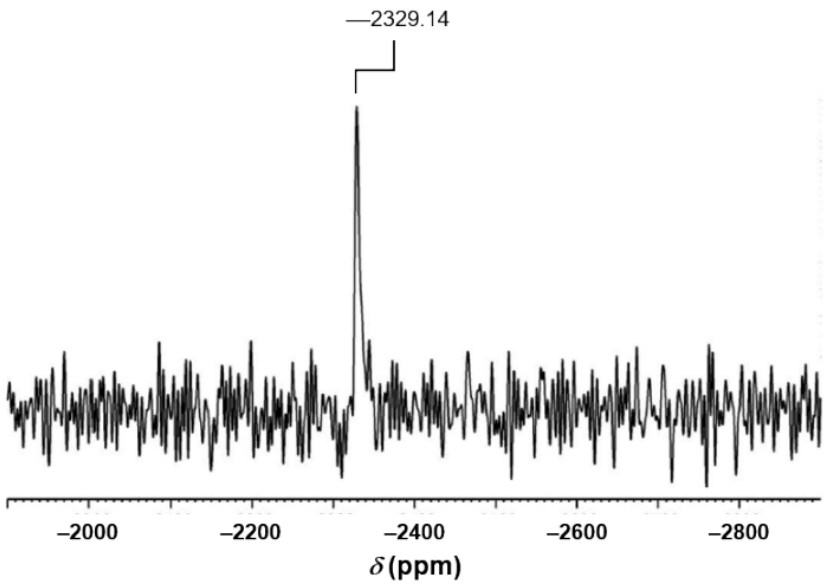

Figure 37: ^{195}Pt-NMR spectrum of **4** (400 MHz, d_6-DMSO, 298 K).

3 DOSY spectra

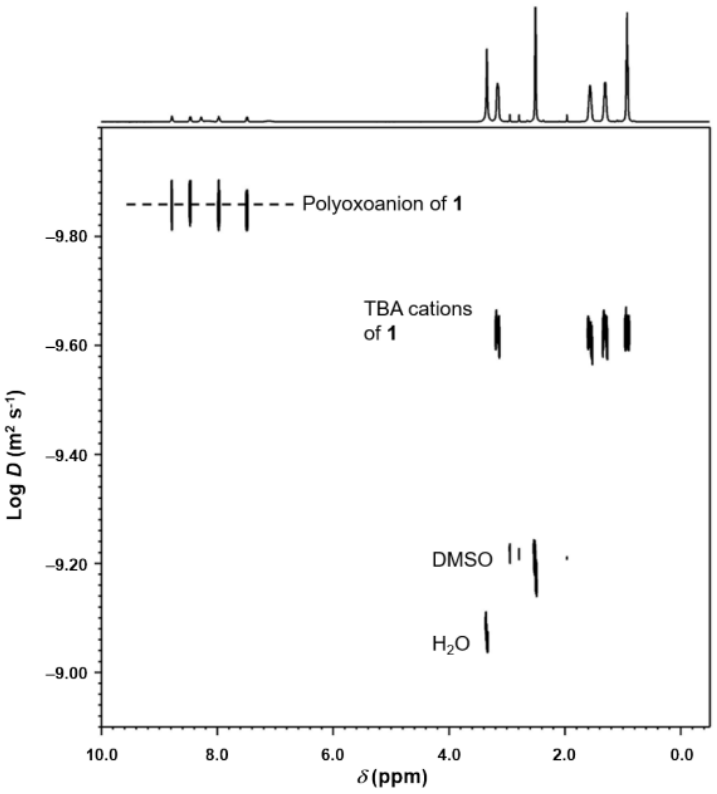

Figure 38: ^{1}H-DOSY of **1** (500 MHz, d_6-DMSO, 298 K).

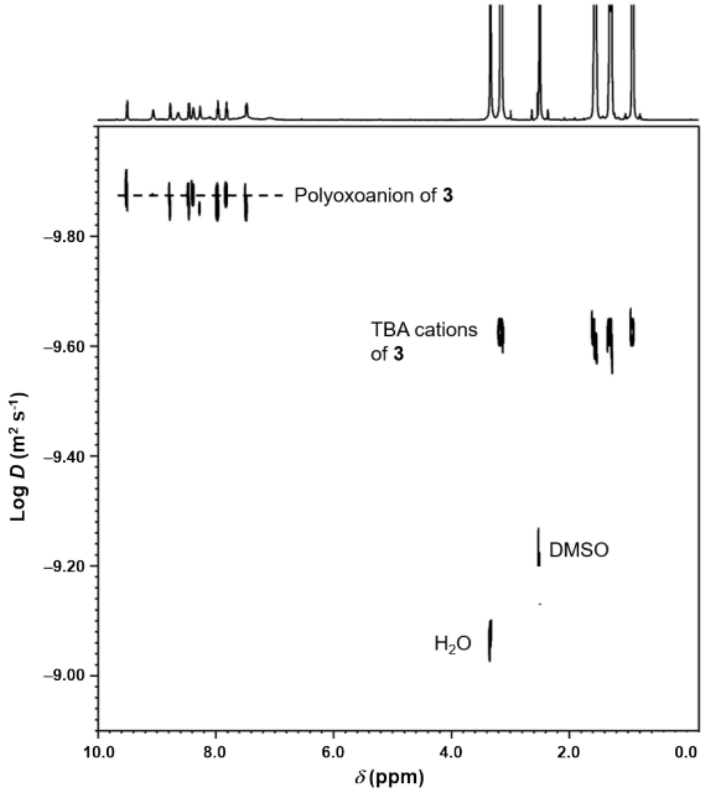

Figure 39: ^{1}H-DOSY of **3** (500 MHz, d_6-DMSO, 298 K).

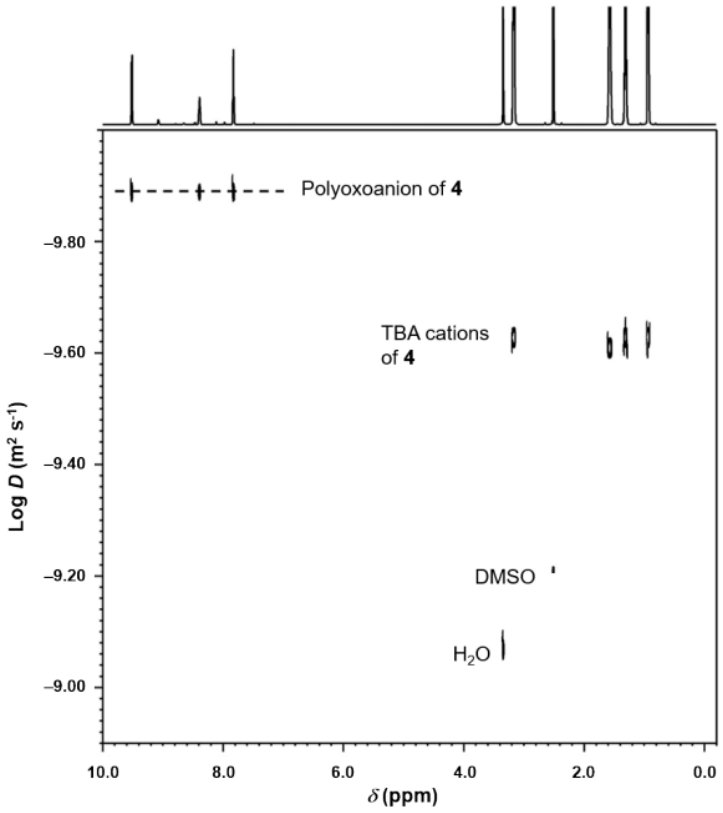

Figure 40: ^{1}H-DOSY of **4** (500 MHz, d_6-DMSO, 298 K)

Table 2: Summary of the measured and calculated diffusion coefficients.

Compounds	M_w [a]	D_{exp} (10^{-10} m^2 s^{-1})	SE model [b]	SEGWE model [b]
			$D \rightarrow M_w$ (g mol^{-1})	$D \rightarrow M_w$ (g mol^{-1})
			$M_w \rightarrow D$ (10^{-10} m^2 s^{-1})	$M_w \rightarrow D$ (10^{-10} m^2 s^{-1})
1	1433.158	1.33	1745.50	1466.42
			1.01	1.31
3	1699.142	1.27	718.22	1553.00
			1.35	1.25
4	1965.126	1.22	810.20	1706.24
			0.84	1.18

[a] For the calculation of the diffusion coefficients, the Mw values of the respective polyoxoanions were used (i.e., the independently diffusing TBA cations were excluded). [b] Morris' SEGWE D/MW calculator was used for the calculations according to both models.[191]

The SEGWE method represents a powerful tool for the estimation of a compound's molar mass from its diffusion coefficient (or vice versa) based on DOSY measurements. The SEGWE method provides more accurate results than the traditional SE methods. This holds particularly true for compounds of low molar mass (i.e., <1000 g mol^{-1}), that only contain "light" atoms (i.e., sulfur or lighter).[189] Although the analyzed compounds are far from being predestined for such a consideration, the calculations according to the SEGWE model delivered realistic results. The molar masses, which were calculated from the experimental D values were underestimated by 9 to 14%. Whereas the estimation of the D values from the molar masses yielded an excellent match, i.e., underestimation of the measured D values by only 2 to 4%. On the other hand, the traditional SE model could hardly be applied to assemblies **3** and **4** – the deviation between calculated and measured values were hardly meaningful. To further validate the applicability of the tool, compound **1** was also analyzed by ^{1}H-DOSY and the SEGWE model. Also in this case, an excellent agreement between the measured and calculated D values was found.

4 MALDI-TOF

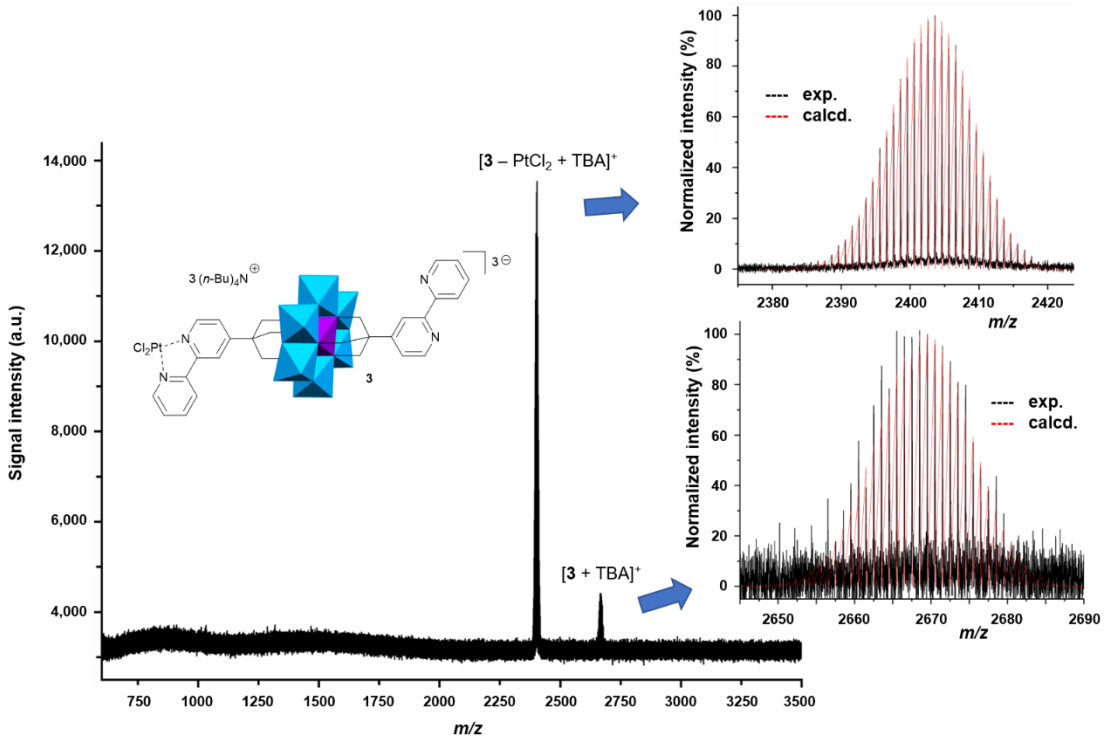

Figure 41: MALDI-TOF MS of **3** (positive reflector mode, matrix: DCTB + KCl).

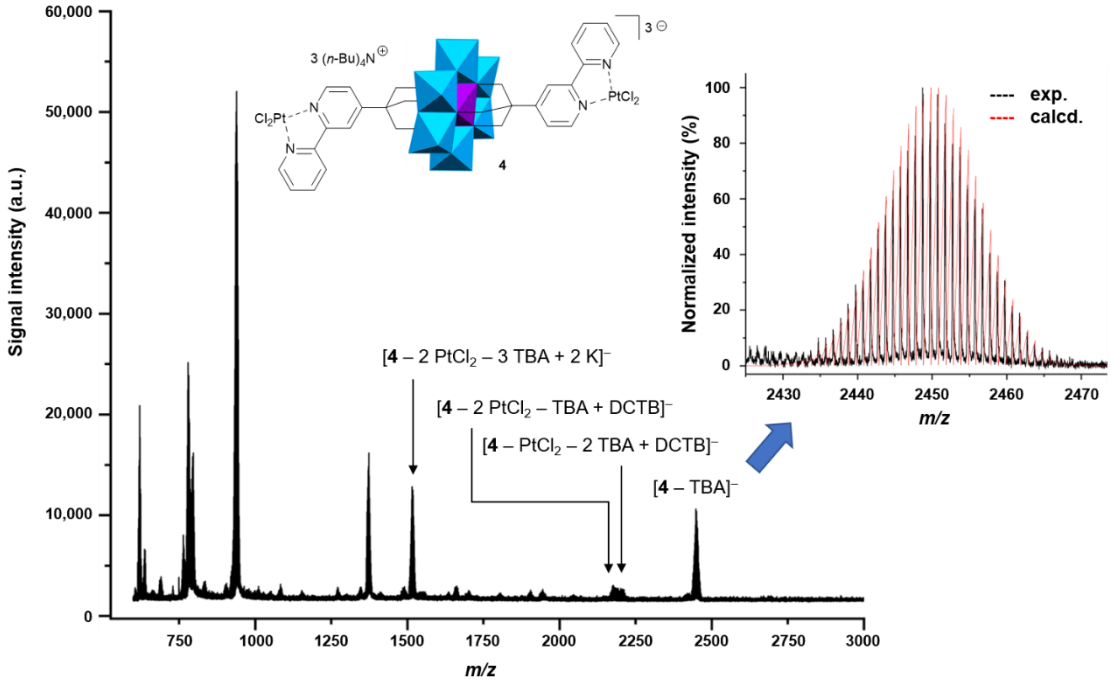

Figure 42: MALDI-TOF MS of **4** (positive reflector mode, matrix: DCTB + KCl).

5 X-ray photoelectron spectroscopy (XPS)

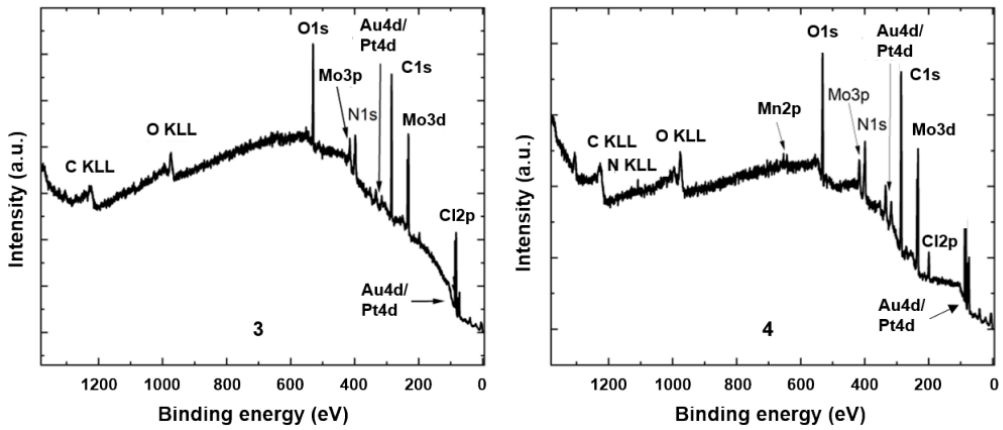

Figure 43: XPS overview spectra of the hybrid POMs **3** (left) and **4** (right).

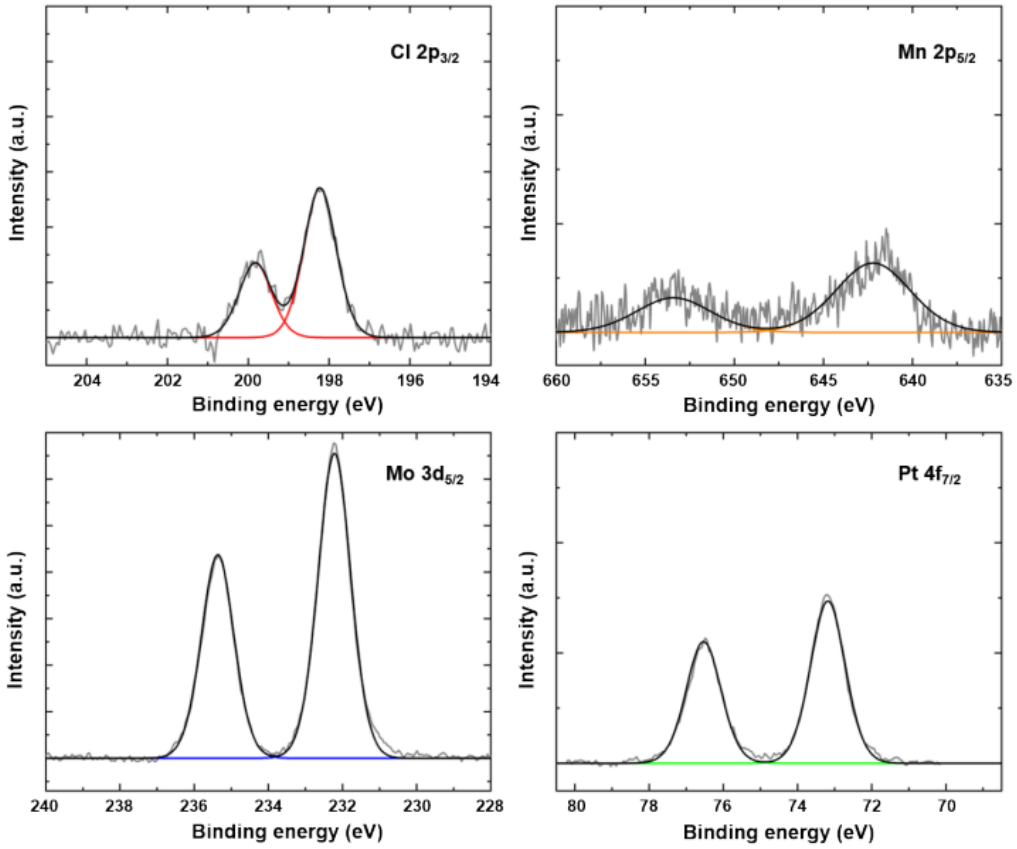

Figure 44: High resolution Cl 2p, Mn 2p, Mo 3d and Pt 4f XPS spectra of the hybrid POM **3**.

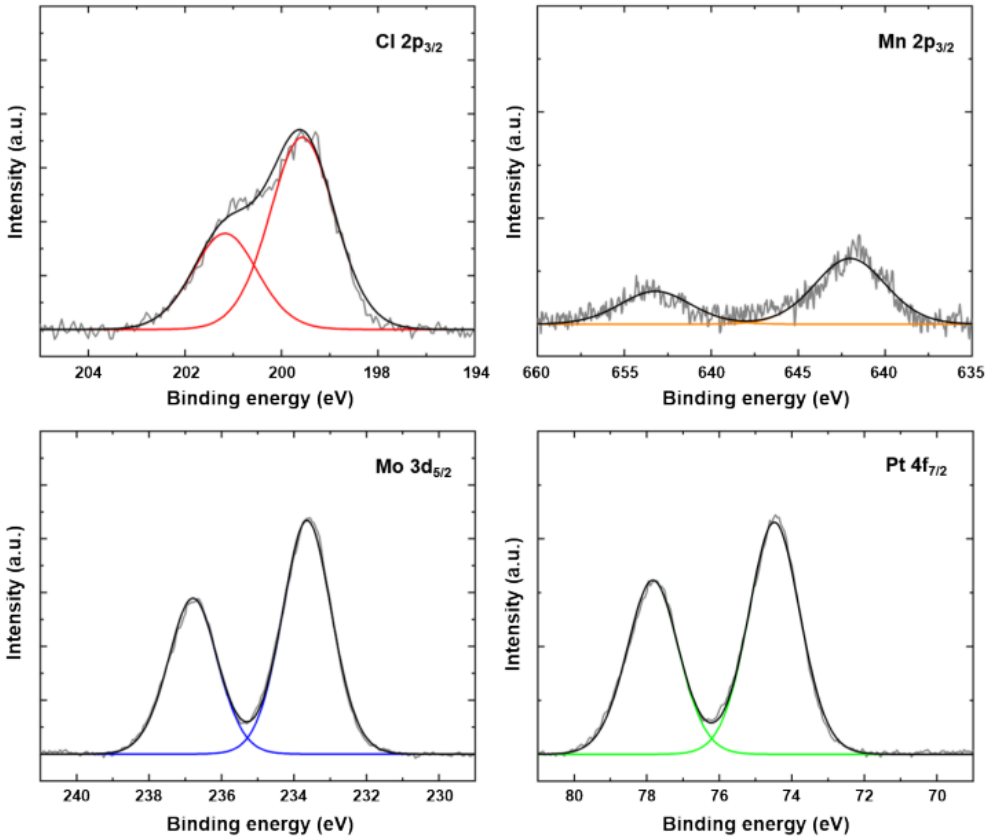

Figure 45: High resolution Cl 2p, Mn 2p, Mo 3d and Pt 4f XPS spectra of the hybrid POM **4**.

Table 3: Quantitative analysis of the high-resolution XPS spectra of compounds **3** and **4** including peak assignment, binding energies and full width at half maximum (FWHM) values obtained from the spectra deconvolution.

	Peak assignment	**Type of Photoelectron**	**FWHM (eV)**	**Binding energy (eV)**
Pt-POM-bpy	$PtCl_2$	Cl $2p_{3/2}$	0.9	198.2
(**3**)	$PtCl_2$	Pt $4f_{7/2}$	1.1	73.1
	$[MnMo_6O_{24}]$	Mo $3d_{5/2}$	1.1	232.2
	$[MnMo_6O_{24}]$	Mn $2p_{3/2}$	4.8	642.0
Pt-POM-Pt	$PtCl_2$	Cl $2p_{3/2}$	1.5	198.2
(**4**)	$PtCl_2$	Pt $4f_{7/2}$	1.7	73.1
	$[MnMo_6O_{24}]$	Mo $3d_{5/2}$	1.6	232.3
	$[MnMo_6O_{24}]$	Mn $2p_{3/2}$	4.8	642.0

The peak fitting of the doublets was performed using fixed intensity ratios due to the spin-orbit coupling of the p, d and f photoelectrons, respectively. With respect to the determination of the elemental ratio (see the main manuscript), the following relative sensitivity factors (RSFs) were used: 1.51 (for Cl $2p_{3/2}$), 8.65 (for Pt $4f_{7/2}$), 5.62 (for Mo $3d_{5/2}$) and 9.17 (for Mn $2p_{3/2}$).[198,199]

Table 4: Relative elemental composition as determined by XPS analysis.

	Pt-to-Cl ratio	Mn-to-Mo ratio	Pt-to-Mn ratio	Pt-to-Mo ratio
Pt-POM-bpy (**3**)	1 : (2.3 ± 0.3)	1 : (6.0 ± 0.7)	1 : (0.9 ± 0.1)	1 : (6.5 ± 0.7)
Pt-POM-Pt (**4**)	1 : (2.2 ± 0.3)	1 : (6.3 ± 0.7)	1 : (2.1 ± 0.2)	1 : (3.0 ± 0.4)

The commonly accepted uncertainty in XPS elemental quantification is 10%; in the case of poor signal-to-noise ratios, the uncertainty is typically estimated as 15%.[200]

6 X-ray diffraction analysis of 4

Structure Determination: The intensity data for compound **4** were collected on a Nonius KappaCCD diffractometer using graphite-monochromated Mo-Kα radiation. The data were corrected for Lorentz and polarization effects; absorption was considered on a semi-empirical basis using multiple-scans.[201–203] The structure was solved by intrinsic phases (SHELXT[204]) and refined by full-matrix least squares techniques against Fo^2 (SHELXL-2018[205]). All hydrogen atoms were included at calculated positions with fixed thermal parameters. All non-hydrogen atoms were refined anisotropically.[205] Disordered moieties of the TBA cations of **4** were refined using displacement parameter restraints (i.e., instructions DFIX, EADP). The crystal of **4** contains large voids, filled with disordered solvent molecules. The overall size of the voids is 4989 $Å^3$ per unit cell. Their contribution to the structure factors was secured by back-Fourier transformation using the SQUEEZE routine of the PLATON program[206] resulting in 1284 electrons per unit cell. The MERCURY software (vs. 2024.3.1) was used to generate the structure representations.[207]

Supporting Information available: Crystallographic data for **4** (excluding structure factors) has been deposited with the Cambridge Crystallographic Data Centre as supplementary publication (CCDC deposition number 2484790). Copies of the data can be obtained free of charge on application to CCDC, 12 Union Road, Cambridge CB2 1EZ, UK (e-mail: deposit@ccdc.cam.ac.uk) or online *via* https://www.ccdc.cam.ac.uk.

Table 5: Crystal data and structure-refinement parameters for **4**.

	4
Identification code	fo6877
Empirical formula	$C_{60}H_{98}C_{14}MnMo_6N_6O_{24}Pt_2$ [a]
Formula weight	2450.00 g mol^{-1}
Temperature	173(2) K
Wavelength	0.701073 Å
Crystal system	Monoclinic
Space group	C2/c
Unit-cell dimensions	a = 30.8643(5) Å α = 90°
	b = 17.6137(3) Å β = 101.059(1)°
	c = 23.0669(3) Å γ = 90°
Volume	12307.1(3) $Å^3$
Z	4
Calculated density	1.322 g cm^{-3} [a]
Absorption coefficient	30.87 cm^{-1} [a]
F(000)	4772
Crystal size	0.062 × 0.060 × 0.058 mm^3
Theta range for data collection	2.136° ≤ Θ ≤ 27.485°
Reflections collected	36614 in h(–26/40), k(–22/20), l(–29/29)
Independent reflections	14048 [R(int) = 0.0421]
Completeness	99.8%
Absorption correction	Semi-empirical from equivalents
Max. and min. transitions	0.7456 / 0.5120
Refinement method	Full-matrix least squares on F^2
Data / restraints / parameters	14048 / 3 / 426
Goodness-of-fit on F^2	1.070
Final R indices [I > 2σ(I)]	R1 = 0.0459, wR2 = 0.0983
R indices (all data)	R1 = 0.0616, wR2 = 0.1058
Extinction coefficient	n/a
Largest diff. peak / hole	1.562 / –0.981 e $Å^{-3}$
CCDC deposition number	2484790

[a] Derived parameters do not contain the contribution of the disordered solvent.

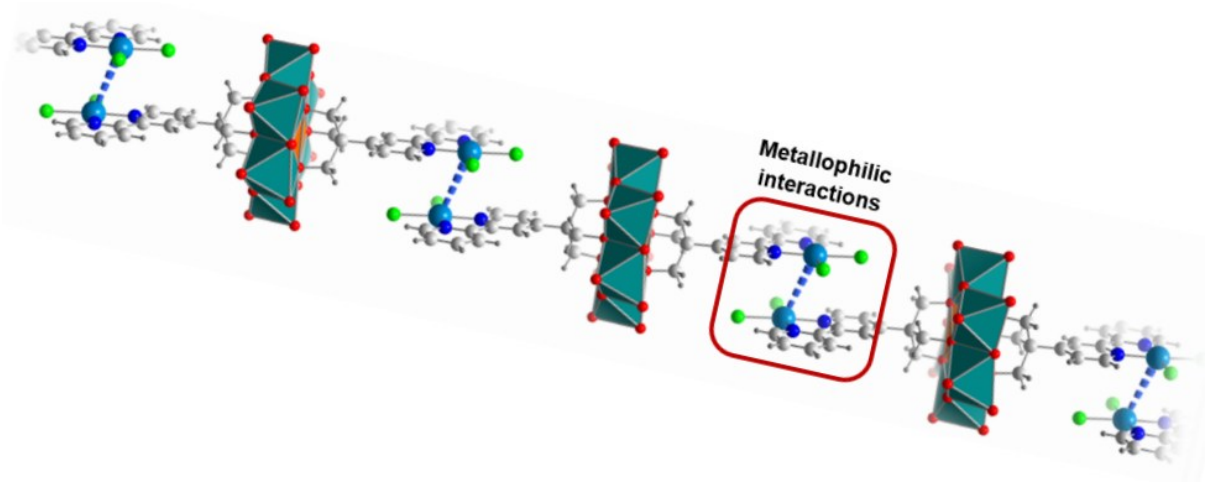

Figure 46: Excerpt from the solid-state structure of **4** showing the 1D supramolecular chains, which were formed by metallophilic Pt···Pt interactions.

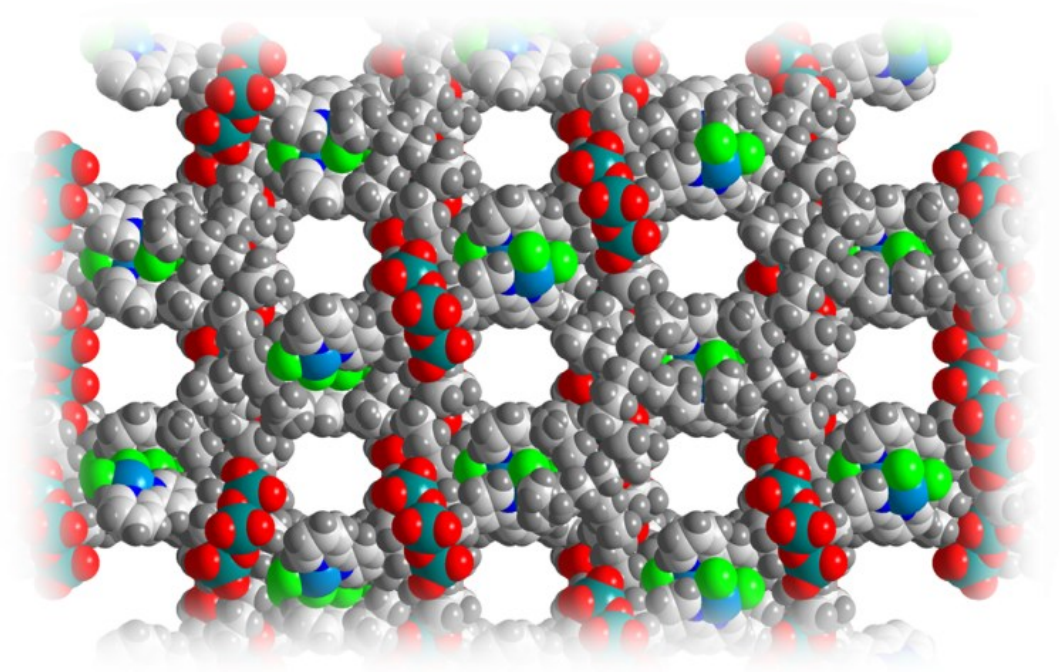

Figure 47: Excerpt from the solid-state structure of **4** showing the channels and voids, which contributed by *ca.* 40% to the overall crystal volume.

Table 6: Atomic coordinates (x,y,z $\times$ 10^4) and equivalent isotropic displacement parameters (U(eq) $\times$ 10^3 Å^2) for **4**.

	x	***y***	***z***	**U(eq)** [a]
Pt(1)	5363(1)	9400(1)	5508(1)	46(1)
Mn(1)	2500	7500	5000	35(1)
Mo(1)	2595(1)	7514(1)	6472(1)	45(1)
Mo(2)	2900(1)	5966(1)	5805(1)	46(1)
Mo(3)	2810(1)	5960(1)	4330(1)	45(1)
Cl(1)	6087(1)	9738(1)	5550(1)	64(1)
Cl(2)	5347(1)	10186(1)	6295(1)	66(1)
O(1)	2979(1)	7304(2)	5707(1)	41(1)
O(2)	2633(1)	8632(2)	5014(1)	40(1)
O(3)	2887(1)	7310(2)	4463(1)	37(1)
O(4)	3061(1)	7473(2)	6999(2)	61(1)
O(5)	2175(2)	7587(2)	6841(2)	62(1)
O(6)	2502(1)	6474(2)	6218(1)	44(1)
O(7)	3373(2)	5922(3)	6326(2)	68(1)
O(8)	2682(2)	5076(2)	5774(2)	64(1)
O(9)	3162(1)	5999(2)	5115(2)	47(1)
O(10)	2614(2)	5059(2)	4287(2)	61(1)
O(11)	2353(1)	6454(2)	3783(1)	45(1)
O(12)	3230(1)	5956(3)	3950(2)	61(1)
N(1)	4733(1)	9030(3)	5433(2)	44(1)
N(2)	5332(2)	8706(3)	4814(2)	55(1)
C(1)	3394(2)	7656(3)	5706(2)	44(1)
C(2)	3091(2)	8834(3)	5083(2)	43(1)
C(3)	3319(2)	7641(3)	4586(2)	40(1)
C(4)	3406(2)	8143(3)	5146(2)	42(1)
C(5)	4456(2)	9243(3)	5773(2)	50(1)
C(6)	4029(2)	8965(3)	5687(2)	46(1)
C(7)	3881(2)	8450(3)	5235(2)	42(1)
C(8)	4176(2)	8250(3)	4884(2)	42(1)
C(9)	4600(2)	8538(3)	4987(2)	44(1)
C(10)	4933(2)	8350(3)	4641(3)	54(1)
C(11)	4867(2)	7843(4)	4175(3)	68(2)
C(12)	5206(3)	7706(6)	3869(4)	94(3)

C(13)	5598(3)	8090(6)	4038(4)	100(3)
C(14)	5645(2)	8591(5)	4521(3)	73(2)
N(3)	1968(2)	4866(3)	7277(2)	59(1)
C(15)	2348(2)	5097(4)	7760(3)	71(2)
C(16)	2702(3)	5576(5)	7567(3)	84(1)
C(17)	3093(3)	5696(6)	8107(4)	99(1)
C(18)	3457(5)	6167(8)	7963(6)	149(3)
C(18A)	2980(40)	6390(60)	8380(50)	149(3)
C(19)	1729(2)	5557(4)	6981(2)	61(2)
C(20)	1525(3)	6085(5)	7370(3)	84(1)
C(21)	1244(3)	6687(5)	7019(4)	99(1)
C(22)	949(11)	7130(18)	7349(10)	149(3)
C(22A)	1170(20)	7350(20)	7404(15)	149(3)
C(23)	2109(2)	4421(4)	6788(3)	64(2)
C(24)	2357(3)	3695(5)	6981(3)	84(1)
C(25)	2421(3)	3266(5)	6424(4)	99(1)
C(26)	2687(4)	2540(7)	6574(5)	149(3)
C(27)	1672(2)	4393(4)	7595(3)	62(2)
C(28)	1276(3)	4031(5)	7199(3)	84(1)
C(29)	978(3)	3676(6)	7571(4)	99(1)
C(30)	594(5)	3251(9)	7208(7)	149(3)
C(30A)	592(9)	4153(17)	7668(16)	149(3)

[a] U(eq) is defined as one third of the trace of the orthogonalized U^{ij} tensor

Table 7: Complete list of bond lengths for **4**.

Atom1-Atom2	**bond length (Å)**
Pt(1)-N(2)	2.001(5)
Pt(1)-N(1)	2.027(4)
Pt(1)-Cl(2)	2.2913(17)
Pt(1)-Cl(1)	2.2948(15)
Mn(1)-O(3) [a]	1.909(3)

Mn(1)-O(3)	1.909(3)
Mn(1)-O(1) [a]	2.010(3)
Mn(1)-O(1)	2.010(3)
Mn(1)-O(2) [a]	2.035(3)
Mn(1)-O(2)	2.035(3)
Mo(1)-O(5)	1.688(4)
Mo(1)-O(4)	1.697(4)
Mo(1)-O(11) [a]	1.926(4)
Mo(1)-O(6)	1.927(3)
Mo(1)-O(1)	2.335(3)
Mo(1)-O(3) [a]	2.395(3)
Mo(2)-O(8)	1.702(4)
Mo(2)-O(7)	1.706(4)
Mo(2)-O(6)	1.916(4)
Mo(2)-O(9)	1.920(4)
Mo(2)-O(2) [a]	2.362(3)
Mo(2)-O(1)	2.384(3)
Mo(3)-O(10)	1.695(4)
Mo(3)-O(12)	1.700(4)
Mo(3)-O(11)	1.911(4)
Mo(3)-O(9)	1.925(4)
Mo(3)-O(2) [a]	2.339(3)
Mo(3)-O(3)	2.402(3)
O(1)-C(1)	1.425(6)
O(2)-C(2)	1.435(6)
O(3)-C(3)	1.432(5)
N(1)-C(5)	1.320(7)
N(1)-C(9)	1.348(6)
N(2)-C(14)	1.297(8)
N(2)-C(10)	1.371(7)
C(1)-C(4)	1.557(7)
C(1)-H(1A)	0.9900
C(1)-H(1B)	0.9900
C(2)-C(4)	1.549(8)
C(2)-H(2A)	0.9900
C(2)-H(2B)	0.9900

C(3)-C(4)	1.546(6)
C(3)-H(3A)	0.9900
C(3)-H(3B)	0.9900
C(4)-C(7)	1.539(7)
C(5)-C(6)	1.384(7)
C(5)-H(5A)	0.9500
C(6)-C(7)	1.392(7)
C(6)-H(6A)	0.9500
C(7)-C(8)	1.376(7)
C(8)-C(9)	1.379(7)
C(8)-H(8A)	0.9500
C(9)-C(10)	1.456(8)
C(10)-C(11)	1.383(8)
C(11)-C(12)	1.390(10)
C(11)-H(11A)	0.9500
C(12)-C(13)	1.375(11)
C(12)-H(12A)	0.9500
C(13)-C(14)	1.407(10)
C(13)-H(13A)	0.9500
C(14)-H(14A)	0.9500
N(3)-C(23)	1.505(8)
N(3)-C(15)	1.511(8)
N(3)-C(19)	1.516(7)
N(3)-C(27)	1.521(7)
C(15)-C(16)	1.515(10)
C(15)-H(15A)	0.9900
C(15)-H(15B)	0.9900
C(16)-C(17)	1.574(11)
C(16)-H(16A)	0.9900
C(16)-H(16B)	0.9900
C(17)-C(18)	1.484(15)
C(17)-C(18A)	1.45(11)
C(17)-H(17A)	0.9900
C(17)-H(17B)	0.9900
C(17)-H(17C)	0.9900
C(17)-H(17D)	0.9900

C(18)-H(18A)	0.9800
C(18)-H(18B)	0.9800
C(18)-H(18C)	0.9800
C(18A)-H(18D)	0.9800
C(18A)-H(18E)	0.9800
C(18A)-H(18F)	0.9800
C(19)-C(20)	1.512(10)
C(19)-H(19A)	0.9900
C(19)-H(19B)	0.9900
C(20)-C(21)	1.502(11)
C(20)-H(20A)	0.9900
C(20)-H(20B)	0.9900
C(21)-C(22)	1.511(2)
C(21)-C(22A)	1.51(3)
C(21)-H(21A)	0.9900
C(21)-H(21B)	0.9900
C(21)-H(21C)	0.9900
C(21)-H(21D)	0.9900
C(22)-H(22A)	0.9800
C(22)-H(22B)	0.9800
C(22)-H(22C)	0.9800
C(22A)-H(22D)	0.9800
C(22A)-H(22E)	0.9800
C(22A)-H(22F)	0.9800
C(23)-C(24)	1.513(10)
C(23)-H(23A)	0.9900
C(23)-H(23B)	0.9900
C(24)-C(25)	1.535(11)
C(24)-H(24A)	0.9900
C(24)-H(24B)	0.9900
C(25)-C(26)	1.525(13)
C(25)-H(25A)	0.9900
C(25)-H(25B)	0.9900
C(26)-H(26A)	0.9800
C(26)-H(26B)	0.9800
C(26)-H(26C)	0.9800

C(27)-C(28)	1.519(10)
C(27)-H(27A)	0.9900
C(27)-H(27B)	0.9900
C(28)-C(29)	1.509(11)
C(28)-H(28A)	0.9900
C(28)-H(28B)	0.9900
C(29)-C(30A)	1.510(2)
C(29)-C(30)	1.510(2)
C(29)-H(29A)	0.9900
C(29)-H(29B)	0.9900
C(29)-H(29C)	0.9900
C(29)-H(29D)	0.9900
C(30)-H(30A)	0.9800
C(30)-H(30B)	0.9800
C(30)-H(30C)	0.9800
C(30A)-H(30D)	0.9800
C(30A)-H(30E)	0.9800
C(30A)-H(30F)	0.9800

[a] Symmetry transformation used to generate equivalent atoms: -x+1/2,-y+3/2,-z+1

Table 8: Complete list of bond angles for **4**.

Atom1-Atom2-Atom3	bond angle (°)
N(2)-Pt(1)-N(1)	80.66(19)
N(2)-Pt(1)-Cl(2)	176.07(14)
N(1)-Pt(1)-Cl(2)	95.48(14)
N(2)-Pt(1)-Cl(1)	95.07(14)
N(1)-Pt(1)-Cl(1)	175.47(14)
Cl(2)-Pt(1)-Cl(1)	88.81(6)
O(3)-Mn(1)-O(3) [a]	180.0
O(3)-Mn(1)-O(1) [a]	92.42(14)
O(3)-Mn(1)-O(1) [a]	87.58(14)
O(3)-Mn(1)-O(1) [a]	87.58(14)
O(3)-Mn(1)-O(1)	92.42(14)
O(1)-Mn(1)-O(1) [a]	180.0
O(3)-Mn(1)-O(2) [a]	91.87(13)
O(3)-Mn(1)-O(2) [a]	88.13(13)

O(1)-Mn(1)-O(2) [a]	92.35(13)
O(1)-Mn(1)-O(2) [a]	87.65(13)
O(3)-Mn(1)-O(2) [a]	88.13(13)
O(3)-Mn(1)-O(2)	91.87(13)
O(1)-Mn(1)-O(2) [a]	87.65(13)
O(1)-Mn(1)-O(2)	92.35(13)
O(2)-Mn(1)-O(2) [a]	180.00(4)
O(5)-Mo(1)-O(4)	105.6(2)
O(5)-Mo(1)-O(11) [a]	101.45(19)
O(4)-Mo(1)-O(11) [a]	98.71(18)
O(5)-Mo(1)-O(6)	98.07(17)
O(4)-Mo(1)-O(6)	103.55(19)
O(11)-Mo(1)-O(6) [a]	145.06(13)
O(5)-Mo(1)-O(1)	160.61(16)
O(4)-Mo(1)-O(1)	92.99(17)
O(11)-Mo(1)-O(1) [a]	80.54(13)
O(6)-Mo(1)-O(1)	71.81(13)
O(5)-Mo(1)-O(3) [a]	92.22(16)
O(4)-Mo(1)-O(3) [a]	161.07(16)
O(11)-Mo(1)-O(3) [a]	71.07(12)
O(6)-Mo(1)-O(3) [a]	79.53(13)
O(1)-Mo(1)-O(3) [a]	69.98(11)
O(8)-Mo(2)-O(7)	105.4(2)
O(8)-Mo(2)-O(6)	99.50(18)
O(7)-Mo(2)-O(6)	102.41(19)
O(8)-Mo(2)-O(9)	102.62(18)
O(7)-Mo(2)-O(9)	98.40(19)
O(6)-Mo(2)-O(9)	144.20(15)
O(8)-Mo(2)-O(2) [a]	91.86(17)
O(7)-Mo(2)-O(2) [a]	161.39(17)
O(6)-Mo(2)-O(2) [a]	80.97(13)
O(9)-Mo(2)-O(2) [a]	70.57(13)
O(8)-Mo(2)-O(1)	162.35(18)
O(7)-Mo(2)-O(1)	91.30(18)
O(6)-Mo(2)-O(1)	70.86(13)
O(9)-Mo(2)-O(1)	79.93(14)

O(2)#1-Mo(2)-O(1)	72.34(11)
O(10)-Mo(3)-O(12)	105.4(2)
O(10)-Mo(3)-O(11)	100.22(18)
O(12)-Mo(3)-O(11)	101.57(19)
O(10)-Mo(3)-O(9)	102.66(18)
O(12)-Mo(3)-O(9)	97.84(18)
O(11)-Mo(3)-O(9)	144.71(15)
O(10)-Mo(3)-O(2) [a]	94.52(16)
O(12)-Mo(3)-O(2) [a]	159.10(16)
O(11)-Mo(3)-O(2) [a]	80.75(13)
O(9)-Mo(3)-O(2) [a]	71.03(13)
O(10)-Mo(3)-O(3)	163.65(17)
O(12)-Mo(3)-O(3)	90.20(17)
O(11)-Mo(3)-O(3)	71.13(13)
O(9)-Mo(3)-O(3)	79.68(13)
O(2)-Mo(3)-O(3) [a]	70.73(11)
C(1)-O(1)-Mn(1)	116.4(3)
C(1)-O(1)-Mo(1)	121.3(3)
Mn(1)-O(1)-Mo(1)	100.71(14)
C(1)-O(1)-Mo(2)	122.6(3)
Mn(1)-O(1)-Mo(2)	100.03(13)
Mo(1)-O(1)-Mo(2)	90.54(11)
C(2)-O(2)-Mn(1)	115.9(3)
C(2)-O(2)-Mo(3) [a]	122.4(3)
Mn(1)-O(2)-Mo(3) [a]	99.76(13)
C(2)-O(2)-Mo(2) [a]	122.3(3)
Mn(1)-O(2)-Mo(2) [a]	99.99(12)
Mo(3)#1-O(2)-Mo(2) [a]	91.24(12)
C(3)-O(3)-Mn(1)	118.3(3)
C(3)-O(3)-Mo(1)#1	121.3(3)
Mn(1)-O(3)-Mo(1)#1	101.72(14)
C(3)-O(3)-Mo(3)	119.6(3)
Mn(1)-O(3)-Mo(3)	101.38(13)
Mo(1)#1-O(3)-Mo(3)	89.09(10)
Mo(2)-O(6)-Mo(1)	121.48(17)
Mo(2)-O(9)-Mo(3)	121.84(19)

Mo(3)-O(11)-Mo(1)#1	122.55(18)
C(5)-N(1)-C(9)	120.0(4)
C(5)-N(1)-Pt(1)	125.2(4)
C(9)-N(1)-Pt(1)	114.8(4)
C(14)-N(2)-C(10)	119.5(5)
C(14)-N(2)-Pt(1)	126.0(4)
C(10)-N(2)-Pt(1)	114.5(4)
O(1)-C(1)-C(4)	114.0(4)
O(1)-C(1)-H(1A)	108.7
C(4)-C(1)-H(1A)	108.7
O(1)-C(1)-H(1B)	108.7
C(4)-C(1)-H(1B)	108.7
H(1A)-C(1)-H(1B)	107.6
O(2)-C(2)-C(4)	113.8(4)
O(2)-C(2)-H(2A)	108.8
C(4)-C(2)-H(2A)	108.8
O(2)-C(2)-H(2B)	108.8
C(4)-C(2)-H(2B)	108.8
H(2A)-C(2)-H(2B)	107.7
O(3)-C(3)-C(4)	113.9(4)
O(3)-C(3)-H(3A)	108.8
C(4)-C(3)-H(3A)	108.8
O(3)-C(3)-H(3B)	108.8
C(4)-C(3)-H(3B)	108.8
H(3A)-C(3)-H(3B)	107.7
C(7)-C(4)-C(3)	108.8(4)
C(7)-C(4)-C(2)	107.5(4)
C(3)-C(4)-C(2)	111.5(4)
C(7)-C(4)-C(1)	104.9(4)
C(3)-C(4)-C(1)	110.5(4)
C(2)-C(4)-C(1)	113.3(4)
N(1)-C(5)-C(6)	121.4(5)
N(1)-C(5)-H(5A)	119.3
C(6)-C(5)-H(5A)	119.3
C(5)-C(6)-C(7)	120.4(5)
C(5)-C(6)-H(6A)	119.8

C(7)-C(6)-H(6A)	119.8
C(8)-C(7)-C(6)	116.6(5)
C(8)-C(7)-C(4)	123.5(4)
C(6)-C(7)-C(4)	119.8(5)
C(7)-C(8)-C(9)	121.2(5)
C(7)-C(8)-H(8A)	119.4
C(9)-C(8)-H(8A)	119.4
N(1)-C(9)-C(8)	120.5(5)
N(1)-C(9)-C(10)	114.8(5)
C(8)-C(9)-C(10)	124.7(5)
N(2)-C(10)-C(11)	120.8(6)
N(2)-C(10)-C(9)	115.3(5)
C(11)-C(10)-C(9)	123.9(6)
C(10)-C(11)-C(12)	119.6(7)
C(10)-C(11)-H(11A)	120.2
C(12)-C(11)-H(11A)	120.2
C(13)-C(12)-C(11)	118.5(7)
C(13)-C(12)-H(12A)	120.7
C(11)-C(12)-H(12A)	120.7
C(12)-C(13)-C(14)	119.0(7)
C(12)-C(13)-H(13A)	120.5
C(14)-C(13)-H(13A)	120.5
N(2)-C(14)-C(13)	122.5(6)
N(2)-C(14)-H(14A)	118.7
C(13)-C(14)-H(14A)	118.7
C(23)-N(3)-C(15)	113.4(5)
C(23)-N(3)-C(19)	105.4(4)
C(15)-N(3)-C(19)	110.9(5)
C(23)-N(3)-C(27)	111.2(5)
C(15)-N(3)-C(27)	104.2(4)
C(19)-N(3)-C(27)	111.9(5)
N(3)-C(15)-C(16)	115.9(5)
N(3)-C(15)-H(15A)	108.3
C(16)-C(15)-H(15A)	108.3
N(3)-C(15)-H(15B)	108.3
C(16)-C(15)-H(15B)	108.3

H(15A)-C(15)-H(15B)	107.4
C(15)-C(16)-C(17)	109.2(6)
C(15)-C(16)-H(16A)	109.8
C(17)-C(16)-H(16A)	109.8
C(15)-C(16)-H(16B)	109.8
C(17)-C(16)-H(16B)	109.8
H(16A)-C(16)-H(16B)	108.3
C(18)-C(17)-C(16)	113.3(8)
C(18A)-C(17)-C(16)	104(4)
C(18)-C(17)-H(17A)	108.9
C(16)-C(17)-H(17A)	108.9
C(18)-C(17)-H(17B)	108.9
C(16)-C(17)-H(17B)	108.9
H(17A)-C(17)-H(17B)	107.7
C(18A)-C(17)-H(17C)	110.9
C(16)-C(17)-H(17C)	110.9
C(18A)-C(17)-H(17D)	110.9
C(16)-C(17)-H(17D)	110.9
H(17C)-C(17)-H(17D)	108.9
C(17)-C(18)-H(18A)	109.5
C(17)-C(18)-H(18B)	109.5
H(18A)-C(18)-H(18B)	109.5
C(17)-C(18)-H(18C)	109.5
H(18A)-C(18)-H(18C)	109.5
H(18B)-C(18)-H(18C)	109.5
C(17)-C(18A)-H(18D)	109.5
C(17)-C(18A)-H(18E)	109.5
H(18D)-C(18A)-H(18E)	109.5
C(17)-C(18A)-H(18F)	109.5
H(18D)-C(18A)-H(18F)	109.5
H(18E)-C(18A)-H(18F)	109.5
C(20)-C(19)-N(3)	116.7(5)
C(20)-C(19)-H(19A)	108.1
N(3)-C(19)-H(19A)	108.1
C(20)-C(19)-H(19B)	108.1
N(3)-C(19)-H(19B)	108.1

H(19A)-C(19)-H(19B)	107.3
C(21)-C(20)-C(19)	112.3(6)
C(21)-C(20)-H(20A)	109.1
C(19)-C(20)-H(20A)	109.1
C(21)-C(20)-H(20B)	109.1
C(19)-C(20)-H(20B)	109.1
H(20A)-C(20)-H(20B)	107.9
C(20)-C(21)-C(22)	115.8(11)
C(20)-C(21)-C(22A)	111.5(16)
C(20)-C(21)-H(21A)	108.3
C(22)-C(21)-H(21A)	108.3
C(20)-C(21)-H(21B)	108.3
C(22)-C(21)-H(21B)	108.3
H(21A)-C(21)-H(21B)	107.4
C(20)-C(21)-H(21C)	109.3
C(22A)-C(21)-H(21C)	109.3
C(20)-C(21)-H(21D)	109.3
C(22A)-C(21)-H(21D)	109.3
H(21C)-C(21)-H(21D)	108.0
C(21)-C(22)-H(22A)	109.5
C(21)-C(22)-H(22B)	109.5
H(22A)-C(22)-H(22B)	109.5
C(21)-C(22)-H(22C)	109.5
H(22A)-C(22)-H(22C)	109.5
H(22B)-C(22)-H(22C)	109.5
C(21)-C(22A)-H(22D)	109.5
C(21)-C(22A)-H(22E)	109.5
H(22D)-C(22A)-H(22E)	109.5
C(21)-C(22A)-H(22F)	109.5
H(22D)-C(22A)-H(22F)	109.5
H(22E)-C(22A)-H(22F)	109.5
N(3)-C(23)-C(24)	114.9(5)
N(3)-C(23)-H(23A)	108.5
C(24)-C(23)-H(23A)	108.5
N(3)-C(23)-H(23B)	108.5
C(24)-C(23)-H(23B)	108.5

H(23A)-C(23)-H(23B)	107.5
C(23)-C(24)-C(25)	107.9(6)
C(23)-C(24)-H(24A)	110.1
C(25)-C(24)-H(24A)	110.1
C(23)-C(24)-H(24B)	110.1
C(25)-C(24)-H(24B)	110.1
H(24A)-C(24)-H(24B)	108.4
C(26)-C(25)-C(24)	111.9(8)
C(26)-C(25)-H(25A)	109.2
C(24)-C(25)-H(25A)	109.2
C(26)-C(25)-H(25B)	109.2
C(24)-C(25)-H(25B)	109.2
H(25A)-C(25)-H(25B)	107.9
C(25)-C(26)-H(26A)	109.5
C(25)-C(26)-H(26B)	109.5
H(26A)-C(26)-H(26B)	109.5
C(25)-C(26)-H(26C)	109.5
H(26A)-C(26)-H(26C)	109.5
H(26B)-C(26)-H(26C)	109.5
C(28)-C(27)-N(3)	115.3(5)
C(28)-C(27)-H(27A)	108.4
N(3)-C(27)-H(27A)	108.4
C(28)-C(27)-H(27B)	108.4
N(3)-C(27)-H(27B)	108.4
H(27A)-C(27)-H(27B)	107.5
C(29)-C(28)-C(27)	109.9(6)
C(29)-C(28)-H(28A)	109.7
C(27)-C(28)-H(28A)	109.7
C(29)-C(28)-H(28B)	109.7
C(27)-C(28)-H(28B)	109.7
H(28A)-C(28)-H(28B)	108.2
C(28)-C(29)-C(30A)	116.1(15)
C(28)-C(29)-C(30)	112.9(10)
C(28)-C(29)-H(29A)	109.0
C(30)-C(29)-H(29A)	109.0
C(28)-C(29)-H(29B)	109.0

C(30)-C(29)-H(29B)	109.0
H(29A)-C(29)-H(29B)	107.8
C(28)-C(29)-H(29C)	108.3
C(30A)-C(29)-H(29C)	108.3
C(28)-C(29)-H(29D)	108.3
C(30A)-C(29)-H(29D)	108.3
H(29C)-C(29)-H(29D)	107.4
C(29)-C(30)-H(30A)	109.5
C(29)-C(30)-H(30B)	109.5
H(30A)-C(30)-H(30B)	109.5
C(29)-C(30)-H(30C)	109.5
H(30A)-C(30)-H(30C)	109.5
H(30B)-C(30)-H(30C)	109.5
C(29)-C(30A)-H(30D)	109.5
C(29)-C(30A)-H(30E)	109.5
H(30D)-C(30A)-H(30E)	109.5
C(29)-C(30A)-H(30F)	109.5
H(30D)-C(30A)-H(30F)	109.5
H(30E)-C(30A)-H(30F)	109.5

[a] Symmetry transformation used to generate equivalent atoms: -x+1/2,-y+3/2,-z+1

7 Electrochemical Analysis

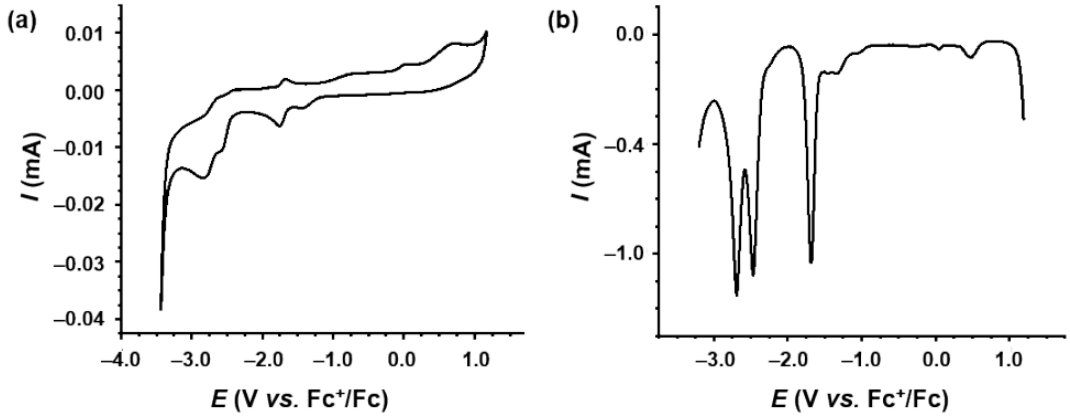

Figure 48: (a) CV and (b) SWV of **4** over the full potential range from –3.5 to +1.5 V. In all experiments, 0.1 M $TBAPF_6$ in DMF was used as the electrolyte, the scan rate was always 100 mV s^{-1}.

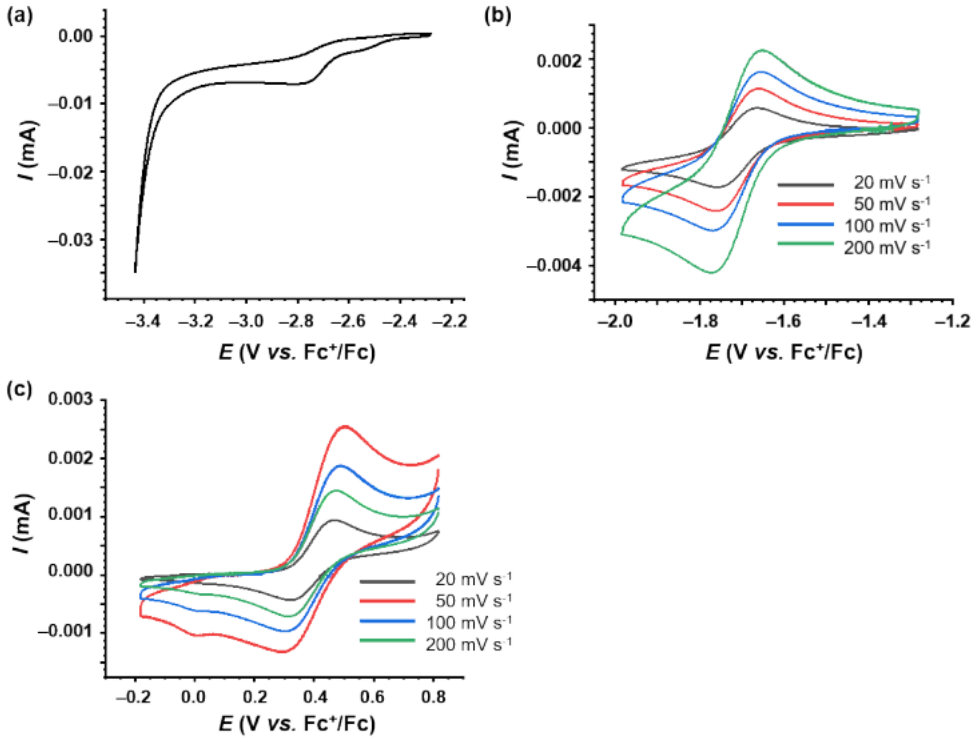

Figure 49: CV of **4** at three different potential ranges. In all experiments, 0.1 M $TBAPF_6$ in DMF was used as the electrolyte (a: scan rate of 100 mV s -1; b and c: different scan rates were applied).

Table 9: Half-wave potentials of **1**and **4**, as extracted from the CV curves.

	$E_{1/2}$ (V)	$E_{1/2}$ (V)	$E_{1/2}$ (V)
1 [a]	0.35 [b]	–1.21 [b]	n/a
4	0.40 [c]	–1.06 [b]	–1.71 [b]

[a] Data taken from Schubert *et al.*.[179] [b] Reversible redox process. [c] Irreversible redox process.

Table 10: Reduction potentials of **1** and **4**, as extracted from the SWV curves.

	E_{red} (V)	E_{red} (V)	E_{red} (V)	E_{red} (V)	E_{red} (V)	E_{red} (V)
1 [a]	n/a	0.39 [b]	–1.26 [b]	–2.71 [c]	n/a	n/a
4	0.9 [c]	0.47 [c]	–1.34 [b]	–1.68 [b]	–2.47 [c]	–2.69 [c]

[a] Data taken from Schubert *et al.*.[179] [b] Reversible redox process. [c] Irreversible redox process.

The redox potentials of **4** have been compared to those of **1**, which were already published beforehand.[179] In line with the numerous studies on hybrid POMs containing the [$MnMo_6O_{24}$] cluster, the process at *ca.* 0.4 V vs. Fc/Fc^+ has been assigned to the Mn(III)/Mn(IV) redox couple (Table 9). The shift of the redox potentials of **1** upon its complexation with $PtCl_2$ can be explained to the altered electronic structure of the [$MnMo_6O_{24}$] cluster: As one result from its complexation, the HOMO energy level is lowered, thus making the system harder to be oxidized. Secondly, the reversible process at –1.06 V vs. Fc/Fc^+ is due to the Mn(II)/Mn(III) redox couple. The last redox process, which could be analyzed by CV, is a ligand-centered reduction – in the case of the [$Pt(bpy)Cl_2$] moieties, which are present in **4**, this process occurred at *ca.* –1.7 V vs. Fc/Fc^+. For some other process, an analysis *via* CV was disabled, due to the highly irreversible nature of these processes. To counteract this, SWV measurements were also performed. Three additional redox processes could be identified – those at negative potentials have been assigned to the reduction of the Mo(VI) centers, whereas the redox process at +0.9 V is presumably due to the irreversible oxidation of the Pt(II) center to the +IV state.

8 Light-driven hydrogen evolution catalysis

General methodology for visible-light-driven catalytic experiments:

In a typical experiment, the microwave or catalytic vial (11 cm^3) equipped with a stirring bar was filled with $Ru(bpy)_3(PF_6)_2$ as a photosensitizer (125 µM), the respective catalyst (12.5 µM), sacrificial electron donor (triethylamine, 0.9 M, 500 µL), a proton source (water, 0.7 M, 50 µL) and de-aerated DMF to make the total volume of 4 mL. The catalytic vials were irradiated with LED light source (λ_{max} = 465 nm, P ~ 13 mW) for the specific interval of time (3 h, 7 h). After irradiation, head-space gas samples (100 µL) were successively taken *via* a gas-tight syringe, and analyzed by head space gas chromatography. All the experiments were repeated twice, and the reported values are averaged over the three runs. Note that the catalytic experiments were performed in the glovebox and the reactor style opted for these catalytic studies was designed by Ziegenbalg et al..[208]

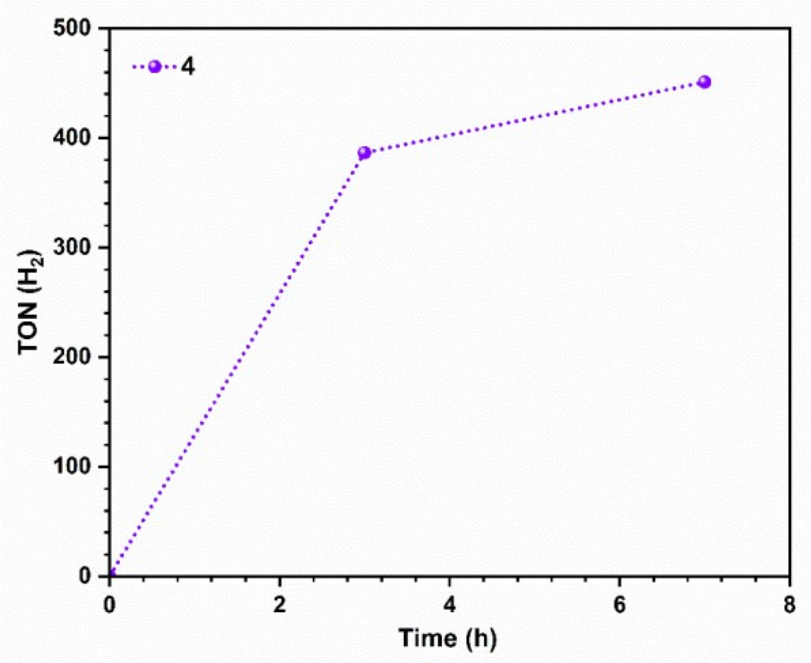

Figure 50: Light-driven HER activity of **4**. Conditions: **4** (12.5 μM), PS (125 μM), TEA (0.9 M), water (0.7 M) in dry, de-oxygenated DMF, λ_{max} = 465 nm.

Table 11: Comparison of TON with various catalysts for the light-driven HER reaction.

Entry	Catalyst/Dyads	TON/ time (h)	Reference
1.	$TBA_6[P_2W_{17}O_{61}\{O(SiC_{36}H_{23}N_3O_2Ir)_2\}]$	41/ 168	[125]
2.	$Na_{10}[Mn_4(H_2O)_2(VW_9O_{34})_2]$	33/ 5.5	[133]
3.	$Na_6K_4[Ni_4(H_2O)_2(PW_9O_{34})_2]\cdot 32\ H_2O$	290/ 2.5	[134]
4.	$TBA[MnMo_6O_{18}\{(OCH_2)_3CNCH(C_{33}H_{26}N_4Ir)\}_2]$	80/ 168	[126]
5.	**4**	451/ 7	**This work**
6.	**3**	345/ 7	**This work**

9 Post-catalytic analysis

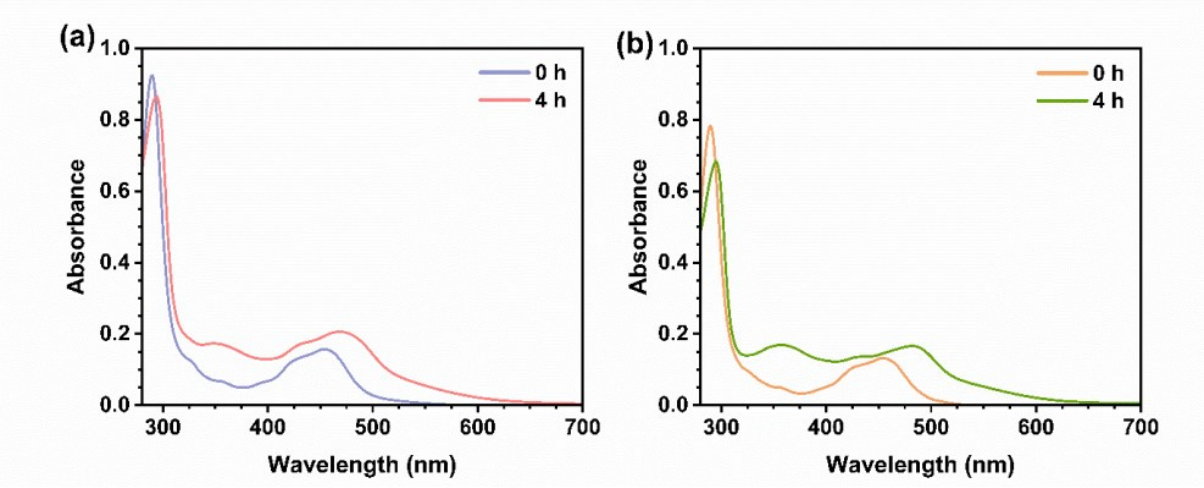

Figure 51: UV/Vis spectra of (a) Catalyst **4** and (b) Catalyst **3** before and after 4 h of irradiation. For catalytic conditions refer to the experimental section. The changes observed are associated with partial degradation of the photosensitizer as illustrated by changes of the characteristic photosensitizer MLCT transitions between 400 and 550 nm.

Acknowledgements

The authors gratefully acknowledge financial support by the Deutsche Forschungsgemeinschaft (DFG) within the Priority Program “Light-controlled reactivity of metal complexes” (SPP-2102, LCRMC, project number 493768838) and the Collaborative Research Centre TRR 234 “CataLight” (project number: 364549901; projects A4, A5, B2, B3, B7, B9 and Z2). Moreover, the Thüringer Aufbaubank (TAB) supported the acquisition of the rapifleX MALDI TOF/TOF spectrometer (grant number 2016/IZN/0009). Likewise, the authors thank the DFG for their support in acquiring the XPS and the 500 MHz NMR spectrometer (infrastructure grants INST 275/ 25 7-1 FUGG and INST 275/442-1 FUGG, respectively).

Conflict of Interest

There are no conflicts to declare.

Data availability

The experimental data supporting this article have been included as part of the supplementary information (SI). Supplementary information is available. See DOI: https://doi. org/10.1039/d5qi02141c.CCDC 2484790 (4) contains the supplementary crystallographic data for this paper.[209]

Authors Contributions

P. Endres	Investigation and visualization
G. Sachdeva	Data curation, investigation, visualization, and writing original draft
A. Winter	Conceptualization, supervision, validation, visualization, writing original draft
D. Díaz	Data curation, formal analysis, investigation, validation, visualization, writing – original draft
H. Görls	Data curation, formal analysis, investigation, validation, visualization, writing – original draft
N. Fritz	Data curation, investigation
C. Neumann	Data curation, formal analysis, investigation, validation, visualization, writing – original draft

A. Turchanin	Funding acquisition, project administration, resources, supervision, writing – review & editing
C. Streb	Conceptualization, funding acquisition, project administration, resources, supervision, visualization, writing – review & editing
U. Schubert	Funding acquisition, project administration, resources, supervision, writing – review & editing

Modifications for the Dissertation

This chapter is based on an article published under the Creative Commons Attribution 3.0 International License (CC BY 3.0). Minor modifications were made for integration into the dissertation. Specifically, the abstract was removed, and the numbering of figures, tables and references was adjusted accordingly. Additionally, Fig. was modified as Figure. No other changes were made.

3.3 Photosensitizer-polyoxometalate-catalyst triad for light-driven hydrogen evolution

Note: The following data is a part of the manuscript and will be published as: “Visible Light-Driven Hydrogen Evolution By Covalent Photosensitizer-Polyoxometalate-Catalyst Triads” by G. Sachdeva, P. Endres, A. Winter, D. Díaz, C. Titze, C. Neumann, A. Turchanin, S.S. Akbari, L. Zedler, A.K. Mengele, S. Rau, B. D. Ivanšić*, S. Kupfer*, U.S. Schubert*, C. Streb*. The copyright is currently held by the authors, **DOI:** https://doi.org/10.26434/chemrxiv-2025-3tz9z. The corresponding authors are indicated with an asterisk “*”.

3.3.1 Introduction

Solar energy offers a renewable alternative to fossil fuels, with solar hydrogen emerging as a promising approach for sustainable fuel generation and climate mitigation.[210–213] Solar hydrogen production relies on a sequence of fundamental steps: light harvesting, charge separation, charge accumulation, and catalysis.[214] Charge accumulation is particularly crucial, as fuel forming reactions are multi-electronic processes,[215,216] hence a functional molecular system should efficiently store electrons and release. One promising strategy in artificial photosynthesis is to integrate all these essential functions within a single molecular unit. Photochemical molecular dyads or triads achieve this by combining a photosensitizer, charge transfer unit, and HER catalyst in one molecular or supramolecular architecture.[16,121,217,218] Pioneering studies on photochemical dyads have demonstrated their potential for light-driven HER, where a molecular photosensitizer (e.g., Ru-complexes)[219–221] is linked to a HER-active metal catalyst (e.g., Rh, Pt, Pd, Co)[107,186,219–222] *via* ditopic bridging ligands to enable charge transfer.[223] These molecular models provide a means to investigate the correlation between light absorption, electron transfer, and HER activity using various spectroscopic techniques. Furthermore, significant attempts in component optimization through chemical modification provided insights into functional and reactivity limitations in these systems.[108,186,219]

Over the recent years, molecular metal oxides or polyoxometalates (POMs) have emerged as focal point in this field due to their exceptional redox characteristics and multi-electron storage abilities.[68,171] POMs are versatile molecules with wide structural and chemical tunability, making them ideal for photo- or electro-catalysis, energy storage and conversion.[43,114,224,225] Moreover, the possibility of covalent functionalization of POMs with organic or metal complexes has enabled significant progress in the development of inorganic-organic hybrid complexes having fascinating properties. This has led to their applications in the areas of light-driven HER,[125,226] supramolecular nanostructures,[77,227] photo-electrochemistry,[228] and energy storage.[46,229]

In particular, for solar energy conversion POMs are covalently linked to photoactive groups, as their absorption is confined to the UV region. This design provides a versatile platform to fine-tune the electronic properties of both photosensitizer and POM to improve the charge transfer and charge accumulation, thus broadening the potential applications. Inspired by these possibilities, Proust, Izzet, and co-workers have reported organo-functionalized Keggin and Dawson type polyoxotungstates covalently linked to Ru(II) and Ir(III) photosensitizers and shown their improved charge separation and electron transfer process.[124,125,230,231] In one seminal work, Izzet, Gibson, and colleagues have designed photoactive dyads based on Keggin-type POM functionalized with BODIPY (boron dipyrromethene) photosensitizer *via* silyl and stannyl linkages.[232,233] The synthesized dyads showed rapid charge transfer and a significantly long-lived charge-separated state, making them ideal for photoelectrochemical devices. The authors also explored how the solvent and counter-ion influence the photo-induced electron transfer in the Dawson-BODIPY hybrids.[176] In a related study, Hasenknopf, Ruhlmann, Lacôte, and co-workers developed co-polymeric films based on porphyrin and organo-functionalized Dawson POMs with different geometries.[234,235] The resulting films showed homogeneous charge transfer and significant photocurrent. Pioneering work on organo-functionalized Dawson polyoxotungstate linked to cyclometalated Ir(III)-complex was performed by Proust, Izzet, Artero, and colleagues, who reported the photo-induced charge accumulation on the POM and light-driven HER in presence of sacrificial electron donor and proton source.[125] Building on these studies, Streb, Rau, and co-workers have investigated the role of tuning the heteroatoms (Mn, Fe, Co) of

Anderson-molybdate POMs with an Ir-complex towards light-driven HER. Time-resolved optical spectroscopy and spectro-electrochemistry revealed electron transfer dynamics and identified limiting factors towards the hydrogen activity.[126,127,184,194]

To-date, to the best of our knowledge, previous reports have largely relied on the symmetric functionalization of Anderson polyoxometalate, highlighting the significant challenge of achieving asymmetric modification. However, very recently, some of us reported a new route which paves the way for stepwise Anderson POM functionalization with metal complexes.[236] Building on this approach, we now demonstrate how asymmetric, stepwise metal complex functionalization of 2,2'-bipyridine-functionalized Anderson anions enables the design of visible-photoactive HER triads. The mechanistic, experimental and theoretical insights support the catalytic results presented, and shed light on future challenges and opportunities in the field.

3.3.2 Results and Discussion

Catalyst Synthesis and Characterization:

Synthesis of the triad was based on a recent protocol reported by some of us.[236] Briefly, in a two-step procedure, the 2,2'-bipyridine functionalized Anderson anion, $(n\text{Bu}_4\text{N})_3[\text{MnMo}_6\text{O}_{24}\text{C}_{28}\text{H}_{26}\text{N}_4]$ (= **bpy-POM-bpy**)[179] was first equipped with the $\{\text{PtCl}_2\}$ group to yield $(n\text{Bu}_4\text{N})_3[\text{MnMo}_6\text{O}_{26}\text{C}_{28}\text{H}_{26}\text{N}_4\text{PtCl}_2]$ (= **bpy-POM-Pt**).[236] The selective single-side complexation allowed for the subsequent coordination of the $[\text{Ir(ppy)}_2]^+$ fragment to afford the triad $(n\text{Bu}_4\text{N})_2[\text{MnMo}_6\text{O}_{24}\text{C}_{50}\text{H}_{42}\text{N}_6\text{IrPtCl}_2]$ (= **Ir-POM-Pt**) (Figure 52), for synthetic and analytical details, see SI, section 3.4.2.1 and 3.4.3.

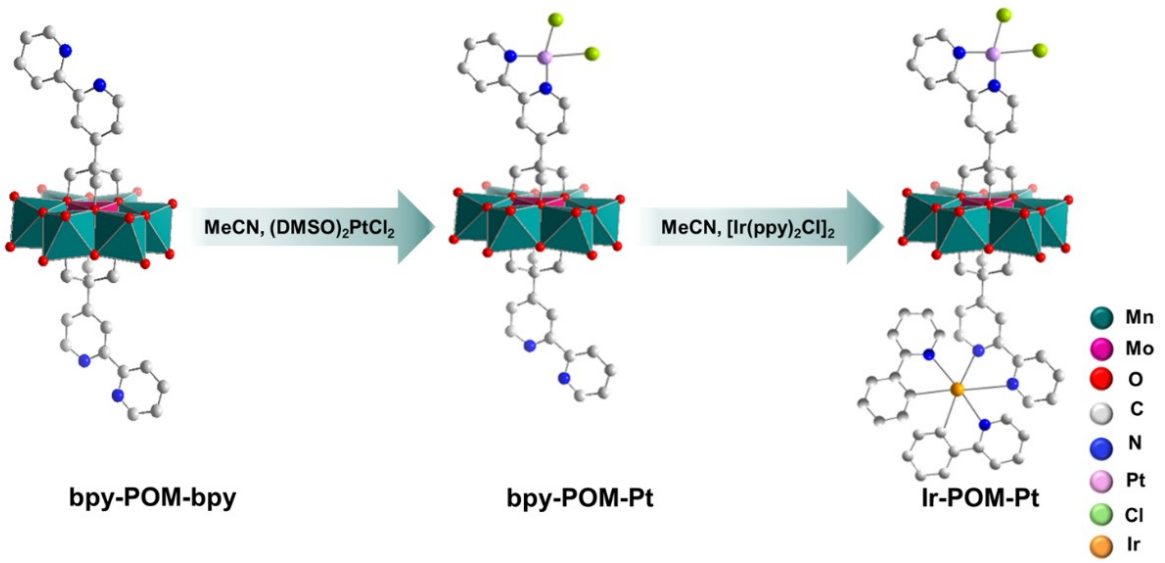

Figure 52: Schematic representation of the two-step metal-introduction to access the **Ir-POM-Pt** triad.

The triad was characterized by FT-IR spectroscopy, 1D/2D NMR spectroscopy, matrix-assisted laser desorption/ionization time-of-flight (MALDI-TOF) mass spectrometry and X-ray photoelectron spectroscopy (XPS) (Figure 57-63, Table 13 and 14, SI). However, single crystals suitable for X-ray diffraction analysis have not yet been obtained. In the ^{1}H-NMR spectra of **Ir-POM-Pt** the characteristic signals of both coordinated entities – the [$PtCl_2$(bpy)] and [$Ir(ppy)_2(bpy)]^+$ fragments were identified unambiguously. However, signal broadening and signal overlay disabled a detailed signal assignment. A comparison of the ^{1}H-NMR spectra (aromatic region) of **Ir-POM-Pt** with those of previously reported (nBu$_4$N)$_3$[$MnMo_6O_{26}C_{28}H_{26}N_4Pt_2Cl_4$] (= **Pt-POM-Pt)** and **bpy-POM-Pt** is shown in Figure 53.[236] Note, the signal in the ^{195}Pt-NMR spectrum at –2328 ppm was in the typical range for complexes of the [$PtCl_2$(bpy)] family (Figure 59, SI).[188]

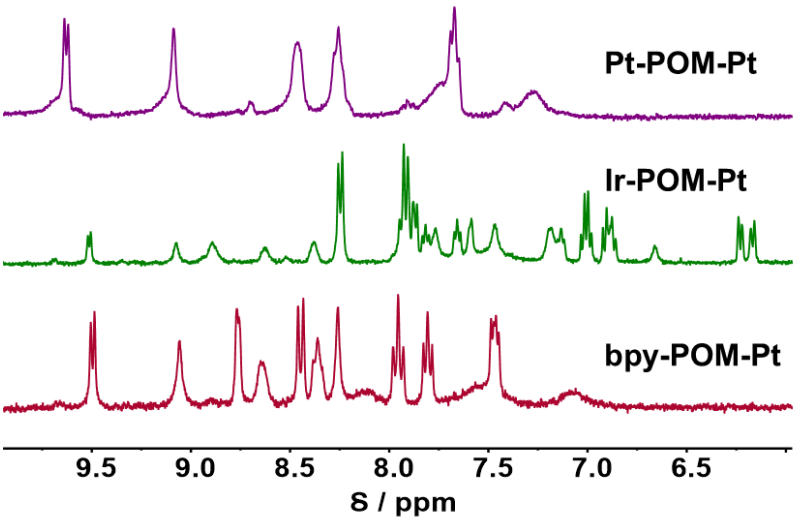

Figure 53: Comparison of the ^{1}H-NMR spectra of **Pt-POM-Pt**, **Ir-POM-Pt** and **bpy-POM-Pt** (DMSO-d_6,400 MHz, 298 K) respectively. For clarity, only the aromatic region is shown.

We previously showed that ^{1}H-DOSY NMR spectroscopy is a versatile tool to probe the structure of hybrid POMs in solution.[236] In line with these studies, the diffusion behaviour of **Ir-POM-Pt** was analysed by ^{1}H-DOSY NMR (Figure 60, SI). As one characteristic feature, the polyoxoanion diffused independent from its TBA counterions. We also used the SEGWE model,[189,190] to compare the experimental and predicted diffusion coefficients (D) of **Ir-POM-Pt** and observed excellent agreement (i.e., ΔD < 2%; Table 12).

Table 12: Results of the ^{1}H-DOSY measurements. [a]

Compound	M_w (g mol^{-1}) [c]	D (10^{-10} m^2 s^{-1}) experimental	D (10^{-10} m^2 s^{-1}) predicted [d]
bpy-POM-bpy [b]	1433.15	1.33	1.31
bpy-POM-Pt [b]	1699.14	1.27	1.25
Ir-POM-Pt	2199.74	1.15	1.13

[a] Further detail on the ^{1}H-DOSY results can be found in the SI. [b] Data taken from Schubert et al.[236] [c] Molar mass of the polyoxoanion excluding the TBA cations. [d] The D values were estimated using the SEGWE D/MW calculator.[189,190]

While both precursor compounds, **bpy-POM-bpy** and **bpy-POM-Pt**, were detected by MALDI-TOF mass spectrometry, for **Ir-POM-Pt** we observed partial fragmentation due to the loss of oxo ligands from the POM framework, as well as aggregation of the POM with the matrix compound (Figure 61, SI).

Next, we used XPS to verify the metal contents of **Ir-POM-Pt**. The XP survey spectrum demonstrates the presence of all the expected elements (Figure 62a, SI). Elemental ratios obtained from the high-resolution XP spectra were in good agreement with the calculated values, thus supporting identity and purity of **Ir-POM-Pt** (Figure 62, Table 13 and 14, SI). For instance, observed metal ratio for Pt-to-Mn-to-Ir were (1.1±0.1) : (1.1 ± 0.1) : 1.0 (calcd: 1.0 : 1.0 : 1.0). In sum, comprehensive characterization confirms the successful formation of the asymmetric POM triad **Ir-POM-Pt**.

To gain insights into the redox activity of **Ir-POM-Pt**, cyclic voltammetry (CV) was performed in anhydrous, de-aerated DMF containing 0.1 M (nBu$_4$N)PF$_6$ as a supporting electrolyte (Figure 63, SI). All potentials were referenced against the ferrocene/ferrocenium (Fc^+/Fc) redox couple. An irreversible oxidation at 0.65 V is assigned to the $Ir^{IV/III}$ couple. POM-based redox processes associated with $Mn^{III/II}$ and $Mo^{VI/V}$ were observed at 0.33 V and -1.37 V, respectively. At more negative potentials (-1.70 V and -1.92 V), redox transitions corresponding to Ir-ligands (bpy/ppy) were detected, as previously reported for related POM-based systems.[126,135]

Franck-Condon Photophysics:

In order to gain further insights into the electronic structure of the **Ir-POM-Pt** triad and the electronic transitions underlying its electronic absorption spectrum, we performed steady-state UV-Vis spectroscopy (Figure 54) and a series of quantum chemical simulations at the density and time-dependent density functional level of theory (DFT and TD-DFT; see supporting information for details).

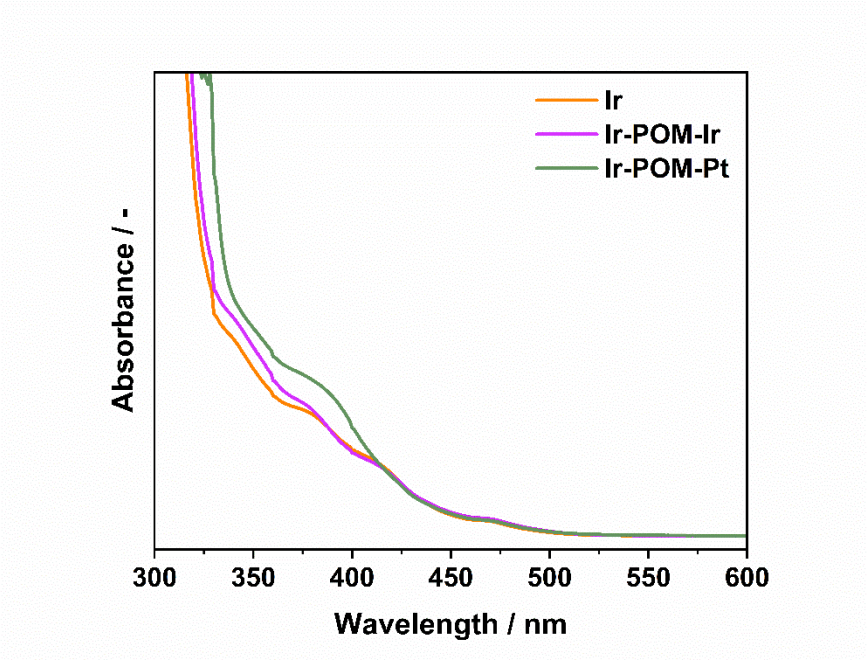

Figure 54: Steady-state UV-Vis absorption spectrum of **Ir**, **Ir-POM-Ir** and **Ir-POM-Pt** in de-aerated DMF and schematic depiction of the structure of **Ir-POM-Pt**.

UV-Vis absorption spectroscopy of the **Ir** photosensitizer (Figure 54) shows the expected characteristic absorption features assigned to metal-to-ligand charge transfer (MLCT) transitions located around 380 nm, mainly involving acceptor orbitals from the bipyridine ligand. In addition, the strong absorption features below 350 nm are assigned to π–π ligand-centred (LC) transitions within the ligands. The results from UV-Vis spectroscopy are consistent with literature reports for **Ir**. UV-Vis spectra of **Ir-POM-Pt** and the symmetric reference $(n\mathrm{Bu_4N})_3[\mathrm{MnMo_6O_{18}\{(OCH_2)_3C(C_{10}H_7N_2)Ir(C_{11}H_8N)_2\}_2}]$ (= **Ir-POM-Ir**) essentially show identical features as the POM-free **Ir** PS.

Next, electronic structure and the excited state properties of **Ir-POM-Pt** were further investigated by means of quantum chemical modelling. Notably, several scenarios regarding the spin state of the $Mn^{III}(d^4)$ center of the POM moiety are feasible within the electronic ground state, *i.e.* a (closed-shell or low-spin) singlet ground state, as well as a triplet or a quintet species with two or four unpaired electrons mainly localized at the central manganese atom. Our calculations show that the quintet species is energetically highly favourable and features four unpaired electrons at the Mn, giving the configuration $(d_{xy})^1$, $(d_{xz})^1$, $(d_{yz})^1$, $(d_{z^2})^1$, $(d_{x^2-y^2})^0$ (Figure 55a). This finding is in agreement with a recent comprehensive investigation on related Anderson-Evans-

type POMs.[185] Next, TD-DFT simulations were performed to elucidate the electronic transitions involved in the Franck-Condon photophysics of **^{5}[Ir-POM-Pt]**. These simulations assign the weak absorption feature at ~470 nm to a weakly dipole-allowed $MLCT_{Ir}$ transition into quintet state Q_5 at 454 nm (2.73 eV). Furthermore, a weakly absorbing charge-transfer transition from the POM to the lowest-lying π^*_{bpy} orbital of the platinum-based catalyst unit (Q_8, 442 nm, 2.81 eV) as well as a slightly higher lying $MLCT_{Ir}$ transition (Q_{14}, 423 nm, 2.93 eV) are predicted in the visible region. In a similar fashion MLCT transitions contribute to the band at approximately 380 nm, e.g., into the $MLCT_{Ir}$ states Q_{26} and Q_{37} at 381 and 382 nm (3.25 and 3.34 eV) as well as into Q_{35} of $MLCT_{Pt}$ character (374 nm, 3.31 eV). Notably, the computational modelling also predicts a rather low-energy metal centered state of the POM (MC_{POM}) at an energy of merely 0.96 eV, which reflects the flexible electronic structure in the vicinity of the manganese atom (Figure 55b). Further details are presented in the Tables 15 and 16, SI.

Excited State Relaxation Pathways:

The non-radiative decay pathways of **Ir–POM–Pt** were investigated by femtosecond transient absorption (fs-TA) spectroscopy and compared to the reference dyad **Ir–POM–Ir** as well as the isolated photosensitizer **Ir** (Figure 55c, d and 67, SI). Excitation of **Ir–POM–Pt** at 400 nm reveals the formation of a broad excited-state absorption (ESA) extending from 450–700 nm with a maximum at ~510 nm immediately after photoexcitation (Figure 55c). Similar transient absorption features at early delay times (i.e., 0.5 ps after photoexcitation) are observed for **Ir-POM-Ir** and **Ir,** thereby confirming the formation of the ^{3}MLCT manifold in the photosensitizer.[194,237–239] However, in contrast to **Ir**, pronounced spectral evolution occurs within 100 ps for the triad and dyad and the ESA band at 375 nm does not increase as observed for **Ir**, which is also reflected in the kinetic traces (Figure 55d, inset and 67, SI). Concomitantly an enhanced ESA signal develops in the visible region (i.e., 520-700 nm), characteristic for the one-electron reduced POM. These observations indicate that electron transfer from the photoexcited Ir to the POM occurs ultrafast and in concert with vibrational relaxation to the ^{3}MLCT state. Furthermore, for **Ir-POM-Pt** and **Ir-POM-Ir** the overall TA signal significantly decays, although not completely within the experimentally accessible delay time window of 1.85 ns (Figure 55d (inset) and 67, SI). Spectral changes associated with each kinetic process are obtained from global analysis. The

fastest component for **Ir-POM-Pt** and **Ir-POM-Ir** (DAS τ_1 = 3.8 ps) shows clear signatures of simultaneous decay of the $^3MLCT_{bpy}$ character and population of $POM^{\bullet-}$, confirming the rapid formation of the charge-separated state, i.e., $Ir^{\bullet+}$-$POM^{\bullet-}$-Pt. This is reflected by positive absorption contributions in $(DAS)\tau_1$ between 530 nm to 700 nm for the triad and dyad, which is absent in $(DAS)\tau_1$ for the isolated photosensitizer (Figure 67, SI). The prompt emergence of a charge-separated state points to effective electronic communication between the excited MLCT state of the photosensitizer and the POM. $(DAS)\tau_2$ of **Ir-POM-Pt** and **Ir-POM-Ir** differs significantly in shape from that of **Ir**. In **Ir-POM-Pt** and **Ir-POM-Ir**, this component is assigned to the decay of the charge-separated state, whose absorption characteristics were reproduced using UV-Vis spectroelectrochemical measurements (Figure 55d and 67, SI). The $(DAS)\tau_2$ for **Ir-POM-Pt** differs from that for **Ir-POM-Ir** in a way that it shows a decrease of the $POM^{\bullet-}$ signature accompanied by the emergence of a broad low intensity absorption in $(DAS)\tau_3$ spanning from 450 to 700 nm. This observation may suggest that charge-separation is not only established but also directed towards the catalytic Pt unit. The resulting $Ir^{\bullet+}$-POM-$Pt^{\bullet-}$ state could decrease the probability of rapid charge recombination and thereby offer a plausible mechanistic basis for light-driven catalytic turnover.

In synergy with time-resolved spectroscopy and spectroelectrochemical measurements, TD-DFT simulations were carried out to elucidate the spectral (differential) signatures of key excited state intermediates, which are associated with excited state relaxation processes upon initial excitation within the visible region. As photoexcitation in the visible region is mainly associated with $MLCT_{Ir}$ transitions, relativistic effects introduced by the Ir heavy atom led to an efficient and ultrafast intersystem (ISC) crossing as typically observed for such Ir(III) photosensitizers.[240–243] As the ground state of ^{5}**[Ir-POM-Pt]** is a quintet, spin state switching allows population transfer to the energetically adjacent triplet or septet states (^{3}**[Ir-POM-Pt]** and ^{7}**[Ir-POM-Pt]**). Both, the triplet as well as the quintet species were fully optimized at the unrestricted DFT level of theory and surprisingly, both excited state intermediates relax to analogous charge-transfer state, i.e., $CT_{Ir\text{-}Pt}$, where electron density is shifted from the Ir-based PS to the Pt-based CAT while the POM still features four unpaired electrons. The electronic configuration of the of spin states (triplet and septet) are visualized in Figure 55e and 69d, SI. Therefore, such charge-separated

intermediates translate to (photo-redox) intermediates with an oxidized PS and a reduced catalyst. Energetically, the triplet and septet species are degenerate – with an energy of 2.56 eV relative to the relaxed quintet species. This degeneracy is a consequence of the rather large distance between the unpaired electrons at the Ir, POM and Pt units, thus a neglectable impact of the exchange integral follows. TA spectra were simulated as difference spectra based on the excited-state absorption (ESA) stemming from triplet-triplet transitions and the quintet-quintet transitions within the Franck-Condon point (i.e., quintet ground state bleach, GSB).[135,244–246] Again, both **^{3}[Ir-POM-Pt]** and **^{7}[Ir-POM-Pt]** feature nearly identical spectral signatures, while the broad ESA band between 800 and 600 nm is assigned to one IL_{Pt} transition ($\pi^*_{bpy} \rightarrow \pi^*_{bpy}$; T_{30} at 781 nm / 7_{27} at 787 nm) of the photoreduced catalyst as well as to $LMCT_{Ir}$ states ($\pi_{bpy/ppy} \rightarrow d_{Ir}$; $T_{36,43,45}$ between 704 and 611 nm / $7_{33,38,41}$ between 703 and 611 nm) of the photooxidized PS (Figure 55f and 69e, SI). Finally, the sharp ESA feature at ~500 nm can be associated with a II_{Pt} transition 442 nm (T_{87} / 7_{83}). Thus, the simulated and experimental signatures are in excellent agreement, which further supports the population of the $CT_{Ir\text{-}Pt}$ species at longer delay times (e.g., at 100 ps). However, as the spectral signatures of the isoenergetic triplet and septet species are quasi-identical, we cannot provide a further assignment of the spin state of the charge-separated species. Further information with respect to the electron transition involved in the ESA are collected in Tables 17-20, SI.

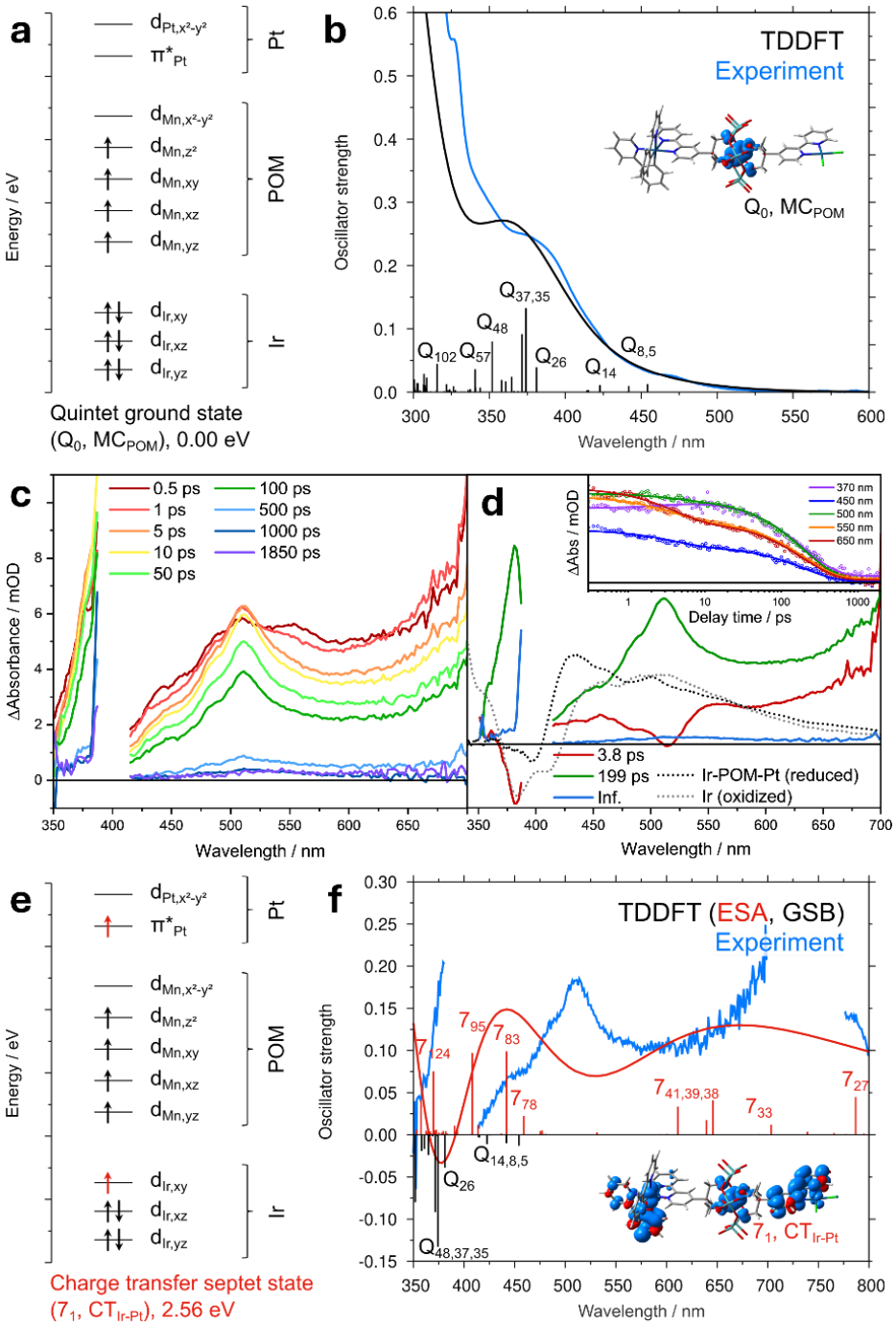

Figure 55: a) Electronic structure of the quintet ground state (Q_0). b) Associated electronic absorption spectrum of **Ir-POM-Pt**. Key electronic transitions are highlighted; the nature of the quintet ground state (with four unpaired electrons at the Mn) is illustrated by the spin density. c) Absorption difference spectra measured at the indicated delay times after pulsed 400 nm light excitation of **Ir-POM-Pt** in de-aerated DMF. d) Spectral changes associated with each kinetic process obtained from global analysis (decay associated spectra, DAS) for **Ir-POM-Pt**. Inset: selected transient kinetic traces with corresponding fit, respectively. The grey dotted lines in d) show the differential absorption spectra of single oxidized **Ir** and single reduced **Ir-POM-Pt** according to spectroelectrochemical results. e) Electronic structure of the fully related septet charge-separated species (7_1). f) Associated transient absorption spectrum of the triad. Key electronic transitions contributing to the excited state absorption (ESA, septet-septet excitations in red) and ground state bleach (GSB, quintet-quintet excitations in black) are labelled; the nature of 7_1 is illustrated by the spin density.

Light-driven hydrogen evolution:

The visible-light-driven hydrogen evolution activity of **Ir-POM-Pt** was investigated in the view of the reported ability of Ir-based photosensitizers to transfer photoexcited electrons to POMs.[125,135,184] The standard catalytic experiments involved water-free, de-aerated DMF solutions containing **Ir-POM-Pt** (0.1 mM), sacrificial electron donor (triethylamine, 0.9 M, 500 µL), a proton source (water, 0.7 M, 50 µL) in a microwave vial. The reaction solution was irradiated with a monochromatic LED source (λ_{max} = 465 nm, P ~ 13 mW) at room temperature for a specific duration (for experimental details, see SI, section 3.4.2.2). The sustained hydrogen evolution was quantified by head-space gas chromatography. The experiments were conducted in duplicate and reported turnover numbers (TONs) are averaged values. A non-covalent reference system comprising of structurally analogous Ir-photosensitizer ([$Ir(ppy)_2(bpy)$](PF_6)) (0.2 mM) and **bpy-POM-bpy** (0.1 mM) as catalyst were employed under identical experimental conditions.

As shown in Figure 56, hydrogen production increased linearly with irradiation time, reaching a TONs of *ca.* 189 after 24 h of continuous irradiation, while irradiation for another 24 h did not significantly increase the TONs (203), indicating loss of catalytic function. In contrast, after 24 h irradiation, the non-covalent reference showed notably lower TONs of *ca.* 6 (-97%), illustrating the advantage of covalent linkage in **Ir-POM-Pt** under the given reaction conditions. Furthermore, controlled experiments in the absence of **Ir-POM-Pt**, TEA or without irradiation showed no H_2 evolution.

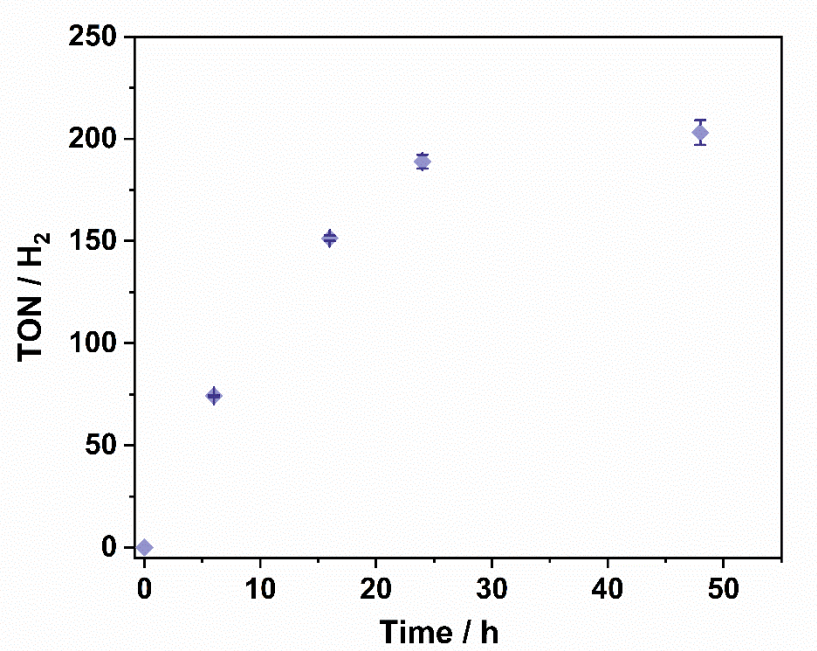

Figure 56: Light-driven HER activity of **Ir-POM-Pt**, representing the HER TONs over time. Conditions: **Ir-POM-Pt** (0.1 mM), TEA (0.9 M), H_2O (0.7 M), in water-free, de-oxygenated DMF, λ_{max} = 465 nm.

Previous studies on photocatalysis revealed that the catalytic metal center undergoes decomposition through formation of colloidal metal particles, that may contribute to catalytic hydrogen evolution.[108] In order to assess the formation of Pt-colloids, a classical mercury amalgam test was employed.[247,248] To this end, **Ir-POM-Pt** was dissolved in DMF or DMSO-d_6 for UV-Vis and ^{1}H-NMR spectroscopy, respectively. The solutions were stirred overnight in presence of elemental mercury in the dark. Comparison of the UV-Vis and ^{1}H-NMR spectra of **Ir-POM-Pt** with and without mercury treatment confirmed no redox reaction occurred (Figure 64 and 65, SI). Based on these findings, we examined the activity of **Ir-POM-Pt** towards light-driven hydrogen evolution upon addition of elemental mercury (2-3 drops). Following the addition of mercury, the catalytic solution was irradiated overnight (for experimental details, refer SI, section 3.4.2.3 and 3.4.2.4). Note that the irradiation was performed from the side to prevent photon reflection by the mercury drop at the bottom of the vial. **Ir-POM-Pt** exhibited TONs of *ca.*176 in the absence of mercury, while in the presence of elemental mercury, **Ir-POM-Pt** showed TONs of *ca.* 114, indicating that hydrogen evolution activity of **Ir-POM-Pt** was qualitatively retained in the presence of mercury. Therefore, the decomposition of **Ir-POM-Pt** and formation of Pt-colloids within the catalytic system is unlikely. This was further supported by scanning electron

microscopy together with energy dispersive X-ray spectroscopy (SEM-EDX) analysis, which shows uniform distribution of C, N, O, Mo, Mn, Cl, Ir and Pt throughout **Ir-POM-Pt** (Figure S66, SI), while no metallic Pt aggregates were observed.

Post-Catalytic Analysis:

Stability is a critical parameter in the evaluation of catalyst performance. To gain insights into the intrinsic stability of **Ir-POM-Pt** under photocatalytic conditions optical changes were monitored by UV-Vis absorption and emission spectroscopy. UV-Vis spectroscopic analysis of the catalytic solution revealed the partial degradation of the Ir-photosensitizer over time, as evidenced by the spectral changes between 325 nm to 400 nm (Figure 70a, SI). Similar observation has been reported previously, where the Ir-photosensitizer was electrostatically coupled to Anderson POMs covalently functionalized with Pt(II)-complex.[135] To further assess the stability of **Ir-POM-Pt**, time-dependent emission spectroscopy was employed. Significant spectral changes were observed between 500 nm – 550 nm, corresponding to the formation of reduced species under photocatalytic conditions (Figure S70b, SI). The obtained results are in line with the earlier studies which report the formation of reduced dyad upon catalysis, indicative of the formation of Ir-ligand radicals as described by spectro-electrochemistry.[126]

3.3.3 Conclusion

In sum, we report the first example of a covalent photosensitizer-polyoxometalate-catalyst triad for visible-light-driven hydrogen evolution. Based on an asymmetric two-step synthetic approach, we obtain the Ir-PS-Anderson-POM-$PtCl_2$ HER triad and report its light-driven catalytic performance together with principal mechanistic, photophysical and theoretical studies. In future, this design concept can be expanded with the aim to replacing the noble metals with earth-abundant alternatives.

3.4 Supplementary Information

3.4.1 Instrumentation

Attenuated total reflectance-Fourier transform infrared spectroscopy (ATR-FT-IR) was carried out on a Bruker Alpha II FT-IR spectrophotometer containing a Diamond crystal ATR unit. Signals are presented as wave numbers in cm^{-1} using the following abbreviations: vs = very strong, s = strong, m = medium, w = weak and b = broad.

NMR spectroscopy the 1D ^{1}H- and ^{195}Pt-NMR spectra were recorded at 298 K on Bruker 400 MHz spectrometers – Avance III (equipped with a BBF broadband probe head) or AVANCE NEO (equipped with a 5 mm inverse probe head). The spectra were acquired in DMSO-d_6, which was purchased from Euristop. The ^{1}H-NMR resonances were referenced to the residual solvent signal at 2.50 ppm. The ^{195}Pt resonances were referenced to the unified Ξ scale (K_2PtCl_4 was used as the external reference).[197] For these measurements, a spectral width of 200 ppm was used, the data size was 16k and 200,000 scans were collected. The NMR spectra were processed and analysed using the NMRium software, which is available online free-of-charge.[249]

The 2D ^{1}H-DOSY spectra were recorded on a Bruker Avance NEO spectrometer (500 MHz) equipped with a Prodigy broadband probe head. For this purpose, the double-stimulated echo (DSTE) sequence with bipolar gradient pulses and three spoil gradients with convection compensation was used (corresponding to Bruker's pulse program dstebpgp3s). The diffusion time and the duration of the magnetic field pulse gradients were 50 ms and 2 ms, respectively. The delay for gradient recovery and the eddy current delay were 0.2 ms and 5 ms, respectively. For each experiment, a series of 32 spectra on 32k data points was collected. After Fourier transformation and baseline correction, the diffusion dimension was processed with Bruker's Topspin software (vs. 4.4) and the diffusion coefficients were calculated by Gaussian fits with the relaxation *T*1/*T*2 tool, which is implemented in Topspin. The theoretical diffusion coefficients were calculated from the compounds molar masses using the modified Stokes-Einstein Gierer-Wirtz Estimation (SEGWE) model; likewise, the apparent molar masses were calculated from the experimental diffusion coefficients. These calculations were performed using the SEGWE D/W calculator, which is available online free-of-charge.[189,190]

Matrix-assisted laser desorption/ionization time-of-flight (MALDI-TOF) mass spectra were acquired with a rapifleX™ MALDI TOF/TOF from Bruker Daltonics. The instrument is equipped with a smartbeam™ 3D laser (355 nm wavelength). The spectra were measured in the positive and negative reflector mode. The instrument was calibrated with fleXstandard Polymers from Bruker Daltonics in the positive ionization mode; whereas, Merck's CsI3 was used as the standard for the negative ionization mode. Samples were spotted using the dried droplet technique applying DCTB (trans-2-[3-(4-tert-butylphenyl)-2-methyl-2-propenyliden]-malononitrile) as the matrix. In the positive ionization mode, KCl was used to support the ionization.

X-ray photoelectron spectroscopy (XPS) was performed in a UHV Multiprobe system equipped with a monochromatic X-ray source (Al-K_α) and an electron analyser (Argus CU) with an energy resolution of 0.6 eV (Scienta Omicron). The samples were prepared by drop-casting a CH_3CN solution of the material (2 µL) onto Au substrates, which were pre-cleaned by oxygen-plasma treatment. Subsequently, the samples were dried under ambient conditions and introduced into the UHV system for measurements. For quantitative analysis, the secondary electron background was subtracted using linear (Cl 2p) or shirley background (Pt 4f, Ir 4f, Mo 3d and Mn 2p) from the high-resolution spectra, and the peaks were fitted using Voigt functions.

Steady-state UV-Vis Spectroscopy was performed on a Cary 3500 UV-Vis Spectrophotometer equipped with a Xenon flash lamp (250 Hz). Measurements were performed in a glass quartz cuvette (d = 10 mm).

Steady-state Emission spectroscopy was performed on an Edinburgh Instrument FS5 Spectrofluorometer at room temperature, with a xenon lamp as an excitation source.

Scanning electron microscopy (SEM) and **Energy dispersive X-ray (EDX)** images were collected using FEI-Nova NanoSEM 650 at an accelerating voltage of 20 kV, equipped with an EDX detector.

Electrochemical analyses Cyclic voltammetry (CV) experiment was performed using a CH instrument, CHI 760E electrochemical workstation equipped with a standard three electrode configuration: a glassy carbon (d = 3 mm) was used as a working electrode, Ag wire (in a glass frit containing electrolyte solution) as a reference electrode and Pt wire was used as a counter electrode. The experiment was performed

in an argon-filled glovebox (MBraun LABmaster130/M200B eco) in a water-free, degassed DMF at room temperature, using 0.1 M (nBu$_4$N)PF$_6$ as a supporting electrolyte. The recorded potentials were referenced against the internal standard ferrocenium/ferrocene (Fc^+/Fc), unless stated otherwise.

Spectro-electrochemistry UV-Vis-spectro-electrochemistry and electrochemical measurements were performed using a three-electrode thin-layer spectro-electrochemical cell with a path length of 1 mm (Hellma, Bioanalytical Systems, USA). A three-electrode arrangement using a Pt counter electrode, an Ag/AgCl pseudo-reference electrode and a glassy carbon working electrode was utilized. CV and potential controlled monitoring were performed using a VersaSTAT 3 (Princeton Applied Research) potentiostat. UV-Vis spectra were recorded immediately after applying the reduction potential to track the changes that occur during this process. UV-Vis spectra were collected in transmission mode by using a coupled UV-Vis absorption spectrometer (Avantes, AvaSpec-ULS2048XL), equipped with a deuterium-halogen light source (AvaLight DH-S-BAL). For preparing the analyte solutions, first a 0.1 M electrolyte solution of tetra-n-butylammonium hexafluorophosphate (nBu$_4$NPF$_6$), Sigma-Aldrich, ≥ 99.0%) in anhydrous DMF (Sigma-Aldrich) was prepared. Then the **Ir-POM-Pt** triad and **Ir** was dissolved in this solution. The solutions were degassed with nitrogen before each measurement.

Transient absorption spectroscopy Femtosecond transient absorption (fs-TA) experiments on **Ir-POM-Pt**, **Ir-POM-Ir** and **Ir** were performed using a custom-built setup described previously.[250,251] Pulses from a Ti:sapphire regenerative amplifier (Astrella, Coherent, USA; 800 nm, 1 kHz) were split, with one portion producing a broadband white-light probe *via* a rotating CaF_2 crystal (300–700 nm), which was subsequently divided into reference and probe paths. The remaining portion was used to generate pump pulses through an optical parametric amplifier (TOPAS Prime, Light Conversion, Lithuania). Pump and probe beams were spatially and temporally overlapped at the sample, with the relative polarization set to the magic angle (54.7°), and excitation was performed at 400 nm.

Samples were contained in 1 mm inert quartz cuvettes with optical densities of 0.3 at the excitation wavelength, and the pump energy was maintained at 0.45 µJ per pulse. UV-Vis spectra were recorded before and after each experiment to verify sample

stability. Data processing was carried out using KiMoPack, applying chirp correction to account for wavelength-dependent dispersion and global analysis based on a sequential kinetic model with 95% confidence.[252] The first 400 fs around time zero were excluded to avoid coherent artifacts.[253]

Gas Chromatography (GC) Hydrogen evolution was measured by headspace GC on a Shimadzu Nexis GC-2030 equipped with a barrier ionization discharge (BID) detector. Helium gas with a purity of 99.9999% was used as the carrier gas. The column was heated to a constant temperature of 80˚C.

Computational details

All quantum chemical calculations were performed using the Gaussian 16(C.02)[254] software package to investigate structural and electronic properties of the present **Ir-POM-Pt** triad. Four electronic scenarios were considered, namely the (closed-shell or low-spin) singlet ground state, **^{1}[Ir-POM-Pt]**, as well as two (opened-shell) high-spin species – the triplet, quintet and septet ground states (i.e., **^{3}[Ir-POM-Pt]**, **^{5}[Ir-POM-Pt]** and **^{5}[Ir-POM-Pt]**, respectively). These scenarios account for the complex electronic structure of the central Mn(III) ion. The initial structural properties of all four species (singlet, triplet quintet and septet) were extracted from our recent joint synthetic-spectroscopic-theoretical investigations on the Anderson-Evans-type POM[185] as well on a related BODIPY-decorated POM dyad.[177] The B3LYP exchange-correlation functional[255,256] was applied in combination with the all-electron def2-SVP[257] basis set. In addition, a modified version of B3LYP which features 35% of exact exchange, which is typically beneficial to describe the electronic structure of 5d transition metal complexes with comparably sizeable ligand-field splitting.[244,258–260] All structures were fully optimized while considering implicit solvent effects (DMF: ε = 37.219) using the solute electron density (SMD) variant of the integral equation formalism of the polarizable continuum model (equilibrium procedure).[261,262] All calculations were performed including D3 dispersion correction with Becke-Johnson damping.[263] Subsequently, a vibrational analysis was carried out for each optimized ground state structure to verify that a (local) minimum on the 3*N*-6-dimensional potential energy (hyper-)surface (PES) was obtained.

Consistent with our recent studies on the trimethylolmethane-capped Anderson-Evans-type POM, both hybrid functionals (B3LYP and B3LYP35) suggest that the

quintet species in the present **Ir-POM-Pt** triad is thermodynamically favoured. This spin state feature four unpaired electrons at the Mn, i.e., $(d_{xy})^1$, $(d_{xz})^1$, $(d_{yz})^1$, $(d_{z^2})^1$, $(d_{x^2-y^2})^0$. Subsequently, TD-DFT simulations were performed to elucidate the electronic transitions involved in the Franck-Condon photophysics of **^{5}[Ir-POM-Pt]** based on the lowest 300 excited states. To this aim the same computational setup was applied as in the previous ground state calculations (using B3LYP and B3LYP35), while the non-equilibrium model was utilized to account for implicit solvent effects.

Furthermore, the transient absorption (TA) signals were modelled based on the optimized **^{3}[Ir-POM-Pt]** and **^{7}[Ir-POM-Pt]** species. Surprisingly, the triplet species also features four unpaired (α-)electrons at manganese, while two unpaired (β-)electrons are observed at the Ir-based PS and at the Pt-based catalyst, respectively. Therefore, such charge-separated intermediate translates to a (photo-redox) intermediate with an oxidized PS and a reduced catalyst. Notably, the respective septet species features the analogous configuration, while all six unpaired electrons are of α-spin. Energetically, these triplet and septet species are degenerate due to the rather large distance between the unpaired electrons at the Ir, POM and Pt units, which leads to a neglectable further stabilization based on the exchange integral. TA spectra were simulated as difference spectra based on the excited state absorption (ESA) stemming from triplet-triplet transitions (within T_1 equilibrium; 300 triplet-triplet transitions as well as within 7_1 equilibrium; 300 septet-septet transitions, only B3LYP functional) and the quintet-quintet transitions within the Franck-Condon point (i.e., quintet ground state bleach, GSB). Thereby, a relative population of 1:1 was assumed for the excited state vs. the ground state species.[245,246,258,264]

All calculated equilibrium structures as well as high resolution images (charge density differences and spin densities) are available from the free online repository Zenodo.

3.4.2 Experimental Data

Commercially available reagents were purchased from Sigma Aldrich, TCI chemicals and Fischer Scientific. The materials were used as received without further purification unless stated otherwise. The hybrid POMs **bpy-POM-bpy**[179], **bpy-POM-Pt**[236], **Ir-POM-Ir**[179] as well as the dimeric precursor $[Ir(ppy)_2Cl]_2$[196] were synthesized according to literature procedures.

3.4.2.1 Synthesis of (nBu$_4$N)$_2$[MnMo$_6$O$_{24}$C$_{50}$H$_{42}$N$_6$IrPtCl$_2$] (Ir-POM-Pt)

A microwave vial (20 mL) was equipped with **bpy-POM-Pt** (200 mg, 82.4 µmol), [Ir(ppy)$_2$Cl]$_2$ (44.18 mg, 41.2 µmol) and CH_3CN (8.5 mL) as a solvent. After purging the suspension for 5 min with N_2, the vial was capped. The reaction mixture was stirred for 3 h at 80°C. A fine precipitate was removed by filtration. The product was isolated by dropping the reaction mixture into diethyl ether (20 mL). **Ir-POM-Pt** was obtained as an orange powder (175 mg, 79% yield).

FT-IR (in cm^{-1}): 3457 (b)**,** 2960 (v CH,s), 2932 (v CH, s), 2871 (v CH, s), 1419 (m), 1234 (w), 1161 (w), 1073 (s), 1034 (v CO, s), 942 (v Mo=O, s), 921 (v Mo=O, s), 901 (v Mo=O, s), 655 (v Mo-O-Mo, vs) , 563 (m), 454 (m), 409 (m).

^{1}H-NMR (400 MHz, DMSO-d$_6$, 298 K): δ = 9.64 (d, ^3J = 5.7 Hz, 1H), 9.09 (s, 1H), 8.80–8.64 (m, 1H), 8.52–8.41 (m, 1H), 8.31–8.22 (m, 1H), 8.16–8.02 (m, 4H), 7.96 (m 1H), 7.91–7.78 (m, 5H), 7.75 (m, 1H), 7.68 (m, 1H), 7.53 (m, 2H), 7.47 (m, 1H), 7.32 – 7.21 (brs, 1H), 7.11–7.01 (m, 5H), 6.92 (m, 2H), 6.32 (m, 1H), 6.27 (m, 1H), 3.16 (m, 16H), 1.56 (m, 16H), 1.30 (m, 16H), 0.93 (t, ^3J = 7.1 Hz, 24H) ppm.

^{195}Pt-NMR (400 MHz, DMSO-d$_6$, 298 K): δ = –2328.16 ppm.

MALDI-TOF MS (DCTB + KCl, positive mode): *m/z* calcd. for [4 – O – H + DCTB]$^+$ corresponding to [C$_{99}$H$_{33}$Cl$_2$IrMnMo$_6$N$_{10}$O$_{23}$Pt]$^+$ = 2920.044; found = 2920.058.

3.4.2.2 Visible-light-driven hydrogen evolution catalysis

In a typical experiment, the microwave vial (11 mL) equipped with a stirring bar was filled with the **Ir-POM-Pt** triad (0.1 mM), sacrificial electron donor (triethylamine, 0.9 M, 500 µL), a proton source (water, 0.7 M, 50 µL) and water-free, de-aerated DMF to make the total volume of 4 mL. Note that as a non-covalent reference system, structurally similar Ir-photosensitizer ([Ir(ppy)$_2$(bpy)](PF$_6$)) (0.2 mM) and **bpy-POM-bpy** (0.1 mM) as catalyst were investigated under identical conditions. The vials were irradiated with a LED light source (λ_{max} = 465 nm, P ~ 13 mW) at 25˚C. After irradiation, head-space gas samples (50 µL) were successively taken *via* a gas-tight syringe and analysed by head space GC. All the experiments were performed twice, and reported values are averaged over the two runs. The sample preparation for catalytic experiments was carried out inside an argon-filled glovebox (MBraun

LABmaster130/M200B eco). Note that the opted reactor for the catalytic studies was designed by Ziegenbalg *et al.*[208]

3.4.2.3 Mercury poisoning test

Catalyst poisoning experiments with elemental mercury were conducted under identical conditions to the light-driven hydrogen evolution catalysis. Before sealing the vials, 2-3 drops of elemental mercury were added into the catalytic solution. To exclude any potential artefacts due to sidewise illumination, the catalytic mixture without Hg was also stirred. Both the catalytic vials were irradiated overnight, and the amount of hydrogen evolution was quantified by head space GC.

3.4.2.4 Control experiments on the mercury test

The stability of **Ir-POM-Pt** towards elemental mercury was examined using UV-Vis and ^{1}H-NMR spectroscopy. For UV-Vis measurements, the stock solution of **Ir-POM-Pt** (1.8 mg, 0.67 µmol) was prepared in DMF (6 mL). 3 mL of this mixture was divided into two vials: one with elemental mercury (2-3 drops), and the other without mercury as a control. The samples were stirred overnight at room temperature under exclusion of light. After stirring, the solutions were filtered using 0.2 µm syringe filter to remove any solid particles. The yellow-coloured solutions were diluted to 5 µM for UV-Vis analysis. Similarly, for ^{1}H-NMR analysis **Ir-POM-Pt** (0.75 mM) was prepared in DMSO-d_6 (2 mL) in two vials: one with elemental mercury (2-3 drops) and other without. The solutions were stirred overnight in dark at ambient temperature conditions. Afterwards, solutions were filtered with syringe filter (0.2 µm) and were analysed *via* ^{1}H-NMR spectroscopy.

3.4.3 Characterization

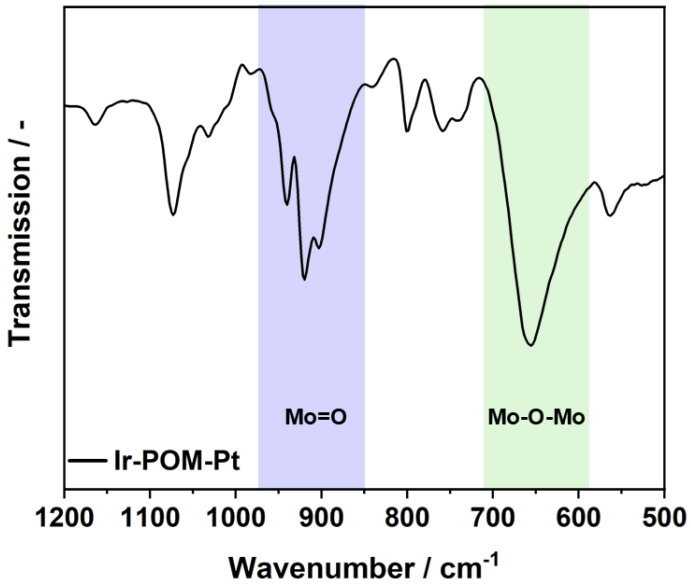

Figure 57: FT-IR spectrum of **Ir-POM-Pt**, exhibiting the characteristic metal oxo vibrational bands expected for Anderson anions.

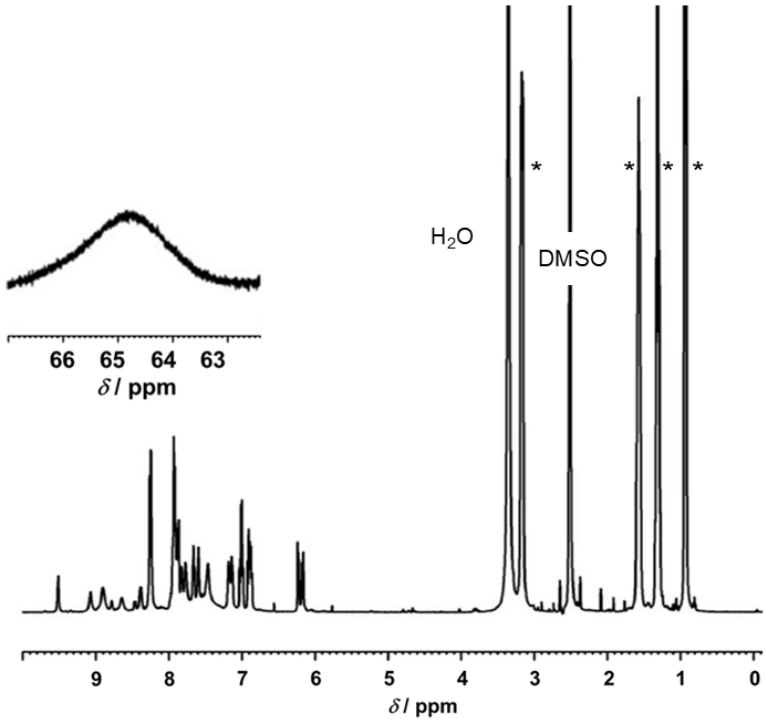

Figure 58: ^{1}H-NMR spectrum of **Ir-POM-Pt** (DMSO-d_6, 400 MHz, 298 K). The signals assigned to the protons of the TBA cations are marked with an asterisk.

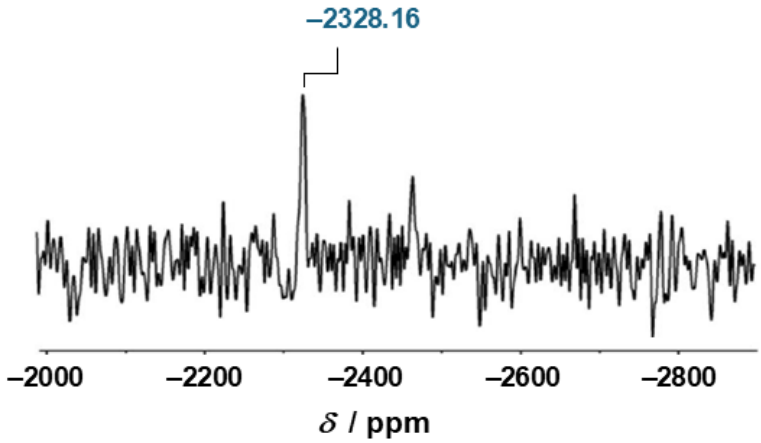

Figure 59: ^{195}Pt-NMR of **Ir-POM-Pt** (DMSO-d_6, 400 MHz, 298 K).

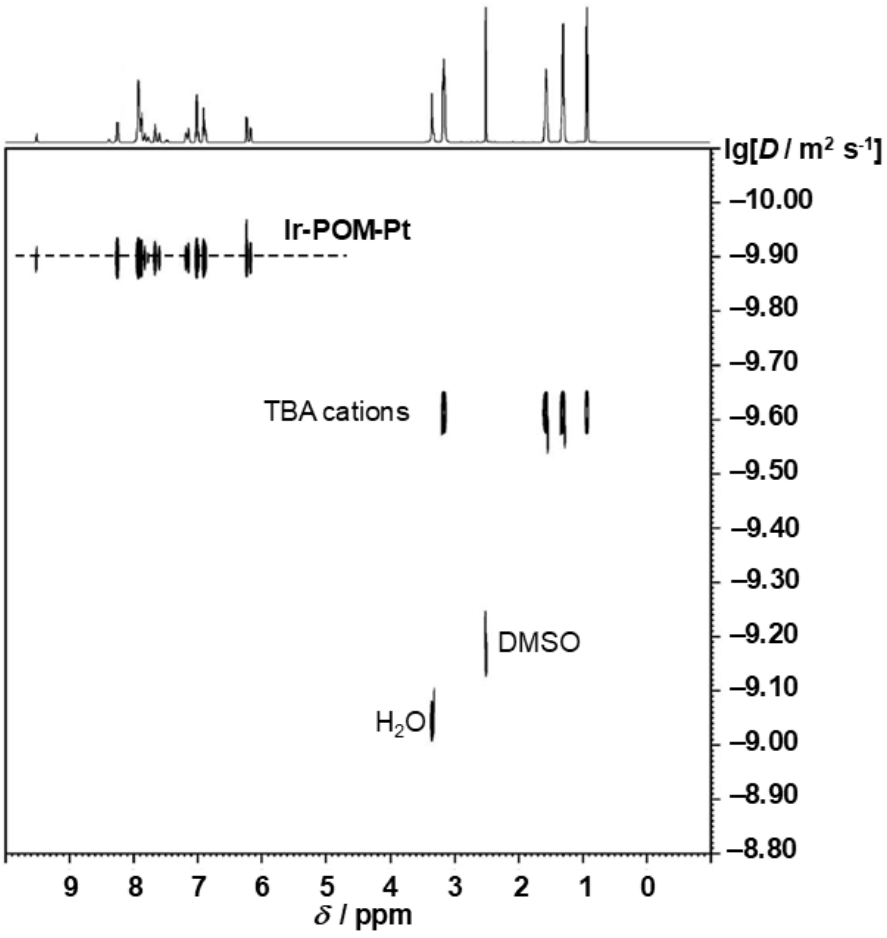

Figure 60: ^{1}H-DOSY of **Ir-POM-Pt** (DMSO-d_6, 500 MHz, 298 K).

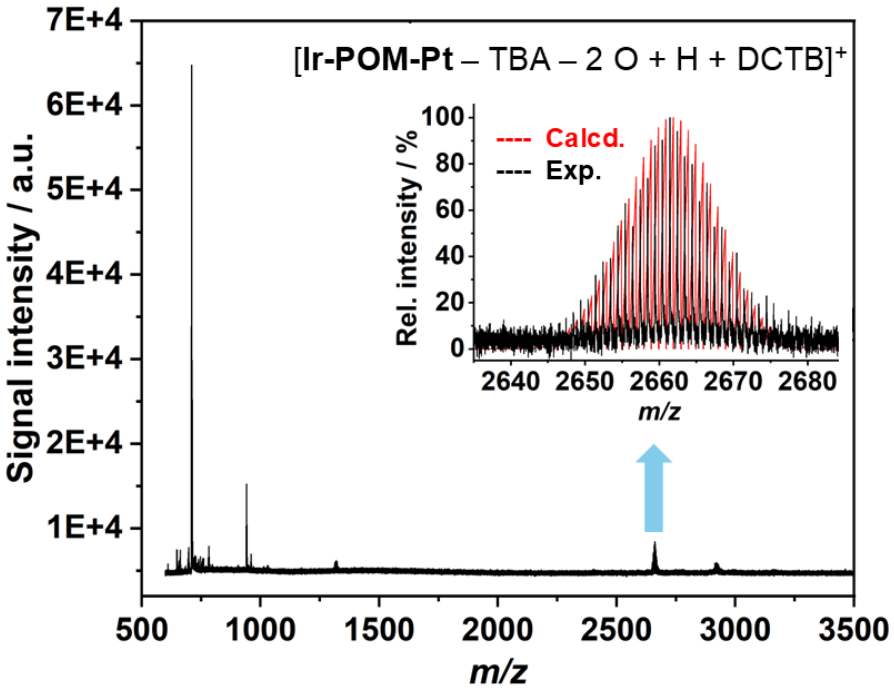

Figure 61: MALDI-TOF MS of **Ir-POM-Pt** (positive reflector mode, DCTB as matrix, KCl as additive).

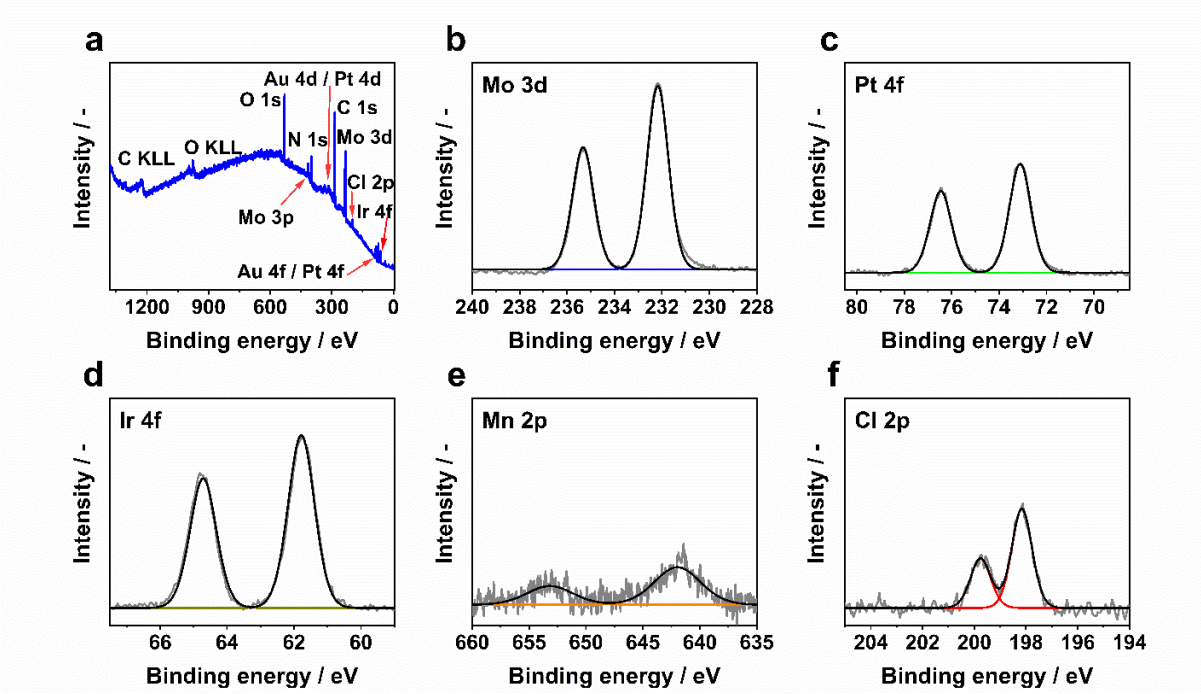

Figure 62: a) Overview XP spectrum of **Ir-POM-Pt**. Deconvoluted high-resolution b) Mo 3d, c) Pt 4f, d) Ir 4f, e) Mn 2p, and f) Cl 2p spectra of **Ir-POM-Pt**.

Table 13: Quantitative analysis of the high-resolution XP spectra of **Ir-POM-Pt** including peak assignment, binding energies and full width at half maximum (FWHM) values obtained from the spectral deconvolution.

	Peak assignment	Type of Photoelectron	FWHM (eV)	Binding energy (eV)
Ir-POM-Pt	$[Ir(ppy)_2]$	Ir $4f_{7/2}$	0.9	61.8
	$PtCl_2$	Cl $2p_{3/2}$	1.1	198.2
	$PtCl_2$	Pt $4f_{7/2}$	0.9	73.1
	$\{MnMo_6O_{24}\}$	Mo $3d_{5/2}$	1.1	232.2
	$\{MnMo_6O_{24}\}$	Mn $2p_{3/2}$	4.9	642.0

The peak fitting of the doublets was performed using fixed intensity ratios due to the spin-orbit coupling of the p, d and f photoelectrons, respectively. With respect to the determination of the elemental ratio (see the main manuscript), the following relative sensitivity factors (RSFs)[198] were used: 7.78 (for Ir $4f_{7/2}$), 1.51 (for Cl $2p_{3/2}$), 8.65 (for Pt $4f_{7/2}$), 5.62 (for Mo $3d_{5/2}$) and 9.17 (for Mn $2p_{3/2}$).

Table 14: Relative elemental composition as determined by XPS analysis.

	Mn-to-Mo ratio	Mn-to-Pt ratio	Pt-to-Mo ratio	Pt-to-Cl ratio
Ir-POM-Pt	1 : 6.7 ± 0.7	1 : 1.1 ± 0.1	1 : 6.0 ± 0.6	1 : 2.2 ± 0.2
	Ir-to-Mn ratio	**Ir-to-Mo ratio**	**Ir-to-Pt ratio**	
	1 : 1.1 ± 0.1	1 : 7.5 ± 0.8	1 : 1.3 ± 0.2	

The commonly accepted uncertainty in XPS elemental quantification is 10%; in the case of poor signal-to-noise ratios, the uncertainty is typically estimated as 15%.

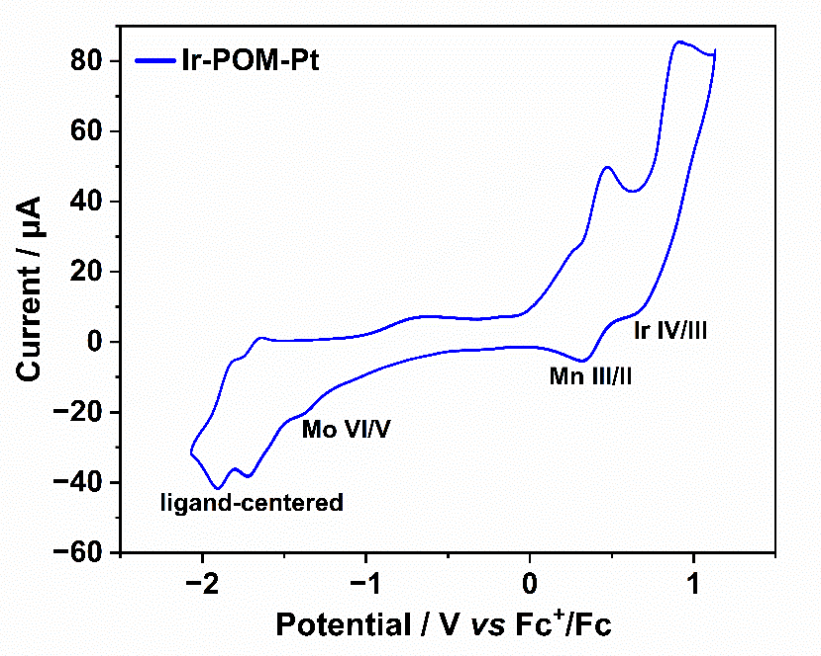

Figure 63: Cyclic voltammogram of **Ir-POM-Pt**. Conditions: water-free, derated DMF, containing 0.1 M (nBu$_4$N)PF$_6$ as a supporting electrolyte, scan rate: 0.1 Vs^{-1}, ([**Ir-POM-Pt**] *ca.* 0.1 mM), Argon atmosphere.

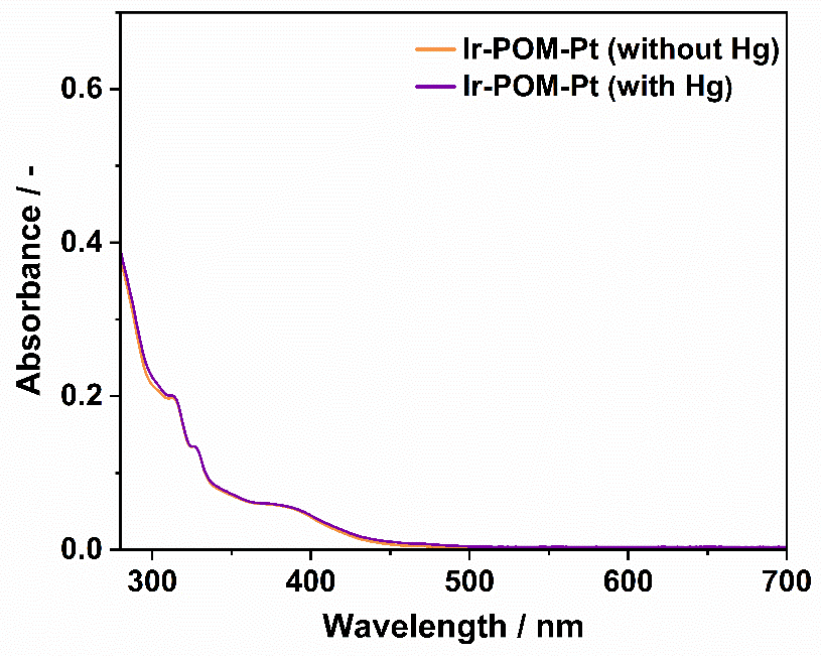

Figure 64: UV-Vis spectroscopic analysis of the reaction solution of **Ir-POM-Pt** with and without elemental mercury treatment (c = 5 µM). No changes in band positions and intensities were observed.

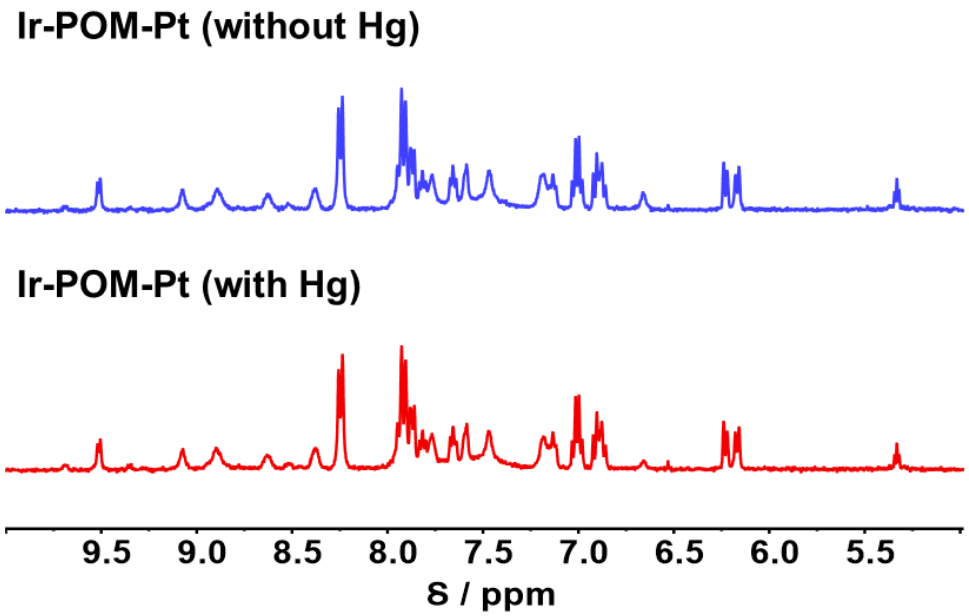

Figure 65: ^{1}H-NMR spectra of **Ir-POM-Pt** in the absence and presence of an elemental mercury in DMSO-d_6. No changes in the spectral features are observed.

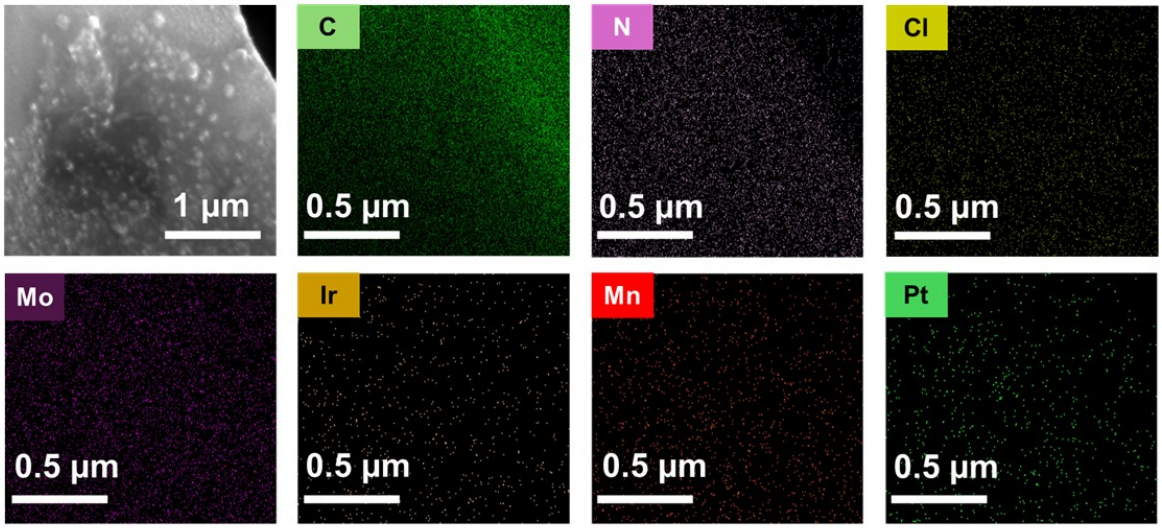

Figure 66: SEM image and corresponding elemental mapping of C, N, Cl, Mo, Ir, Mn, Pt elements of **Ir-POM-Pt** after stirring over Hg, revealing no observable formation of Pt-colloids

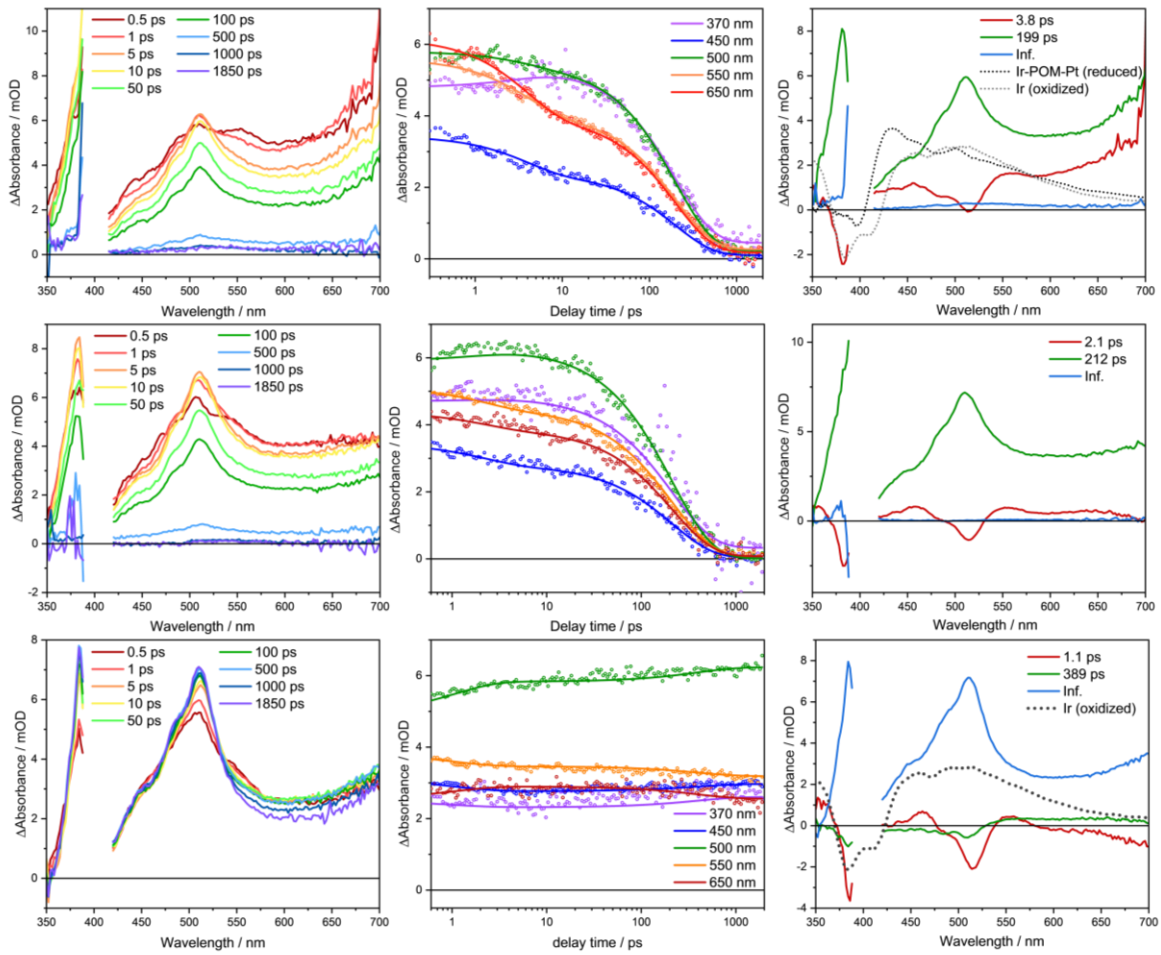

Figure 67: Transient absorption spectroscopic data for **Ir-POM-Pt** (top), **Ir-POM-Ir** (middle) and **Ir** (bottom) with transient absorption spectra at selected delay times, transient kinetics at selected wavelengths and spectral changes associated with each kinetic process (decay associated spectra, DAS). Conditions: solvent: water-free, de-aerated DMF, pump wavelength: 403 nm.

3.4.4 Computational Data

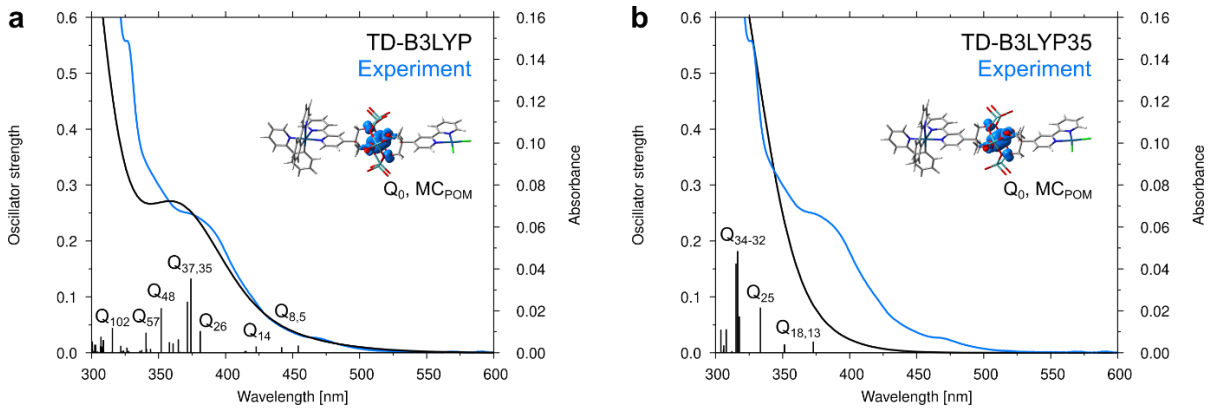

Figure 68: a) TD-B3LYP and b) TD-B3LYP35 simulated (in black) and experimental (in blue) electronic absorption spectra of **Ir-POM-Pt** within its fully optimized quintet ground state (see spin density inset) in DMF. Key electronic transitions are indicated.

Table 15: Selected electronic transitions simulated at the TD-DFT (B3LYP/def2-SVP) level of theory for the quintet species of the **Ir-POM-Pt** triad in DMF. Electronic character based on the three subcomponents, excitation energies, excitation wavelengths, oscillator strengths and spin-contamination. Dipole-allowed transitions are shown in black, while additional low-energy yet dipole-forbidden transitions are shown in grey.

Excitation $Q_0 \rightarrow Q_i$	Character	ΔE / eV	λ / nm	f	$\langle \hat{s}^2 \rangle$
Q_1	MC_{POM}	0.96	1292	0.0000	6.06
Q_2	MC_{POM}	2.58	480	0.0000	6.14
Q_3	$MLCT_{Ir}$	2.62	473	0.0000	8.04
Q_4	$MLCT_{Pt}$	2.70	459	0.0001	8.03
Q_5	$MLCT_{Ir}$	2.73	454	0.0130	6.04
Q_6	MC_{POM}	2.77	447	0.0000	6.17
Q_7	$MLCT_{Ir}$	2.79	444	0.0000	8.04
Q_8	CT_{POM-Pt}	2.81	442	0.0100	6.43
Q_9	MC_{Pt}	2.85	435	0.0000	8.04
Q_{10}	$MLCT_{Ir}$	2.87	432	0.0000	8.02
Q_{11}	$MLCT_{Ir}$	2.89	429	0.0001	8.00
Q_{12}	$MLCT_{Pt}$	2.91	426	0.0009	7.93
Q_{13}	$MLCT_{Ir}$	2.92	425	0.0009	7.82
Q_{14}	$MLCT_{Ir}$	2.93	423	0.0112	6.06
Q_{15}	CT_{Ir-POM}	2.96	419	0.0000	7.00
Q_{16}	$MLCT_{Pt}$	2.99	415	0.0033	6.04

Q_{17}	CT_{POM-Ir}	2.99	414	0.0030	6.56
Q_{18}	MC_{Pt}	3.06	406	0.0000	8.04
Q_{19}	CT_{Ir-Pt}	3.10	399	0.0000	7.04
Q_{20}	CT_{Ir-Pt}	3.11	399	0.0000	7.04
Q_{21}	CT_{Ir-POM}	3.13	396	0.0002	7.01
Q_{22}	MC_{Pt}	3.18	390	0.0000	8.04
Q_{23}	MC_{Pt}	3.21	386	0.0000	8.04
Q_{24}	$MLCT_{Ir}$	3.23	384	0.0000	8.04
Q_{25}	MC_{Pt}	3.23	383	0.0000	8.04
Q_{26}	$MLCT_{Ir}$	3.25	381	0.0391	6.04
Q_{35}	$MLCT_{Pt}$	3.31	374	0.1328	6.05
Q_{37}	$MLCT_{Ir}$	3.34	372	0.0916	6.05
Q_{41}	$MLCT_{Ir}$	3.40	365	0.0241	6.04
Q_{43}	MC_{POM}/CT_{Pt-POM}	3.44	361	0.0169	7.05
Q_{46}	$MC_{POM}/CT_{Ir/Pt-POM}$	3.46	358	0.0191	7.05
Q_{48}	$MLCT_{Ir}$	3.52	352	0.0799	6.04
Q_{57}	$MLCT_{Ir}$	3.64	341	0.0361	6.35
Q_{102}	$MLCT_{Ir}$	3.93	316	0.0445	6.06
Q_{172}	$MLCT_{Pt}$	4.21	295	0.1615	6.31
Q_{236}	IL_{Ir}	4.35	285	0.1525	6.05
Q_{246}	IL_{Ir}	4.37	284	0.1944	6.11
Q_{289}	$MLCT_{Ir}/CT_{POM-Ir}$	4.47	277	0.1349	6.68

Table 16: Electronic character of the quintet electronic ground state (Q_0, MC_{POM}) as visualized by means of the spin density as well as charge density difference plots of selected electronic transitions; charge transfer takes place from red to blue. Dipole-allowed transitions are shown in black, while additional low-energy yet dipole-forbidden transitions are shown in grey.

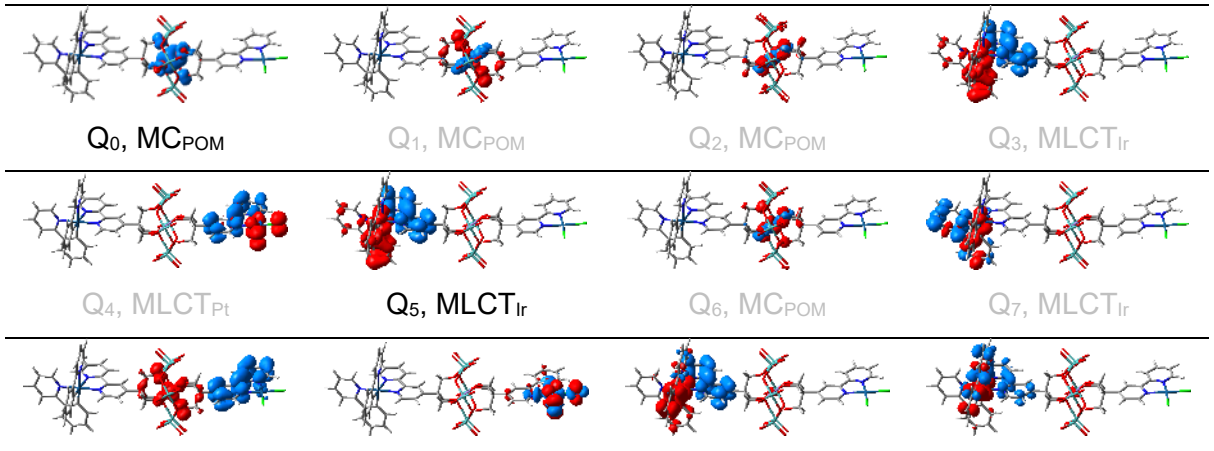

Q_8, CT_{POM-Pt}	Q_9, MC_{Pt}	Q_{10}, $MLCT_{Ir}$	Q_{11}, $MLCT_{Ir}$
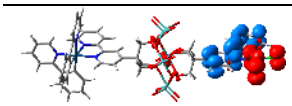	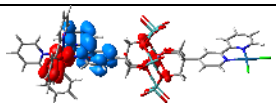	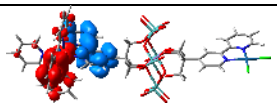	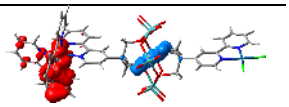
Q_{12}, $MLCT_{Pt}$	Q_{13}, $MLCT_{Ir}$	Q_{14}, $MLCT_{Ir}$	Q_{15}, CT_{Ir-POM}
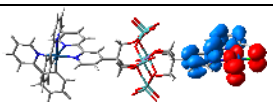	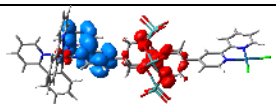	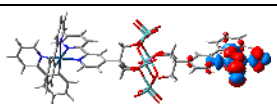	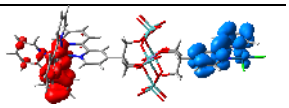
Q_{16}, $MLCT_{Pt}$	Q_{17}, CT_{POM-Ir}	Q_{18}, MC_{Pt}	Q_{19}, CT_{Ir-Pt}
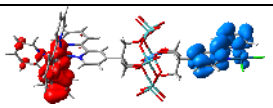	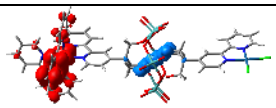	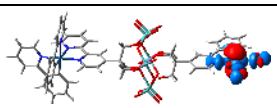	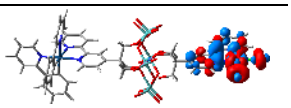
Q_{20}, CT_{Ir-Pt}	Q_{21}, CT_{Ir-POM}	Q_{22}, MC_{Pt}	Q_{23}, MC_{Pt}
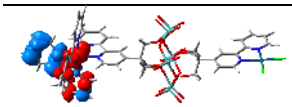	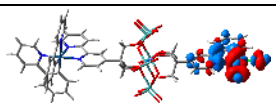	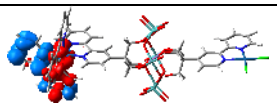	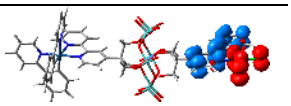
Q_{24}, $MLCT_{Ir}$	Q_{25}, MC_{Pt}	Q_{26}, $MLCT_{Ir}$	Q_{35}, $MLCT_{Pt}$
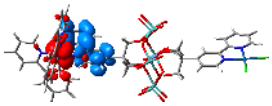	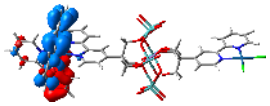	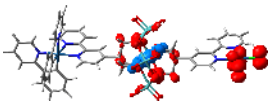	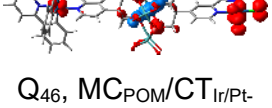
Q_{37}, $MLCT_{Ir}$	Q_{41}, $MLCT_{Ir}$	Q_{43}, MC_{POM}/CT_{Pt-POM}	Q_{46}, $MC_{POM}/CT_{Ir/Pt-POM}$
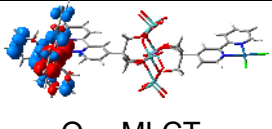	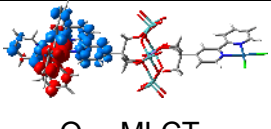	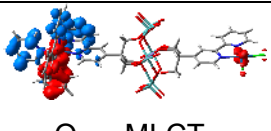	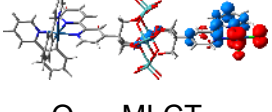
Q_{48}, $MLCT_{Ir}$	Q_{57}, $MLCT_{Ir}$	Q_{102}, $MLCT_{Ir}$	Q_{172}, $MLCT_{Pt}$
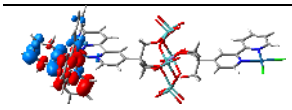	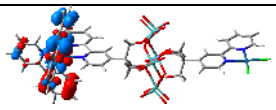	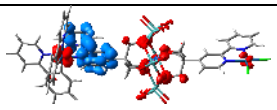	
Q_{236}, IL_{Ir}	Q_{246}, IL_{Ir}	Q_{289}, $MLCT_{Ir}/CT_{POM-Ir}$	

Table 17: Selected electronic transitions simulated at the TD-DFT (B3LYP/def2-SVP) level of theory for the triplet charge-separated species of the **Ir-POM-Pt** triad in DMF. Electronic character based on the three subcomponents, excitation energies, excitation wavelengths, oscillator strengths and spin-contamination.

Excitation $T_1 \rightarrow T_i$	Character	ΔE / eV	λ / nm	f	$\langle \hat{s}^2 \rangle$
T_{16}	$LMCT_{Ir}$	1.16	1069	0.0153	4.07
T_{27}	$CT_{Pt\text{-}Ir}$	1.55	798	0.0103	3.75
T_{28}	$CT_{Pt\text{-}Ir}$	1.57	791	0.0084	3.87
T_{30}	IL_{Pt}	1.59	781	0.0286	3.82
T_{36}	$LMCT_{Ir}$	1.76	704	0.0114	4.06
T_{43}	$LMCT_{Ir}$	1.93	644	0.0556	4.06
T_{45}	$LMCT_{Ir}$	2.03	611	0.034	4.06
T_{82}	$LMCT_{Ir}$	2.70	460	0.0222	4.11
T_{87}	IL_{Pt}	2.80	442	0.0911	4.12
T_{97}	$CT_{Pt\text{-}POM}$	3.03	409	0.0643	3.80
T_{100}	$CT_{Pt\text{-}POM}$	3.06	405	0.0401	3.51
T_{128}	$MLCT_{Pt}$	3.35	370	0.0783	4.15
T_{141}	MC_{POM}	3.48	356	0.0466	5.10
T_{169}	$MLCT_{Pt}/IL_{Pt}$	3.70	335	0.2077	4.19
T_{182}	$MLCT_{Ir}$	3.77	329	0.0677	4.52
T_{214}	$MLCT_{Ir}/CT_{POM\text{-}Ir}$	3.96	313	0.0411	5.20
T_{215}	IL_{Ir}	3.96	313	0.0825	4.56

Table 18: Electronic character of the charge-separated triplet state (T_1, $CT_{Ir\text{-}Pt}$) as visualized by means of the spin density as well as charge density difference plots of selected electronic transitions; charge transfer takes place from red to blue.

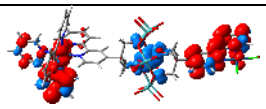	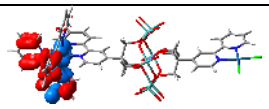	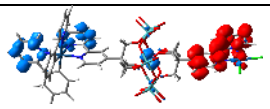	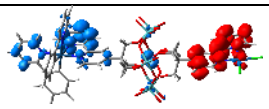
T_1, $CT_{Ir\text{-}Pt}$	T_{16}, $LMCT_{Ir}$	T_{27}, $CT_{Pt\text{-}Ir}$	T_{28}, $CT_{Pt\text{-}Ir}$
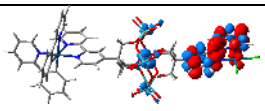	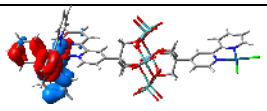	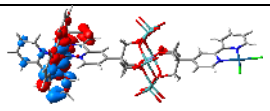	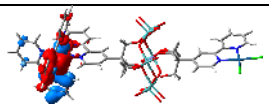
T_{30}, IL_{Pt}	T_{36}, $LMCT_{Ir}$	T_{43}, $LMCT_{Ir}$	T_{45}, $LMCT_{Ir}$
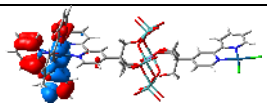	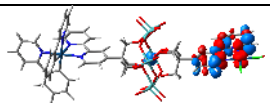	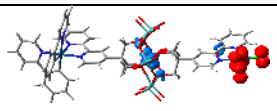	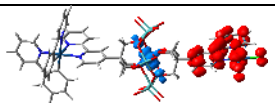

T_{82}, $LMCT_{Ir}$	T_{87}, IL_{Pt}	T_{97}, $CT_{Pt\text{-}POM}$	T_{100}, $CT_{Pt\text{-}POM}$
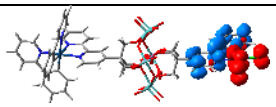	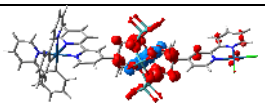	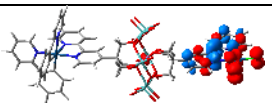	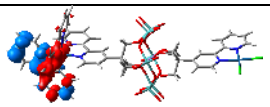
T_{128}, $MLCT_{Pt}$	T_{141}, MC_{POM}	T_{169}, $MLCT_{Pt}/IL_{Pt}$	T_{182}, $MLCT_{Ir}$
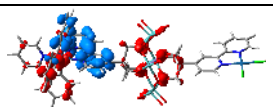	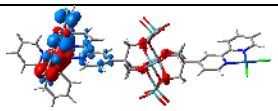		
T_{214}, $MLCT_{Ir}/CT_{POM\text{-}Ir}$	T_{215}, IL_{Ir}		

Table 19: Selected electronic transitions simulated at the TD-DFT (B3LYP/def2-SVP) level of theory for the septet charge-separated species of the **Ir-POM-Pt** triad in DMF. Electronic character based on the three subcomponents, excitation energies, excitation wavelengths, oscillator strengths and spin-contamination.

Excitation $7_1 \rightarrow 7_i$	**Character**	**ΔE / eV**	**λ / nm**	***f***	$\langle \hat{s}^2 \rangle$
7_{15}	$LMCT_{Ir}$	1.16	1069	0.0153	12.07
7_{27}	IL_{Pt}	1.58	787	0.0449	12.08
7_{33}	$LMCT_{Ir}$	1.76	703	0.0119	12.07
7_{38}	$LMCT_{Ir}$	1.92	646	0.0412	12.06
7_{39}	$CT_{POM\text{-}Ir}$	1.94	640	0.0173	12.07
7_{41}	$LMCT_{Ir}$	2.03	611	0.0335	12.06
7_{78}	$LMCT_{Ir}$	2.70	459	0.0223	12.11
7_{83}	IL_{Pt}	2.80	442	0.0990	12.13
7_{95}	$MLCT_{Pt}$	3.04	408	0.0970	12.18
7_{124}	$MLCT_{Pt}$	3.35	370	0.0752	12.16
7_{133}	MC_{POM}	3.47	358	0.0406	13.11
7_{156}	IL_{Pt}	3.66	339	0.1094	12.67
7_{163}	MC_{POM}	3.70	335	0.0905	12.74
7_{211}	IL_{Ir}	3.96	313	0.1089	12.17
7_{239}	$CT_{POM\text{-}Pt}$	4.08	304	0.0542	12.61

Table 20: Electronic character of the charge-separated septet state (7_1, $CT_{Ir\text{-}Pt}$) as visualized by means of the spin density as well as charge density difference plots of selected electronic transitions; charge transfer takes place from red to blue.

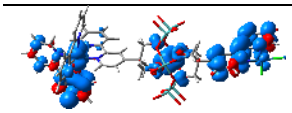	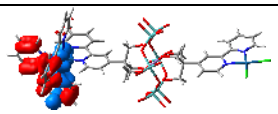	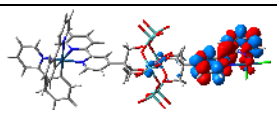	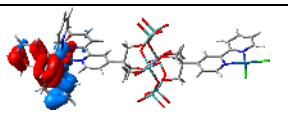
7_1, $CT_{Ir\text{-}Pt}$	7_{15}, $LMCT_{Ir}$	7_{27}, IL_{Pt}	7_{33}, $LMCT_{Ir}$
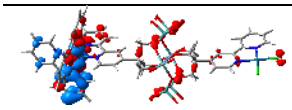	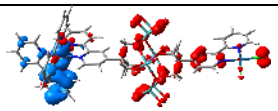	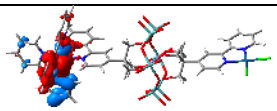	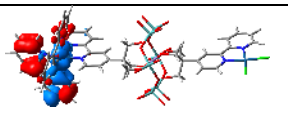
7_{38}, $LMCT_{Ir}$	7_{39}, $CT_{POM\text{-}Ir}$	7_{41}, $LMCT_{Ir}$	7_{78}, $LMCT_{Ir}$
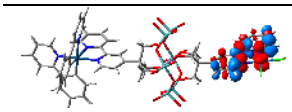	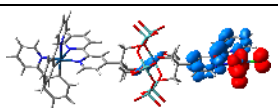	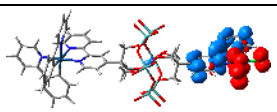	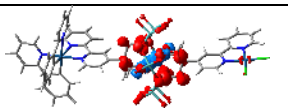
7_{83}, IL_{Pt}	7_{95}, $MLCT_{Pt}$	7_{124}, $MLCT_{Pt}$	7_{133}, MC_{POM}
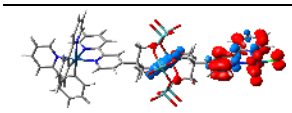	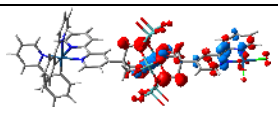	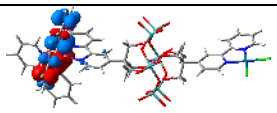	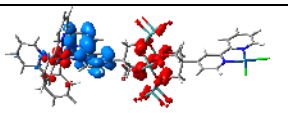
7_{156}, IL_{Pt}	7_{163}, MC_{POM}	7_{211}, IL_{Ir}	7_{239}, $CT_{POM\text{-}Pt}$

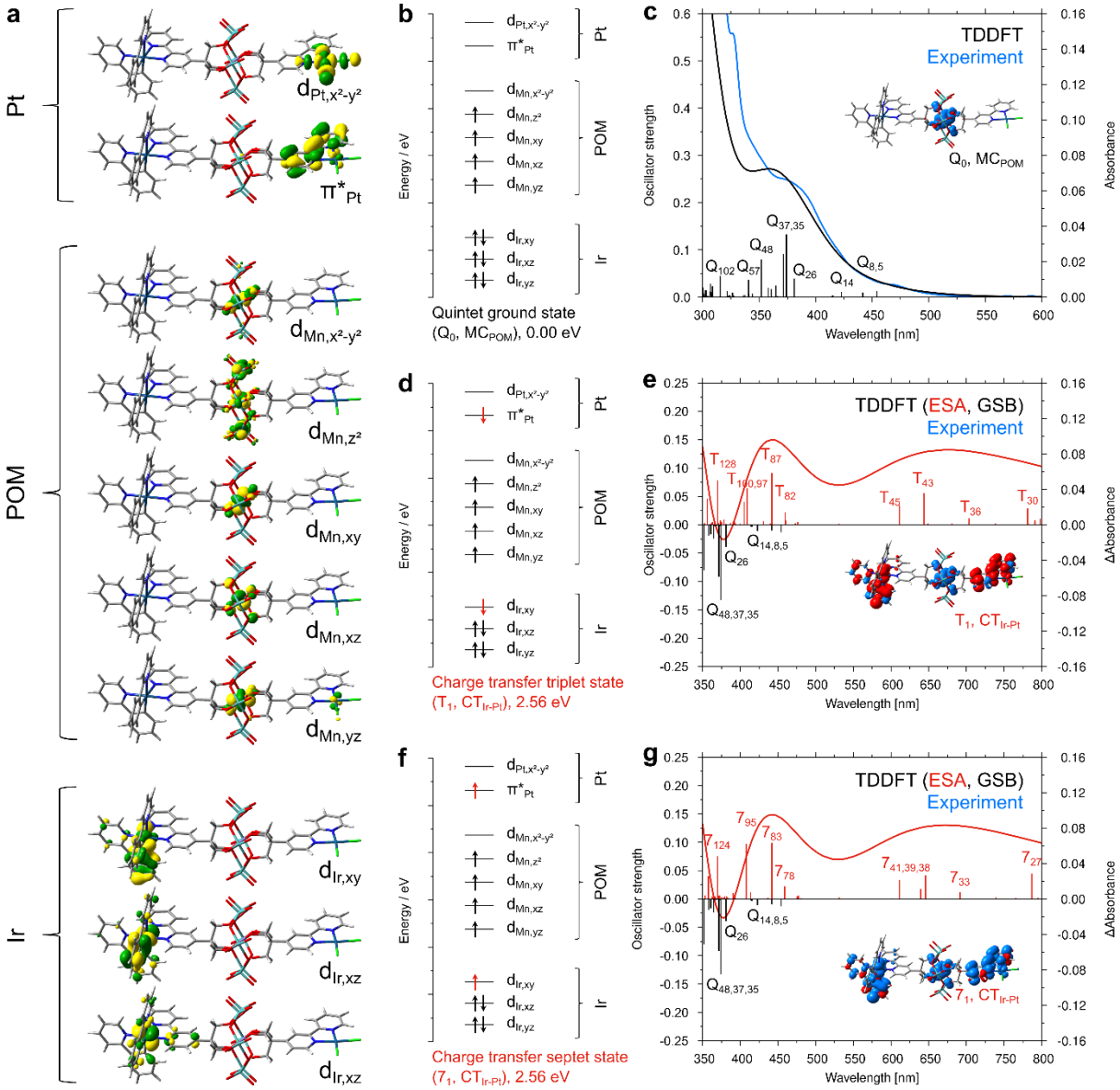

Figure 69: a) Frontier orbitals of the **Ir-POM-Pt** triad, i.e., occupied d-orbitals (or rather mixed d-π-orbitals) of the Ir PS, d-orbitals of the Mn(III) core of the POM as well as lowest-energy unoccupied π^*_{Pt} and $d_{x^2-y^2}$ (or rather $\sigma^*_{x^2-y^2}$ in a molecular orbital picture). Orbitals are visualized by means of the closed-shell species. b) Electronic structure of the quintet ground state (Q_0). c) Associated electronic absorption spectrum of **Ir-POM-Pt**. Key electronic transitions are highlighted; the nature of the quintet ground state (with four unpaired electrons at the Mn) is illustrated by the spin density. d) Electronic structure of the fully related triplet charge-separated species (T_1). e) Associated transient absorption spectrum of the triad. Key electronic transitions contributing to the excited state absorption (ESA, triplet-triplet excitations in red) and ground state bleach (GSB, quintet-quintet excitations in black) are labelled; the nature of T_1 is illustrated by the spin density. f) Electronic structure of the fully related septet charge-separated species (7_1). g) Associated transient absorption spectrum of the triad. Key electronic transitions contributing to the excited state absorption (ESA, septet-septet excitations in red) and ground state bleach (GSB, quintet-quintet excitations in black) are labeled; the nature of 7_1 is illustrated by the spin density.

3.4.5 Post-catalytic analysis

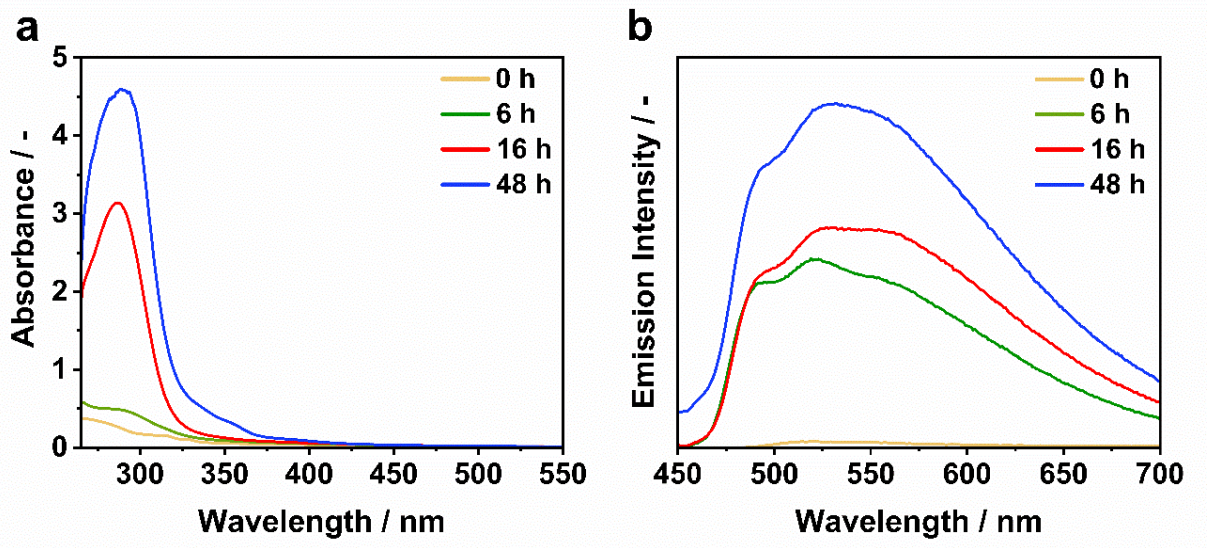

Figure 70: Steady-state a) UV-Vis absorption, and b) Emission spectra of the catalytic solution of **Ir-POM-Pt** over 48 h of irradiation (c = 5 µM).

Acknowledgements

This project was funded by the Deutsche Forschungsgemeinschaft DFG through the TRR 234 “CataLight” (project no: 364549901; A4). USS, AW and CS acknowledge financial support by the DFG through the Priority Program “Light-controlled reactivity of metal complexes” (SPP-2102, LCRMC, project numbers 493768838, 494988281). C.S. gratefully acknowledges financial support from the Top-Level Research Area SunInnoScience and the Gutenberg Research College. The Thüringer Aufbaubank (TAB) supported the acquisition of the rapifleX MALDI TOF/TOF spectrometer (grant number 2016/IZN/0009). The authors thank Nicole Fritz and Rene Burges for the measurement and discussion of the MALDI-TOF mass spectra. We thank the DFG for their support in acquiring the 500 MHz NMR spectrometer (INST 275/442-1 FUGG) and XPS (INST 275/25 7-1 FUGG).

Authors Contributions

G. Sachdeva	Data curation, investigation, project administration, validation, visualization, and writing original draft
P. Endres	Investigation
A. Winter	Conceptualization, methodology, supervision, visualization, and writing original draft
D. Díaz	Data curation, investigation, validation, and visualization
C. Titze	Investigation, formal analysis
C. Neumann	Data curation, investigation, validation, and writing original draft
A. Turchanin	Data curation, funding acquisition, project administration, supervision, writing original draft
S.S. Akbari	Data curation
L. Zedler	Data curation, investigation, methodology, project administration, supervision, visualization, and writing original draft
A.K. Mengele	Investigation, formal analysis
S. Rau	Funding acquisition, supervision
B. D. Ivanšic	Project administration, resources, supervision, and writing original draft

S. Kupfer	Funding acquisition, methodology, project administration, software, supervision, visualization, and writing original draft
U.S. Schubert	Funding acquisition, project administration, resources, supervision,
C. Streb	Conceptualization, funding acquisition, project administration, resources, supervision, writing original draft

3.5 Organofunctionalized Anderson POMs as building block for aerogel formation

Note: This chapter is based on the published journal article: G. Sachdeva, S. Maloul, J. Zolg, R. Müller, M. Mondeshki, E. Ebrahimi, D. Abid, S.A. Chala, C. Neumann, A. Turchanin, J. Biskupek, U. Kaiser, K. Leopold* and C. Streb*, Polyoxometalate Aerogels Formed by Organofunctionalized Anderson Polyoxometalates as Low Molecular Weight Gelators. Adv. Mater. Interfaces 12, no. 22, (2025): e00597. https://doi.org/10.1002/admi.202500597. The corresponding authors are indicated with an asterisk "*".

3.5.1 Introduction

Supramolecular gels are a promising class of functional soft materials with unique structure and function.[143,265,266] Metallogels in particular are attractive, as classical coordination chemistry between metal cations and suitable organic ligands can be used to design and tune the gel properties and reactivities.[145,267,268] Further, this linkage is assisted *via* non-covalent interactions such as hydrogen bonding, electrostatic, or hydrophobic interactions.[148,269] This has led to applications ranging from catalysis and sensing to optoelectronics and magnetism.[270–274] Rational design of metallogelators, therefore, is challenging, and significant attempts in molecular synthesis and design are requisite to create systems in which metal is accountable for both cross-linking and coordination.[275,276] Metallogels can also be converted into technologically important aerogels[158,277] using freeze-drying.[159] This approach removes the solvent from the gel structure while maintaining its 3D architecture. Aerogels are unique materials that feature high specific surface area, low density, and hierarchical pore structures.[161] The exceptional features of the aerogels have led to their development in the areas of catalysis,[278] biomedicine,[279] energy storage,[280] and water treatment.[281] Furthermore, the use of numerous materials and their modification in the construction of aerogels has broadened their application area, ranging from photocatalysis to the food industry.[282] Recently, metal-based aerogels

have been widely explored for their unique function in catalysis,[283] engineering materials,[284] and sensing.[285]

In particular, molecular metal oxide anions, so-called polyoxometalates (POMs),[286] have recently been put forward as a new low molecular weight gelator class for the design of metallogels. POMs are versatile molecules having tunable structures and reactivities. In addition, they are excellent electron reservoirs and possess rich redox chemistry, making them ideal for catalysis, energy storage, and conversion.[287,288] POMs can be cross-linked by a number of interactions, including electrostatics or hydrogen bonding. Moreover, POMs can be covalently functionalized with a range of organic ligands, which opens the pathway to use the ligands for further linkage and to control the properties of the resulting gels.[289] Inspired by these possibilities, Zhou, Wang, and colleagues have reported metallogels based on Keggin-type anions $[PMo_{12}O_{40}]^{3-}$ which were employed as anode materials for lithium-ion batteries and displayed promising rate capability, high reversible capacity, and decent cycling stability.[290] Izzet, Bo, and co-workers have developed dumbbell-type dimers linked *via* Co(II) or Co(III) made of Keggin and Dawson POMs functionalized with terpyridine ligands. The resulting metallogels showed intriguing solvent exchange properties, opening the path to form hydrogels.[157]

One prototype gel-forming POM is the organofunctionalized Anderson-Evans polyoxometalate[74] $[XMo_6O_{18}\{RC(CH_2O)_3\}_2]^{3-}$ (where X = Mn, Fe, Co, and R = $-NH_2$, $-CH_3$, $-CH_2OH$) which features two organic ligands arranged in a linear fashion on opposite sides of the cluster, tethered by tris-alkoxide groups(Figure 71a). Pioneering work on Anderson-based gels was performed by Hasenknopf and colleagues, who reported the formation of an anisotropic supramolecular gel showing good thermal stability and birefringence.[139] The gel was formed by the coordination of Pd(II) salt to Anderson anions covalently functionalized with pyridyl moieties.[139] In a related study, Li and co-workers showed that the intermolecular combination of pyridyl functionalized Anderson POM with suitable dicarboxylic acids resulted in the immediate formation of a supramolecular gel, which showed rapid stimuli-responsiveness to organic acids and bases.[291] More recently, Izzet, Merland, Davidson, Solé-Daura, and co-workers designed supramolecular metallogels by linking terpyridine-functionalized Anderson anions with Zn(II) or Co(II)cations. The hybrid gels exhibited intriguing properties, including luminescence, birefringence, and spin-crossover.[292]

To date, to the best of our knowledge, the conversion of purely POM-based metallogels into aerogels has not been reported. However, there is widespread interest in POM-containing aerogels, as they have been utilized in areas ranging from electrocatalysis[168] and batteries[293] to pollutant removal[294] and aerospace materials.[295] The structural and chemical tunability and redox behaviour offered by POM make them an ideal candidate for utilization in several applications as compared to conventional aerogels.[296,297]

Furthermore, in recent years, Anderson-Evans POMs have been widely studied as catalysts for several oxidation reactions, showing their potential to oxidize several organic compounds, such as thioanisoles and furan-based chemicals.[298,299] Building on these studies, we now report the use of POM-based aerogel in the oxidation of primary alcohols, paving the path to using POM-based porous catalysts in the transformation of organic reactions.

Herein, we report the development of a POM-based organogel, formed within 10 s by reaction of $ZnCl_2$ with TRIS-functionalized Anderson POM in acetonitrile solution. The resulting organogel can easily be converted into an aerogel by freeze-drying. We provide a full characterization of the aerogel and demonstrate its principal suitability for selective alcohol oxidation reactions using benzyl alcohol, furfuryl alcohol, and octanol as model substrates. In addition, initial insights into the scope of gel formation are presented with a focus on the role of the POM, the $ZnCl_2$, and the solvent.

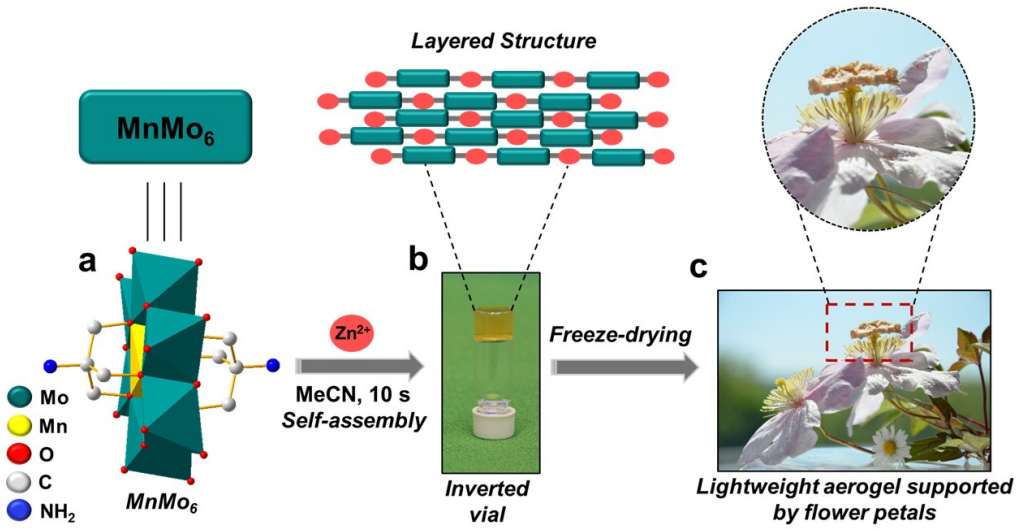

Figure 71: a) Illustration of the TRIS-functionalized Anderson POM low molecular weight gelator. b) Illustration of the organogel formation. c) Photograph of the low-weight aerogel placed on top of a flower.

3.5.2 Results and Discussion

3.5.2.1 Catalyst Synthesis and Characterization

Briefly, the POM-based organogel was prepared by combining acetonitrile solutions of $ZnCl_2$ and the TRIS-functionalized Anderson $(n\text{Bu}_4\text{N})_3[\text{MnMo}_6\text{O}_{18}\{(\text{OCH}_2)_3\text{CNH}_2\}_2]$[66] (here-after: $\{\text{MnMo}_6\}$). Reaction of both solutions resulted in near-instantaneous gel formation (gelation time *ca.* 10 s). The vial inversion test[300,301] was used to demonstrate the stability and viscoelasticity of the gel, see Figure 71b. Next, the organogel was converted into an aerogel (1) by freeze-drying (for synthetic and characterization details of the organogel and 1, see Supporting Information).

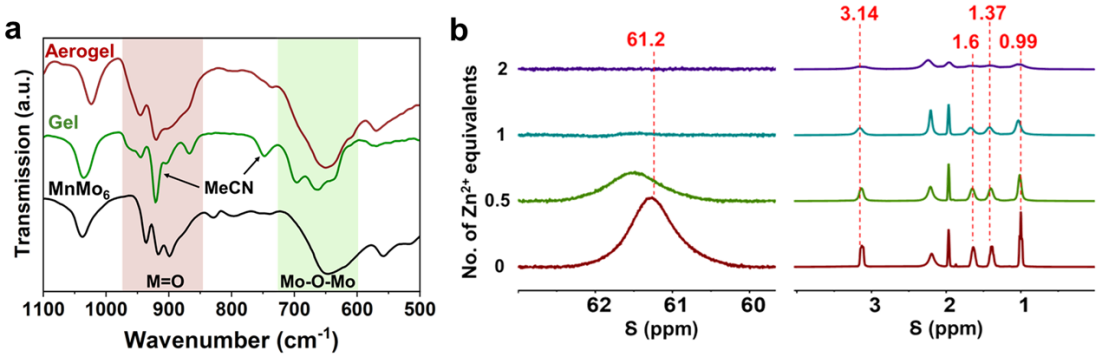

Figure 72: a) Stacked FT-IR spectra of the organogel and the aerogel (1), and their comparison with the distinctive peaks of reference $\{\text{MnMo}_6\}$. b) Stacked ^{1}H NMR spectra of deuterated acetonitrile solutions of $\{\text{MnMo}_6\}$ and varying equivalents of Zn(II). Conditions: $[\text{MnMo}_6]$ = 63.7 mM, and $[\text{ZnCl}_2]$ = 82.8 mM, solvent = acetonitrile-d_3.

The structural changes occurring during gelation and freeze-drying were investigated using FT-IR spectroscopy (Figure 72a). Upon gelation, both the bridging Mo—O—Mo band (*ca.* 650 cm^{-1}) as well as the terminal Mo═O feature (890–950 cm^{-1}) showed minor, but characteristic changes (peak splitting, peak broadening). These changes indicate that the outer oxo ligands of $\{\text{MnMo}_6\}$ are involved in the gelation process. In addition, the presence of the bands at *ca.* 749 and 920 cm^{-1} corresponding to the acetonitrile molecules[302,303] suggests the possibility of solvent coordination for the stabilization of the Zn(II) center. Further, upon freeze-drying and removal of the MeCN solvent, further broadening of these signals is observed, in particular for the band located at *ca.* 900 cm^{-1}. This indicates that further molecular-level structure changes of the gel network occur upon freeze-drying. One plausible interpretation of these findings is that acetonitrile-stabilized Zn(II) coordinates to the oxo ligands of $\{\text{MnMo}_6\}$

to trigger the gelation process. Upon solvent removal, minor structural changes at the Zn(II) center might occur, which would be in line with the observed spectroscopic changes reported.

To gain more structural insights into the gelation process, we performed ^{1}H NMR spectroscopic titrations, where 0 to 2 molar equivalents of $ZnCl_2$ were added to the {$MnMo_6$} solution in deuterated acetonitrile (Figure 72b). Note that the methylene protons of the TRIS-NH_2 experience a significant paramagnetic shift due to the effect of the Mn(III) center of the Anderson POM.[66] Upon the addition of increasing amounts of $ZnCl_2$, we observe a broadening and intensity decrease of all ^{1}H NMR signals. The reduced molecular mobility as a result of gelation results in the partial reintroduction of the anisotropic chemical shift and dipole-dipole couplings, which affect the spectral lines. Previous reports also have shown similar observations of line broadening of characteristic peaks, where Keggin-type POMs have triggered the hydrogel formation with γ-cyclodextrin.[304]

The thermal stability of 1 was examined by thermogravimetric analysis (TGA) in an air atmosphere (Figure 77, Supporting Information). A significant weight loss of 27.6% (calculated: 28.3%) is observed between 200 and 385 °C, which is attributed to the loss of three $n$$Bu_4N^+$ cations. A second weight loss of 18.4% between 410 to 555 °C is associated with the simultaneous decomposition of the TRIS moieties[305] and volatilization of $ZnCl_2$.[306,307] This data was supported by CHN elemental analysis, which is in line with the presence of three $n$$Bu_4N^+$ cations and two TRIS moieties per formula unit (Table 26, Supporting Information). Next, the elemental composition and oxidation states at the surface of 1 were investigated by X-ray photoelectron spectroscopy (XPS). The survey XP spectrum verifies the presence of all expected elements (Figure 78, Supporting Information). The deconvoluted high-resolution Mo 3d spectrum (Figure 73a) shows two peaks at binding energies of 232.4 and 235.6 eV corresponding to Mo $3d_{5/2}$ and Mo $3d_{3/2}$, respectively, indicating the presence of Mo(VI).[308] A spin-orbit coupled doublet of Mn 2p at binding energies of 640.9 and 652.7 eV is assigned to Mn $2p_{3/2}$ and Mn$2p_{1/2}$ of Mn(III), respectively (Figure 73b).[309,310] The Cl 2p spectrum (Figure 73c) shows binding energies at 200.2 eV (Cl $2p_{1/2}$) and 198.5 eV (Cl $2p_{3/2}$), assigned to Cl-Zn coordination.[311] Moreover, the Zn 2p XP spectrum revealed two peaks at 1045.3 and1022.4 eV, which are assigned to Zn $2p_{1/2}$ and Zn $2p_{3/2}$ signals of the Zn(II) species (Figure 73d).[312,313]

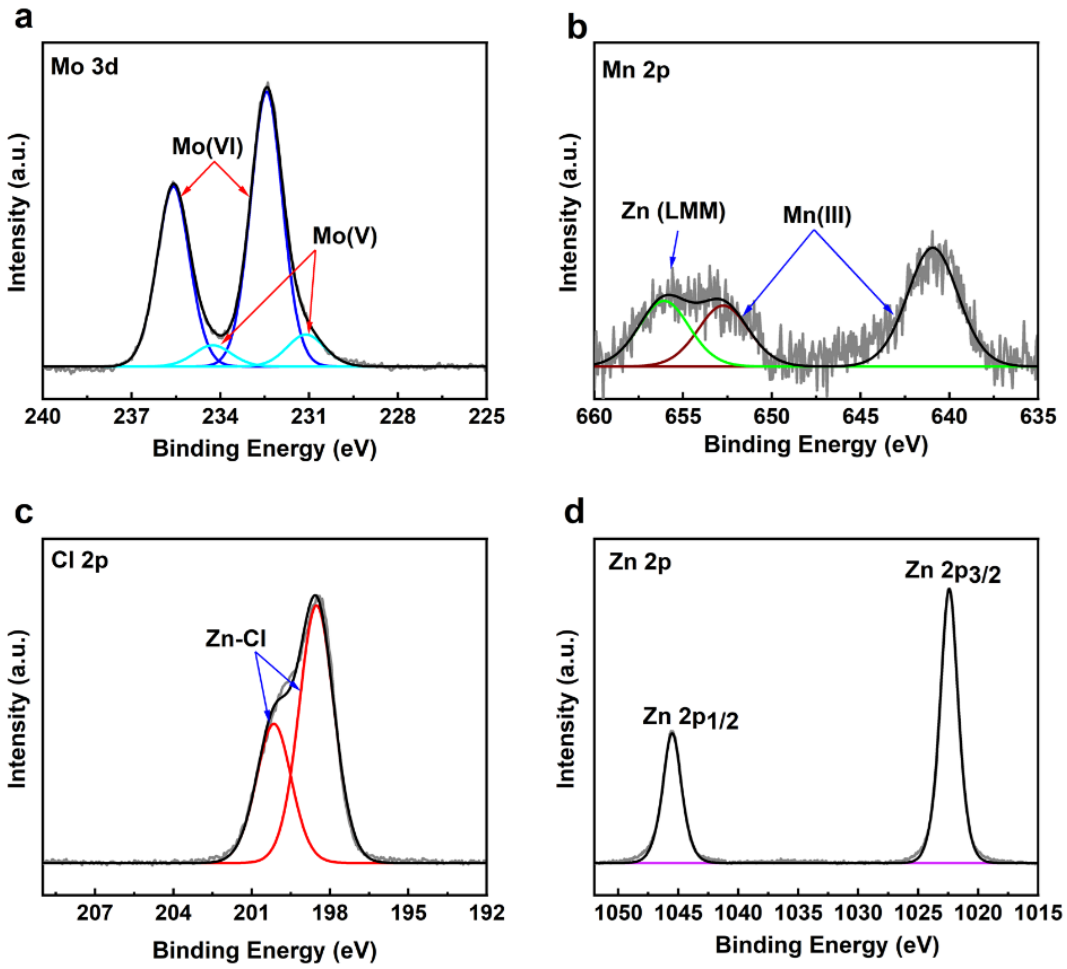

Figure 73: Deconvoluted high-resolution a) Mo 3d, b) Mn 2p, c) Cl 2p, d) Zn 2p XP spectra for 1.

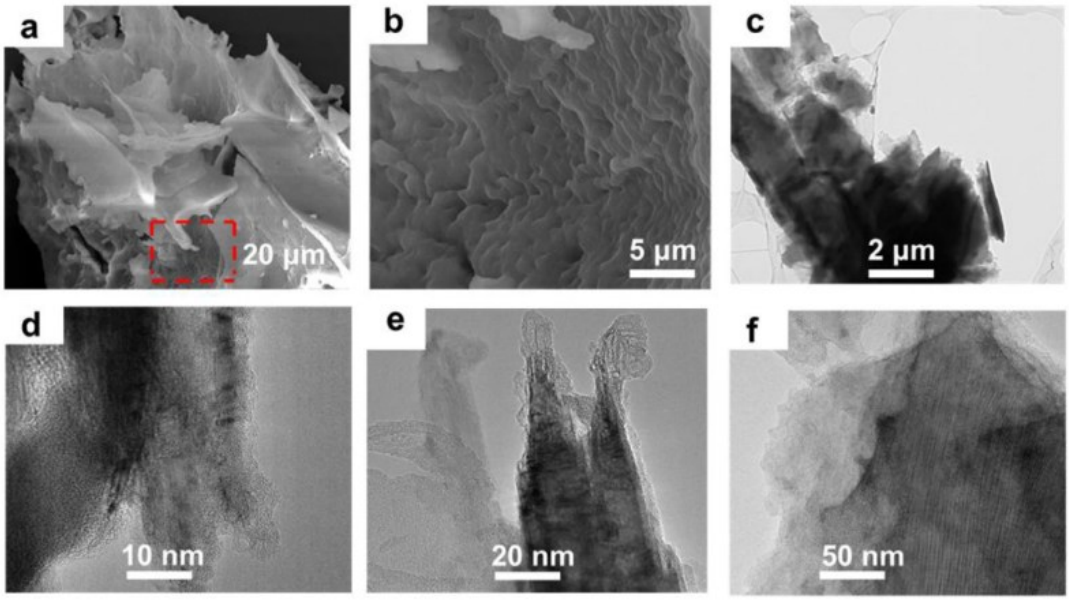

Figure 74: Electron microscopy of 1. a) SEM image, b) magnification of the selected area (in a red rectangle), c,d) TEM images, e,f) HRTEM images.

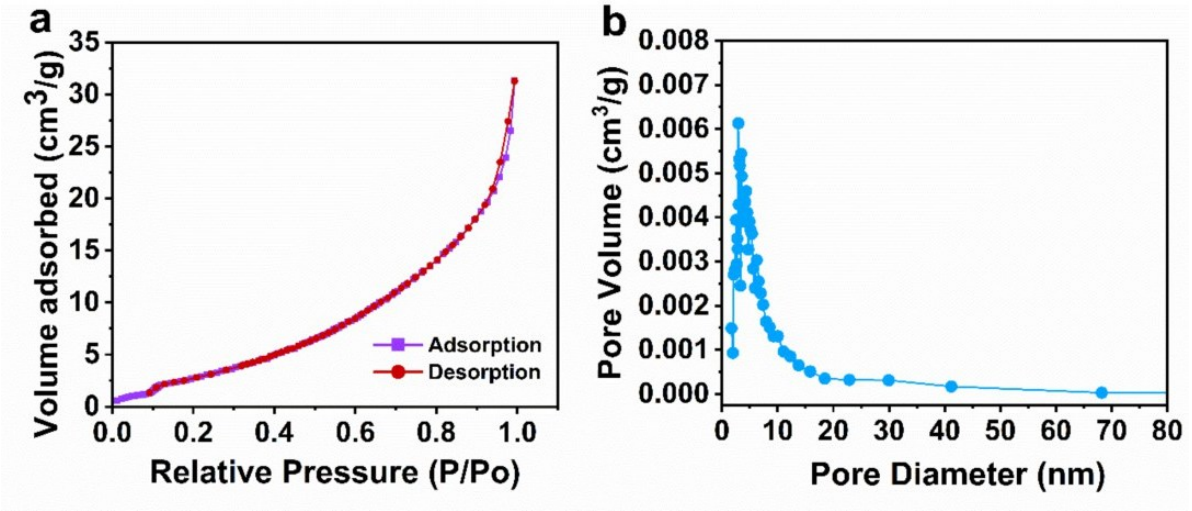

Figure 75: Representative Histograms of a) N_2 adsorption-desorption isotherm, b) Pore size distribution of 1.

The morphology of 1 was studied by scanning electron microscopy (SEM, Figure 74 a,b). This analysis showed a layered structure composed of stacked and agglomerated sheets. To obtain further insights into the morphological and structural properties of as synthesized 1, transmission electron microscopy (TEM), high-resolution transmission electron microscopy (HRTEM), and scanning-transmission electron microscopy (STEM) together with energy dispersive X-ray spectroscopy (EDS) were employed. As shown in Figure 74 c,d, the structure of 1 consists of thin and long fibrous sheets that appear stacked. Furthermore, HRTEM analysis (Figure

74 e,f) indicates the existence of both long fibrous and layered structures, which might be due to the supramolecular linkage of the Anderson anions. Moreover, high-angle annular dark field scanning TEM (HAADF-STEM) imaging and the corresponding EDS elemental mapping (Figure 79a, Supporting Information) verify the uniform distribution of C, N, O, Cl, Mn, Zn, and Mo throughout 1. Additionally, local selected area electron diffraction (SAED) analysis (Figure 79b, Supporting Information) indicates its crystalline characteristic, and the d-spacing calculated from SAED is 4.83 nm^{-1}, which is indeed in line with the d-spacing value calculated from powder X-ray diffraction (pXRD), which is 4.40 nm^{-1} (Figure 79c, Supporting Information).

In addition, to examine the elemental distribution of Mn, Zn, Cl, and Mo of the bulk material, a small piece of 1, 2D micro X-ray fluorescence spectroscopy (2D-μXRF; resolution ≈25 μm) was employed. Homogeneous distribution of the four elements is reflected by similar intensities, i.e., coloring of the bulk material, notably within the selected area of (1 × 1) mm^2 in the bulk material as indicated by the green square (Figure 81a, Supporting Information). This becomes more obvious when assessing the intensity histograms that were generated for this area (Figure 81b, Supporting Information), displaying a normal distribution of intensities and no extreme values. The parameters of the intensity histograms are listed in (Table 27, Supporting Information), showing relative standard deviations of 9% to max. 20%. In order to investigate possible inhomogeneities in the element composition within the sample, the elemental intensity ratios were calculated along three exemplary lines, each 2.5 to 3.5 mm long. As illustrated in (Figure 82, Supporting Information), a constant elemental ratio with a spread width of less than 0.01 (see insert) was achieved in comparison to a spread width in the range of 2 for the background. Hence, high homogeneity in the elemental distribution and composition within the investigated sample is proven. In addition, EDX analyses showed the expected atomic metal ratios for Mn: Mo (calcd: 1: 6, obsd: 1: 5.6), confirming the presence of the two Anderson-metal components at the expected ratio.

In order to probe the porosity of 1, N_2 sorption studies were performed using Brunauer–Emmett–Teller (BET) and Barrett-Joyner–Halenda (BJH) analysis (Figure 75). 1 showed an IUPAC Type III isotherm (Figure 75a),[314] indicating weak interactions between the N_2 gas and the surface of 1. The BET surface area of 15.9

m^2g^{-1} and narrow pore size distribution with an average pore diameter of 11.5 nm (Figure 75b) is displayed by 1.

3.5.2.2 Oxidation of Benzyl alcohol, Furfuryl alcohol and Octanol

POMs have been widely investigated as catalysts for a range of organic oxidation reactions.[315–318] Anderson-type POMs in particular have proven to be efficient catalysts for alcohol oxidation reactions.[319–321] Therefore, we explored the selective heterogeneous oxidation of primary alcohols using benzyl alcohol, furfuryl alcohol, and octanol as substrates with *tert*-butyl hydroperoxide (*t*BuOOH) in decane as an oxidant to study the catalytic performance of 1. In brief, a typical experiment was performed using a stock solution of toluene-d_8 (9.8 mL) containing the corresponding alcohol (1 mmol), and *t*BuOOH (1 mmol), as well as 1 as a heterogeneous catalyst (10 mg). 1 mL of this reaction solution was added to catalytic vials, which were heated at 65 °C for a specific time. After the reaction, the catalyst was separated *via* centrifugation, and analysis of the products was performed by quantitative ^{1}H NMR spectroscopy (for experimental and characterization details, see Section 3.6.2.2 and Figure 83, Supporting Information). For benzyl alcohol oxidation, our data show that in the presence of 1, we observe significantly higher yields of benzaldehyde compared with the blank reference reaction (Figure 76a). Similarly, significantly higher furfural and octanal yields were observed in the presence of 1 catalyst (Figure 76b; Figure 84, Supporting Information) over time. These findings suggest that 1 shows higher performance for benzyl alcohol oxidation compared with furfuryl alcohol and octanol oxidation. This might be related to the more complex structure of furfuryl alcohol and octanol, and mechanistic studies are ongoing.

To further examine the activity of different catalysts under identical conditions, we opted to use benzyl alcohol as a test reaction. Significantly, lower yields of benzaldehyde were observed with various catalysts, whereas catalyst 1 showed a 30% yield of benzaldehyde after 48 h, highlighting that under the given reaction conditions, catalyst 1 is the superior catalyst (Table 28, Supporting Information, entries 1–4). Also, a controlled experiment without *t*BuOOH shows noticeably low benzaldehyde yield, signifying the role of the oxidant in the catalysis (Table 28, Supporting Information, entry 5).

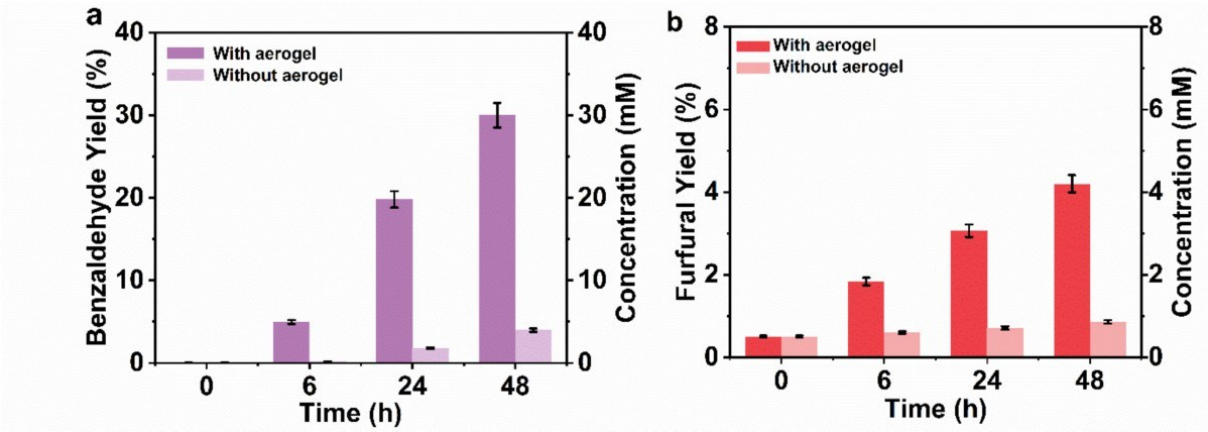

Figure 76: Catalytic oxidation of a) benzyl alcohol; b) furfuryl alcohol. Reaction conditions: catalyst: 1 (10 mg), solvent: toluene-d_8 (9.8 mL), substrate: benzyl alcohol, furfuryl alcohol (1 mmol), oxidant: *t*BuOOH (1 mmol). T = 65 °C.

The recyclability of 1 was investigated in four catalytic runs using the benzyl alcohol oxidation as a test reaction. After each run, the catalyst was separated from the reaction solution *via* centrifugation, washed twice with toluene and diethyl ether, and vacuum dried. Then, the dried catalyst was employed for the subsequent reaction batch. It was noticed that the catalyst can be recovered and reused at least 4 times without a major loss in its catalytic activity (Figure 85, Supporting Information). The observed reduction in benzaldehyde yield might be due to the loss of catalyst during the washing process, as well as the leaching of the catalyst.

3.5.2.3 Post-Catalytic Studies

Stability is one of the crucial parameters to evaluate the catalytic performance of a catalyst. Therefore, to gain insights into the stability of 1, we recovered the catalyst after 48 h of the reaction cycle of benzyl alcohol oxidation. The morphology and structural changes of 1 after catalysis were studied by SEM, FT-IR, and XPS. The SEM image of 1 (Figure 86c, Supporting Information) after catalysis displayed that the original layered structure was mostly maintained. Furthermore, the FT-IR spectrum of 1 (Figure 86a, Supporting Information) showed that the positions of characteristic bands of {$MnMo_6$} are retained. Deconvoluted XPS data (Figure 87, Supporting Information) revealed the retention of the elemental composition and oxidation states in 1. Moreover, the elemental composition (in at. %) of 1 was calculated from XPS, indicating the leaching of the catalyst (Table 29, Supporting Information). The results suggest that the structural and morphological features of 1 are maintained during catalytic runs.

3.5.2.4 Mechanistic Insights of the Gelation

It was observed that the addition of $ZnCl_2$ solution (in MeCN) to the {$MnMo_6$} solution (in MeCN) led to the immediate formation of a gel. A systematic investigation was conducted to understand the factors influencing the gel formation, such as POM type, metal salts used, solvent, etc. (for details see Section 3.6.2.3, Tables 21–25, Supporting Information). Attempts to replace $ZnCl_2$ with other metal cations, including transition metals, alkali, and alkaline earth metals, did not result in the formation of a stable gel. However, when $CoCl_2.6H_2O$ was used, we observed the formation of a gel that was unstable and showed syneresis (release of solvent from the gel) over the course of a day. A similar behaviour was observed when using $Zn(NO_3)_2.6H_2O$, however, syneresis occurred within a 15 min timeframe. Based on these analyses, we can state that formation of a stable gel under the given conditions is specific to $ZnCl_2$, and both Zn(II) as well as Cl^- are required to form the stable gel. Efforts to substitute acetonitrile with other protic and aprotic organic solvents showed that formation of gel particles was observed when benzonitrile was employed, suggesting that nitrile groups might be involved in the gelation process. Also, a variety of POM anions were tested; however, only the TRIS-bearing Anderson POM resulted in gelation.

3.5.3 Conclusion

In summary, we have demonstrated a facile approach to synthesize 1 based on TRIS-functionalized Anderson polyoxometalate anions as low molecular weight gelators when crosslinked with $ZnCl_2$ in acetonitrile. The resulting gel showed promising initial alcohol oxidation reactivity for benzyl alcohol and the bio-based furfuryl alcohol. Initial insights into the individual roles of POM anion, metal salt, and solvent are provided to guide the future development of this new class of POM-based porous catalyst.

3.6 Supplementary Information

3.6.1 Instrumentation

Attenuated total Reflectance-Fourier transform Infrared Spectroscopy (ATR-FTIR) was carried out on a Bruker Alpha II FTIR spectrophotometer containing a Diamond crystal ATR unit. Signals are presented as wave numbers in cm^{-1} using the following abbreviations: vs = very strong, s = strong, m = medium, w = weak and b = broad.

^{1}H-NMR spectroscopy ^{1}H spectra were recorded on Bruker AVANCE NEO 400 MHz Spectrometer equipped with 5mm inverse probe head operating at 400.13 MHz ^{1}H frequency at ambient temperature conditions. The ^{1}H spectra were recorded applying a 30º pulse averaging 32 scans with a 2 s recycle delay.

Thermogravimetric analysis (TGA) analysis was performed on METTLER TOLEDO TGA 2 STARe system at a heating rate of 10 K min^{-1} under air flow in a polycrystalline Al_2O_3 crucible in a temperature range of 30º to 650 ºC.

Brunauer-Emmett-Teller (BET) measurements were done on 3P Micro300 Surface area and Pore Size Analyzer to assess the surface area, pore volume, and size distribution of the sample at 77 K. The measurement was executed under vacuum with nitrogen gas as adsorbate. The pore size distribution was determined using the Barrett-Joyner-Halenda (BJH) method.

Powder X-ray diffraction (pXRD) data was carried out on a Bruker D2 Phaser instrument with CuKα radiation (λ=1.5406 Å).

CHN Elemental Analysis was performed by the central analytical service of the Department of Chemistry at Johannes Gutenberg University Mainz using an Elementar Vario EL Cube.

Scanning electron microscopy (SEM) images were collected using FEI-Nova NanoSEM 650 at an accelerating voltage of 15 kV.

Transmission electron microscopy (TEM) and scanning transmission electron microscopy (STEM) investigations of the sample were performed using a Thermofisher Talos 200 X microscope operated at an accelerating voltage of 120 kV and 200 kV. **Energy dispersive X-ray (EDX)** spectra and elemental maps were

acquired using a "Super-X" windowless 4-quadrant EDX detector. Prior to TEM analysis, the samples were first dispersed in ethanol *via* ultrasonication, and the resulting dispersion was then drop-cast on a copper TEM support grid with holey carbon film and allowed to dry. Quantification of EDX data (mappings, spectra, elemental ratios) was determined using the Velox software package (Thermofisher Scientific company) applying background subtraction and Schreiber-Wims k-Factor quantification.

Micro X-ray Fluorescence Spectroscopy (μXRF) was conducted using 2D micro-X-ray fluorescence spectrometer M4 Tornado (Bruker Nano GmbH, Berlin, Germany) equipped with a Rh X-ray tube. The polychromatic beam was focused *via* polycapillary lenses to a spot size of 25 μm. The instrument was operated at maximum power (50 kV, 600 μA) and reduced pressure (20 mbar). The X-ray fluorescence photons are detected by a XFlash 430-PA detector with an active area of 30 mm^2 and a resolution of <145 eV for Mn-K_α. No filters were applied for these measurements. A rectangular area - with a length of 4 mm and a width of 3 mm – including the complete sample piece was scanned using a dwell time of 10 ms per pixel corresponding to a resolution of approx. 25 μm. For homogeneity investigation, a piece of the aerogel sample was placed on an Ultralene ® foil (SPEX Sample Prep, Metuchen, NJ, USA) stretched on 31 mm open-ended X-cells (SPEX Sample Prep). The sample was covered with another stretched Ultralene ® foil to keep the sample in place, creating a kind of sandwich (see Figure 80a). Obtained elemental intensity data are presented as heat maps (Figure 81a) using Fiji software (1.54f 13/02/2025) for data visualization and fire lookup table and histograms for a selected area of 40 x 40 pixels (Figure 81b).[322] In addition, line scans with a line width of 1 pixel were evaluated (Figure 82) calculating the intensity ratios for elements Zn, Mo, Mn, and Cl.

X-ray photoelectron spectroscopy (XPS) measurements were done using a K-Alpha X-ray Photoelectron Spectrometer System (Thermo Fisher Scientific) with a monochromatic X-ray source (Al K_α) having a spot diameter of 400 μm and an electron detector with 0.5 eV energy resolution. An internal electron flood gun was used to compensate the potential surface charge due to electrically insulating species. The spectra were calibrated using the C 1s peak (284.6 eV) and fitted using Voigt functions after background subtraction.

3.6.2 Experimental Data

Commercially available reagents were purchased from Sigma Aldrich, TCI chemicals and Fischer Scientific. The materials were used as obtained without further purification unless stated otherwise. $(n\text{Bu}_4\text{N})_3[\text{MnMo}_6\text{O}_{18}\{(\text{OCH}_2)_3\text{CNH}_2\}_2]$ ($\{\text{MnMo}_6\}$) was synthesized as reported previously.[66]

3.6.2.1 Synthesis of Metallogel and Aerogel (1)

$(n\text{Bu}_4\text{N})_3[\text{MnMo}_6\text{O}_{18}\{(\text{OCH}_2)_3\text{CNH}_2\}_2]$ (= $\{\text{MnMo}_6\}$), (1 eq., 0.026 mmol, 49 mg) was dissolved in MeCN (1 mL) and $ZnCl_2$ (5 eq., 0.13 mmol, 18 mg) was dissolved in MeCN (1 mL). The $ZnCl_2$ solution was added to the $\{\text{MnMo}_6\}$ solution *via* syringe which led to the gel formation in *ca.* 10 seconds at ambient temperature. The prepared metallogel was freeze-dried at -84.3 ºC temperature and 223 µbar pressure for 24 h to give the final aerogel 1.

Yield (aerogel 1): 98% based on Mo.

FT-IR gel (in cm^{-1}): 1036 (v CO, s), 947 (v Mo=O, b), 920 (v Mo=O, s), 860 (m).

FT-IR 1 (in cm^{-1}): 1025 (v CO, s), 945 (v Mo=O, s), 920 (v Mo=O, s), 651 (v Mo-O-Mo, vs), 568 (w).

3.6.2.2 General procedure for Catalysis

The standard oxidation catalysis reaction system contained toluene-d_8 as a solvent, respective alcohol (benzyl alcohol, furfuryl alcohol, octanol) and *t*BuOOH (5.0-6.0 M in decane) as an oxidant. The stock solution was prepared with toluene-d_8 (9.8 mL), benzyl alcohol (1 mmol, 0.104 mL), furfuryl alcohol (1 mmol, 0.086 mL), or octanol (1 mmol, 0.188 mL) and *t*BuOOH (1 mmol, 0.096 mL). 1 mL of this mixture was added to reaction vials containing 1 (10 mg) and no 1 equipped with magnetic bars and were heated at 65 ºC. After specific interval of reaction time (6 h, 24 h, 48 h, and 120 h (for octanol)) mixture was cooled down to room temperature and centrifuged to separate the catalyst. The colourless reaction solution was quantitatively analysed *via* ^{1}H NMR spectroscopy. Note that, while performing the quantitative measurements, 1,3,5-trioxane (0.1 mmol, 9.0 mg) dissolved in toluene-d_8 (1 mL) was used as a reference compound.

3.6.2.3 Investigation of several parameters on gelation:

1 Effect of Concentration

Different amounts of $ZnCl_2$ and $\{MnMo_6\}$ were dissolved in the fixed amount of acetonitrile (0.5 mL). In the first experiment, the concentration of $\{MnMo_6\}$ was kept constant (0.026 M) and $ZnCl_2$ concentration was varied. Different equivalents of $ZnCl_2$ based on $\{MnMo_6\}$ were dissolved in acetonitrile. The effect of various equivalents is listed below in Table 21.

Table 21: Different equivalents of $ZnCl_2$ in 0.5 mL of acetonitrile and their effects on gelation after adding into $\{MnMo_6\}$ solution (0.026 M).

No.	$ZnCl_2$ (mg)	$ZnCl_2$ Concentration (mol/L)	Observation
1.	1.80	0.026	Viscosity increase, but still liquid sample.
2.	3.60	0.052	Higher viscosity than above case, still liquid.
3.	5.40	0.078	Gelation occurred in 2-3 h.
4.	7.10	0.104	Instantaneous gelation, but unstable gel formed.
5.	9.00	0.130	Mechanically stable gel formed instantaneously.
6.	10.80	0.156	Gelation occurred rapidly, but phase-separation into gel and liquid observed.
7.	12.60	0.182	Mechanically unstable gel formed.

In the second experiment, the $\{MnMo_6\}$ concentration was modified, whereas the $ZnCl_2$ concentration was kept constant (0.13 M). The influence of varying concentration of $\{MnMo_6\}$ is summarized in Table 22.

Table 22: Different equivalents of {$MnMo_6$} in 0.5 mL of acetonitrile and their effects on gelation after addition of $ZnCl_2$ solution (0.13 M).

No.	$MnMo_6$ (mg)	{$MnMo_6$} Concentration (mol/L)	Observation
1	10	0.0104	Rapid gelation; gel was liquefied after 2 h.
2	15	0.0156	Rapid gelation, but phase-separation (gel/liquid) after 2 h.
3	20	0.0208	Uneven gel was formed.
4	25	0.026	Mechanically Stable gel formed instantaneously.
5	30	0.0312	Stable gel formed instantaneously.
6	35	0.0364	Viscosity increased, but no gel formed.

In accordance with above results, 1 equivalent of {$MnMo_6$} and 5 equivalents of $ZnCl_2$ were chosen for the gelation experiment.

2 Screening of Solvent/Co-solvent

Since acetonitrile was employed as a solvent for gelation to take place, the consequence of other solvents was also checked to know if acetonitrile is necessary to form gel. The results are mentioned in Table 23, implying that properties of nitrile group are essential for gelation to take place.

Table 23: Utilization of various solvents and co-solvents for gel formation.

S.No.	Solvent/Co-solvent	Observations
1.	Water + MeCN	Precipitate was formed.
2.	Ethanol + MeCN	Formation of suspension.
3.	DMF	No gelation.
4.	Acetonitrile	Stable gel was formed.
5.	Benzonitrile	Uneven gel formation in few minutes.

3 Scope of using various metal salts

Several alkali, alkaline earth metal and transition metal salts were tested to know their behaviour towards gelation. In some cases, metal salts didn't dissolve in acetonitrile, so other solvents were used for dissolving the salts. The effect of exchanging the metal salt is tabulated in Table 24.

Table 24: Screening of different metal salts.

S.No.	Metal salt	Solvent Used	Observations
1.	$CaCl_2$	H_2O	White precipitate.
2.	$MgCl_2$	H_2O	Orange solution, no gel.
3.	NaCl	H_2O	Orange solution, no gel.
4.	KI	H_2O	Orange suspension, no gel.
5.	$NiCl_2.6H_2O$	MeOH	Light yellow suspension, no gel.
6.	$CoCl_2.6H_2O$	MeCN	Blue gel, took 2 h to form, liquified next day.
7.	$NiCl_2$	H_2O	Light green solution, no gel.
8.	$Cu(NO_3)_2$	MeCN	Gel formed rapidly, but liquified within 30 min.
9.	$FeCl_2$	H_2O	Dark orange suspension, no gel.
10.	$AgNO_3$	MeCN	Viscosity increased instantaneously, no gel.
11.	$Zn(NO_3)_2.6H_2O$	MeCN	Instant gelation, but liquified within 15 min.

4 Effect of Temperature

To examine the influence of temperature on gelation, the precursor solutions were prepared at different temperature conditions. At room temperature, evenly distributed gel was formed within 10 s. When both the solutions were heated at 60 ºC using water bath, followed by the addition of warmed $ZnCl_2$ to the warmed $\{MnMo_6\}$. This led to the formation of partial gelation, while rest of the sample remained in the liquid state. Even, the consistency did not change after cooling the sample at room temperature. In the other experiment, both the solutions were cooled to 0 ºC by using ice bath, when the $ZnCl_2$ was added to the $\{MnMo_6\}$, like the above-mentioned case partial gelation was seen, but still a lot of liquid was left behind. In contrast to the gel sample prepared by heating the precursors, the consistency of the sample was changed to even gel after being warmed up at room temperature. We speculate that for the pre-heated system,

because of more kinetic energy due to the higher temperature, molecules were moving rapidly so not all the acetonitrile molecules could be entrapped into the network, and after cooling to the room temperature entrapment of acetonitrile molecules was not possible anymore because of the already existing coordination network. On the other hand, for the pre-cooled system, the movement of molecules was deaccelerated because of low temperature and thus, network formation took longer time. However, warming up the sample to room temperature allowed the entrapment of remaining acetonitrile molecules because of incomplete network.

Furthermore, the gel formed at room temperature was exposed to post-heating and post-cooling temperature conditions to check its stability. When the gel was heated to the boiling point of acetonitrile, some syneresis was observed. While in the other experiment, the prepared gel sample was stored at -10 ºC for two weeks, and its consistency was not changed, but in the third week it started showing syneresis behaviour.

5 Use of Functionalized and unfunctionalized Polyoxometalates

The use of numerous functionalized and unfunctionalized POMs were explored to understand more about the role of polyoxometalate towards gelation and the results of which are indicated in Table 25.

Table 25: Effect of different POMs on gelation.

S.No.	POM	Observations	Gel
1.	$(n\text{Bu}_4\text{N})_4[\text{Mo}_8\text{O}_{26}]$	Solution turned green after addition of $ZnCl_2$.	✕
2.	$(n\text{Bu}_4\text{N})_3[\text{CoMo}_6\text{O}_{18}\{(\text{OCH}_2)_3\text{CNH}_2\}_2]/\{\text{CoMo}_6\}$	Light blue gel was formed immediately.	✓
3.	$(n\text{Bu}_4\text{N})_3[\text{FeMo}_6\text{O}_{18}\{(\text{OCH}_2)_3\text{CNH}_2\}_2]/\{\text{FeMo}_6\}$	Clear gel was obtained after 30 s.	✓
4.	$\{\text{CoMo}_6\}$ + $\{\text{FeMo}_6\}$	After 45 s, even green gel was formed.	✓
5.	$(n\text{Bu}_4\text{N})_3[\text{MnMo}_6\text{O}_{18}\{(\text{OCH}_2)_3\text{CCH}_3\}_2]$	No gel formed; mixture turned cloudy.	✕

6.	$(n\text{Bu}_4\text{N})_3[\text{MnMo}_6\text{O}_{18}\{(\text{OCH}_2)_3\text{CN=C}(\text{C}_6\text{H}_5)\}_2]$	Precipitate, but some gel particles were formed.	✕
7.	$(n\text{Bu}_4\text{N})_2[\text{V}_6\text{O}_{13}\{(\text{OCH}_2)_3\text{CNH}_2\}_2])$	Generation of precipitate.	✕

From the before mentioned results, it could be inferred that the presence of Anderson POM functionalized with TRIS functionality is essential for the gel formation. Findings also suggest that may be zinc coordinates to the binding sites of the nitrogen atom, as some gel was obtained with $[\text{MnMo}_6\text{O}_{18}\{(\text{OCH}_2)_3\text{CN=C}(\text{C}_6\text{H}_5)\}_2]^{-3}$. Another important factor for gelation seems to be the type of POM used, since no gel was formed with Lindqvist POM functionalized with TRIS. Although further screening is needed to find the possible reasons for these observations which could be the distance between binding sites in the POM, used addenda atoms, charge on the POM, or some other properties.

3.6.3 Characterization

1 TGA profile and CHN analysis

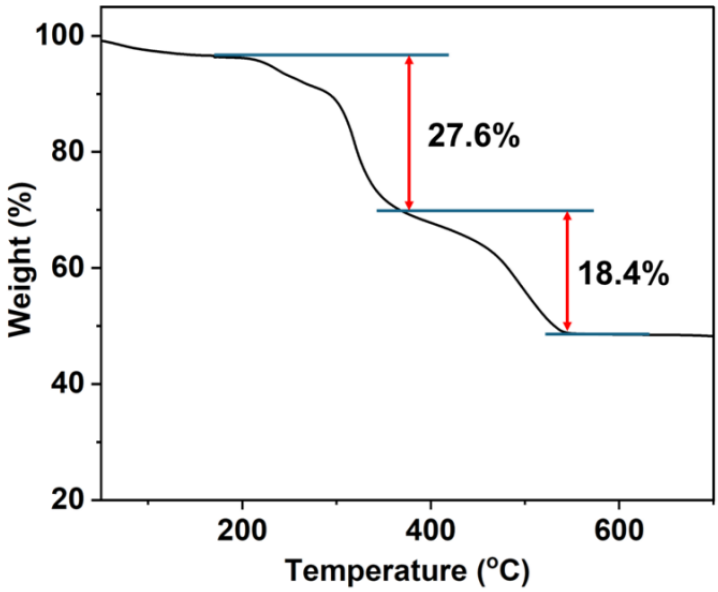

Figure 77: TGA measurement of 1, representing the weight loss associated with three $n\text{Bu}_4\text{N}^+$ cations (27.6%) and two TRIS ligands (18.4%) from 200 ºC to 555 ºC.[305]

Table 26: CHN Elemental Analysis of 1, verifying the amount of three nBu_4N^+ cations, two TRIS ligands.

Mass Percentage	Found	Calculated
%C	26.30	26.28
%H	5.07	4.87
%N	3.02	2.73

2 X-ray photoelectron spectroscopy

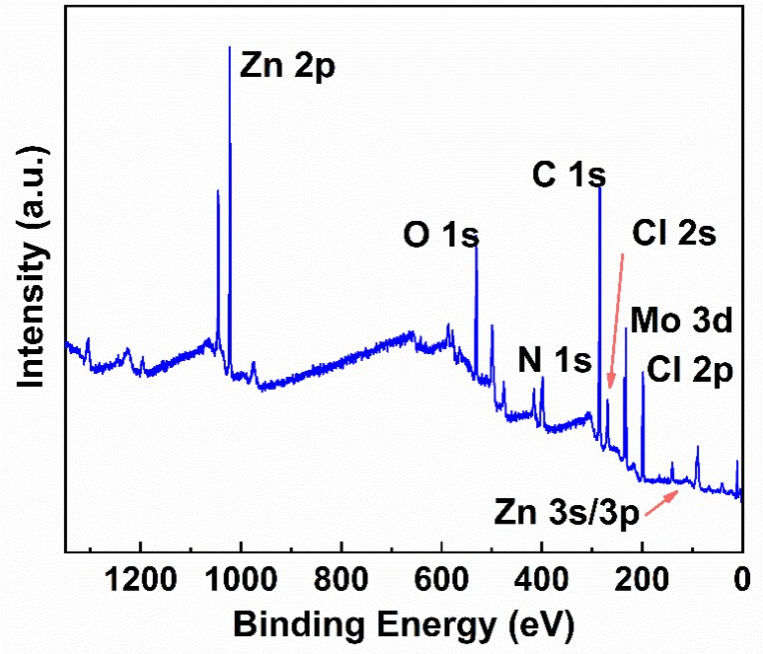

Figure 78: XP overview spectrum of 1.

3 Transmission Electron Microscopy (TEM) and powder X-ray diffraction (pXRD)

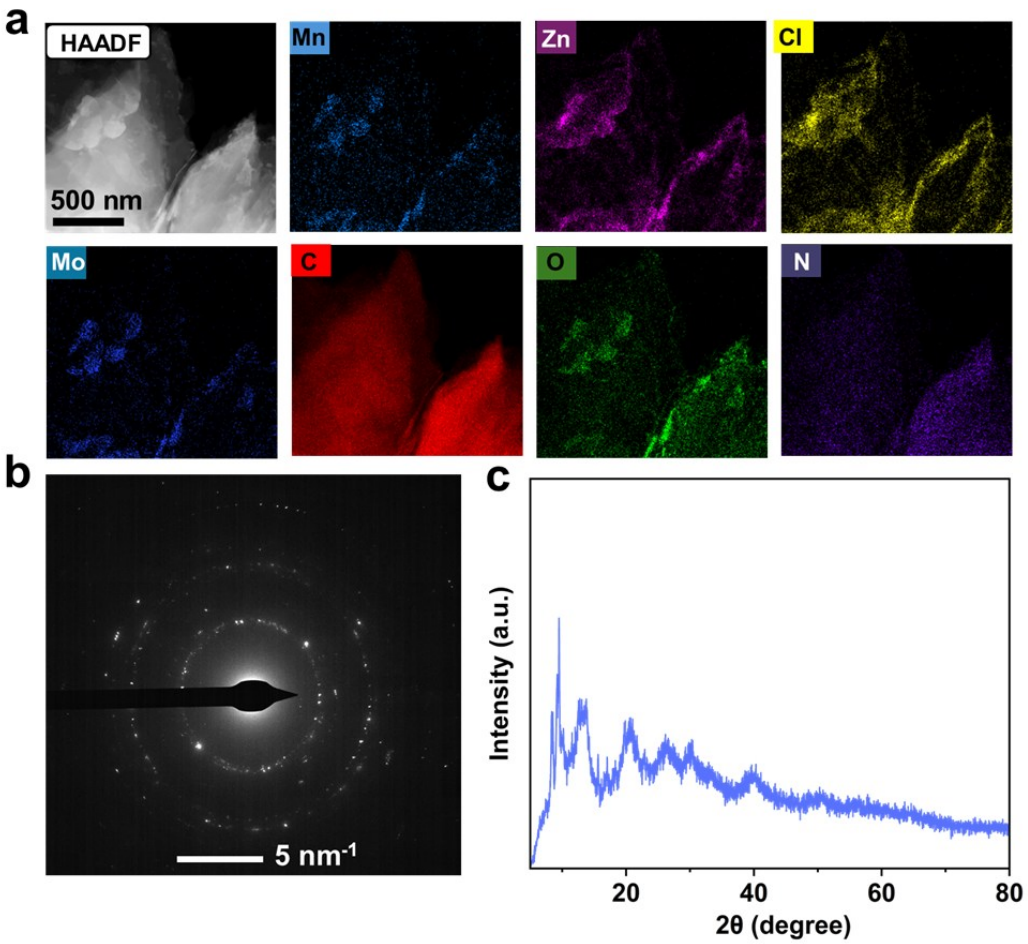

Figure 79: (a) HAADF-STEM image and corresponding elemental mapping of Mn, Zn, Cl, Mo, C, O and N elements (b) SAED pattern and (c) pXRD pattern of 1.

4 Micro-Xray-Fluorescence Spectroscopy

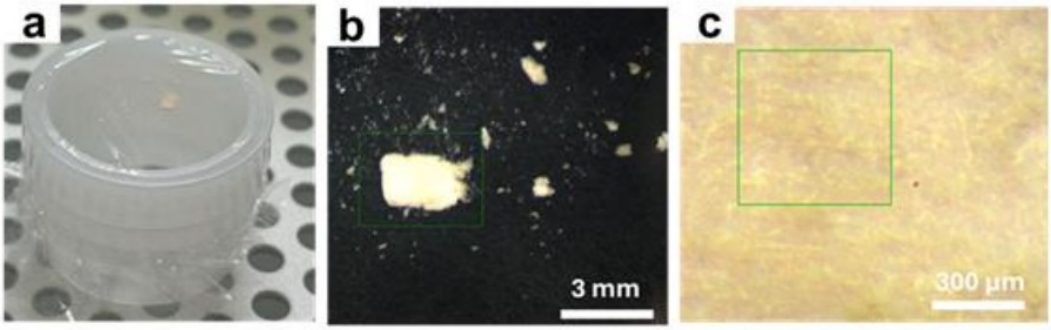

Figure 80: Images of (a) sample in foil sandwich measurement setup (b) measured sample in 10x magnification and (c) in 100x magnification for elemental distribution analysis using µXRF.

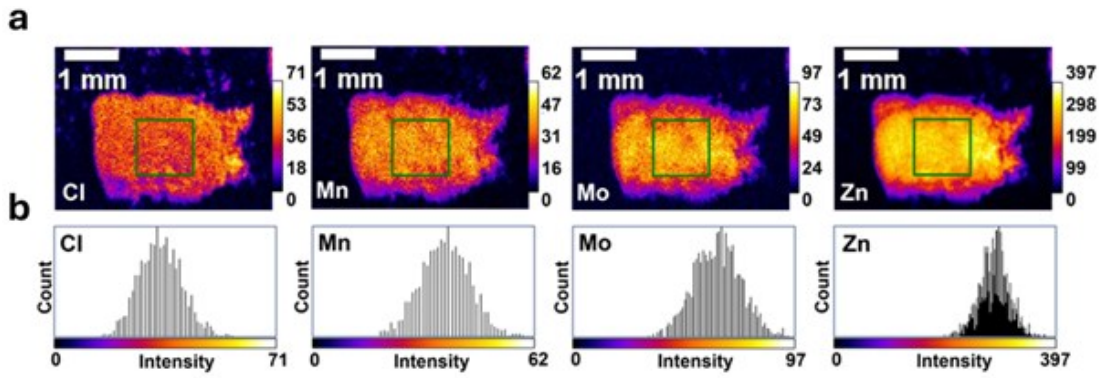

Figure 81: (a) Elemental distribution of Cl, Mn, Mo, Zn in 1 (Note: The reduced intensity at the outer edges of the samples is attributable to the thinner thickness of the sample towards the periphery) and (b) corresponding intensity histograms of a selected area (green square, 40x40 pixel, 1x1 mm, n=1600).

Table 27: Elemental distribution parameters derived from the intensity histograms (n=1600).

	Cl	Mn	Mo	Zn
Mean value	34	37	63	287
SD	7	7	10	27
Rel. SD	20%	19%	16%	9%
Min - Max	15-57	19-59	33-94	197-377

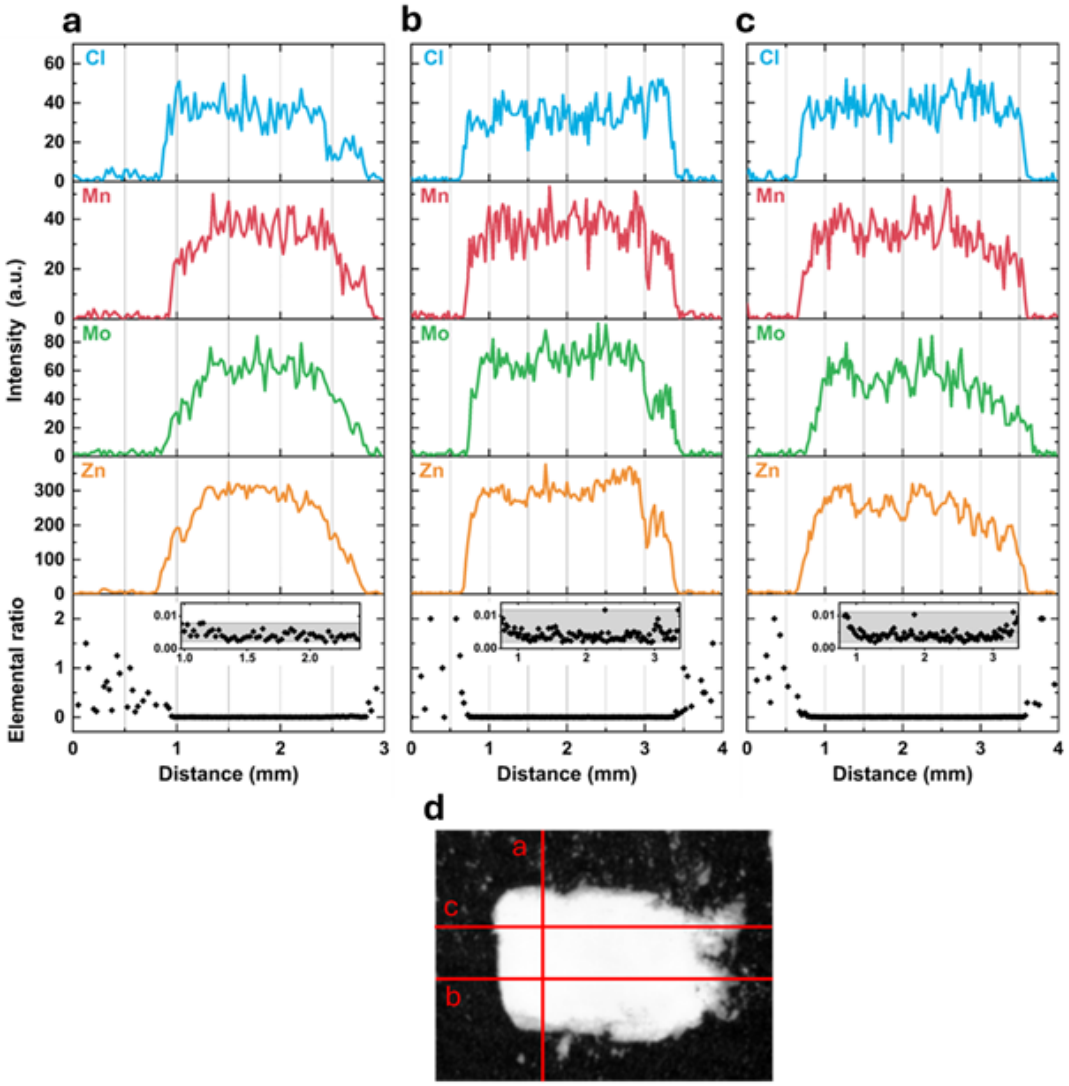

Figure 82: Evaluation of intensity ratios along exemplary lines (a), (b), and (c) as marked in (Figure 82d). (a-c) Line scans of the element intensities for Cl (blue), Mn (red), Mo (green), and Zn (orange) and resulting elemental ratios (black) with insets of the line scan (Zn/Mo/Mn/Cl). (d) Optical image of 1 with marked lines for intensity ratio evaluation.

5 Oxidation of alcohols

5.1 ^{1}H NMR

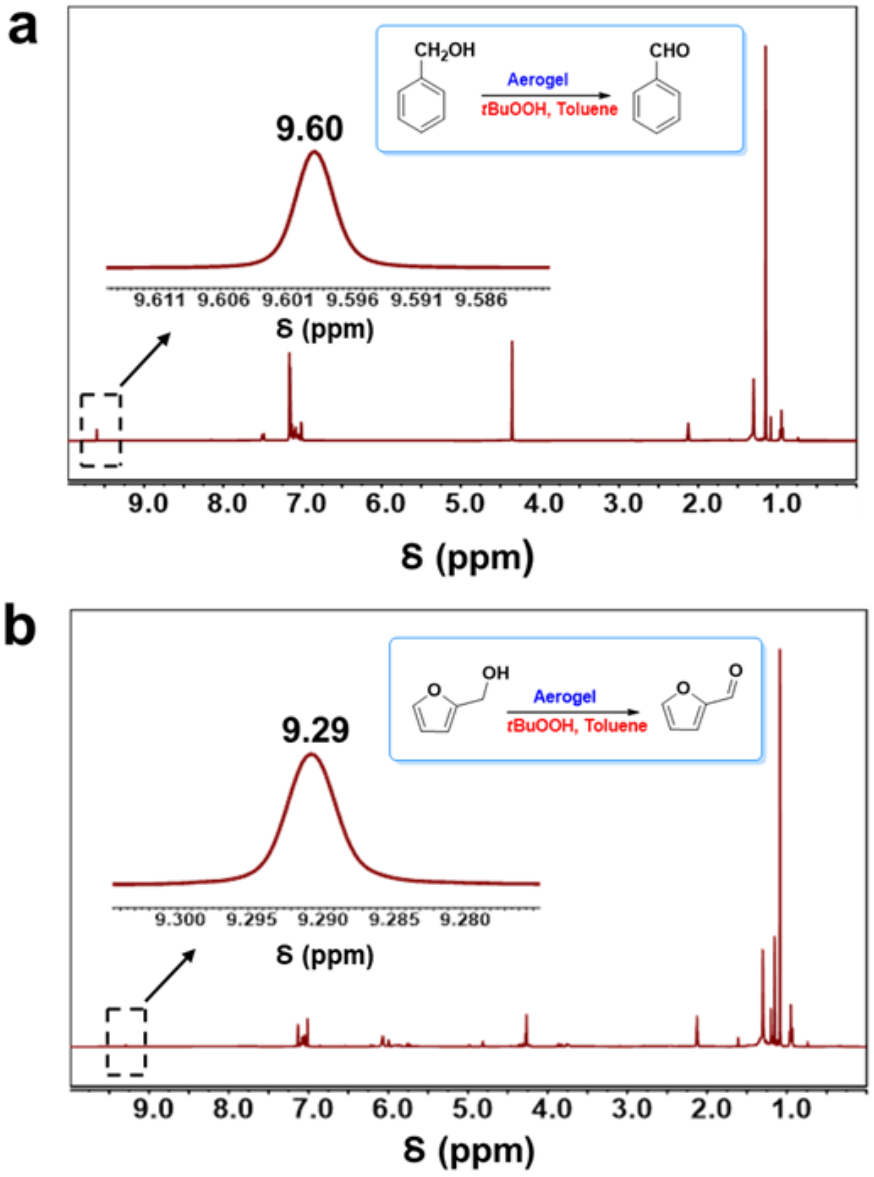

Figure 83: 1H NMR spectra for oxidation of (a) Benzyl alcohol (b) Furfuryl alcohol.

5.2 Catalytic oxidation of Octanol to Octanal

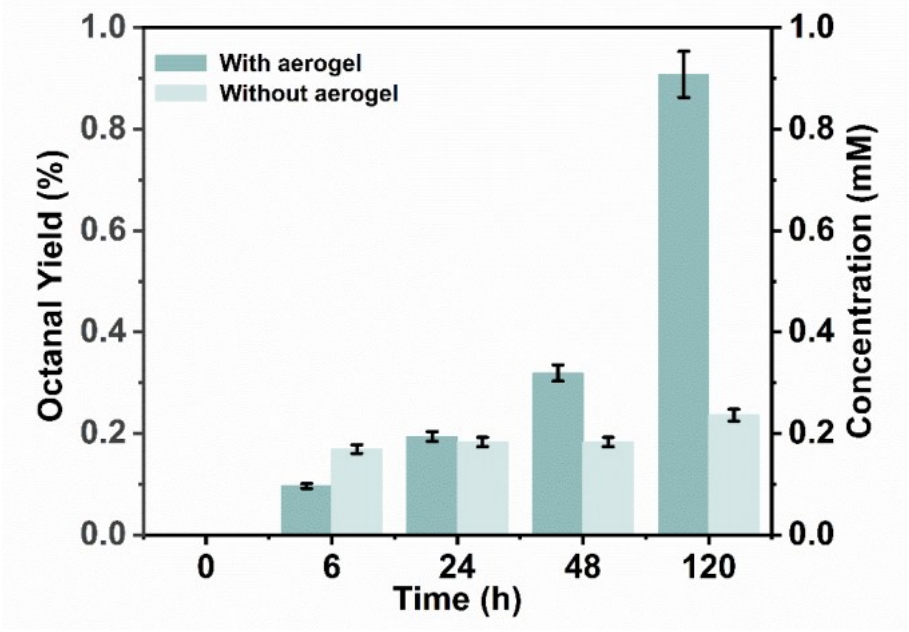

Figure 84: Catalytic oxidation of octanol. Reaction conditions: catalyst: 1 (10 mg), solvent: toluene-d8 (9.8 mL), octanol (1 mmol), oxidant: *t*BuOOH (1 mmol). T = 65ºC.

Table 28: Catalysts screening and effect of oxidant towards the benzyl alcohol oxidation.

Entry	Catalysts	Oxidising agent	% Yield of Benzaldehyde
1.	**1**	*t*BuOOH (in decane)	30%
2.	{$MnMo_6$}	*t*BuOOH (in decane)	21.0%
3.	$ZnCl_2$	*t*BuOOH (in decane)	2.5%
4.	$K_3PW_{12}O_{40}$	*t*BuOOH (in decane)	0.7%
5.	**1**	-	0.3%

Reaction conditions: catalyst: (10 mg), solvent: toluene-d_8 (9.8 mL), substrate: benzyl alcohol (1 mmol), oxidant: *t*BuOOH (1 mmol). *T* = 65ºC, 48 h.

6 Recyclability and Reusability Tests

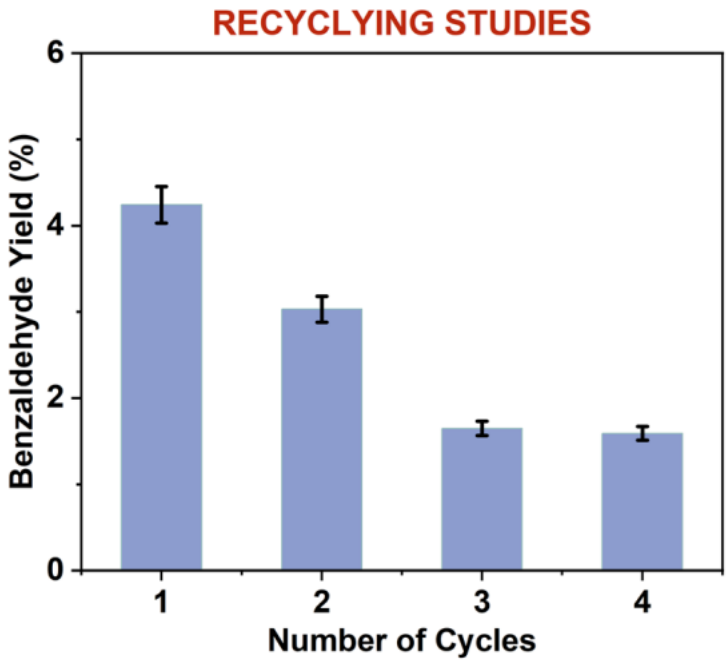

Figure 85: Recovery and reuse of 1 for benzaldehyde formation.

7. Post catalytic studies

7.1 FT-IR and SEM

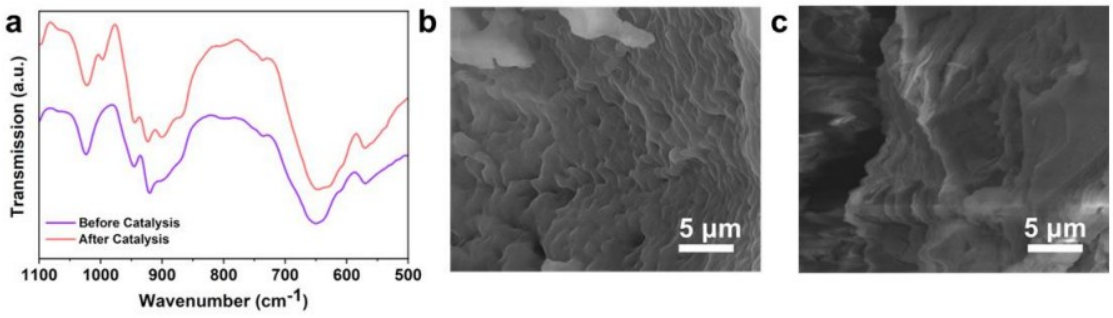

Figure 86: (a) FT-IR spectra (b) and (c) SEM images of 1 before and after catalysis respectively.

7.2 XP-spectra

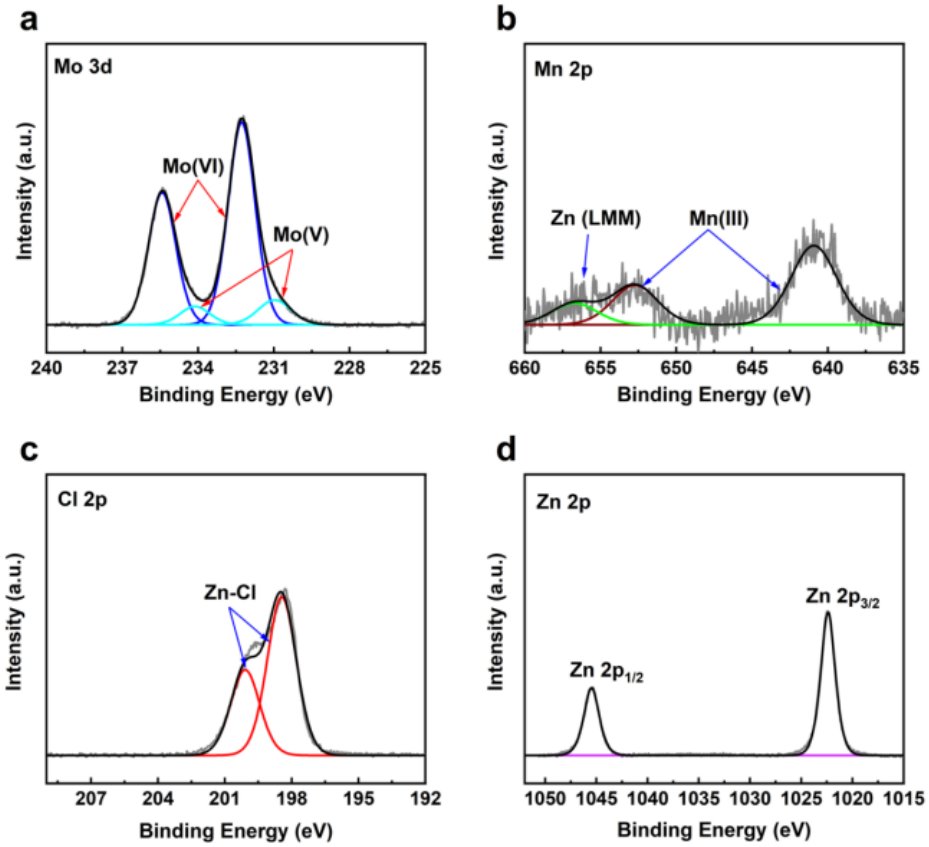

Figure 87: Post-catalytic deconvoluted high-resolution (a) Mo 3d (b) Mn 2p (c) Cl 2p (d) Zn 2p XP spectra of 1.

Table 29: Comparison of elemental composition in 1 before and after catalysis.

Element	Before catalysis (at.%)	After catalysis (at.%)
C	59.3	66.2
O	15.3	13.7
N	3.4	3.2
Cl	10.7	7.6
Zn	7.7	4.6
Mn	0.6	0.5
Mo	3.0	2.6

Acknowledgements

This work was funded by the Deutsche Forschungsgemeinschaft *via* the Transregio SFB TRR 234 “CataLight”, projects no A4, B3, B7, B8, Z2 (project no: 364549901) and the SFB 1633 “PCET” (project no:510228793). S. A. C. and D.A. gratefully acknowledge financial support from the Alexander von Humboldt Foundation. C.S. gratefully acknowledges financial support from the Top-Level Research Area SunInnoScience and the Gutenberg Research College. The authors gratefully acknowledge Daniel Hönders and Prof. Andreas Walther, JGU Mainz, for instrumental access. Open access funding enabled and organized by Projekt DEAL.

The data that support the findings of this study are openly available in zenodo.org at https://doi.org/10.5281/zenodo.15771544, reference number 15771544.

Conflict of Interest

The authors declare no conflict of interest.

Authors Contributions

G. Sachdeva	Data curation, formal analysis, methodology, project administration, and writing original draft
S. Maloul	Data curation and formal analysis
J. Zolg	Data curation and formal analysis
R. Müller	Data curation, formal analysis, and methodology
M. Mondeshki	Data curation and formal analysis
E. Ebrahimi	Data curation and formal analysis
D. Abid	Data curation and formal analysis
S.A. Chala	Data curation, formal analysis, and methodology
C. Neumann	Formal analysis
A. Turchanin	Formal analysis, funding acquisition, and investigation
J. Biskupek	Formal analysis
U. Kaiser	Data curation, formal analysis, funding acquisition
K. Leopold	Funding acquisition, investigation, and methodology
C. Streb	Conceptualization, formal analysis, funding acquisition, methodology, supervision, and writing – original draft

Modifications for the Dissertation

This chapter is based on an article published under the Creative Commons Attribution 4.0 International License (CC BY 4.0). Minor modifications were made for integration into the dissertation. Specifically, the abstract was removed, the numbering of figures, tables and references and the notation of the POM was standardized (e.g., $MnMo_6$ has been modified to $\{MnMo_6\}$). No other changes were made.

4 Summary and Perspective

Anderson polyoxometalates are one of the most interesting candidates in the POM family. Their flexible topological structure and ability to undergo functionalization with organic ligands to yield hybrid materials make them unique materials for various applications. Therefore, within this work, strategies to build Anderson POM-based hybrids for homogeneous light-driven HER are presented. Additionally, the formation of POM-based aerogel and its use as a heterogeneous catalyst for oxidation catalysis was investigated.

4.1 A new strategy for the design of symmetric and asymmetric Anderson POM hybrids for Photocatalytic HER

The use of tris-ligands and their derivatives having different reactive groups is a well-known approach for forming hybrid Anderson POMs. Based on this strategy, rigid organofunctionalized polyoxomolybdates were first synthesized using a triol ligand bearing bpy-coordinating sites. These sites were further used to attach a Pt(II) complex, yielding mono- and bis-functionalized Anderson dyads through a stoichiometry-controlled complexation. Analytical techniques such as NMR spectroscopy, MALDI-TOF, and XPS were employed to characterize the synthesized symmetric and asymmetric dyads. Furthermore, single-crystal X-ray diffraction showed the successful formation of the di-functionalized species. The resulting dyads were then examined as catalysts for light-driven HER when coupled with a $[Ru(bpy)_3]^{2+}$ photosensitizer in the presence of TEA as an electron donor and water as a proton source. Under these conditions, initial catalytic results showed that TONs of *ca.* 345 were achieved by the mono-functionalized complex, whereas the di-functionalized complex exhibited *ca.* 451 TONs. This result demonstrates that the number of Pt sites present in the catalyst controls the HER activity. However, the obtained TONs increased by 30%, not by 100% as expected theoretically. Additionally, preliminary post-catalytic analysis revealed the partial degradation of the PS under photocatalytic conditions, as changes in the MLCT transitions were observed.

Overall, this study reveals that the HER activity of the catalysts is governed by the variation in the number of Pt HER sites. Further insights into the observed catalytic TONs will be gained by mechanistic photophysical and theoretical studies. The asymmetric functionalization approach provides a route to incorporate two different

components on opposite sides of the Anderson POM, thus enabling multiple functions to be combined within a single hybrid molecule.

4.2 Photosensitizer-polyoxometalate-catalyst triad for light-driven hydrogen evolution

To extend the concept of asymmetric functionalization of Anderson POMs, we demonstrated the formation of a photosensitizer-polyoxometalate-catalyst triad through a two-step approach. First, the HER-active Pt catalyst was anchored to one binding site of the bpy-functionalized Anderson-type POM, and then the cyclometalated Ir photosensitizer was attached to the second site to afford Ir-POM-Pt. The successful functionalization of the triad was supported by FT-IR, 1D and 2D NMR, UV-Vis spectroscopy, MALDI-TOF, and XPS. In the presence of an electron donor and a proton source, the molecular triad produced hydrogen with TONs of *ca.* 200 after 24 h of continuous irradiation. Under similar reaction conditions, the non-covalent system showed significantly lower TONs, highlighting the significance of covalent attachment in the triad. Moreover, to investigate the formation of Pt colloids during photocatalysis, elemental mercury was added to the catalytic solution prior to irradiation. The results indicated that, even in the presence of elemental mercury, a notable amount of hydrogen was produced. This suggests that the hydrogen evolution from Pt colloids is unlikely. SEM-EDX analysis further supported this by showing a homogeneous distribution of elements, while no Pt colloids were observed. Initial post-catalytic UV-Vis spectroscopic analysis revealed the partial degradation of the PS over time. Further, time-dependent emission spectroscopic results suggested the formation of reduced species of the ligands during photocatalysis.

Mechanistic photophysical studies indicated that the established charge-separated state is directed towards the Pt catalytic center, i.e., $Ir^{\bullet+}$-POM-$Pt^{\bullet-}$. DFT calculations further supported that the electron density shifts from the Ir PS toward the Pt center. In addition, the simulated and experimental TA spectra demonstrated the population of a charge-transfer state at longer delay times.

In conclusion, we successfully presented the formation of a POM-based photoactive triad by incorporating two different functionalities onto a single POM unit. This study provides a basis for designing molecular POM hybrids with light-harvesting and catalytic entities attached in a single framework. Future studies will focus on replacing

noble metal complexes with noble-metal-free alternatives; for example, Pt-based catalysts could be replaced with thiomolybdates, which are known as effective HER catalysts.

4.3 Organofunctionalized Anderson POMs as building block for aerogel formation

POM-based aerogels have gained considerable interest because POM clusters introduce additional properties into the materials. However, the conversion of purely POM-containing metallogels to aerogels has not yet been achieved. To address this, we showed how a {$MnMo_6$}-based organogel can be converted into a catalytically active aerogel. First, the POM-based organogel was prepared within 10 s by adding an acetonitrile solution of $ZnCl_2$ to an acetonitrile solution of {$MnMo_6$}. The obtained organogel was then converted into an aerogel by freeze-drying. A range of parameters such as metal salt, solvent, POM type, and temperature was explored to understand the factors affecting gelation. FT-IR spectroscopy was used to follow the transformation of {$MnMo_6$} into organogel and aerogel. Furthermore, the aerogel was characterized by FT-IR, TGA, XPS, electron microscopy, and 2D-μXRF techniques. Surface area and pore diameter of the aerogel were determined by BET and BJH analyses. To explore the catalytic activity of the aerogel, the selective heterogeneous oxidation of benzyl alcohol, bio-based furfuryl alcohol, and octanol was investigated. Initial data showed notably higher yields of benzaldehyde, furfural, and octanal in the presence of the aerogel catalyst compared to control experiments. Furthermore, it was shown that the catalyst can be recycled and reused at least 4 times, with partial loss of its activity possibly due to washing processes and leaching of the catalyst over time. The layered morphology and characteristic band positions of the aerogel were preserved during the catalytic runs, as confirmed by SEM and FT-IR spectroscopy. Further, post-catalytic XPS measurements showed retention of both the oxidation state and elemental composition within the aerogel.

In summary, a novel approach to access POM-based aerogels was demonstrated by converting a POM metallogel into an aerogel using a scalable freeze-drying procedure. Insights into the role of metal salt, the type of POM, and solvent are presented to develop more POM-based porous catalysts for various applications. Furthermore, to expand the use of organofunctionalized Anderson POMs and metal salts for the

formation of POM-based metallogels. We utilized a pyridine functionalized Anderson POM as a gelator molecule for gelation with hydrous $CoCl_2$ in acetonitrile. This led to the formation of precipitates instead of a metallogel. These initial findings indicate that other factors such as concentration, temperature, and solvent should be optimized in the future.

5 References

[1] J. Wang, W. Azam, *Geosci. Front.* **2024**, *15*, 101757.

[2] S. Wolf, R. Bullard, J. J. Buonocore, N. Donley, T. Farrelly, J. Fleming, D. J. X. González, N. Oreskes, W. Ripple, R. Saha, M. D. Willis, *Oxford Open Climate Change* **2025**, *5*,1-26.

[3] M. Höök, X. Tang, *Energy Policy* **2013**, *52*, 797–809.

[4] C. W. Su, X. Y. Song, J. Dou, M. Qin, *Renew. Energy* **2025**, *238*, 121950.

[5] M. K. G. Deshmukh, M. Sameeroddin, D. Abdul, M. Abdul Sattar, *Mater. Today Proc.* **2023**, *80*, 1756–1759.

[6] B. Hussain, K. Batool, S. A. A. Naqvi, A. A. Nassani, S. Ali, *Appl. Energy* **2025**, *390*, 124847.

[7] N. Sazali," *Int. J. Hydrog. Energy* **2020**, *45*, 18753–18771.

[8] E. Abbasian Hamedani, S. A. Alenabi, S. Talebi, *Energy Rep.* **2024**, *12*, 3778–3794.

[9] N. F. Guerrero-Rodríguez, D. A. De La Rosa-Leonardo, R. Tapia-Marte, F. A. Ramírez-Rivera, J. Faxas-Guzmán, A. B. Rey-Boué, E. Reyes-Archundia, *Sustainability* **2024**, *16*, 5569.

[10] E. Herzinger, M. Wolf, *Chem. Ing. Tech.* **2024**, *96*, 65–73.

[11] N. Kannan, D. Vakeesan, *Renew. Sustain. Energ. Rev.* **2016**, *62*, 1092–1105.

[12] D. R. Whang, D. H. Apaydin, *ChemPhotoChem* **2018**, *2*, 148–160.

[13] S. Berardi, S. Drouet, L. Francàs, C. Gimbert-Suriñach, M. Guttentag, C. Richmond, T. Stoll, A. Llobet, *Chem. Soc. Rev.* **2014**, *43*, 7501–7519.

[14] J. Barber, P. D. Tran, *J. R. Soc. Interface,* **2013**, *10***,** 20120984.

[15] C. Wang, M. P. O'Hagan, B. Willner, I. Willner, *Chem. Eur. J.* **2022**, *28*, e202103595.

[16] V. Balzani, A. Credi, M. Venturi, **2008**,*1*, 26–58.

[17] J. Alemán, A. V. Chadwick, J. He, M. Hess, K. Horie, R. G. Jones, P. Kratochvíl, I. Meisel, I. Mita, G. Moad, S. Penczek, R. F. T. Stepto, *Pure Appl. Chem.* **2007**, *79*, 1801–1829.

[18] G. Kickelbick, N. Hüsing, *Monatsh. Chem.* **2006**, *137*, 5–8.

[19] P. Gomez-Romero, A. Pokhriyal, D. Rueda-García, L. N. Bengoa, R. M. González-Gil, *Chem. Mater.* **2024**, *36*, 8–27.

[20] M. Faustini, L. Nicole, E. Ruiz-Hitzky, C. Sanchez, *Adv. Funct. Mater.* **2018**, *28*, 1–30.

[21] G. L. Drisko, C. Sanchez, *Eur. J. Inorg. Chem.* **2012**, *2012*, 5097–5105.

[22] C. Sanchez, F. Ribot, B. Lebeau, *J. Mater. Chem.* **1999**, *9*, 35–44.

[23] C. Sanchez, B. Julián, P. Belleville, M. Popall, *J. Mater. Chem.* **2005**, *15*, 3559–3592.

[24] J. J. Berzelius, *Ann. Phys.* **1826**, *82*, 369–392.

[25] J.F. Keggin, *Nature* **1933**, *132*, 351.

[26] J. F. Keggin, *Proc. R. Soc. London A* **1934**, *144*, 75–100.

[27] C. Streb, in *Structure and Bonding in Molecular Vanadium Oxides: From Templates via Host–Guest Chemistry to Applications*, in: *Polyoxometalate Based Assemblies and Functional Materials* (Ed.: YF. Song), Springer, Cham, **2017**, pp. 31–47.

[28] A. Bijelic, A. Rompel, *ChemTexts* **2018**, *4*, 1–27.

[29] M. T. Pope, in *Introduction to Polyoxometalate Chemistry*, in *Polyoxometalate Molecular Science*, Springer, Dordrecht **2003**, pp. 3–31.

[30] A. Müller, S. Roy, *Coord. Chem. Rev.* **2003**, *245*, 153–166.

[31] L. C. W. Baker, D. C. Glick, *Chem. Rev.* **1998**, *98*, 3–49.

[32] D. L. Long, R. Tsunashima, L. Cronin, *Angew. Chem. Int. Ed.* **2010**, *49*, 1736–1758.

[33] D. L. Long, E. Burkholder, L. Cronin, *Chem. Soc. Rev.* **2007**, *36*, 105–121.

[34] D. L. Long, L. Cronin, *Chem. Eur. J.* **2006**, *12*, 3698–3706.

[35] H. N. Miras, L. Vilà-Nadal, L. Cronin, *Chem. Soc. Rev.* **2014**, *43*, 5679–5699.

[36] X. Su, S. Li, L. Yan, *Inorg. Chem.* **2023**, *62*, 15673–15679.

[37] S. Greiner, B. Schwarz, C. Streb, M. Anjass, *Chem. Eur. J.* **2021**, *27*, 13435–13441.

[38] A. Müller, E. Krickemeyer, J. Meyer, H. Bögge, F. Peters, W. Plass, E. Diemann, S. Dillinger, F. Nonnenbruch, M. Randerath, C. Menke, *Angew. Chem. Int. Ed.* **1995**, *34*, 2122–2124.

[39] A. Müller, E. Krickemeyer, H. Bögge, M. Schmidtmann, F. Peters, *Angew. Chem. Int. Ed.* **1998**, *37*, 3359–3363.

[40] M. Ammam, *J. Mater. Chem. A* **2013**, *1*, 6291–6312.

[41] K. Li, S. Liu, J. Niu, J. Wang, *Chem. Commun.* **2026**, 1800–1819.

[42] A. Misra, C. Zambrzycki, G. Kloker, A. Kotyrba, M. H. Anjass, I. Franco Castillo, S. G. Mitchell, R. Güttel, C. Streb, *Angew. Chem. Int. Ed.* **2020**, *59*, 1601–1605.

[43] Y. Zhang, Y. Li, H. Guo, Y. Guo, R. Song*Mater. Chem. Front.* **2023**, *8*, 732–768.

[44] A. Bijelic, M. Aureliano, A. Rompel, *Angew. Chem. Int. Ed.* **2019**, *58*, 2980–2999.

[45] J. M. Clemente-Juan, E. Coronado, A. Gaita-Ariñoa, *Chem. Soc. Rev.* **2012**, *41*, 7464–7478.

[46] Y. Ji, L. Huang, J. Hu, C. Streb, Y. F. Song, *Energy Environ. Sci.* **2015**, *8*, 776–789.

[47] H. N. Miras, J. Yan, D. L. Long, L. Cronin, *Chem. Soc. Rev.* **2012**, *41*, 7403–7430.

[48] W. D. Yu, Y. Zhang, Y. Y. Han, B. Li, S. Shao, L. P. Zhang, H. K. Xie, J. Yan, *Inorg. Chem.* **2021**, *60*, 3980–3987.

[49] T. Yamase, M. Suzuki, K. Ohtaka, *Dalton Trans.* **1997**, *44*, 2463–2472.

[50] N. I. Gumerova, A. Rompel, *Chem. Soc. Rev.* **2020**, *49*, 7568–7601.

[51] L. V. Nadal, A. Rodríguez-Fortea, L. K. Yan, E. F. Wilson, L. Cronin, J. M. Poblet, *Angew. Chem. Int. Ed.* **2009**, *48*, 5452–5456.

[52] E. F. Wilson, H. N. Miras, M. H. Rosnes, L. Cronin, *Angew. Chem. Int. Ed.* **2011**, *50*, 3720–3724.

[53] J. J. Hastings, O. W. Howarth, *Dalton Trans.* **1992**, *1992*, 209–215.

[54] S. Himeno, T. Katsuta, M. Takamoto, M. Hashimoto, *Bull. Chem. Soc. Jpn.* **2006**, *79*, 100–105.

[55] A. Misra, K. Kozma, C. Streb, M. Nyman, *Angew. Chem. Int. Ed.* **2020**, *59*, 596–612.

[56] C. Zhao, H. Ma, H. Pang, S. Li, Y. Yu, T. Yu, Z. Zhang, *J. Coord. Chem.* **2014**, *67*, 2820–2829.

[57] J. M. Cameron, D. J. Wales, G. N. Newton, *Dalton Trans.* **2018**, *47*, 5120–5136.

[58] M. A. Moussawi, S. Floquet, P. A. Abramov, C. Vicent, M. Haouas, E. Cadot, *Inorg. Chem.* **2018**, *57*, 56–63.

[59] A. Patel, N. Narkhede, S. Singh, S. Pathan, *Catal. Rev. Sci. Eng.* **2016**, *58*, 337–370.

[60] K. Suzuki, F. Tang, Y. Kikukawa, K. Yamaguchi, N. Mizuno, *Angew. Chem. Int. Ed.* **2014**, *53*, 5356–5360.

[61] J. X. Liu, X. B. Zhang, Y. L. Li, S. L. Huang, G. Y. Yang, *Coord. Chem. Rev.* **2020**, *414*, 213260.

[62] A. Jimbo, C. Li, K. Yonesato, T. Ushiyama, K. Yamaguchi, K. Suzuki, *Chem. Sci.* **2023**, *14*, 10280–10284.

[63] A. V. Anyushin, A. Kondinski, T. N. Parac-Vogt, *Chem. Soc. Rev.* **2020**, *49*, 382–432.

[64] C. Li, N. Mizuno, K. Yamaguchi, K. Suzuki, *J. Am. Chem. Soc.* **2019**, *141*, 7687–7692.

[65] C. Li, K. Yamaguchi, K. Suzuki, *Angew. Chem.* **2021**, *133*, 7036–7040.

[66] P. R. Marcoux, B. Hasenknopf, J. Vaissermann, P. Gouzerh, *Eur. J. Inorg. Chem.* **2003**, 2406–2412.

[67] G. Kalandia, C. L. Liu, D. E. Salazar Marcano, M. A. Moussawi, S. Bleus, B. Van Meerbeek, W. Dehaen, T. N. Parac-Vogt, *Angew. Chem. Int. Ed.* **2025**, *64*, e202420773.

[68] A. Dolbecq, E. Dumas, C. R. Mayer, P. Mialane, *Chem. Rev.* **2010**, *110*, 6009–6048.

[69] D. E. Salazar Marcano, G. Kalandia, M. A. Moussawi, K. Van Hecke, T. N. Parac-Vogt, *Chem. Sci.* **2023**, *14*, 5405–5414.

[70] G. Izzet, A. Macdonell, C. Rinfray, M. Piot, S. Renaudineau, E. Derat, B. Abécassis, C. Afonso, A. Proust, *Chem. Eur. J.* **2015**, *21*, 19010–19015.

[71] J.S. Anderson, *Nature* **1937**, *140*, 850–850.

[72] H.T. Evans, *J. Am. Chem. Soc.* **1948**, *70*, 1291–1292.

[73] P. Wu, Y. Wang, B. Huang, Z. Xiao, *Nanoscale* **2021**, *13*, 7119–7133.

[74] A. Blazevic, A. Rompel, *Coord. Chem. Rev.* **2016**, *307*, 42–64.

[75] X. X. Li, X. Ma, W. X. Zheng, Y. J. Qi, S. T. Zheng, G. Y. Yang, *Inorg. Chem.* **2016**, *55*, 8257–8259.

[76] J. Zhang, J. Luo, P. Wang, B. Ding, Y. Huang, Z. Zhao, J. Zhang, Y. Wei, *Inorg. Chem.* **2015**, *54*, 2551–2559.

[77] E. Hampson, J. M. Cameron, S. Amin, J. Kyo, J. A. Watts, H. Oshio, G. N. Newton, *Angew. Chem. Int. Ed.* **2019**, *58*, 18281–18285.

[78] J. M. Cameron, G. Guillemot, T. Galambos, S. S. Amin, E. Hampson, K. Mall Haidaraly, G. N. Newton, G. Izzet, *Chem. Soc. Rev.* **2022**, *51*, 293–328.

[79] C. Yvon, A. Macdonell, S. Buchwald, A. J. Surman, N. Follet, J. Alex, D. L. Long, L. Cronin, *Chem. Sci.* **2013**, *4*, 3810–3817.

[80] E. Al-Sayed, A. Blazevic, A. Roller, A. Rompel, *Chem. Eur. J.* **2015**, *21*, 17800–17807.

[81] S. Cetindere, H. Ardic Alidagi, M. Anjass, *Inorg. Chim. Acta* **2023**, *545*, 121280.

[82] A. Blazevic, E. Al-Sayed, A. Roller, G. Giester, A. Rompel, *Chem. Eur. J.* **2015**, *21*, 4762–4771.

[83] A. J. Li, S. L. Huang, G. Y. Yang, *Dalton Trans.***2023**, *52*, 18133–18136.

[84] T. S. Teets, D. G. Nocera, *Chem. Commun.* **2011**, *47*, 9268–9274.

[85] E. Deponti, M. Natali, *Dalton Trans.* **2016**, *45*, 9136–9147.

[86] E. Amouyal, *Sol. Energy Mater. Sol. Cells* **1995**, *38*, 249–276.

[87] J. Corredor, M. J. Rivero, C. M. Rangel, F. Gloaguen, I. Ortiz, *J. Chem. Technol. Biotechnol.* **2019**, *94*, 3049–3063.

[88] G. Knör, *Coord. Chem. Rev.* **2015**, *304–305*, 102–108.

[89] J. Bai, J. Wang, H. Zheng, X. Zhao, P. Wu, L. Pei, J. Wang, *Small* **2023**, *19*, 1–8.

[90] A. Inagaki, M. Akita, *Coord. Chem. Rev.* **2010**, *254*, 1220–1239.

[91] S. Mandal, S. Yoosefi, A. K. Mengele, S. Rau, A. Pannwitz, *Inorg. Chem. Front.* **2024**, *11*, 7682–7755.

[92] C. Lin, W. Xiang, G. Wang, Z. Yang, *Int. J. Hydrog.Energy* **2021**, *46*, 34298–34304.

[93] D. Kim, V. Q. Dang, T. S. Teets, *Chem. Sci.* **2023**, *15*, 77–94.

[94] J. H. Shon, T. S. Teets, *ACS Energy Lett.* **2019**, *4*, 558–566.

[95] Y. Wu, D. Kim, T. S. Teets, *Synlett* **2022**, *33*, 1154–1179.

[96] L. Ivanová, J. Truksa, K. Kim, D.R. Whang, B. S. Shim, J. Krajčovič, *ACS Omega* **2026**, *11*, 23670–23690.

[97] D. Hanss, J. C. Freys, G. Bernardinelli, O. S. Wenger, *Eur. J. Inorg. Chem.* **2009**, 4850–4859.

[98] L. Wang, *Catalysts* **2022**, *12*, 919.

[99] A. Juris, V. Balzani, F. Barigelletti, S. Campagna, P. Belser, A. von Zelewsky, *Coord. Chem. Rev.* **1988**, *84*, 85–277.

[100] S. Ladouceur, E. Zysman-Colman, *Eur. J. Inorg. Chem.* **2013**, *2013*, 2985–3007.

[101] H. Rao, W. Q. Yu, H. Q. Zheng, J. Bonin, Y. T. Fan, H. W. Hou, *J. Power Sources* **2016**, *324*, 253–260.

[102] J. Amaro-Gahete, M. V. Pavliuk, H. Tian, D. Esquivel, F. J. Romero-Salguero, S. Ott, *Coord. Chem. Rev.* **2021**, *448*, 214172.

[103] B. B. Beyene, C. H. Hung, *Sustain. Energy Fuels* **2018**, *2*, 2036–2043.

[104] C. Lentz, O. Schott, T. Auvray, G. S. Hanan, B. Elias, *Dalton Trans.* **2019**, *48*, 15567–15576.

[105] C. Kasahara, M. K. Farh, K. Rediger, P. Buday, S. Gräfe, M. Micheel, S. Kupfer, M. Wächtler, W. Weigand, *Cell Rep. Phys. Sci.* **2025**, *6*, 102975.

[106] H. Ozawa, K. Sakai, *Chem. Commun.* **2011**, *47*, 2227–2242.

[107] K. Sakai, H. Ozawa, *Coord. Chem. Rev.* **2007**, *251*, 2753–2766.

[108] M. G. Pfeffer, T. Kowacs, M. Wächtler, J. Guthmuller, B. Dietzek, J. G. Vos, S. Rau, *Angew. Chem. Int. Ed.* **2015**, *54*, 6627–6631.

[109] H. Ozawa, K. Sakai, *Chem. Lett.* **2007**, *36*, 920–921.

[110] H. Ozawa, M. A. Haga, K. Sakai, *J. Am. Chem. Soc.* **2006**, *128*, 4926–4927.

[111] K. Kitamoto, K. Sakai, *Chem. Commun.* **2016**, *52*, 1385–1388.

[112] K. Kitamoto, K. Sakai, *Angew. Chem.* **2014**, *126*, 4706–4710.

[113] D. R. Whang, S. Y. Park, *ChemSusChem* **2015**, *8*, 3204–3207.

[114] C. Streb, *Dalton Trans.* **2012**, *41*, 1651–1659.

[115] M. D. Tzirakis, I. N. Lykakis, M. Orfanopoulos, *Chem. Soc. Rev.* **2009**, *38*, 2609–2621.

[116] S. S. Wang, G. Y. Yang, *Chem. Rev.* **2015**, *115*, 4893–4962.

[117] X. Liu, Y. Li, S. Peng, G. Lu, S. Li*Int. J. Hydrog. Energy* **2012**, *37*, 12150–12157.

[118] A. Harriman, K. J. Elliott, M. A. H. Alamiry, L. Le Pieux, M. Séverac, Y. Pellegrin, E. Blart, C. Fosse, C. Cannizzo, C. R. Mayer, F. Odobel, *J. Phys. Chem. C* **2009**, *113*, 5834–5842.

[119] N. Queyriaux, M. Wächtler, C. Cariño, S. Alves, B. Dietzek-Ivanšić, V. Artero, A. Proust, M. Chavarot-Kerlidou, G. Izzet, *Chem.Commun.* **2025**, *61*, 9682–9685.

[120] W. Wang, L. M. Chamoreau, G. Izzet, A. Proust, M. Orio, S. Blanchard, *J. Am. Chem. Soc.* **2023**, *145*, 12136–12147.

[121] F. Odobel, M. Séverac, Y. Pellegrin, E. Blart, C. Fosse, C. Cannizzo, C. R. Mayer, K. J. Elliott, A. Harriman, *Chem. Eur. J.* **2009**, *15*, 3130–3138.

[122] K. J. Elliott, A. Harriman, L. Le Pleux, Y. Pellegrin, E. Blart, C. R. Mayer, F. Odobel, *Phys. Chem. Chem. Phys.* **2009**, *11*, 8767–8773.

[123] B. Matt, S. Renaudineau, L. M. Chamoreau, C. Afonso, G. Izzet, A. Proust, *J. Org. Chem.* **2011**, *76*, 3107–3112.

[124] B. Matt, X. Xiang, A. L. Kaledin, N. Han, J. Moussa, H. Amouri, S. Alves, C. L. Hill, T. Lian, D. G. Musaev, G. Izzet, A. Proust, *Chem. Sci.* **2013**, *4*, 1737–1745.

[125] B. Matt, J. Fize, J. Moussa, H. Amouri, A. Pereira, V. Artero, G. Izzet, A. Proust, *Energy Environ. Sci.* **2013**, *6*, 1504–1508.

[126] S. Schönweiz, S. A. Rommel, J. Kübel, M. Micheel, B. Dietzek, S. Rau, C. Streb, *Chem. Eur. J.* **2016**, *22*, 12002–12005.

[127] S. Schönweiz, M. Heiland, M. Anjass, T. Jacob, S. Rau, C. Streb, *Chem. Eur. J.* **2017**, *23*, 15370–15376.

[128] H. Lv, J. Song, Y. V. Geletii, J. W. Vickers, J. M. Sumliner, D. G. Musaev, P. Kögerler, P. F. Zhuk, J. Bacsa, G. Zhu, C. L. Hill, *J. Am. Chem. Soc.* **2014**, *136*, 9268–9271.

[129] I. C. M. S. Santos, S. L. H. Rebelo, M. S. S. Balula, R. R. L. Martins, M. M. M. S. Pereira, M. M. Q. Simões, M. G. P. M. S. Neves, J. A. S. Cavaleiro, A. M. V. Cavaleiro, *J. Mol. Catal. A Chem.* **2005**, *231*, 35–45.

[130] C. Costa-Coquelard, S. Sorgues, L. Ruhlmann, *J. Phys. Chem. A* **2010**, *114*, 6394–6400.

[131] T. E. Keyes, E. Gicquel, L. Guerin, R. J. Forster, V. Hultgren, A. M. Bond, A. G. Wedd, *Inorg. Chem.* **2003**, *42*, 7897–7905.

[132] M. K. Seery, L. Guerin, R. J. Forster, E. Gicquel, V. Hultgren, A. M. Bond, A. G. Wedd, T. E. Keyes, *J. Phys. Chem. A* **2004**, *108*, 7399–7405.

[133] H. Lv, J. Song, H. Zhu, Y. V. Geletii, J. Bacsa, C. Zhao, T. Lian, D. G. Musaev, C. L. Hill, *J. Catal.* **2013**, *307*, 48–54.

[134] H. Lv, W. Guo, K. Wu, Z. Chen, J. Bacsa, D. G. Musaev, Y. V Geletii, S. M. Lauinger, T. Lian, C. L. Hill, *J. Am. Chem. Soc.* **2014**, *136*, 14015–14018.

[135] S. Maloul, M. Van Den Borg, C. Müller, L. Zedler, A. K. Mengele, D. Gaissmaier, T. Jacob, S. Rau, B. Dietzek-Ivanšić, C. Streb, *Chem. Eur. J.* **2021**, *27*, 16846–16852.

[136] X. Wang, X. Bai, H. Lin, J. Sun, X. Wang, G. Liu, *RSC Adv.* **2018**, *8*, 22676–22686.

[137] M. Piot, S. Hupin, H. Lavanant, C. Afonso, L. Bouteiller, A. Proust, G. Izzet, *Inorg. Chem.* **2017**, *56*, 8490–8496.

[138] X. X. Li, Y. X. Wang, R. H. Wang, C. Y. Cui, C. Bin Tian, G. Y. Yang, *Angew. Chem. Int. Ed.* **2016**, *55*, 6462–6466.

[139] S. Favette, B. Hasenknopf, J. Vaissermann, P. Gouzerh, C. Roux, *Chem.Commun.* **2003**, 2664–2665.

[140] F. C. Li, L. K. Tan, X. L. Li, H. J. Kong, L. M. Ge, L. Y. Yue, L. F. Han, *Dalton Trans.* **2019**, *48*, 5831–5841.

[141] Z. An, X. Li, Z. Zhang, X. Wang, *Inorg. Chem.* **2024**, *63*, 19956–19963.

[142] D. K. Smith, *Angew. Chem. Int. Ed.* **2025**, *137*, e202502053.

[143] N. M. Sangeetha, U. Maitra, *Chem. Soc. Rev.* **2005**, *34*, 821–836.

[144] J. Yu, X. Chen, Y. Yang, X. Zhao, X. Chen, T. Jing, Y. Zhou, J. Xu, Y. Zhang, Y. Cheng, *J. Mater. Chem. B* **2020**, *8*, 3058–3063.

[145] M. M. Piepenbrock, G. O. Lloyd, N. Clarke, J. W. Steed, *Chem. Rev.* **2010**, *110*, 1960–2004.

[146] E. R. Draper, D. J. Adams, *Chem* **2017**, *3*, 390–410.

[147] M. Tautz, J. Torras, S. Grijalvo, R. Eritja, C. Saldías, C. Alemán, D. D. Díaz, *RSC Adv.* **2019**, *9*, 20841–20851.

[148] J. W. Steed, *Chem. Soc. Rev.* **2010**, *39*, 3686–3699.

[149] D. J. Adams, *Macromol. Biosci.* **2011**, *11*, 160–173.

[150] S. Dong, Y. Luo, X. Yan, B. Zheng, X. Ding, Y. Yu, Z. Ma, Q. Zhao, F. Huang, *Angew. Chem. Int. Ed.* **2011**, *50*, 1905–1909.

[151] M. Xiong, C. Wang, G. Zhang, D. Zhang, M. Xiong, C. Wang, G. Zhang, D. Zhang, in *Functional Molecular Gels* (Eds.: B. Escuder, J. F. Miravet), The Royal Society of Chemistry, Cambridge 2013, pp. 67–94.

[152] X. Yang, G. Zhang, D. Zhang, *J. Mater. Chem.* **2012**, *22*, 38–50.

[153] T. Jiao, in *Supramolecular gels: materials and emerging applications* (Ed.: T. Jiao), Wiley-VCH, **2021**, pp. 1-262.

[154] H. Wu, J. Zheng, A. L. Kjøniksen, W. Wang, Y. Zhang, J. Ma, *Adv. Mater.* **2019**, *31*, 1–23.

[155] B. O. Okesola, D. K. Smith, *Chem. Soc. Rev.* **2016**, *45*, 4226–4251.

[156] S. Kimura, K. Adachi, Y. Ishii, T. Komiyama, T. Saito, N. Nakayama, M. Yokoya, H. Takaya, S. Yagai, S. Kawai, T. Uchihashi, M. Yamanaka, *Nat. Commun.* **2025**, *16*, 1–13.

[157] M. S. Centellas, M. Piot, R. Salles, A. Proust, L. Tortech, D. Brouri, S. Hupin, B. Abécassis, D. Landy, C. Bo, G. Izzet, *Chem. Sci.* **2020**, *11*, 11072–11080.

[158] S. S. Sonu, N. Rai, I. Chauhan, *J. Sol-Gel Sci. Technol.* **2023**, *105*, 324–336.

[159] R. C. Walker, A. E. Potochniak, A. P. Hyer, J. K. Ferri, *Adv. Colloid Interface Sci.* **2021**, *295*, 102464.

[160] B. Mishra, S. Varshney, M. K. Gupta, P. Jagadeesh, M. R. Sanjay, S. Siengchin, *Int. J. Biol. Macromol.* **2025**, *328*, 147701.

[161] I. Smirnova, P. Gurikov, *J. Supercrit. Fluids* **2018**, *134*, 228–233.

[162] Y. Liu, J. Liu, P. Song, *Sustain. Mater. Technol.* **2021**, *27*, e00240.

[163] S. J. Wang, H. Bu, H. J. Chen, T. Hu, W. Z. Chen, J. H. Wu, H. J. Hu, M. Z. Lin, Y. Li, G. B. Jiang, *Chem. Eng. J.* **2020**, *399*, 125760.

[164] N. Luengo, A. Ciruela-Zunzunegui, M. Perfecto-Irigaray, O. Castillo, P. Ferrer, M. A. van Spronsen, S. Pérez-Yáñez, G. Beobide, *Inorg. Chem.* **2025**, *64*, 25089–25104.

[165] P. Xue, S. Zhou, G. Li, D. Wen, *Chem. Commun.* **2025**, *61*, 4774–4783.

[166] C. Jalkh, C. Ghazaly, H. El-Rassy, *Mater. Chem. Phys.* **2020**, *252*, 123296.

[167] R. Al-Oweini, S. Aghyarian, H. El-Rassy, *J. Sol-Gel Sci. Technol.* **2012**, *61*, 541–550.

[168] C. Dong, X. Liu, Z. Li, K. Guo, C. Song, Y. Zhang, M. Zhang, F. Ma, F. Rosei, X. Zhang, X. Huang, *Adv. Funct. Mater.* **2025**, *35*, 1–9.

[169] F. Yahya, H. El-Rassy, G. Younes, R. Al-Oweini, *Int. J. Environ. Anal. Chem.* **2019**, *99*, 1375–1396.

[170] A. Proust, B. Matt, R. Villanneau, G. Guillemot, P. Gouzerh, G. Izzet, *Chem. Soc. Rev.* **2012**, *41*, 7605–7622.

[171] J. J. Walsh, A. M. Bond, R. J. Forster, T. E. Keyes, *Coord. Chem. Rev.* **2016**, *306*, 217–234.

[172] M. J. Woźniak-Budych, K. Staszak, A. Bajek, F. Pniewski, R. Jastrząb, M. Staszak, B. Tylkowski, K. Wieszczycka, *Coord. Chem. Rev.* **2023**, *493*, 215306.

[173] L. Qin, C. Zhao, L. Y. Yao, H. Dou, M. Zhang, J. Xie, T. C. Weng, H. Lv, G. Y. Yang, *CCS Chem.* **2022**, *4*, 259–271.

[174] D. Schaming, C. Allain, R. Farha, M. Goldmann, S. Lobstein, A. Giraudeau, B. Hasenknopf, L. Ruhlmann, *Langmuir* **2010**, *26*, 5101–5109.

[175] S. Amthor, S. Knoll, M. Heiland, L. Zedler, C. Li, D. Nauroozi, W. Tobaschus, A. K. Mengele, M. Anjass, U. S. Schubert, B. Dietzek-Ivanšić, S. Rau, C. Streb, *Nat. Chem.* **2022**, *14*, 321–327.

[176] G. Toupalas, J. Karlsson, F. A. Black, A. Masip-Sánchez, X. López, Y. Ben M'Barek, S. Blanchard, A. Proust, S. Alves, P. Chabera, I. P. Clark, T. Pullerits, J. M. Poblet, E. A. Gibson, G. Izzet, *Angew. Chem. Int. Ed.* **2021**, *60*, 6518–6525.

[177] S. Cetindere, S. T. Clausing, M. Anjass, Y. Luo, S. Kupfer, B. Dietzek, C. Streb, *Chem. Eur. J.* **2021**, *27*, 17181–17187.

[178] F. A. Black, A. Jacquart, G. Toupalas, S. Alves, A. Proust, I. P. Clark, E. A. Gibson, G. Izzet, *Chem. Sci.* **2018**, *9*, 5578–5584.

[179] A. Winter, P. Endres, E. Schröter, M. Jäger, H. Görls, C. Neumann, A. Turchanin, U. S. Schubert, *Molecules* **2019**, *24*, 4446.

[180] Y. Luo, S. Maloul, P. Endres, S. Schönweiz, C. Ritchie, M. Wächtler, A. Winter, U. S. Schubert, C. Streb, B. Dietzek, *Sustain. Energy Fuels* **2020**, *4*, 4688–4693.

[181] Q. Zhuang, Z. Sun, C. G. Lin, B. Qi, Y. F. Song, *Inorg. Chem. Front.* **2023**, *10*, 1695–1711.

[182] M. H. Rosnes, C. Musumeci, C. P. Pradeep, J. S. Mathieson, D. L. Long, Y. F. Song, B. Pignataro, R. Cogdell, L. Cronin, *J. Am. Chem. Soc.* **2010**, *132*, 15490–15492.

[183] M. M. Zhang, Y. A. Yin, W. J. Chen, C. G. Lin, Y. Wei, Y. F. Song, *Inorg. Chem. Front.* **2022**, *10*, 1712–1720.

[184] Y. Luo, S. Maloul, M. Wächtler, A. Winter, U. S. Schubert, C. Streb, B. Dietzek, *Chem. Commun.* **2020**, *56*, 10485–10488.

[185] A. Winter, P. Endres, N. Singh, N. E. Schlörer, H. Görls, S. Kupfer, U. S. Schubert, *Inorganics* **2025**, *13*, 1–15.

[186] M. G. Pfeffer, B. Schäfer, G. Smolentsev, J. Uhlig, E. Nazarenko, J. Guthmuller, C. Kuhnt, M. Wächtler, B. Dietzek, V. Sundström, S. Rau, *Angew. Chem. Int. Ed.* **2015**, *54*, 5044–5048.

[187] M. Lämmle, A. K. Mengele, G. E. Shillito, S. Kupfer, S. Rau, *Chem. Eur. J.* **2023**, *29*, e202202722.

[188] T. Pawlak, L. Pazderski, J. Sitkowski, L. Kozerski, E. Szłyk, *Magn. Reson. Chem.* **2011**, *49*, 59–64.

[189] R. Evans, G. Dal Poggetto, M. Nilsson, G. A. Morris, *Anal. Chem.* **2018**, *90*, 3987–3994.

[190] R. Evans, Z. Deng, A. K. Rogerson, A. S. McLachlan, J. J. Richards, M. Nilsson, G. A. Morris, *Angew. Chem. Int. Ed.* **2013**, *52*, 3199–3202.

[191] Estimation of Diffusion Coefficients, https://nmr.chemistry.manchester.ac.uk/?q=node/432, (accessed 2025-10-01).

[192] B. Hasenknopf, R. Delmont, P. Herson, P. Gouzerh, *Eur. J. Inorg. Chem.* **2002**, 1081–1087.

[193] A. Solé-Daura, Y. Benseghir, M. H. Ha-Thi, M. Fontecave, P. Mialane, A. Dolbecq, C. Mellot-Draznieks, *ACS Catal.* **2022**, *12*, 9244–9255.

[194] Y. Luo, S. Maloul, S. Schönweiz, M. Wächtler, C. Streb, B. Dietzek, *Chem. Eur. J.* **2020**, *26*, 8045–8052.

[195] S. Ikegami, A. Yagasaki, *Materials* **2009**, *2*, 869–875.

[196] A. Winter, C. Ulbricht, E. Holder, N. Risch, U. S. Schubert, *Aust. J. Chem.* **2006**, *59*, 773–782.

[197] R. K. Harris, E. D. Becker, S. M. Cabral De Menezes, R. Goodfellow, P. Granger, *Concepts Magn. Reson. Part A Bridg. Educ. Res.* **2002**, *14*, 326–346.

[198] D. J. H. Cant, J. M. Gorham, C. A. Clifford, A. G. Shard, *Surf. Interface Anal.* **2025**, *57*, 148–152.

[199] International Standardization Organization, Surface Chemical Analysis - Auger Electron Spectroscopy and X-Ray Photoelectron Spectroscopy - Guide to the Use of Experimentally Determined Relative Sensitivity Factors for the Quantitative Analysis of Homogeneous Materials. ISO 18118:2024, Vernier, 2024.

[200] A. G. Shard, B. P. Reed, D. J. H. Cant, *Surf. Interface Anal.* **2025**, *57*, 389–395.

[201] R. W. W. Hooft, COLLECT - *Data Collection Software*, Nonius B.V., Delft, The Netherlands, 1998.

[202] Z. Otwinowski, W. Minor, in *Processing of X-ray diffraction data collected in oscillation mode, in Methods in Enzymology Macromolecular Crystallography (Part A)*, (Eds.: C. W. Carter, R. M. Sweet), Academic Press, London & Oxford, **1997**, pp. 307-326.

[203] G. M. Sheldrick, SADABS - Version 2.10, University of Göttingen, Göttingen, Germany, 2002

[204] G. M. Sheldrick, *Acta Crystallogr. A* **2015**, *71*, 3–8.

[205] G. M. Sheldrick, *Acta Crystallogr. C Struct. Chem.* **2015**, *71*, 3–8.

[206] A. L. Spek, *Acta Crystallogr. C Struct. Chem.* **2015**, *71*, 9–18.

[207] C. F. Macrae, P. R. Edgington, P. McCabe, E. Pidcock, G. P. Shields, R. Taylor, M. Towler, J. Van De Streek, *J. Appl. Crystallogr.* **2006**, *39*, 453–457.

[208] D. Kowalczyk, P. Li, A. Abbas, J. Eichhorn, P. Buday, M. Heiland, A. Pannwitz, F. H. Schacher, W. Weigand, C. Streb, D. Ziegenbalg, *ChemPhotoChem* **2022**, 6, e202200044.

[209] CCDC 2484790: Experimental Crystal Structure Determination, 2025, DOI: 10.5517/ccdc.csd.cc2pdmj8.

[210] X. Ji, J. Wang, Y. Kang, L. Mei, Z. Su, S. Wang, G. Ma, J. Shi, S. Zhang, *ACS Catal.* **2018**, 8, 10732–10745.

[211] M. R. A. Bhuiyan, *Micro Nano Lett.* **2022**, *17*, 402–416.

[212] M. M. Hossain Bhuiyan, Z. Siddique, *Int. J. Hydrogen Energy* **2025**, *102*, 1026–1044.

[213] J. A. Martens, *Front. Sci.* **2024**, *2*, 3–5.

[214] K. L. Bren, *Interface Focus* **2015**, *5*, 1–12.

[215] Y. Pellegrin, F. Odobel, *Coord. Chem. Rev.* **2011**, *255*, 2578–2593.

[216] M. Brändlin, B. Pfund, O. S. Wenger, *Nat. Chem.* **2025**, *17*, 1777–1784.

[217] C. Lentz, O. Schott, T. Auvray, G. Hanan, B. Elias, *Inorg. Chem.* **2017**, *56*, 10875–10881.

[218] G. F. Manbeck, E. Fujita, K. J. Brewer, *J. Am. Chem. Soc.* **2017**, *139*, 7843–7854.

[219] T. A. White, B. N. Whitaker, K. J. Brewer, *J. Am. Chem. Soc.* **2011**, *133*, 15332–15334.

[220] S. Tschierlei, M. Karnahl, M. Presselt, B. Dietzek, J. Guthmuller, L. González, M. Schmitt, S. Rau, J. Popp, *Angew. Chem. Int. Ed.* **2010**, *49*, 3981–3984.

[221] A. Fihri, V. Artero, M. Razavet, C. Baffert, W. Leibl, M. Fontecave, *Angew. Chem.* **2008**, *120*, 574 –577.

[222] S. Rau, B. Schäfer, D. Gleich, E. Anders, M. Rudolph, M. Friedrich, H. Görls, W. Henry, J. G. Vos, *Angew. Chem. Int. Ed.* **2006**, *45*, 6215–6218.

[223] M. Schulz, M. Karnahl, M. Schwalbe, J. G. Vos, *Coord. Chem. Rev.* **2012**, *256*, 1682–1705.

[224] J.J. Chen, M. D. Symes, S. C. Fan, M. S Zheng, H. N. Miras, Q. F. Dong, L. Cronin, *Adv. Mater.* **2015**, *27*, 4649–4654.

[225] H. Lv, Y. V. Geletii, C. Zhao, J. W. Vickers, G. Zhu, Z. Luo, J. Song, T. Lian, D. G. Musaev, C. L. Hill, *Chem. Soc. Rev.* **2012**, *41*, 7572–7589.

[226] X. J. Kong, Z. Lin, Z. M. Zhang, T. Zhang, W. Lin, *Angew. Chem. Int. Ed.* **2016**, *55*, 6411–6416.

[227] M. Stuckart, K. Y. Monakhov, *Chem. Sci.* **2019**, *10*, 4364–4376.

[228] Y. Akaishi, G. Yoshimura, Y. Mokuge, K. Sumi, P. Vas-Umnuay, Y. Inomata, T. Kida, T. Kida, *Chem. Commun.* **2024**, *60*, 9042–9045.

[229] M. Anjass, G. A. Lowe, C. Streb, *Angew. Chem. Int. Ed.* **2021**, *60*, 7522–7532.

[230] B. Matt, J. Moussa, L. M. Chamoreau, C. Afonso, A. Proust, H. Amouri, G. Izzet, *Organometallics* **2012**, *31*, 35–38.

[231] B. Matt, C. Coudret, C. Viala, D. Jouvenot, F. Loiseau, G. Izzet, A. Proust, *Inorg. Chem.* **2011**, *50*, 7761–7768.

[232] F. A. Black, A. Jacquart, G. Toupalas, S. Alves, A. Proust, I. P. Clark, E. A. Gibson, G. Izzet, *Chem. Sci.* **2018**, *9*, 5578–5584.

[233] E. Benazzi, J. Karlsson, Y. Ben M'Barek, P. Chabera, S. Blanchard, S. Alves, A. Proust, T. Pullerits, G. Izzet, E. A. Gibson, *Inorg. Chem. Front.* **2021**, *8*, 1610–1618.

[234] I. Azcarate, Z. Huo, R. Farha-, M. Goldmann-, H. Xu, B. Hasenknopf, E. Lacôte-, L. Ruhlmann, *Chem. Eur. J.* **2015**, *21*, 8271–8280.

[235] I. Azcarate, I. Ahmed, R. Farha, M. Goldmann, X. Wang, H. Xu, B. Hasenknopf, E. Lacôte, L. Ruhlmann, *Dalton Trans.* **2013**, *42*, 12688–12698.

[236] P. Endres, G. Sachdeva, A. Winter, D. Díaz, H. Görls, N. Fritz, C. Neumann, A. Turchanin, C. Streb, U. S. Schubert, *Inorg. Chem. Front.* **2025**, *13*, 1442–1448.

[237] S. Tschierlei, A. Neubauer, N. Rockstroh, M. Karnahl, P. Schwarzbach, H. Junge, M. Beller, S. Lochbrunner, *Phys. Chem. Chem. Phys.* **2016**, *18*, 10682–10687.

[238] E. Pomarico, M. Silatani, F. Messina, O. Braem, A. Cannizzo, E. Barranoff, J. H. Klein, C. Lambert, M. Chergui, *J. Phys. Chem. C* **2016**, *120*, 16459–16469.

[239] R. Bevernaegie, L. Marcélis, A. Moreno-Betancourt, B. Laramée-Milette, G. S. Hanan, F. Loiseau, M. Sliwa, B. Elias, *Phys. Chem. Chem. Phys.* **2018**, *20*, 27256–27260.

[240] G. J. Hedley, A. Ruseckas, I. D. W. Samuel, *J. Phys. Chem. A* **2009**, *113*, 2–4.

[241] G. J. Hedley, A. Ruseckas, I. D. W. Samuel, *Chem. Phys. Lett.* **2008**, *450*, 292–296.

[242] J. W. Wang, H. H. Huang, P. Wang, G. Yang, S. Kupfer, Y. Huang, Z. Li, Z. Ke, G. Ouyang, *JACS Au* **2022**, *2*, 1359–1374.

[243] M. Kleinschmidt, C. Van Wüllen, C. M. Marian, *J. Chem. Phys.* **2015**, *142*, 094301.

[244] G. E. Shillito, D. Preston, P. Traber, J. Steinmetzer, C. J. McAdam, J. D. Crowley, P. Wagner, S. Kupfer, K. C. Gordon, *Inorg. Chem.* **2020**, *59*, 6736–6746.

[245] G. Yang, L. Blechschmidt, L. Zedler, C. Zens, K. Witas, M. Schmidt, B. Esser, S. Rau, G. E. Shillito, B. Dietzek-Ivanšić, S. Kupfer, *Chem. Eur. J.* **2025**, *31*, e202404671.

[246] C. Wegeberg, D. Häussinger, S. Kupfer, O. S. Wenger, *J. Am. Chem. Soc.* **2024**, *146*, 4605–4619.

[247] V. Artero, M. Fontecave, *Chem. Soc. Rev.* **2013**, *42*, 2338–2356.

[248] J. A. Widegren, R. G. Finke, *J. Mol. Catal. A Chem.* **2003**, *198*, 317–341.

[249] L. Patiny, H. Musallam, A. Bolaños, M. Zasso, J. Wist, M. Karayilan, E. Ziegler, J. C. Liermann, N. E. Schlörer, *Beilstein J. Org. Chem.* **2024**, *20*, 25–31.

[250] R. Siebert, D. Akimov, M. Schmitt, A. Winter, U. S. Schubert, B. Dietzek, J. Popp, *ChemPhysChem* **2009**, *10*, 910–919.

[251] J. Kübel, R. Schroot, M. Wächtler, U. S. Schubert, B. Dietzek, M. Jäger *J. Phys. Chem. C* **2015**, *119*, 4742–4751.

[252] C. Müller, T. Pascher, A. Eriksson, P. Chabera, J. Uhlig, *J. Phys. Chem. A* **2022**, *126*, 4087–4099.

[253] B. Dietzek, T. Pascher, V. Sundström, A. Yartsev, *Laser Phys. Lett.* **2007**, *4*, 38–43.

[254] Gaussian 16, Revision C.02, M. J. Frisch, G. W. Trucks, H. B. Schlegel, G. E. Scuseria, M. A. Robb, J. R. Cheeseman, G. Scalmani, V. Barone, G. A. Petersson, H. Nakatsuji, X. Li, M. Caricato, A. V. Marenich, J. Bloino, B. G. Janesko, R. Gomperts, B. Mennucci, H. P. Hratchian, J. V. Ortiz, A. F. Izmaylov, J. L. Sonnenberg, D. Williams-Young, F. Ding, F. Lipparini, F. Egidi, J. Goings, B. Peng, A. Petrone, T. Henderson, D. Ranasinghe, V. G. Zakrzewski, J. Gao, N. Rega, G. Zheng, W. Liang, M. Hada, M. Ehara, K. Toyota, R. Fukuda, J. Hasegawa, M. Ishida, T. Nakajima, Y. Honda, O. Kitao, H. Nakai, T. Vreven, K. Throssell, J. A. Montgomery, Jr., J. E. Peralta, F. Ogliaro, M. J. Bearpark, J. J. Heyd, E. N. Brothers, K. N. Kudin, V. N. Staroverov, T. A. Keith, R. Kobayashi, J. Normand, K. Raghavachari, A. P. Rendell, J. C. Burant, S. S. Iyengar, J. Tomasi, M. Cossi, J. M. Millam, M. Klene, C. Adamo, R. Cammi, J. W. Ochterski, R. L. Martin, K. Morokuma, O. Farkas, J. B. Foresman, D. J. Fox, Gaussian, Inc., Wallingford CT, **2016**.

[255] A. D. Becke, *J. Chem. Phys.* **1993**, *98*, 5648–5652.

[256] C. Lee, W. Yang, R. G. Parr, *Phys. Rev. B* **1988**, *37*, 785–789.

[257] F. Weigend, R. Ahlrichs, *Phys. Chem. Chem. Phys.* **2005**, *7*, 3297–3305.

[258] G. E. Shillito, T. B. J. Hall, D. Preston, P. Traber, L. Wu, K. E. A. Reynolds, R. Horvath, X. Z. Sun, N. T. Lucas, J. D. Crowley, M. W. George, S. Kupfer, K. C. Gordon, *J. Am. Chem. Soc.* **2018**, *140*, 4534–4542.

[259] J. J. Sutton, D. Preston, P. Traber, J. Steinmetzer, X. Wu, S. Kayal, X. Z. Sun, J. D. Crowley, M. W. George, S. Kupfer, K. C. Gordon, *J. Am. Chem. Soc.* **2021**, *143*, 9082–9093.

[260] G. E. Shillito, D. Preston, J. D. Crowley, P. Wagner, S. J. Harris, K. C. Gordon, S. Kupfer, *Inorg. Chem.* **2024**, *63*, 4947–4956.

[261] C. Curutchet, G. D. Scholes, B. Mennucci, R. Cammi, *J. Phys. Chem. B* **2007**, *111*, 13253–13265.

[262] A. V. Marenich, C. J. Cramer, D. G. Truhlar, *J. Phys. Chem. B* **2009**, *113*, 6378–6396.

[263] S. Grimme, S. Ehrlich, L. Goerigk, *J. Comput. Chem.* **2011**, *32*, 1456–1465.

[264] L. Zedler, S. Kupfer, H. Schmidt, B. Dietzek-Ivanšić, *Chem. Eur. J.* **2024**, *30*, e202303079.

[265] T. Christoff-Tempesta, A. J. Lew, J. H. Ortony, *Gels* **2018**, *4*, 40.

[266] D. K. Smith, *Soft Matter* **2023**, *20*, 10–70.

[267] G. Picci, C. Caltagirone, A. Garau, V. Lippolis, J. Milia, J. W. Steed, *Coord. Chem. Rev.* **2023**, *492*, 215225.

[268] A. Fortunato, M. Mba, *Gels* **2021**, *7*, 85.

[269] J. Zhang, C. Y. Su, *Coord. Chem. Rev.* **2013**, *257*, 1373–1408.

[270] S. Dhibar, A. Dey, D. Ghosh, S. Majumdar, A. Dey, P. P. Ray, B. Dey, *ACS Omega* **2020**, *5*, 2680–2689.

[271] Q. Lin, T. T. Lu, X. Zhu, B. Sun, Q. P. Yang, T. B. Wei, Y. M. Zhang, *Chem. Commun.* **2015**, *51*, 1635–1638.

[272] P. Grondin, O. Roubeau, M. Castro, H. Saadaoui, A. Colin, R. Clérac, *Langmuir* **2010**, *26*, 5184–5195.

[273] A. Roy, S. Dhibar, S. Kumar, S. Some, P. Garg, P. Ruidas, S. Bhattacharjee, A. Bera, B. Saha, S. J. Ray, *Sci. Rep.* **2024**, *14*, 1–17.

[274] S. Dhibar, A. Dey, A. Dalal, S. Bhattacharjee, R. Sahu, R. Sahoo, A. Mondal, S. Mehebub Rahaman, S. Kundu, B. Saha, *J. Mol. Liq.* **2023**, *370*, 121021.

[275] A. Gasnier, G. Royal, P. Terech, *Langmuir* **2009**, *25*, 8751–8762.

[276] P. Terech, M. Yan, M. Maréchal, G. Royal, J. Galvez, S. K. P. Velu, *Phys. Chem. Chem. Phys.* **2013**, *15*, 7338–7344.

[277] X. Jiang, R. Du, R. Hübner, Y. Hu, A. Eychmüller, *Matter* **2021**, *4*, 54–94.

[278] G. Wang, X. Li, X. Yang, L.-X. Liu, Y. Cai, Y. Wu, S. Wang, H. Li, Y. Zhou, Y. Wang, Y. Zhou, *Chem. Eur. J.* 2022, 28, e202201834.

[279] L. E. Nita, A. Ghilan, A. G. Rusu, I. Neamtu, A. P. Chiriac, *Pharmaceutics* **2020,** *12***,** 449.

[280] J. Mao, J. Iocozzia, J. Huang, K. Meng, Y. Lai, Z. Lin, *Energy Environ. Sci.* **2018**, *11*, 772–799.

[281] R. Ganesamoorthy, V. K. Vadivel, R. Kumar, O. S. Kushwaha, H. Mamane, *J. Clean. Prod.* **2021**, *329*, 129713.

[282] N. R. Khan, T. Sharmin, A. B. Rashid, *Heliyon* **2024**, *10*, e23102.

[283] W. Liu, A. K. Herrmann, N. C. Bigall, P. Rodriguez, D. Wen, M. Oezaslan, T. J. Schmidt, N. Gaponik, A. Eychmüller, *Acc. Chem. Res.* **2015**, *48*, 154–162.

[284] Y. Hu, H. Zhuo, Z. Chen, X. Peng, L. Zhong, R. Sun, *J. Mater. Sci. Technol.* **2021**, *71*, 67–74.

[285] H. Zhang, W. Han, K. Xu, Y. Zhang, Y. Lu, Z. Nie, Y. Du, J. Zhu, W. Huang, *Nano Lett.* **2020**, *20*, 3449–3458.

[286] Q. Liu, X. Wang, *Matter* **2020**, *2*, 816–841.

[287] S. Guo, C. W. Pan, M. Hou, Y. T. Hou, S. Yao, T. B. Lu, Z. M. Zhang, *Angew. Chem. Int. Ed.* **2025**, *64*, e202420398.

[288] Z. R. Zhang, H. Y. Sui, W. X. Shi, J. Ren, S. Yao, Lu, T. B. L.u, Z. M. Zhang, *Angew. Chem., Int. Ed.* **2025**, *64*, e202416711.

[289] B. Li, L. Xuan, L. Wu, L. *Macromol. Rapid Commun.* **2022**, *43*, 2200019.

[290] X. Meng, H. N. Wang, Y. H. Zou, L. S. Wang, Z. Y. Zhou, *Dalton Trans.* **2019**, *48*, 10422–10426.

[291] Z. He, H. Wang, Y. Wang, Y. Wu, H. Li, L. Bi, L. Wu, *Soft Matter* **2012**, *8*, 3315–3321.

[292] L. Casimiro, F. Volatron, G. Boivin, B. Abécassis, S. Alves, D. Brouri, D. Montero, J. M. Guigner, L. M. Chamoreau, G. Gontard, D. Portehault, Y. Li, A. Proust, R. Lescouëzec, G. Ducouret, A. Solé-Daura, P. Davidson, T. Merland, G. Izzet, *JACS Au* **2024**, *4*, 4948–4956.

[293] L. Ni, G. Yang, C. Sun, G. Niu, Z. Wu, C. Chen, X. Gong, C. Zhou, G. Zhao, J. Gu, W. Ji, X. Huo, M. Chen, G. Diao, *Mater. Today Energy* **2017**, *6*, 53–64.

[294] F. Yahya, H. El-Rassy, G. Younes, R. Al-Oweini, *Desalin. Water Treat.* **2020**, *195*, 321–333.

[295] T. Liu, Y. Zhang, C. Wang, Y. Kang, M. Wang, F. Wu, W. Huang, *Small* **2024**, *20*, 1–11.

[296] R. Song, X. Zhang, H. Wang, C. Liu, *Molecules* **2022**, *27*, 1–12.

[297] S. Wang, X. Wang, X. Y. Shi, C. X. Meng, C. L. Sun, Z. S. Wu, *New Carbon Mater.* **2021**, *36*, 189–197.

[298] Y. Wang, X. Kong, W. Xu, F. Jiang, B. Li, L. Wu, *Inorg. Chem.* **2018**, *57*, 3731–3741.

[299] J. C. Raabe, T. Esser, M. J. Poller, J. Albert, *Catal. Today* **2024**, *441*, 114899.

[300] S. C. Karunakaran, B. J. Cafferty, K. S. Jain, G. B. Schuster, N. V. Hud, *ACS Omega* **2020**, *5*, 344–349.

[301] S. R. Raghavan, B. H. Cipriano, in *Gel Formation: Phase Diagrams Using Tabletop Rheology and Calorimetry*, (Eds.: R.G. Weiss, P. Terech), Springer, Dordrecht **2005**, pp. 241–252.

[302] P. Venkateswaslu, *J. Chem. Phys.* **1952**, *20*, 923.

[303] E. L. Pace, L. J. Noe, *J. Chem. Phys.* **1968**, *49*, 5317–5325.

[304] S. Khlifi, S. Yao, C. Falaise, P. Bauduin, V. Guérineau, N. Leclerc, M. Haouas, H. Salmi-Mani, P. Roger, E. Cadot, *Chem. Eur. J.* **2024**, *30*, e202303815.

[305] S. Mahvash, V. A. Zavareh, S. Taymouri, M. Mirian, M. Ramezani-Aliakbari, F. Dousti, M. Rostami, *J. Drug Deliv. Sci. Technol.* **2023**, *87*, 104778.

[306] F. Jones, H. Tran, D. Lindberg, L. Zhao, M. Hupa, *Energy and Fuels* **2013**, *27*, 5663–5669.

[307] N. Tancredi, M. Gabús, M. I. Yoshida, A. C. Suárez, *Eur. J. Wood Wood Prod.* **2017**, *75*, 633–638.

[308] A. Marciel, M. Graça, A. Bastos, L. Pereira, J. S. Kumar, J. Borges, F. Vaz, M. Peres, S. Magalhães, K. Lorenz, R. Silva, *Materials* **2021**, *14*, 1–20.

[309] C. Peng, T. Chen, B. Zeng, G. Chen, C. Yuan, Y. Xu, L. Dai, *Compos. B Eng.* **2020**, *186*, 107780.

[310] Z. Y. Tian, P. M. Kouotou, N. Bahlawane, P. H. T. Ngamou, *J. Phys. Chem. C* **2013**, *117*, 6218–6224.

[311] D. Hoang, Y. Li, M. S. Jung, S. K. Sandstrom, A. M. Scida, H. Jiang, T. C. Gallagher, B. A. Pollard, R. Jensen, N. C. Chiu, K. Stylianou, W. F. Stickle, P. A. Greaney, X. Ji, *Adv. Energy Mater.* **2023**, *13*, 1–8.

[312] S. A. Schmidt, N. Kumar, A. Shchukarev, K. Eränen, J. P. Mikkola, D. Y. Murzin, T. Salmi, *Appl. Catal. A Gen.* **2013**, *468*, 120–134.

[313] L. Han, S. Song, M. Liu, S. Yao, Z. Liang, H. Cheng, W. Liu, R. Lin, G. Qi, X. Liu, Q. Wu, J. Luo, H. L. Xin, *J. Am. Chem. Soc.* **2020**, *142*, 12563.

[314] M. Thommes, K. Kaneko, A. V. Neimark, J. P. Olivier, F. Rodriguez-Reinoso, J. Rouquerol, K. S. W. Sing, Pure Appl. Chem. **2015**, *87*, 1051–1069.

[315] C. L. Hill, C. M. Prosser-McCartha, *Coord. Chem. Rev.* **1995**, *143*, 407–455.

[316] Z. Wei, J. Wang, H. Yu, S. Han, Y. Wei, *Molecules* **2022**, *27*, 5212.

[317] D. Barats, R. Neumann, *Adv. Synth. Catal.* **2010**, *352*, 293–298.

[318] A. M. Khenkin, L. J. W. Shimon, R. Neumann, *Inorg. Chem.* **2003**, *42*, 3331–3339.

[319] Y. Wang, Z. Wu, H. Yu, S. Han, Y. Wei, *Green Chem.* **2020**, *22*, 3150–3154.

[320] M. Zhang, Y. Zhai, S. Ru, D. Zang, S. Han, H. Yu, Y. Wei, *Chem. Commun.* **2018**, *54*, 10164–10167.

[321] Z. Wei, S. Ru, Q. Zhao, H. Yu, G. Zhang, Y. Wei, *Green Chem.* **2019**, *21*, 4069–4075.

[322] J. Schindelin, I. Arganda-carreras, E. Frise, V. Kaynig, M. Longair, T. Pietzsch, S. Preibisch, C. Rueden, S. Saalfeld, B. Schmid, J. Tinevez, D. J. White, V. Hartenstein, K. Eliceiri, P. Tomancak, A. Cardona, *Nat. Methods* **2019**, *9*, 676–682.

6 List of Figures

7 List of Tables

Scientific Contributions

Publications in Peer-reviewed Journals

1. **GS 1- G. Sachdeva**, S. Maloul, J. Zolg, et al. “Polyoxometalate Aerogels Formed by Organofunctionalized Anderson Polyoxometalates as Low Molecular Weight Gelators.” Adv. Mater. Interfaces 12, no. 22 (2025): e00597. https://doi.org/10.1002/admi.202500597.
2. **GS 2-** P. Endres, **G. Sachdeva**, A. Winter, D. Díaz, H. Görls, N. Fritz, C. Neumann, A. Turchanin, C. Streb and U. S. Schubert, *Inorg. Chem. Front.*, 2026, **13**, 1442. https://doi.org/10.1039/D5QI02141C.

Conferences and Workshops attended

Date	Conference / Workshop	Contribution
27.03.23 - 31.03.23	CataLight Spring School, Kloster Banz	Participation
12.06.23 - 14.06.23	CataLight NFDI-RDM Workshop, Mainz	Participation
25.07.23 - 29.07.23	25th International Symposium on the Photochemistry and Photophysics of Coordination Compounds, 2023, Ulm.	Poster
20.10.23 - 21.10.23	POM Symposium, Paris	Poster
04.06.24 – 06.06.23	CataLight Symposium and Workshop, Ulm	Participation
09.09.24 - 12.09.24	LightCheC Summer School 2024, Switzerland	Poster Poster prize
16.09.24 - 18.09.24	29th Lecture Conference on Photochemistry, Mainz	Poster
21.07.25 - 25.07.25	FMOCS VIII: Frontiers in Metal Oxide Cluster Science, Mainz	Poster
22.09.25 - 26.09.25	CataLight Summer School and Workshop, Eisenach	Participation

Curriculum Vitae

This page has been removed for reasons of data protection.

Acknowledgements

This page has been removed for reasons of data protection.

This page has been removed for reasons of data protection.

Statutory Declaration

The present work was carried out during the period from January 2023 to May 2026 in the research group of [redacted] at the Department of Chemistry, Johannes Gutenberg University, Mainz.

I, Garima Sachdeva, hereby declare that I have written this thesis, titled “Organofunctionalized Polyoxometalates as Functional Components in (Photo-) Catalysis.” on my own and have used no sources other than those cited. All verbatim or paraphrased texts are clearly cited and acknowledged in accordance with the bibliographical rules. I affirm that I have not used any sources whose use the examiner has explicitly prohibited. Throughout this research work, I followed the rules of standard scientific practice as formulated by the statutes of Johannes Gutenberg University, Mainz.

The AI-tools used for writing this work are mentioned in Table 30. By submitting this work, I assume responsibility for the entire submitted product. Thus, I am responsible for any AI-generated content that I have incorporated in this work. I have certified the accuracy of included (AI-generated) statements and content to the best of my knowledge and belief.

I am aware that a violation of the aforementioned points will result in disciplinary consequences and, particularly, may lead to the doctoral thesis being graded as “failed.” Enrollment may be revoked for up to two years if a student cheats on examinations on two or more cases (§ 69 (4) and (5) HochSchG).

Furthermore, I declare that the presented work has not been submitted to the same or any university or institution for the award of another academic degree or qualification. I have not completed or failed a doctorate or a comparable graduation procedure in this doctoral subject with the doctoral degree “Dr. rer. nat.”. Also, I have not applied for admission to a doctoral examination or a comparable graduation procedure in the subject of this doctorate “Dr. rer. nat.” at the Johannes Gutenberg University Mainz or any other university with the right to award doctorates. I also affirm that I have not used any paid assistance from the third-parties, in particular no doctoral recommendation or mediation.

I am aware of the current doctoral degree regulations at the Johannes Gutenberg University, Mainz dated October 18, 2021 in the version of February 17, 2025 for the completion of “Dr. rer. nat.” degree.

I hereby apply for the doctoral degree in natural science from Johannes Gutenberg University, Mainz for the first time.

Place, Date and Signature

Table 30: Use of AI-tools

AI-tool	Used for	Why	When
ChatGPT and Microsoft Copilot	Rephrasing	Rephrasing the complex structures to improve the readability.	Throughout the entire thesis.
DeepL Translate	English to German translation	To find accurate translation of German words.	For converting Abstract.